

BUREAU OF SHIPS
DEPARTMENT OF THE NAVY

HYDRODYNAMICS OF HYDROFOIL CRAFT
SUBCAVITATING HYDROFOIL SYSTEMS

Authors:
Johan C. Vermeulen
Roderick A. Barr
Milton Martin

Prepared by
HYDRONAUTICS, Incorporated

under

Contract No. NObs-78396
SF-013-02-1

and

Contract No. NObs-90224
SS600-000, Task 1701

APRIL 1964

TABLE OF CONTENTS

CHAPTER 1

CAVITATION INCEPTION ON FOILS, STRUTS AND PODS

	<u>Page</u>
THE INCIPIENT CAVITATION NUMBER	1.7
COMPARISON BETWEEN EXPERIMENT AND THEORY	1.10
FOILS WITH LOW INCIPIENT CAVITATION NUMBER AT DESIGN POINT.....	1.11
Symmetrical Section	1.13
Camber-Line.....	1.14
SELECTION OF OPTIMUM FOILS	1.18
CAVITATION INCEPTION ON PODS (AXISYMMETRIC BODIES).....	1.29
CAVITATION AT FOIL-STRUT-POD INTERSECTIONS.....	1.36
REFERENCES	1.43

TABLE OF CONTENTS (Continued)

CHAPTER 2

CHOICE OF FOIL SYSTEM FOR OPTIMUM PERFORMANCE

	<u>Page</u>
INTRODUCTION.....	2.5
FULLY SUBMERGED FOIL SYSTEMS.....	2.7
Effect of Number of Struts and Aspect Ratio.....	2.7
Determination of Section Modulus \bar{z}	2.10
Calculation of Foil Drag.....	2.13
Estimation of Strut Size.....	2.15
Calculation of the Strut and Interference Drag.....	2.19
Determination of the System of Minimum Drag.....	2.22
APPENDIX 2.1 - THE EFFECT OF THE SEAWAY ON FOIL DESIGN.....	2.24
REFERENCES.....	2.26

TABLE OF CONTENTS (Continued)

CHAPTER 3

VENTILATION INCEPTION OF SURFACE PIERCING
AND SUBMERGED FOILS AND STRUTS

	<u>Page</u>
INTRODUCTION.....	3.4
THE CAUSES OF VENTILATION.....	3.4
THE EFFECTS OF VENTILATION.....	3.6
MECHANISMS OF VENTILATION INCEPTION.....	3.6
SEPARATION ON TYPICAL HYDROFOIL SECTIONS.....	3.8
APPLICABLE TYPES OF SEPARATION.....	3.12
CONDITIONS REQUIRED FOR VENTILATION INCEPTION.....	3.13
Separation.....	3.13
Extent of Separation and Experimental Results.....	3.16
Pressure Requirements.....	3.24
Speeds Required.....	3.25
Ventilation Resulting from Cavitation.....	3.26
APPLICATIONS TO FULLY WETTED HYDROFOILS.....	3.27
Surface Piercing Foils and Struts.....	3.29
Fully Submerged Foils.....	3.30
PREVENTION OF VENTILATION.....	3.31
REFERENCES.....	3.33

TABLE OF CONTENTS (Continued)

CHAPTER 4

TRIM, ALTITUDE AND PRE-TAKEOFF
RESISTANCE OF HYDROFOIL CRAFT

	<u>Page</u>
SUMMARY.....	4.7
INTRODUCTION.....	4.7
THE BASIC EQUATIONS GOVERNING TRIM AND ALTITUDE.....	4.8
The Drag-Thrust Couple or Moment.....	4.14
SOLUTION OF THE EQUATIONS.....	4.16
Methods of Solution.....	4.18
TRIM AND ALTITUDE AFTER TAKEOFF.....	4.20
Fully Submerged Foils with Flaps and/or Incidence Control Forward and Aft.....	4.20
Surface Piercing Foils Forward and Fully Submerged Foils Aft.....	4.25
Solutions of the Equations Before Takeoff.....	4.28
HYDRODYNAMIC COEFFICIENTS.....	4.33
Foil Hydrodynamic Coefficients.....	4.34
Surface Piercing Foil Characteristics.....	4.40
Hull Hydrodynamic Forces.....	4.43
Hull Hydrostatic Forces.....	4.49
Resistance of Hydrofoil Craft Before Takeoff.....	4.51
Factors Influencing Hull Resistance.....	4.59
REFERENCES.....	4.61

TABLE OF CONTENTS (Continued)

CHAPTER 5

LONGITUDINAL STABILITY (CONTROLS FIXED)

	<u>Page</u>
INTRODUCTION.....	5.7
THE LONGITUDINAL STABILITY EQUATIONS.....	5.9
ROUTH'S STABILITY CRITERION.....	5.19
SOLUTIONS OF THE CHARACTERISTIC EQUATION.....	5.23
ROOT-LOCUS METHOD.....	5.30
PRELIMINARY ANALYSIS FOR LONGITUDINAL STABILITY.....	5.35
Uncoupled Heave Damping.....	5.35
Effect of Speed.....	5.38
Uncoupled Heave Stiffness.....	5.39
Effect of Speed.....	5.43
Uncoupled Heave Damping Ratio.....	5.43
Effect of Speed.....	5.46
Uncoupled Pitch Damping.....	5.46
Uncoupled Pitch Stiffness.....	5.48
Effect of Speed.....	5.53
Uncoupled Pitch Damping Ratio.....	5.54
The Coupling Terms.....	5.57
EXAMPLE.....	5.63
Effect of Speed.....	5.73
CONCLUDING REMARKS.....	5.74
REFERENCES.....	5.76

HYDRONAUTICS, Incorporated

1.0

CHAPTER 1

CAVITATION INCEPTION ON FOILS,
STRUTS AND PODS

By

Johan C. Vermeulen

and

Roderick A. Barr

NOTATION

a	NACA mean line designation
b	Foil span
c	Foil chord
\bar{c}	Mean chord of foil
c_l	Two-dimensional lift coefficient
c_{l_i}	Two-dimensional design lift coefficient
Δc_l	$= c_{l_l} - c_{l_u}$
C_L	Three-dimensional lift coefficient of foil
$\left(C_L \right)_{\frac{h}{\bar{c}}}$	Three-dimensional lift coefficient of foil based on mean chord (from Reference 1.11)
C_p	Pressure coefficient defined in Equation 1.1
$C_{p \text{ min}}$	Minimum pressure coefficient
$\left[c_{l_l} \right]_{\frac{h}{c, \Lambda}}$	Two-dimensional lift coefficient on the lower incipient cavitation boundary
$\left[c_{l_u} \right]_{\frac{h}{c, \Lambda}}$	Two-dimensional lift coefficient on the upper incipient cavitation boundary
$\left[\frac{c_l}{C_L} \right]_{\infty, \Lambda}$	Ratio of local to three-dimensional lift coefficient for a swept foil at infinite depth

$\left[\frac{c_l}{C_L} \right]_{\infty, \Lambda=0}$ Ratio of local to three-dimensional lift coefficient for an unswept foil at infinite depth

$\left[\frac{c_l}{C_L} \right]_{\frac{h}{c}, \Lambda}$ Ratio of local to three-dimensional lift coefficient for a swept foil at depth h

$\left[\left(\frac{c_l}{C_L} \right)_{\frac{h}{c}, \Lambda} \right]_{\max}$ Maximum ratio of local to three-dimensional lift coefficient for a swept foil at depth h

$[C_{L_l}]_{\frac{h}{c}, \Lambda}$ Allowable three-dimensional lift coefficient on the lower incipient cavitation boundary

$[C_{L_u}]_{\frac{h}{c}, \Lambda}$ Allowable three-dimensional lift coefficient on the upper incipient cavitation boundary

$[C_{L_\alpha}]_{\frac{h}{c}, \Lambda}$ Three-dimensional lift curve slope

$\left[\frac{C_{L_\alpha}}{[C_{L_\alpha}]_{\infty}} \right]_{\frac{h}{c}}$ Ratio of the three-dimensional lift curve slope at finite depth to that at infinite depth

$[\Delta C_L]_{h/\bar{c}} = [C_{L_u} - C_{L_l}]_{h/\bar{c}, \Lambda}$

d Maximum diameter of pod or body

D = $\pi\lambda(1 - \cos \Lambda)$

g Acceleration of gravity

1.3

h	Depth of submergence
K_h	Parameter defined in Equation 1.16
l	Length of pod or body
l/d	Slenderness ratio of pod or body
$(l/d)_e$	Effective slenderness ratio for ellipsoids
$(l/d)_v$	Effective slenderness ratio including viscous effects
m	Ratio of pod length to foil root chord
p	Ratio of strut chord at pod to foil root chord
p_a	Atmospheric pressure
p_h	Free stream pressure due to submergence
p_{min}	Minimum pressure on foil
p_v	Vapor pressure of fluid
R_e	Reynolds number based on length - $\frac{VL}{\nu}$
S	Low-speed pressure coefficient defined in Reference 1.1
t	Foil thickness
$\frac{t}{c}$	Foil thickness-chord ratio
u	Local velocity on foil
$\frac{u}{V}$	Local velocity ratio on foil

1.4

u_{body}	Perturbation velocity on the surface of a body
u_{flow}	Perturbation velocity away from the body surface
v	Local velocity due to thickness
$\frac{v}{V}$	Local velocity ratio due to thickness
$\frac{\Delta v}{V}$	Local velocity ratio due to camber
$\frac{\Delta v_a}{V}$	Local velocity ratio due to angle of attack
V	Free stream velocity
V_c	Incipient cavitation speed defined in Equation 1.11
$V\sqrt{d}$	Cavitation factor for incipient cavitation number
x	Distance along major axis of body measured from nose
y	Distance from body surface measured normal to surface
$\frac{y}{c}$	Distance from foil surface in foil chords
$\frac{y}{d}$	Distance from body surface in body diameters
y_c	Ordinate of logarithmic camber line
y_t	Ordinate of symmetrical sections
α	Angle of attack

$\Delta\alpha$	Allowable angle of attack range
δ	Boundary layer thickness
δ^*	Boundary layer displacement thickness
η	Nondimensional span station measured from the plane of symmetry ($= 2y/b$)
η_{crit}	Nondimensional span station for maximum $(c_l/C_L)_{\infty, \Lambda}$
λ	Taper ratio ($=$ tip chord/root chord)
ρ	Fluid density
σ	Cavitation number
σ_i	Incipient cavitation number
σ_{i_c}	Incipient cavitation number on the incipient cavitation boundary
σ_{i_n}	Incipient cavitation number of nth component
σ_{i_s}	Incipient cavitation number of the strut
$(\sigma_i)_{\frac{h}{c}}$	Incipient cavitation number at finite depth
σ_{i_∞}	Incipient cavitation number at infinite depth
σ_{i_Λ}	Incipient cavitation number for a swept foil
$(\sigma_{i_s})_{foil}$	Incipient cavitation number at the foil due to the strut

1.6

$$\left(\sigma_{1f}\right)_{\text{strut}}$$

Incipient cavitation number at the strut due to the foil

$$\sigma_{1\text{body}}$$

Incipient cavitation number on the body surface

$$\sigma_{1\text{flow}}$$

Incipient cavitation number due to a body at a point away from the body surface

$$\left(\frac{\sigma_{1\text{flow}}}{\sigma_{1\text{body}}}\right)_c$$

Ratio of incipient cavitation number in the flow and on the foil due to uniform camber

$$\left(\frac{\sigma_{1\text{flow}}}{\sigma_{1\text{body}}}\right)_T$$

Ratio of incipient cavitation number in the flow and on the foil due to foil thickness

Λ

Sweep angle of the quarter-chord line

THE INCIPIENT CAVITATION NUMBER

The selection of subcavitating hydrofoil sections follows very closely that of airfoils with good compressibility characteristics. There are, however, a few characteristics peculiar to the hydrofoil which make separate consideration necessary.

From the Bernoulli equation for potential flow, written for a free-stream point at the same depth as a submerged hydrofoil and at any point on the hydrofoil, we obtain for the pressure coefficient on the hydrofoil:

$$C_p = \frac{p - (p_a + p_h)}{\frac{1}{2}\rho V^2} = 1 - \left(\frac{u}{V}\right)^2 \quad [1.1]$$

where

p is the local pressure on the hydrofoil,

p_a is the atmospheric pressure (~ 2120 psf),

$p_h = \rho gh$ is the free stream pressure due to submergence ($\sim 64h$ psf, h = submergence in feet),

ρ is the fluid density,

V is the free-stream velocity,

and

$$\frac{u}{V} = \frac{v}{V} \pm \frac{\Delta v}{V} \pm \frac{\Delta v_a}{V},$$

is the local velocity ratio on the hydrofoil surface (upper signs refer to points on the cross section upper contour, lower signs refer to points on the section lower contour), which is considered to be composed of three

1.8

separate and independent components as follows (Reference 1.1):

- (1) The velocity ratio, $\frac{v}{V}$, due to the thickness of the basic symmetrical section at zero angle of attack:
- (2) The change in velocity ratio, $\frac{\Delta v}{V}$, due to the shape of the camber line at its ideal angle of attack.
- (3) The change in velocity ratio, $\frac{\Delta v_a}{V}$, associated with the angle of attack.

As the free-stream velocity V increases, the pressure in the fluid in the vicinity of the hydrofoil falls and the smallest pressure that can occur in the fluid is the vapor pressure of the fluid provided gas nuclei of sufficient size are present. When the fluid boils, cavities filled with vapor occur and so-called "cavitation" sets in. Thus when the minimum pressure in the flow field is decreased to the vapor pressure, cavitation begins. If the velocity is increased beyond this inception point (or the ambient pressure decreased) increasing areas of the flow will be brought to the vapor pressure and the cavitation zone will increase in size. In some cases, this cavitation zone consists of individual expanding cavities, in others, the zone may be largely a single vapor filled pocket whose length depends on the degree to which the ambient pressure has been reduced below the inception value.

The state of cavitation is characterized by the "cavitation number"

$$\sigma = \frac{p_a + p_h - p_v}{\frac{1}{2}\rho V^2} \quad [1.2]$$

where p_v is the vapor pressure of the fluid (~ 37 psf at 60°F). Cavitation on a hydrofoil will occur at any point on the surface of the hydrofoil where the local pressure drops to the value of the vapor pressure of the fluid. The cavitation number at which cavitation first begins on a hydrofoil section is known as the "incipient cavitation number". This value is arrived at theoretically by assuming that cavitation begins at the point of minimum pressure on the hydrofoil surface. Hence, if in Equation [1.1] $p = p_{\min} = p_v$ then $C_p = C_{p_{\min}}$ and Equation [1.2] gives for the incipient cavitation number:

$$\sigma_i = -C_{p_{\min.}} = \left[\frac{v}{V} \pm \frac{\Delta v}{V} \pm \frac{\Delta v_a}{V} \right]_{\max.}^2 - 1 \quad [1.3]$$

Experiments on hydrofoil profiles show three typical forms of cavitation (see Figure 1.1):

(1) Cavitation on the upper contour which starts from the leading edge (between points A and B of Figure 1.1) — this occurs if the front stagnation point lies on the lower contour, so that the flow accelerates around the nose from the lower contour and the minimum pressure lies very far forward.

(2) Cavitation which starts approximately from the point of maximum thickness (between points B and C of Figure 1.1) when the hydrofoil profile is at or near the ideal angle of incidence or when the front stagnation point lies near the hydrofoil nose.

(3) Cavitation on the lower contour which starts from the leading edge (between the points C and D of Figure 1.1) — this occurs if the front stagnation point lies on the upper contour, so that the flow accelerates around the nose from the upper contour.

In Figure 1.2, the negative of the computed pressure coefficient for various locations along the chord of an NACA 4412 profile is plotted versus lift coefficient. The envelope of this family of curves, the dividing boundary between cavitating and non-cavitating regions, is the theoretical curve of incipient cavitation number.

COMPARISON BETWEEN EXPERIMENT AND THEORY

The results of Kermeen's cavitation tests (References 1.2 and 1.3) on the NACA 4412 and 66₁-012 sections and Numachi's tests (Reference 1.4) on Clark Y sections of several thickness-chord ratios together with results predicted by the above theory are presented in Figures 1.3 - 1.8. These figures indicate rather poor correlation between theory and experiment. In the following we will discuss the most important factor which could possibly give rise to this difference.

The differences between theory and experiment in Figures 1.3 - 1.8 for incipient leading edge cavitation on the upper contour could for a significant part be due to the laminar "separation bubble"(References 1.5 and 1.6). For hydrofoils having a large change of curvature at or near the leading edge, a high suction pressure peak forms over the nose at a relatively low angle of

attack. A bubble transition region moving forward to the leading edge, appears to reduce (fair off) the change in curvature, having sufficient effect on the flow to reduce this suction peak greatly. There is therefore a considerable reduction in incipient cavitation number for the same incidence. The difference between observed and predicted values of incipient leading edge cavitation on the lower contour of the NACA 4412 section at negative angles of incidence can be explained in a similar way. For the Clark Y sections, tested by Numachi et al., however, we have to keep in mind that the Clark Y sections are flat over most of the bottom surface with a small change of curvature at the nose. A bubble transition region moving forward over these section's lower contour at negative angles of incidence, appears to increase the curvature, having sufficient effect on the flow to increase the peak pressure. Hence there is an increase in incipient cavitation number in this case.

From the preceding it is clear that the "change in curvature" near the leading edge is an important factor. Small differences in the nose contour could easily account for large differences between the observed and predicted values of incipient cavitation number. Insufficient knowledge of the fundamental mechanics of the "separation bubble", however, prevents any conclusive confirmation at this time.

FOILS WITH LOW INCIPIENT CAVITATION NUMBER AT THE DESIGN POINT

Despite the simplifying assumptions made in the prediction of the incipient cavitation number as expressed by Equations [1.3] and the rather poor correlation it gives with experimental results,

1.12

this expression can serve as a useful tool in comparing the effect of angle of attack on the incipient cavitation number for different hydrofoil sections of "similar" shape.

For preliminary and quick comparisons between different hydrofoils one can employ the critical Mach Number curves presented in Reference 1.1. Although there is no physical relationship between Mach Number effects in air and the low subsonic flow about hydrofoils, the existing critical Mach Number curves may be used to predict cavitation inception speeds because both are directly related to the minimum pressure coefficient. For comparison with the theory expressed by Equation [1.3] we have calculated various values of incipient cavitation number for the NACA 4412 airfoil by employing the critical Mach Number curves of Reference 1.1. These values are plotted in Figure 1.3. For a section lift coefficient $c_l = 0$ we find for example, from the curve given on page 116 of Reference 1.1 that the critical Mach Number for the NACA 4412 airfoil is equal to 0.475, which value gives us the low-speed pressure coefficient $S = 2.85$ from the curve given on page 114 of Reference 1.1. Since this S is defined in Reference 1.1 by the expression:

$$S = \left[\frac{v}{V} \pm \frac{\Delta v}{V} \pm \frac{\Delta v_a}{V} \right]_{\max}^2$$

we find for the incipient cavitation number σ_1 at $c_l = 0$,

$$\sigma_1 = S - 1 = 2.85 - 1 = 1.85.$$

The problem of selecting a hydrofoil with high incipient cavitation number is, according to Equation [1.3], reduced to finding a hydrofoil section with a minimum peak value of $(u/V)^2$. To the first order, the velocity increment distributions on symmetrical sections of "similar" shape are proportional to the thickness, and likewise the velocity increment distributions on camber lines of "similar" shape are proportional to the camber. (This follows from the additive property of thin sections of small camber). As a first measure, therefore, a low peak velocity can be obtained by selecting for small thickness and low camber. Having decided on the maximum thickness and camber, it is possible that the peak velocity increment can be further reduced by refinements in section shape. The problem for hydrofoils operating at zero angle of attack can be rephrased as follows: What symmetrical section has the lowest possible peak velocity increment for a given maximum thickness, and what camber-line at zero angle of attack has the lowest possible peak velocity increment for a given design lift coefficient? The answer to this problem has already been found in connection with the design of airfoils having good compressibility characteristics, namely:

Symmetrical Section: The elliptic symmetrical section, having the equation

$$y_t = \frac{t}{c} \sqrt{x(1-x)} \quad [1.4]$$

where (t/c) is the thickness-chord ratio. This section at zero

1.14

incidence, has, to the first order, a constant velocity ratio over both surfaces given by

$$\frac{v}{V} = 1 + \frac{t}{c} \quad [1.5]$$

except at the leading and trailing edges, which are stagnation points.

Camber-Line: The logarithmic camber-line (NACA $a = 1.0$ mean line), having equation

$$y_c = - \frac{c_{l_1}}{4\pi} \left[(1-x) \ln (1-x) + x \ln x \right] \quad [1.6]$$

where c_{l_1} is the design lift coefficient. This mean line has, to the first order, a constant velocity increment on the upper surface given by

$$\frac{\Delta v}{V} = \frac{1}{4} c_{l_1} \quad [1.7]$$

and an equal velocity decrement on the lower surface except at the leading and trailing edges, which are again stagnation points. The ideal angle of incidence is zero degrees.

1.15

For the above symmetrical section and camber-line the velocity increments are constant along the chord. Such distributions are called "flat-topped" and clearly there is no peak at the ideal angle of attack.

The equation of a hydrofoil section of maximum thickness-chord ratio t/c and design lift coefficient c_{l_1} , having theoretically the highest possible incipient cavitation number at zero angle of attack, is therefore:

$$y = -\frac{c_{l_1}}{4\pi} \left[(1-x) \ln(1-x) + x \ln x \right] \pm \frac{t}{c} \sqrt{x(1-x)} \quad [1.8]$$

The velocity distribution for this section is given to first order as:

$$\frac{u}{V} = 1 + \frac{t}{c} \pm \frac{1}{4} c_{l_1} \quad [1.9]$$

and the incipient cavitation number of this section at zero angle of attack is:

$$\sigma_1 = \left[1 + \frac{t}{c} + \frac{1}{4} c_{l_1} \right]^2 - 1 \approx 2\left(\frac{t}{c}\right) + \frac{1}{2} c_{l_1} \quad [1.10]$$

1.16

The theoretical optimum section, developed above, can be regarded as optimum in the sense that it places a limit on the design of sections having the best incipient cavitation characteristics.

There are objections to the practical use of the theoretically optimum section as a hydrofoil section. In the first place a hydrofoil section which is optimum at zero angle of attack is not necessarily optimum at large or even moderate departures from this condition. The nose radius should be such that the "change in curvature" near the leading edge for the operating angle of attack range has a minimum adverse effect on the flow. Another important consideration is that a sharper trailing edge is desirable to avoid prohibitive regions of separation at the rear. Finally the NACA $a = 1.0$ camber-line is not always desirable because of its steep adverse pressure gradient in the trailing region and thus its increased tendency to trailing edge stall.

For practical applications, the NACA 16- and 6-series airfoils combined with an NACA a-type mean line (Reference 1.1), not only have better physical characteristics (relatively sharper leading and trailing edges), but also close to optimum cavitation numbers at design angle of attack. The following table presents a comparison of the incipient cavitation number at design angle of attack for various NACA 16- and 6-series airfoils with the optimum section (elliptic section; $a = 1$) developed above.

TABLE 1

Incipient Cavitation Number at Design Angle of Attack

Elliptic section	}	+ NACA-a mean line	$\sigma_1 = 2.00 \left(\frac{t}{c} \right) + \frac{c_{l_1}}{1+a}$
NACA 16-series			$\sigma_1 = 2.28 \left(\frac{t}{c} \right) + \frac{c_{l_1}}{1+a}$
NACA 66-series			$\sigma_1 = 2.42 \left(\frac{t}{c} \right) + \frac{c_{l_1}}{1+a}$
NACA 65-series			$\sigma_1 = 2.58 \left(\frac{t}{c} \right) + \frac{c_{l_1}}{1+a}$
NACA 64-series			$\sigma_1 = 2.65 \left(\frac{t}{c} \right) + \frac{c_{l_1}}{1+a}$
NACA 63-series			$\sigma_1 = 2.67 \left(\frac{t}{c} \right) + \frac{c_{l_1}}{1+a}$

SELECTION OF OPTIMUM FOILS

Although the foil with 16 series thickness distribution and $a = 1.0$ mean line would appear to be the optimum from Table 1.1, this is not always the case. As the lift coefficient of a foil (and thus the angle of attack) changes from the design value, the incipient cavitation number changes as shown in Figures 1.9-1.11. For small changes in lift coefficient this change is negligible, but as the change in lift coefficient increases beyond a certain value the change in incipient cavitation number becomes very pronounced. The allowable range of lift coefficient in which little change occurs in the incipient cavitation number is highly dependent on the thickness-chord ratio (t/c). The net result of such effects is that the selection of the optimum foil, from a cavitation inception standpoint, must take into account the range of expected lift coefficients (angles of attack), the section type, the thickness ratio (t/c), the camber type and the design lift coefficient.

The NACA 16- and 6-series airfoils, presented in Reference (1.1), have a thickness distribution that gives unusually low incipient cavitation numbers over a relatively wide range of incidence angles. In Figure 1.9 the incipient cavitation diagrams of the NACA 16-(1.5)06 and NACA 63-(1.5)06 ($t/c = 0.06$, $c_{l_1} = 0.15$) are presented. This figure shows that the NACA 16-(1.5)06 is superior to the NACA 63-(1.5)06 for $\sigma_1 = 0.3 - 1.4$, while the NACA 63-(1.5)06 is superior for $\sigma_1 > 1.4$. In Figure 1.10 the same hydrofoils are presented with different camber ($c_{l_1} = 0.375$),

while Figure 1.11 presents the incipient cavitation diagrams of the above hydrofoils for a thickness-chord ratio of 0.12. Figure 1.11 shows that the NACA 16-(1.5)12 is superior to the NACA 63₁-(1.5)12 over the whole range of incipient cavitation numbers. Figures 1.9-1.11 also show the effect of different camber lines (NACA a = 1.0 and 67 mean lines). In Figures 1.9 and 1.10 it is seen that the 67 mean line improves the leading edge cavitation characteristics of the 16 series section over the upper contour for $\sigma_i > 0.9$, while for $\sigma_i < 0.9$ the improvement over the upper contour is at the expense of earlier leading edge cavitation over the lower contour. Figure 1.11 shows that in some cases the 67 mean line improves the leading edge cavitation characteristics over the upper contour at the expense of leading edge cavitation over the lower contour for the whole range of σ_i .

It is apparent from the foregoing that decreasing the thickness and the design c_ℓ both have the effect of decreasing the value of the incipient cavitation number (increasing the cavitation speed) in the vicinity of the design c_ℓ . Also increasing the thickness, while increasing the value of the incipient cavitation number, also increases the value of Δc_ℓ ; i.e., the range of c_ℓ allowable at a particular value of incipient cavitation number before cavitation will occur. The value of the incipient cavitation speed, for the case of zero sweep, is from Equation [1.2]

$$V_c = \left[\frac{2(p_a + \rho gh - p_v)}{\rho \sigma_{ic}} \right]^{\frac{1}{2}} \quad \text{for } \Lambda = 0 \quad [1.11]$$

where σ_{1c} is the value of σ_1 on the cavitation boundary curve for a given value of c_l . If sweep is introduced in such a way that all conditions on the cross section normal to the 1/4 chord line (section, camber, t/c, angle of attack) are held fixed, then the lift coefficient and the inception cavitation number are both decreased by $\cos^2 \Lambda$ since

$$c_l = \frac{L/S}{\frac{1}{2}\rho(V^2 \cos^2 \Lambda)} \cos^2 \Lambda = c_{l\Lambda=0} \cos^2 \Lambda$$

where

$c_{l\Lambda=0}$ is based on the component of speed normal to the 1/4 chord line; i.e., $V \cos \Lambda$,

Λ is the sweep angle of the 1/4 chord line

Therefore

$$c_{l\Lambda=0} = \frac{c_l}{\cos^2 \Lambda}$$

By the same argument

$$\sigma_{1\Lambda=0} = \frac{\sigma_1}{\cos^2 \Lambda}$$

Also the cavitation speed under these conditions increases by a factor of $1/\cos \Lambda$:

$$V_c = \frac{1}{\cos \Lambda} \left[\frac{2(p_a + \rho gh - p_v)}{\rho(\sigma_{1c}/\cos^2 \Lambda)} \right]^{\frac{1}{2}} \quad [1.12]$$

The scales on Figures 1.2-1.11 have accordingly been labeled $c/\cos^2 \Lambda$ and $\sigma_1/\cos^2 \Lambda$.

The prediction of cavitation inception on a hydrofoil surface depends on the accuracy of the prediction of the pressures over the hydrofoil. For a completely submerged, zero dihedral, untwisted wing of constant taper and sweep (see Figure 1.12), the chordwise pressure distribution in the "kinked region" (a region of about one chord total width at midspan) is appreciably different from the chordwise pressure distribution in the "sheared region". Figure 1.13, replotted from Figure VIII of Reference (1.7), illustrates this. The sheared region pressure distribution is essentially what would be expected from two-dimensional theory with a center of pressure at approximately the quarter chord, while the chordwise center of pressure in the kinked region is appreciably further aft and the peak pressure reduction appreciably less.

Because of the difference of the chordwise pressure distributions in the kinked and sheared regions, both regions have to be investigated separately for cavitation inception, especially if a pod and/or strut are located near or at the kink.

In this section, however, we will restrict ourselves to a discussion of cavitation inception in the sheared region, at a

large distance from pods or struts, leaving the discussion of cavitation inception at the foil-strut-pod intersection to the next section.

Cavitation inception in the sheared region first occurs at that spanwise station where (c_l/C_L) is maximum. The spanwise lift distribution on a hydrofoil surface at infinite depth is, according to References (1.8) and (1.9), approximately equal to:

$$\left(\frac{c_l}{C_L}\right)_{\infty, \Lambda} = \left(\frac{c_l}{C_L}\right)_{\infty, \Lambda = 0} - \frac{(1 + \lambda)(1 - \eta)}{1 - \eta(1 - \lambda)} (1 - \cos \Lambda) \quad [1.13]$$

where

$$\left(\frac{c_l}{C_L}\right)_{\infty, \Lambda = 0} = \frac{1}{2} + \frac{1}{\pi} (1 - \eta^2)^{\frac{1}{2}} \frac{1 + \lambda}{1 - \eta(1 - \lambda)} \quad [1.14]$$

Λ = angle of sweep of the quarter-chord-line,

η = $2y/b$ = nondimensional span station measured from the plane of symmetry,

b = wing span

λ = tip chord/root chord = taper ratio

In Reference (1.8) it is shown that the $(c_l/C_L)_{\infty, \Lambda} = 0$ distribution as expressed by Equation [1.14] gives good agreement with experiment for all practical purposes, while in Reference (1.9) four comparisons of the $(c_l/C_L)_{\infty, \Lambda}$ distribution (Equation [1.13]) with other theories as well as experiment are given. The agreement for the four cases considered shown in the table below, was good.

Aspect Ratio	Sweep (Deg.)	Taper Ratio	$\eta_{crit.}$
2.00	56.3	0.00	1.00
3.45	46.4	0.42	0.73
4.66	31.0	0.44	0.70
10.00	35.0	0.33	0.79

It was, however, noted in Reference (1.9) that since complete calculations at many aspect ratios and taper ratios are not available, Equation [1.13] must be used with caution. A more exact method for determining the spanwise lift distribution is presented in Reference (1.10). However this requires considerably more computation.

The value of $(c_l/C_L)_{\infty, \Lambda}$ is a maximum for $\frac{\partial}{\partial \eta} (c_l/C_L)_{\infty, \Lambda} = 0$, or:

1.24

$$\eta = \eta_{\text{crit.}} = \frac{1 - \lambda}{1 + D^2} + D \left[\frac{1}{1 + D^2} - \left(\frac{1 - \lambda}{1 + D^2} \right)^2 \right]^{\frac{1}{2}} \quad [1.15]$$

where $D = \pi\lambda(1 - \cos \Lambda)$.

Substituting the values of λ and Λ of the above four cases into Equation [1.15] gives the computed values of $\eta_{\text{crit.}}$ listed in the above table.

The spanwise lift distribution may be corrected for depth by the following approximation:

$$\left(\frac{c_l}{C_L} \right)_{\frac{h}{c}, \Lambda} = K_h \left(\frac{c_l}{C_L} \right)_{\infty, \Lambda} \quad [1.16]$$

where

$$K_h = \frac{\left[\frac{C_{L\alpha}}{C_{L\alpha}} \right]_{h/c}}{\int \frac{\left[\frac{C_{L\alpha}}{C_{L\alpha}} \right]_{h/c}}{\left[\frac{C_{L\alpha}}{C_{L\alpha}} \right]_{\infty, h/c}} \left(\frac{c_l}{C_L} \right)_{\infty, \Lambda} dS} S$$

$$\left[\frac{C_{L\alpha}}{C_{L\alpha}} \right]_{\frac{h}{c}} = \text{ratio of lift-curve slope at finite depth-chord ratio } \frac{h}{c} \text{ to that at infinite depth}$$

(based on local value of h/c).

c = local chord,

\bar{c} = mean chord,

$\left(\frac{C_L}{c}\right)_{\bar{c}}$ = lift coefficient of entire wing based on mean chord (from Reference (1.11)),

and

$\left(\frac{c_l}{C_L}\right)_{\infty, \Lambda}$ is given by Equation [1.13]

Computations of $C_{L_\alpha} / \left(\frac{C_L}{c}\right)_{\infty}$, for various sweep and taper ratios are given in Figure 18b and Table II of Reference (1.11).

For tapered wings the local depth to chord ratio, h/c , for fixed h varies along the span. The simplest way to find the maximum $\left(\frac{c_l}{C_L}\right)_{h/c, \Lambda}$ (or the spanwise location where cavitation first occurs) in this case is to calculate the local $\left(\frac{c_l}{C_L}\right)_{h/c, \Lambda}$ at say 10 equally spaced stations and obtain the maximum $\left(\frac{c_l}{C_L}\right)_{h/c, \Lambda}$ from a plot of $\left(\frac{c_l}{C_L}\right)_{h/c, \Lambda}$ versus η . For an untapered wing $\lambda = 1$, and the maximum $\left(\frac{c_l}{C_L}\right)_{h/\bar{c}, \Lambda}$ can be obtained from Equations [1.13], [1.15] and [1.16], i.e.,

$$\left[\left(\frac{c_l}{C_L}\right)_{h/c, \Lambda}\right]_{\max} = \left[\frac{1}{2} + \frac{2}{\pi} \left\{ \left[1 + \pi^2 (1 - \cos \Lambda)^2 \right]^{\frac{1}{2}} - \pi (1 - \cos \Lambda) \right\} \right] \quad [1.17]$$

and

$$\eta_{\text{crit.}} = \left[\frac{\pi^2 (1 - \cos \Lambda)^2}{1 + \pi^2 (1 - \cos \Lambda)^2} \right]^{\frac{1}{2}} \quad [1.18]$$

If $\left[c_{l_u} \right]_{h/c, \Lambda}$ and $\left[c_{l_l} \right]_{h/c, \Lambda}$ are the two-dimensional lift coefficients on the upper and lower incipient cavitation boundaries respectively at a given velocity or equivalent incipient cavitation number, as expressed by Equations [1.2] and [1.11], the allowable three-dimensional lift coefficients $\left[C_{L_u} \right]_{h/\bar{c}, \Lambda}$ and $\left[C_{L_l} \right]_{h/\bar{c}, \Lambda}$ are defined by:

$$\left[C_{L_u} \right]_{h/\bar{c}, \Lambda} \leq \left[c_{l_u} \right]_{h/c, \Lambda} / \left[\left(\frac{c_l}{C_L} \right)_{h/c, \Lambda} \right]_{\text{max.}} \quad [1.19]$$

$$\left[C_{L_l} \right]_{h/\bar{c}, \Lambda} \geq \left[c_{l_l} \right]_{h/c, \Lambda} / \left[\left(\frac{c_l}{C_L} \right)_{h/c, \Lambda} \right]_{\text{max.}}$$

The principal effect of dihedral on the local c_l can be approximated by the same type of correction factor used to account for the spanwise variation in local depth-chord ratio given above

for tapered wings. This method is rather approximate but a more exact determination involves considerably more difficult computations and has been carried out for only some simple configurations (see Figure 5a of Reference (1.11)). The allowable angle of attack range $\Delta\alpha$ for the sheared region far from the influence of pods and struts corresponding to $\left[\Delta C_L\right]_{h/\bar{c}} = \left[C_{L_u} - C_{L_t}\right]_{h/\bar{c}, \Lambda}$ is

defined by:

$$\Delta\alpha \cong \left[\Delta C_L\right]_{h/\bar{c}} / \left(C_{L_\alpha}\right)_{h/\bar{c}, \Lambda} \quad [1.20]$$

where $\left(C_{L_\alpha}\right)_{h/c, \Lambda} = f$ [depth, aspect ratio, sweep and dihedral] is the lift curve slope of the hydrofoil defined by Equations 47-49 of Reference (1.11).

One of the advantages of sweep is in the increased range of $\Delta\alpha$ that usually results. If on introducing sweep, the span, area, thickness-chord ratio, and aspect ratio are held constant, then the design camber and design angle of attack, if any, measured on a section normal to the 1/4-chord line, can be increased by the factor $1/\cos^2 \Lambda$, in order to develop the same design lift coefficient as without sweep. Also, since the span of the wing in the direction of the 1/4-chord line increases by $1/\cos \Lambda$, the bending moment also increases approximately by this factor. Furthermore, since the chord and thickness measured on a section normal to the 1/4-chord line each decreased by the factor $\cos \Lambda$, the section modulus

decreased by the factor $(\cos \Lambda)^3$ and hence the stress for the same C_L increased by about $1/(\cos \Lambda)^4$. This stress can be brought back down to its approximate original value by increasing the section thickness by $1/(\cos \Lambda)^2$. Thus, the introduction of sweep in the manner described requires an increase in design camber, design angle of attack, if any, and t/c , by a factor $1/\cos^2 \Lambda$. The net result of this is generally a decrease in the available cavitation free range of ΔC_L . However, more than sufficient compensation for this is possible due to the corresponding decrease in $C_{L\alpha}$ so that a net increase in the cavitation free angle of attack range $\Delta\alpha$ will result. A greater range of $\Delta\alpha$ is possible by decreasing the aspect ratio or by sweeping the wing simply by rotating it about a vertical axis. However, the increase in induced drag is generally greater and detailed calculations of a number of alternate configurations are desirable before arriving at an optimum configuration.

Thus, the introduction of sweep and the reduction of aspect ratio, by reducing the lift curve slope, usually allows a greater range of $\Delta\alpha$ even for a reduced allowable ΔC_L before cavitation inception. This has the advantage of allowing a larger trim range in pitch and larger variations in foil angle of attack, due to boat motions and orbital velocities of waves, within the limits of cavitation inception. Sweep is also of great advantage in the shedding of seaweed and other debris which may cause bad hydrodynamic flow conditions and cavitation.

CAVITATION INCEPTION ON PODS (AXISYMMETRIC BODIES)

Cavitation inception on axisymmetric bodies has been of interest, in the past, mostly with regard to underwater missiles. The use of axisymmetric bodies as pods at foil-strut intersections of hydrofoil boats has only recently become a subject of interest. The problem of cavitation inception on such bodies has nowhere been fully treated.

Techniques for calculating pressure distributions on axisymmetric bodies have been well developed as in (1.12), (1.13) and (1.14). Such methods have been used to calculate pressure distributions on a number of bodies by Brand (1.15) and more recently for a number of bodies suitable for use as pods by Moore (1.16). The results of Brand are somewhat restricted in the range of slenderness ratios. Moore (1.16) considers slenderness ratios of 5, 6 and 7 only. Lange (1.17) has made measurements of the pressure distributions on eight bodies. The effect of slenderness ratio, location of maximum diameter, nose radius, camber and yaw and pitch angle on the pressure distribution have been measured.

As with hydrofoils, the question of using theoretical pressure distributions for predicting cavitation inception arises. The measured pressure distributions of (1.17) are in excellent agreement with theory for all but the higher angles of attack. Good agreement between the calculations of (1.16) and experiment are also shown. Rouse and McNown (1.18) indicate very good agreement between theory and experiment for ellipsoidal heads. The question of agreement between the pressure coefficient and the

incipient cavitation number is not as readily shown, however.

Figures 1.14 and 1.15 give the measured pressure distributions and incipient cavitation number for ellipsoidal and ogival head forms as a function of slenderness ratio. Figure 1.16 shows a comparison of pressure distribution and incipient cavitation number for ogival heads from Knapp (1.19). The ellipsoid data indicates good agreement with theoretical pressure distribution for large slenderness ratios (greater than four). Parkin and Holl (1.20) further indicate that for hemispheres and 1.5 calibre ogives, tested in water, the incipient cavitation number is highly dependent on the parameter $V\sqrt{d}$ as shown in Figure 1.17. Holl (1.21) indicates that, for a smooth stainless steel hemispheric head, the incipient cavitation number (0.7) is in agreement with the measured minimum pressure coefficient given by (1.18) at the largest values of $V\sqrt{d}$. Figure 1.18 indicates, that for a blunt body (a sphere in this case), incipient cavitation number decreases with increasing roughness, probably because of the desirable effect of roughness on hastening transition and reducing separation. For slender bodies, where separation is not a problem, the incipient cavitation number almost certainly increases with roughness, as concluded in (1.18).

The results of Holl (1.21) indicate a further difference between cavitation behavior on bodies and on foils. On bodies the incipient cavitation number rises to some asymptotic value approximately equal to the minimum pressure coefficient as the parameter $V\sqrt{d}$, increases. With foils, on the other hand, the incipient cavitation number does not appear to be a function of a parameter $V\sqrt{c}$. Whereas in two-dimensional foils the incipient cavitation

number is generally less than the measured minimum pressure coefficient, with axisymmetric head forms, the incipient cavitation number for slender bodies (slenderness ratio greater than four) appears to be in good agreement with the minimum pressure coefficient or

$$\sigma_i = C_{p \text{ min}} \quad (l/d \geq 4.0). \quad [1.21]$$

Care must be exercised in using pressure coefficient data for prediction of cavitation for blunt bodies. However, Figure 1.14 might be used as an empirical correction for the incipient cavitation number for the smaller slenderness ratio of interest. The fact that practical bodies will be roughened by exposure may tend to alleviate this discrepancy. From Figure 1.18, a decrease in incipient cavitation number of from three or four percent might be indicated for normal roughness. In general the values of $V\sqrt{c}$ in hydrofoil operations will be large enough to insure the two-dimensional values.

All of these results are for bodies at zero angle of attack or yaw. When the body is at an angle of attack the incipient cavitation number will increase. Unfortunately no values have been tabulated for use in an axisymmetric formula of the form of Equation [1.1]. Lange (1.17) has indicated that for angles of attack of four degrees or less, particularly for the thicker bodies, the effect of incidence on $C_{p \text{ min}}$ is small. It is probable that the effect on incipient cavitation number is also small.

1.32

Rouse (1.22) has shown that the effect of incidence is small for blunter heads but, as would be expected, is appreciable for bodies such as a 4:1 elliptic head. Figure 1.19 indicates the ratio of incipient cavitation number at finite incidence to that at zero incidence as a function of incidence angle. Figure 1.20 from (1.17) indicates the effectiveness of cambering the body in reducing the minimum pressure coefficient due to incidence. The reduction of $C_{p \text{ min}}$ is of course only effective for incidence in one direction.

Cavitation inception data are restricted, as can be seen from the above references, to axisymmetric head forms. No data are available to indicate the occurrence of cavitation near the tail of the body, although this may be the critical region. Despite the prediction by theory of high pressures in this region, the low pressures associated with boundary layer separation may lead to cavitation inception in this area first. It is for this reason that Moore (1.16) indicates the desirability of using body 4162 despite the smaller $C_{p \text{ min}}$ of the constant pressure body. Great care must be exercised in providing a somewhat pointed tail to prevent separation and subsequent cavitation at that point. If such care is exercised, the theoretical pressure distributions of Figures 1.21 through 1.25 and the corrections indicated by Figures 1.14 through 1.19 should prove adequate for pod design. The bodies presented by Moore are probably about the best possible, although in some cases less uniform pressure distributions of the type shown in Figure 1.24 may prove best when pod-foil interference is considered.

Tulin (1.23) has indicated that the velocities on axisymmetric bodies near the free surface are reduced. This results in a decrease in the incipient cavitation number due to the pod, the resulting incipient cavitation at finite depth-diameter ratio h/d being given by:

$$\left(\sigma_i\right)_{h/c} = \left(\frac{\sigma_{i_{h/c}}}{\sigma_{i_\infty}}\right) \sigma_{i_\infty} \quad [1.22]$$

where the factor $\left(\sigma_{i_{h/c}}/\sigma_{i_\infty}\right)$ is given for large Froude numbers by Figure 1.26 from (1.23). This correction should be applied at the upper surface of the body, although some decrease probably results at the sides also, due to the free surface proximity.

One further correction which should be considered, particularly for very slender bodies, is the decrease in slenderness ratio due to boundary layer development. The perturbation velocities on and near the body result from the potential flow outside the boundary layer. Specifically, the pressures result from flow about an effective body whose radius is increased by the boundary layer displacement thickness. The boundary layer thickness δ can be obtained from results for fully developed turbulent flat plate flow (1.24):

$$\delta = 0.37 \times \text{Re}^{-1/5} \quad [1.23]$$

1.34

where x is the distance from the nose of the body to the point of interest. Making use of the fact that the momentum thickness δ^* is given by

$$\delta^* = \frac{1}{8} \delta$$

for fully developed turbulent flow, the effective slenderness ratio $(\ell/d)_v$ is given by

$$\frac{(\ell/d)_v}{(\ell/d)} = \frac{1.0}{1.0 + .046 \ell/d \text{ Re}^{-1/5}} \quad [1.24]$$

In general the decrease in ℓ/d given by [1.24] will be small enough to ignore unless the slenderness ratio is very large and the Reynolds number small.

Because of the absence of a pressure peak in the center portion of a swept foil (the so-called kink region), cavitation may first occur in the sheared region of the foil rather than at the foil-pod intersection. This has been noted in inception tests of two foils systems reported by Johnson (1.25). It is therefore necessary, in such cases, to know the velocities due to the body at some point away from the body surface.

The relationship between the velocity and incipient cavitation number in free flow and on the body surface is given for a Rankine ovoid (1.26) by:

$$\frac{U_{\text{flow}}}{U_{\text{body}}} \approx \frac{\sigma_{i \text{ flow}}}{\sigma_{i \text{ body}}} = \left[\frac{\left(\frac{l}{d} - \frac{1}{2}\right) + 1}{\left(\frac{l}{d} - \frac{1}{2}\right) + \left(\frac{2y}{d}\right)^2} \right]^{3/2} \quad [1.25]$$

where the subscripts refer to values in the flow and on the body surface at mid-length, l is the pod length, d is the pod diameter and y is the radial distance from the centerline of the pod. Equation [1.25] applies at the mid-length of the body but it is probably a good approximation over the portion of the body length of interest. Most pods are likely to be more elliptic than the Rankine body because of the more desirable pressure distributions. Unfortunately, the expressions for the velocities due to a prolate spheroid are given in terms of Green's integral (1.27) which can only be evaluated numerically. Based on the calculations of Maruhn (1.28), it has been found that Equation [1.25] is applicable for spheroids if an equivalent length-diameter ratio $(l/d)_e$ given by:

$$\left(\frac{l}{d}\right)_e = .875 \left(\frac{l}{d}\right)^{1.75} \quad 2 \leq \frac{l}{d} \leq b \quad [1.26]$$

is used in [1.25]. In Equation [1.26] the l/d used is that of the ellipsoid. In general, the decay of velocities is rather slow compared to the body diameter or foil chord, so that the decrease given by [1.25] may be negligible.

CAVITATION AT FOIL-STRUT-POD INTERSECTIONS

At the intersection of two foil system components such as a foil and strut or a foil (strut) and pod, the velocity increments (perturbation velocities) due to each component are additive. Referring to Equation [1.2], it is obvious that as the total perturbation velocity increases, the incipient cavitation number will increase. The total perturbation velocity due to the n'th component (foil, strut or pod) at an intersection can be expressed in terms of the incipient cavitation number σ_{i_n} of that component from Equation [1.11]:

$$\left(\frac{v}{V} + \frac{\Delta v}{V} + \frac{\Delta v_a}{V} - 1.0 \right)_n = \sqrt{1 + \sigma_{i_n}} - 1.0 \quad [1.27]$$

where $\frac{v}{V}$ is the sum of the free stream velocity and the perturbation velocity due to thickness, $\Delta v/V$ is the contribution due to camber for foils and $\Delta v_a/V$ is the contribution due to incidence.

The incipient cavitation number at an intersection of m components is given by

$$\sigma_i = \left[\sum_{n=1}^m \sqrt{\sigma_{i_n} + 1.0} + 1.0 - m \right]^2 - 1.0. \quad [1.28]$$

Where there is no pod at the intersection of a foil and strut, m has a value of two in Equation [1.28]. Where a pod is present,

it may be necessary to consider the contribution of all three components. In this case, m has a value of three in [1.28]. Because of the decay of velocities away from the surface of a body, the values of σ_{1n} for all three components will probably not be the full values indicated at the surface of each.

The reduction of the pressure coefficient, and thus the incipient cavitation number, of a pod away from the body surface has already been given in Equation [1.26]. This reduction will be important only in cases where the kink region of the foil (foil chord) is large compared to the pod size. For cases where the kink region is small or the wing is unswept, cavitation will occur first at the intersection of the pod with the foil or strut. The value of σ_1 for the pod is thus obtained, for a given body, from the minimum pressure coefficients given by Figures 1.21 through 1.25.

The influence of the velocities due to the strut on cavitation on the foil surface, and velocities due to the foil on cavitation at the pod-strut intersection must be estimated, however. The incipient cavitation numbers at the foil and strut surface can be determined from the previous section. It remains to find a correction to account for the decrease in perturbation velocities and incipient cavitation number away from the surface. For the case of a uniform camber loading ($a = 1$ mean line), it can be shown that the velocity and thus the incipient cavitation numbers in the flow is given in the midchord plane by:

$$\left(\frac{u_{\text{flow}}}{u_{\text{body}}}\right)_c \approx \left(\frac{\sigma_{1\text{flow}}}{\sigma_{1\text{body}}}\right)_c = \frac{2}{\pi} \tan^{-1} \left(\frac{c}{2y}\right) \quad [1.29]$$

where c is the foil chord, y is the distance from the foil surface and the subscripts are as before.

As in the case of the ellipsoid, it is not possible to obtain a useful analytic expression for the velocities in the flow for an elliptic foil section. The expression for the velocity decay due to thickness for a Rankine Oval is given by

$$\frac{u_{\text{flow}}}{u_{\text{body}}} = \frac{1 - \left(\frac{1}{\pi} \frac{t}{c}\right)^2 + \left(\frac{t}{c}\right)^2}{\left(1 - \frac{1}{\pi} \frac{t}{c}\right)^2 + \left(\frac{2y}{c}\right)^2} \approx \frac{\sigma_{1\text{flow}}}{\sigma_{1\text{body}}} \quad [1.30]$$

For cases where t/c is moderate ($t/c < .15$), this can be approximated quite accurately by:

$$\left(\frac{\sigma_{1\text{flow}}}{\sigma_{1\text{body}}}\right)_T \approx \frac{1}{1 + \left(\frac{2y}{c}\right)^2} \quad [1.31]$$

No results for elliptic cylinders such as those of Maruhn for spheroids are available to allow an empirical correction so that

[1.30] or [1.31] must therefore be used for all sections. The results of Equation [1.28] indicate this should be conservative in most cases. Because of this approximation, Equation [1.31] is adequate for use with typical foil sections.

The interaction of the foil and strut can now be calculated. In general, the center of the foil, strut and pod will be close enough to assume that the points of minimum pressure lie in a single transverse plane. The distance between the foil and strut can be determined as shown in Figure 1.27. If the length of the pod is assumed to be m foil root chords, the pod slenderness ratio l/d , and the strut chord given by p percent of the foil root chord, then the distance from the strut root to the foil root in strut chords is

$$\left(\frac{y}{c}\right) = \frac{\pi mp}{4 l/d} \quad [1.32]$$

The distance from the strut to the inner edge of the sheared region for swept wings is given by

$$\left(\frac{y}{c}\right) = \frac{p}{2} \sqrt{\left(\frac{m}{l/d}\right)^2 + 1} \quad [1.33]$$

The contribution of the strut at the foil can thus be obtained from Equation [1.31] using [1.32] or [1.33]. Because the strut ends at the pod, it is not hydrodynamically infinite so that velocities due to the strut at the foil surface are less than

those values predicted for infinite two dimensional struts and given by Equation [1.27]. The incipient cavitation number at the foil, due to the strut, $\left(\sigma_{1s}\right)_{\text{foil}}$ is thus given by:

$$\left(\sigma_{1s}\right)_{\text{foil}} = k \sigma_{1s} \left(\frac{\sigma_{1\text{flow}}}{\sigma_{1\text{body}}}\right) \quad .5 \leq k \leq 1 \quad [1.34]$$

The value of k is probably closer to .5, particularly at larger distances from the strut.

In the case of the effect of the foil pressures on cavitation at the strut-pod intersection, the contributions due to thickness and lift must be considered separately. Away from the foil surface, the pressure peaks due to incidence will tend to be averaged out. For this reason it is probably adequate to assume that the contribution of the foil to strut cavitation results from a uniform chordwise foil loading. The incipient cavitation number at the strut due to the foil $\left(\sigma_{1f}\right)_{\text{strut}}$ is given by

$$\left(\sigma_{1f}\right)_{\text{strut}} = \left[\left(\frac{v}{V} - 1\right) \left(\frac{u_{\text{flow}}}{u_{\text{body}}}\right)_T + \frac{\Delta v}{V} \left(\frac{u_{\text{flow}}}{u_{\text{body}}}\right)_c + 1 \right]^2 - 1.0 \quad [1.35]$$

As the difference in pressures due to a kink are not considered here, the distance y/c should be determined from Equation [1.32], where the value of p is assumed as one.

In general the strut chord will be less than the foil chord, particularly for moderate taper ratios. In these cases, the effect of the strut on the foil becomes less important and can in many cases be ignored. The effect of the foil on the cavitation inception at the strut-pod intersection, on the other hand, can rarely be ignored.

For most cases, where the incipient cavitation number is small ($\sigma_i \leq 0.6$), Equation [1.28] can be approximated by the expression

$$\sigma_i = \sum_{n=1}^m \sigma_{i_n} = \sigma_{i_1} + \dots + \sigma_{i_m} . \quad [1.36]$$

The error inherent in the use of [1.36] for $\sigma_i \leq 0.6$ is less than five percent, in all cases, and generally only a few percent. Equation [1.36] is adequate for use in most preliminary design procedures such as outlined in Chapter 2, although Equation [1.28] should be used to check the cavitation resistance of the final design.

Filleting of foil-strut intersections without pods certainly has some beneficial effect on cavitation inception but no quantitative data for this effect are available. One way of increasing resistance to cavitation inception is to increase the chord of the strut, locally near the foil, as shown in Figure 1.28. This reduces velocities considerably at the intersection without appreciably increasing the drag.

The pod slenderness ratio should generally be made as large as possible. For a given pod slenderness ratio, the pod size should be made as large as possible, consistent with drag requirements, to minimize the interaction of foil and strut incipient cavitation number. There is no quick way of determining the optimum pod size. For this reason, calculations have been carried out to determine the optimum foil system as a function of basic foil parameters including the pod slenderness ratio. The results of these calculations are presented in Chapter 2.

REFERENCES

- 1.1. Abbott, I. H., von Doenhoff, A. E. and Stivers, L. S., "Summary of Airfoil Data", NACA Report No. 824, 1945.
- 1.2. Kermeen, R. W., "Water Tunnel Tests of NACA 4412 and Walchner Profile 7 Hydrofoils in Noncavitating and Cavitating Flows", Cal. Tech. Report No. 47-5, February 1956.
- 1.3. Kermeen, R. W., "Water Tunnel Tests of NACA 661-012 Hydrofoil in Noncavitating and Cavitating Flows", Cal. Tech. Report No. 47-7, February 1956.
- 1.4. Numachi, F., Tsunoda, K., and Chida, I., "Cavitation Tests on Clark Y Profiles of Several Thickness Ratios", Report of the Inst. of High Speed Mechanics, Volume 8, pp. 47-65, 1957.
- 1.5. McCullough, G. B., and Gault, D. E., "Examples of Three Representative Types of Airfoil-Section Stall at Low Speeds", NACA Tech. Note 2502, September 1951.
- 1.6. Gault, D. E., "An Experimental Investigation of Regions of Separated Laminar Flow", NACA Tech. Note 3505, September 1955.
- 1.7. Thwaites, B., "Incompressible Aerodynamics," Oxford Univ. Press, Great Britain, 1960.
- 1.8. Schrenk, O., "A Simple Approximation Method for Obtaining the Spanwise Lift Distribution," NACA TM948, 1940.
- 1.9. Pope, A and Haney, W. R. Jr., "Spanwise Lift Distribution for Sweptback Wings," J.A.S., August 1949.
- 1.10. DeYoung, J. and Harper, C.W., "Theoretical Symmetric Span Loading at Subsonic Speeds for Wings Having Arbitrary Plan Form," NACA Report 921, 1948.

- 1.11. Martin, M., "The Stability Derivatives of a Hydrofoil Boat - Part 1," HYDRONAUTICS Tech. Report 001-10(I), January 1963.
- 1.12. Landweber, L., "The Axially Symmetric Potential Flow About Elongated Bodies of Revolution," DTMB Report 761, August 1951.
- 1.13. Adams, Mac C., and Sears, W.R., "Slender Body Theory: Review and Applications," IAS Preprint No. 383, July 1952.
- 1.14. Hess, J. L., and Smith, A.M.O., "Calculation of Non-Lifting Potential Flow about Arbitrary Three-Dimensional Bodies", Douglas Aircraft Report ES40622, March 1962.
- 1.15. Brand, M., "Pressure Distributions Over Bodies of Revolution for Axial Flow," DTMB Translation No. 220, April 1947.
- 1.16. Moore, Wilburn L., "Bodies of Revolution With High Cavitation-Inception Speeds-For Application to the Design of Hydrofoil Boat Nacelles", DTMB Report 1669, September 1962.
- 1.17. Lange, G., "Force and Pressure Distribution Measurements on Eight Fuselages," NACA Technical Memorandum No. 1194, October 1948.
- 1.18. Rouse, Hunter and McNown, John S., "Cavitation and Pressure Distribution, Head Forms at Zero Angle of Yaw," State University of Iowa, Studies in Engineering Bulletin 32, 1948.
- 1.19. Knapp, Robert T., "Nose Cavitation - Ogives and Spherogives," OSRD Report 6.1-sr 207-1906, California Institute of Technology, 1945.
- 1.20. Parkin, Blaine R., and Holl, J.W., "Incipient Cavitation Scaling Experiments for Hemispherical and 1.5 Caliber Ogive-Nosed Bodies," Bureau of Ordnance Report No. NOrd 7958-264, May 1953.

- 1.21. Holl, J. W., "The Effects of Surface Irregularities on Incipient Cavitation," ORL Technical Memorandum No. TM 5.3410-03, June 1948.
- 1.22. Rouse, Hunter, "Cavitation and Pressure Distribution, Head Forms at Angle of Yaw," State University of Iowa Studies in Engineering Bulletin 42, 1962.
- 1.23. Tulin, Marshall P., "The Hydrodynamics of High-Speed Hydrofoil Craft," Transactions of the Third Symposium on Naval Hydrodynamics, Office of Naval Research Publication ACR-65, Washington, D. C., 1962.
- 1.24. Schlichting, Hermann, "Boundary Layer Theory," translated by J. Kestin, McGraw Hill Book Company, New York, 1960.
- 1.25. Johnson, Robert S., "Prediction of Lift and Cavitation Characteristics of Hydrofoil-Strut Arrays," Paper presented at the Southern California Section, SNAME, March 1964.
- 1.26. Streeter, Victor L., "Fluid Dynamics," McGraw-Hill Book Company, New York, 1958.
- 1.27. Durand, William Frederick, Editor, "Aerodynamic Theory, Volume 1, Part C," Fluid Mechanics, - Part II by Max Munk, Dover Publications, New York, 1963.
- 1.28. Maruhn, K., "Druckverteilunrechnungen an Elliptischen Rumpfen und in Ihrem Aussenvaum (Determination of Pressure Distribution on Ellipsoidal Bodies and in the Surrounding Space)," Jahrbuch, Der Deutschen Luftfahrtforschung, 1944.

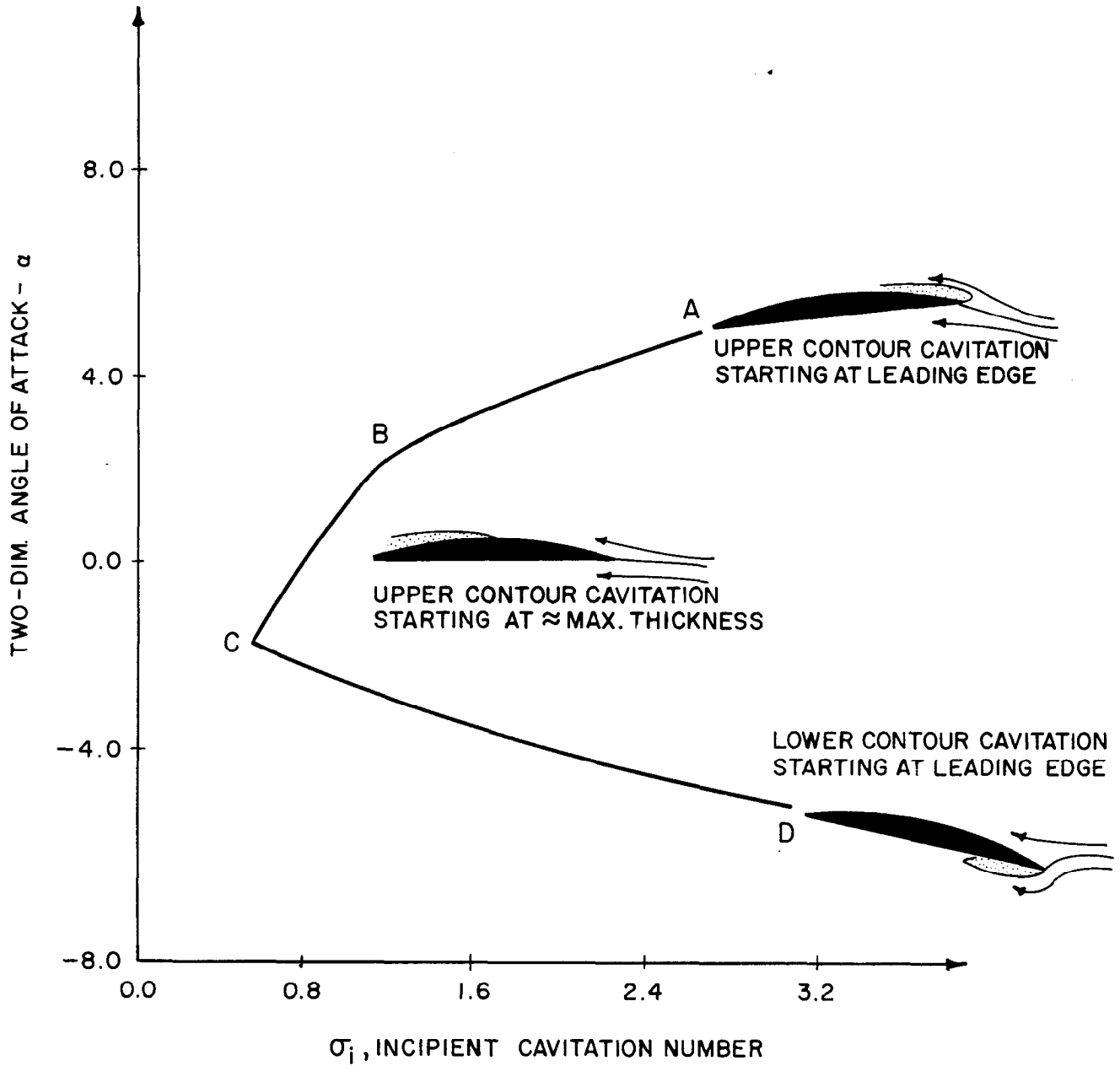


FIGURE I.1 - EFFECT OF ANGLE OF ATTACK ON THE INCIPIENT CAVITATION NUMBER

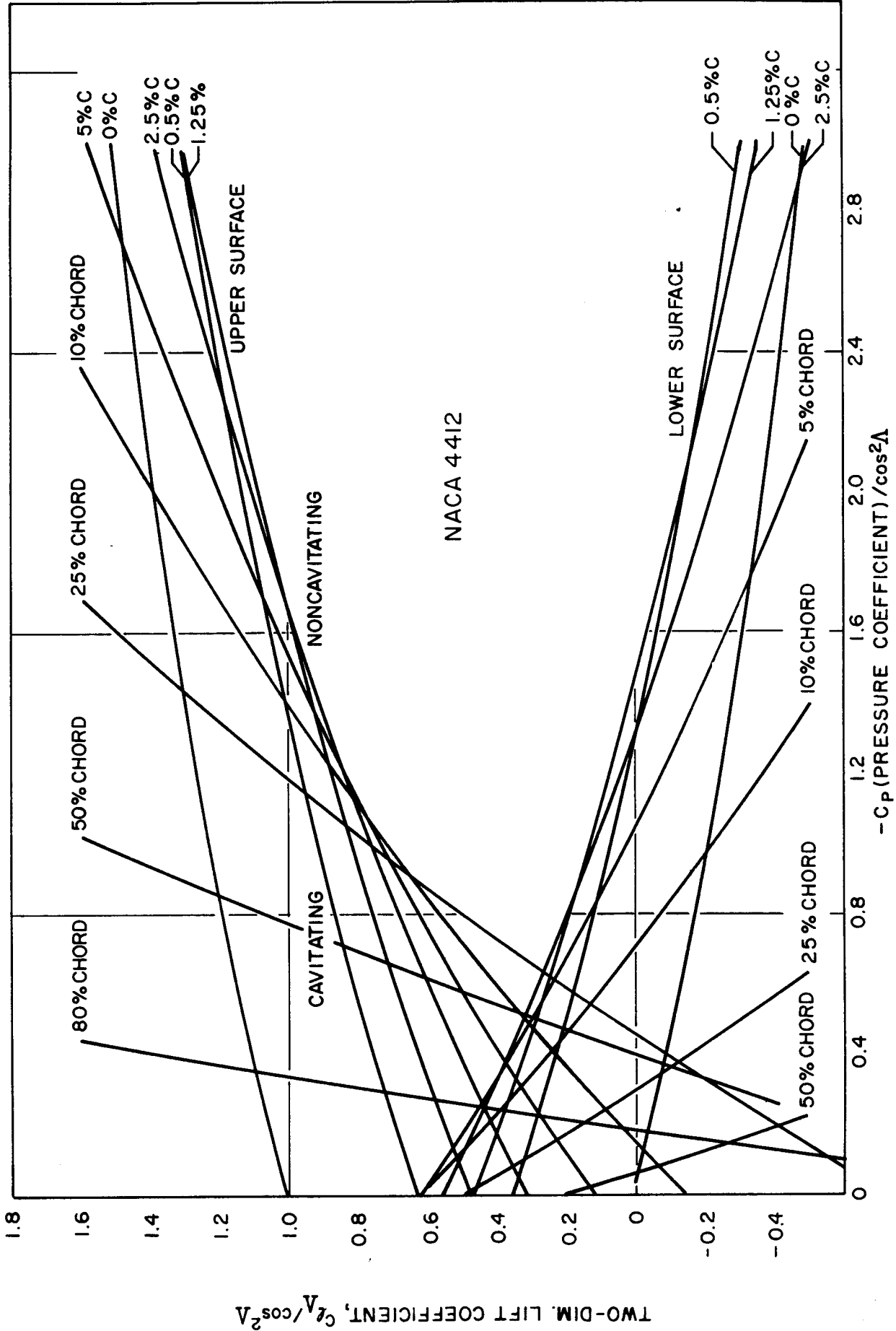


FIGURE 1.2-THE NEGATIVE OF THE PRESSURE COEFFICIENT VERSUS LIFT COEFFICIENT FOR THE NACA 4412

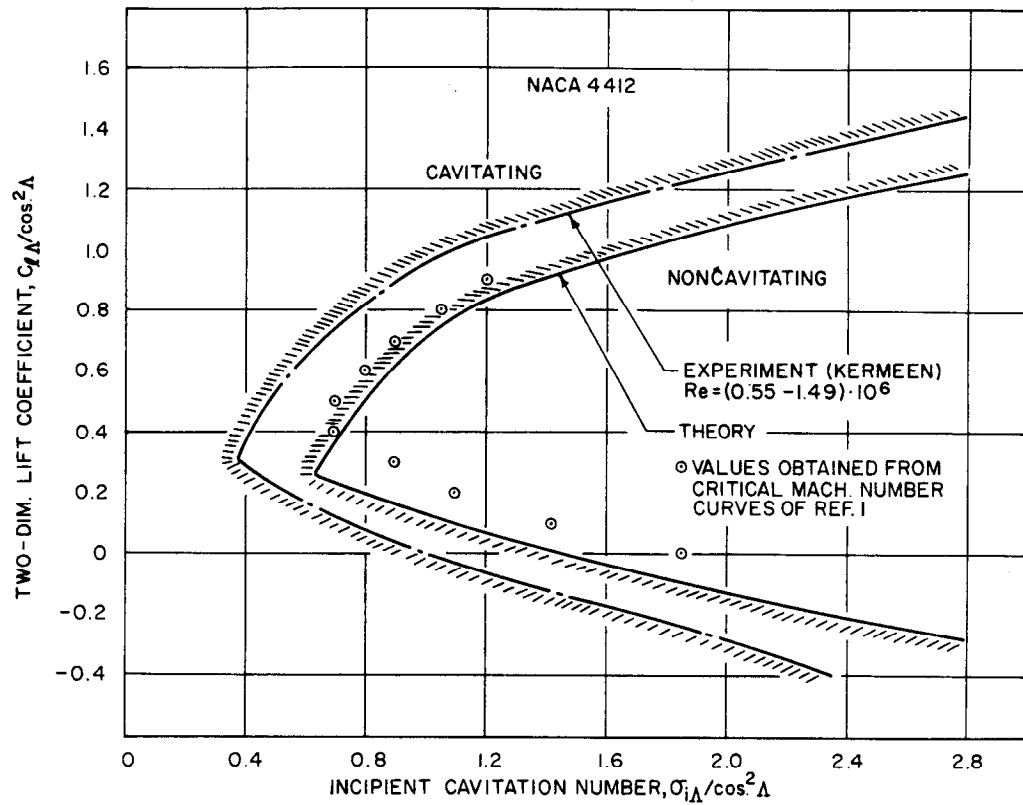


FIGURE I.3 -INCIPIENT CAVITATION DIAGRAM FOR THE NACA 4412

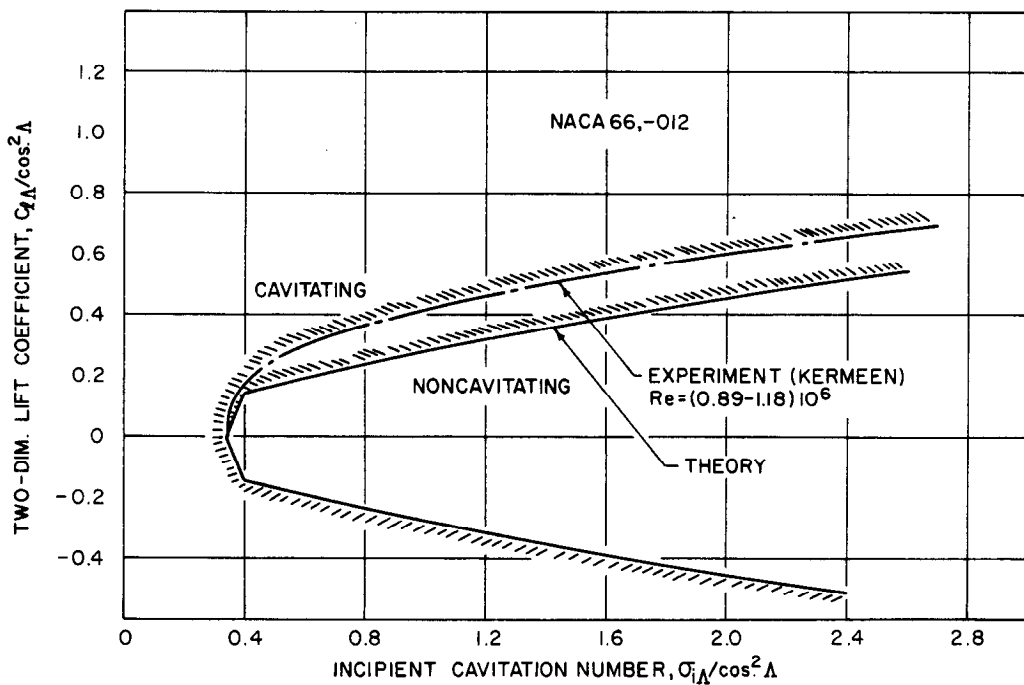


FIGURE I.4 -INCIPIENT CAVITATION DIAGRAM FOR THE NACA66,-012

HYDRONAUTIC, INCORPORATED

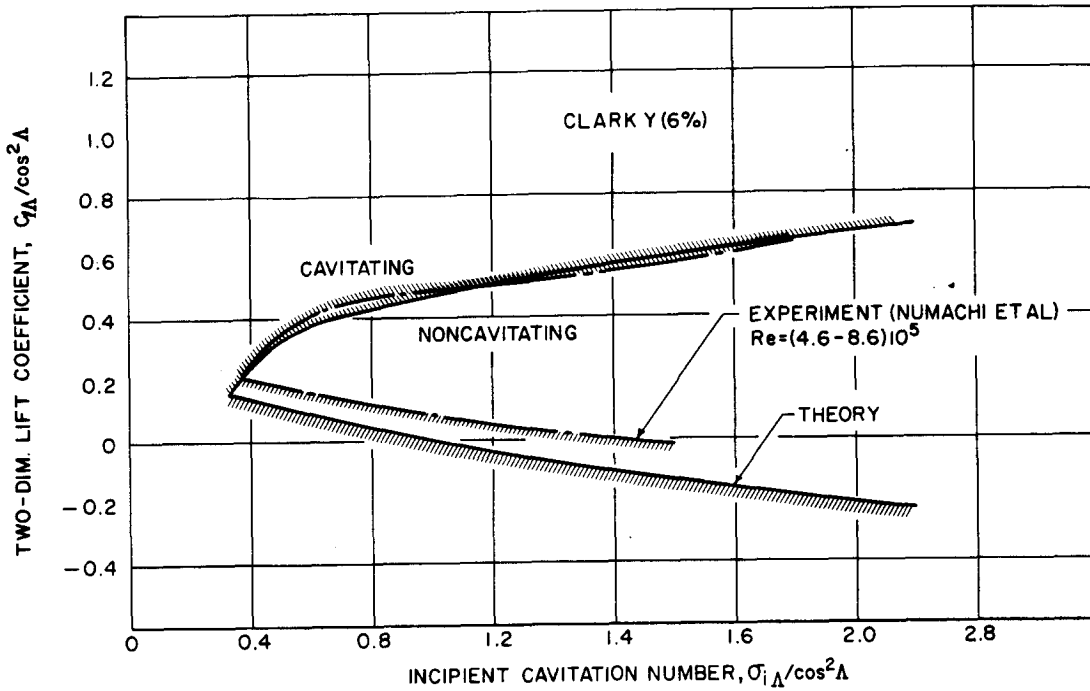


FIGURE I.5 -INCIPIENT CAVITATION DIAGRAM FOR THE CLARK Y(6%)

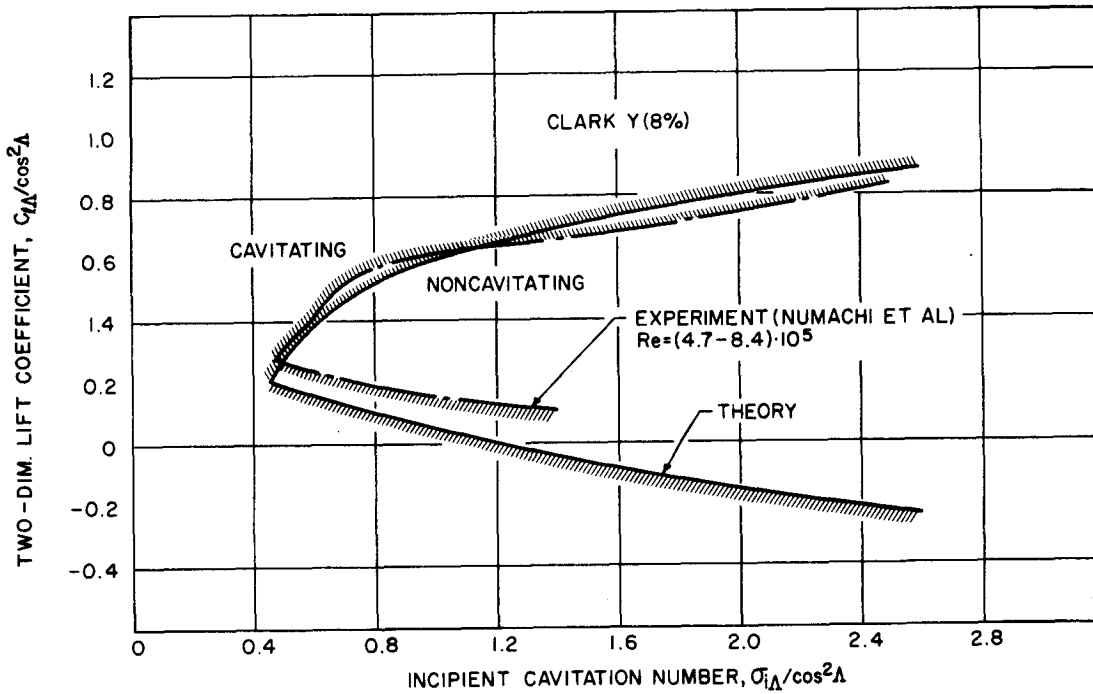


FIGURE I.6 -INCIPIENT CAVITATION DIAGRAM FOR THE CLARK Y(8%)

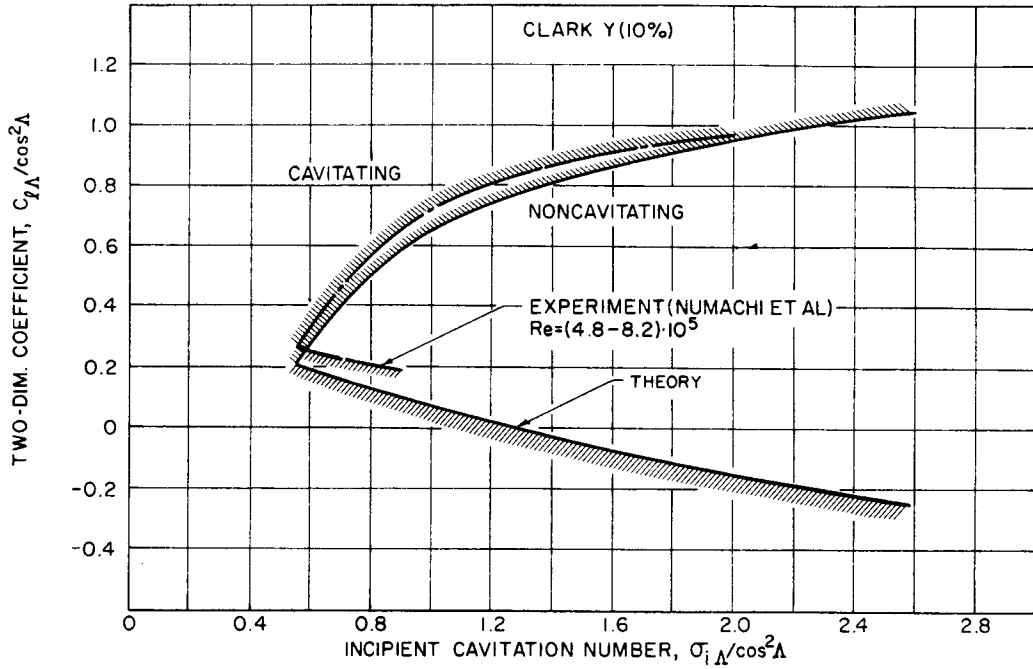


FIGURE 1.7 -INCIPIENT CAVITATION DIAGRAM FOR THE CLARK Y(10%)

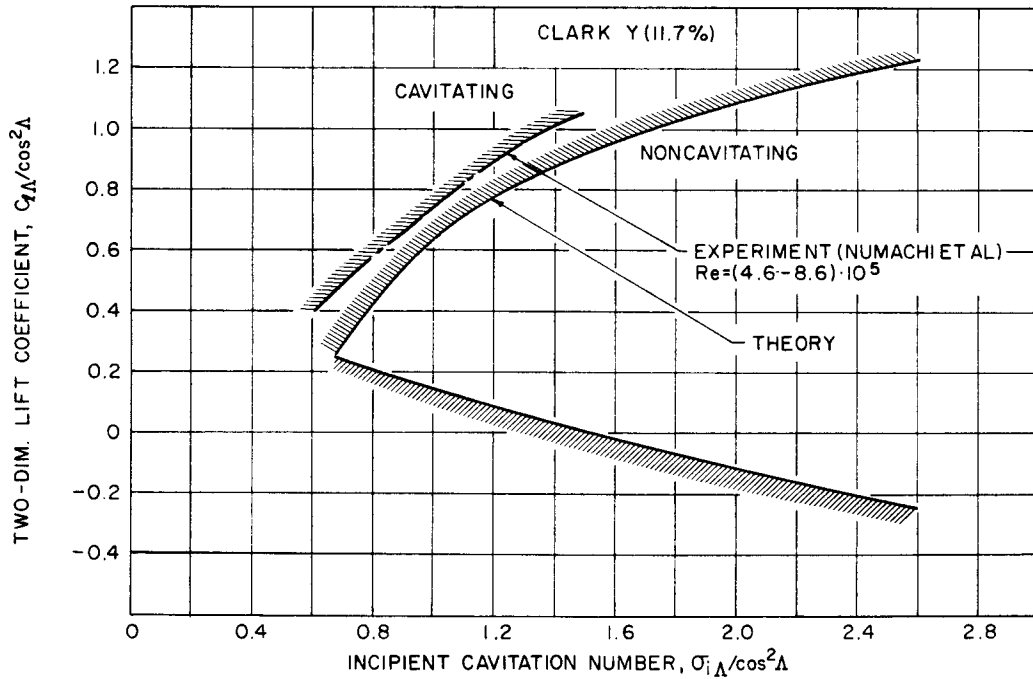


FIGURE 1.8 -INCIPIENT CAVITATION DIAGRAM FOR THE CLARK Y(11.7%)

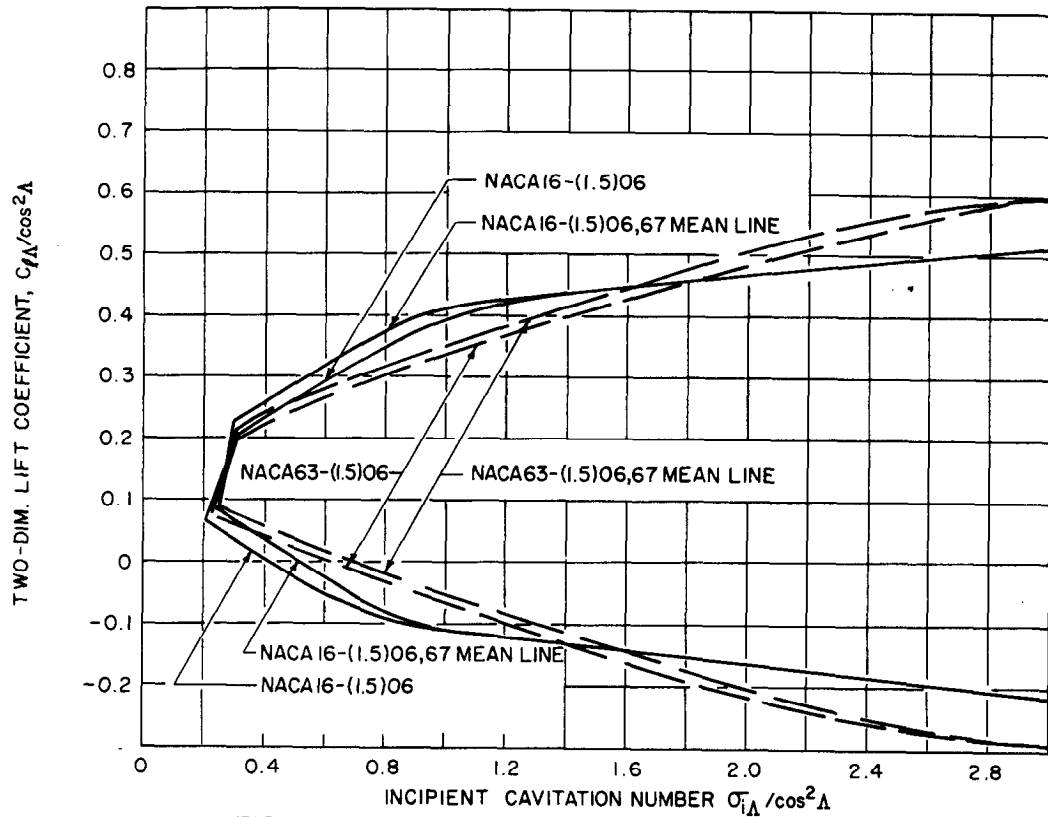


FIGURE 1.9 -INCIPIENT CAVITATION DIAGRAM FOR THE NACA16-(1.5)06 AND NACA63-(1.5)06

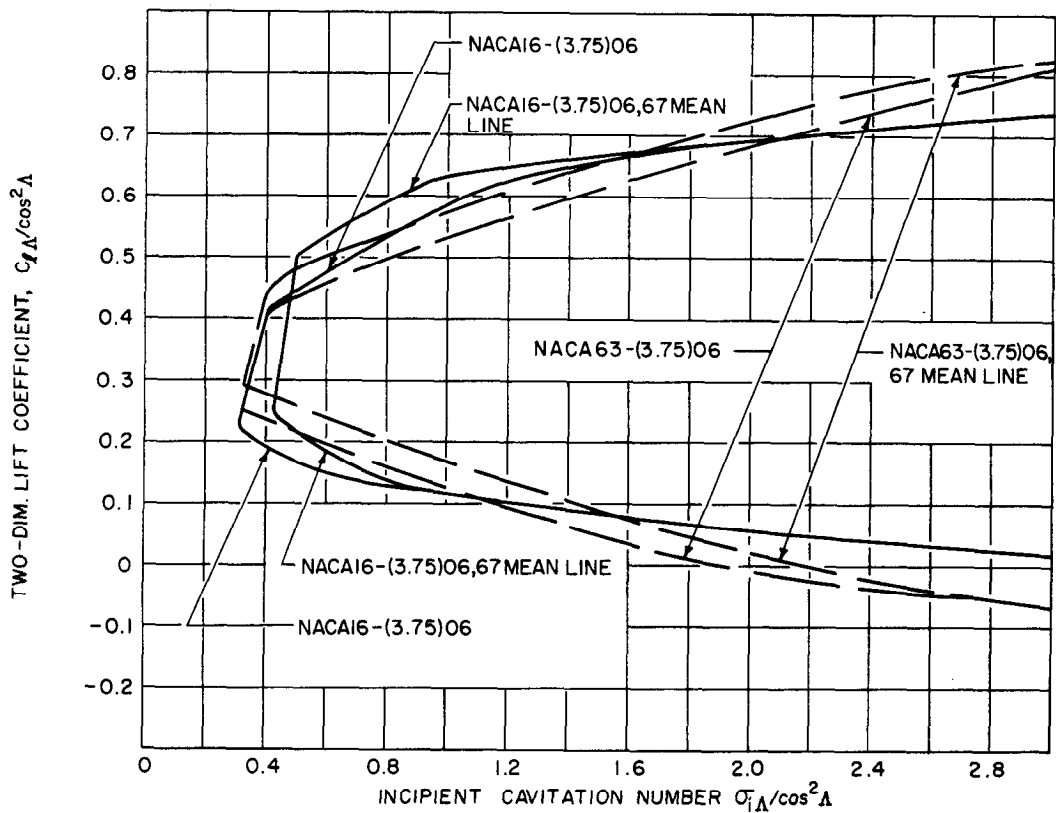


FIGURE 1.10 -INCIPIENT CAVITATION DIAGRAM FOR THE NACA16-(3.75)06 AND NACA63-(3.75)06

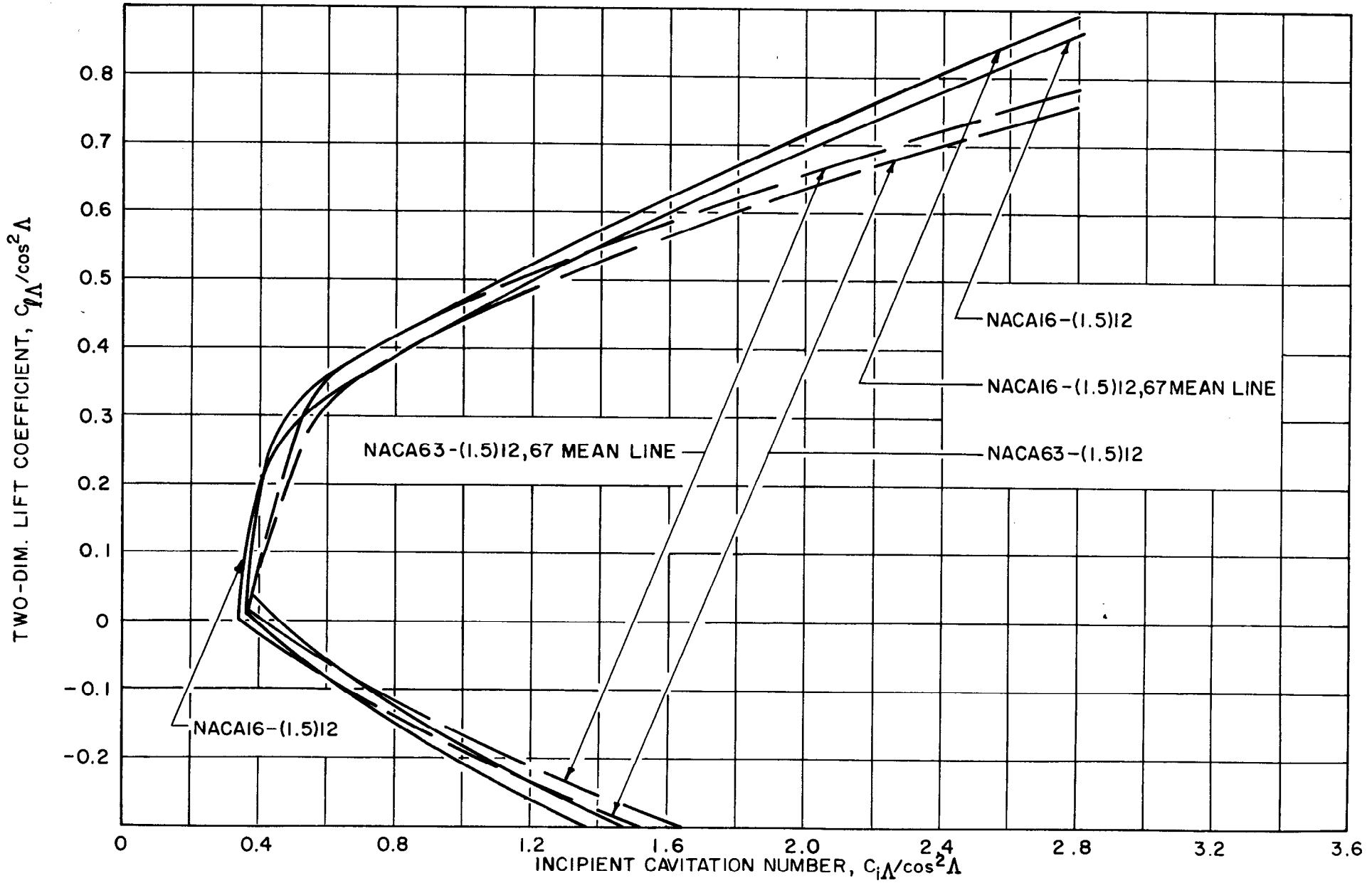


FIGURE I.11 - INCIPIENT CAVITATION DIAGRAM FOR THE NACA16-(1.5)12 AND NACA63-(1.5)12

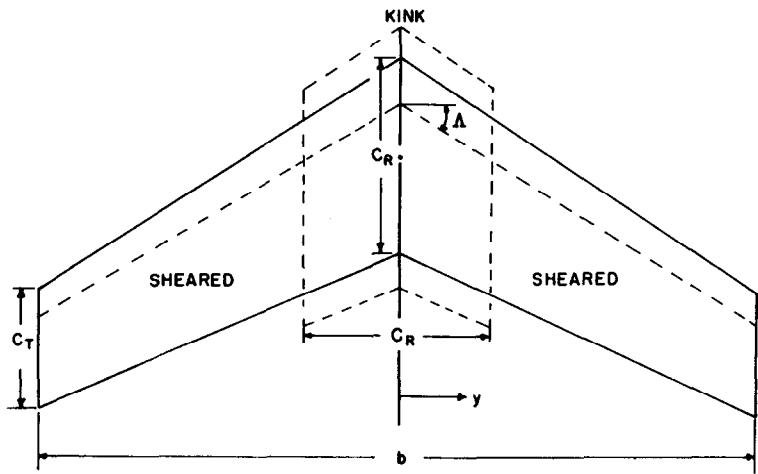


FIGURE 1.12 - GRAPHIC ILLUSTRATION OF KINK AND SHEARED REGIONS OF A SWEEP WING

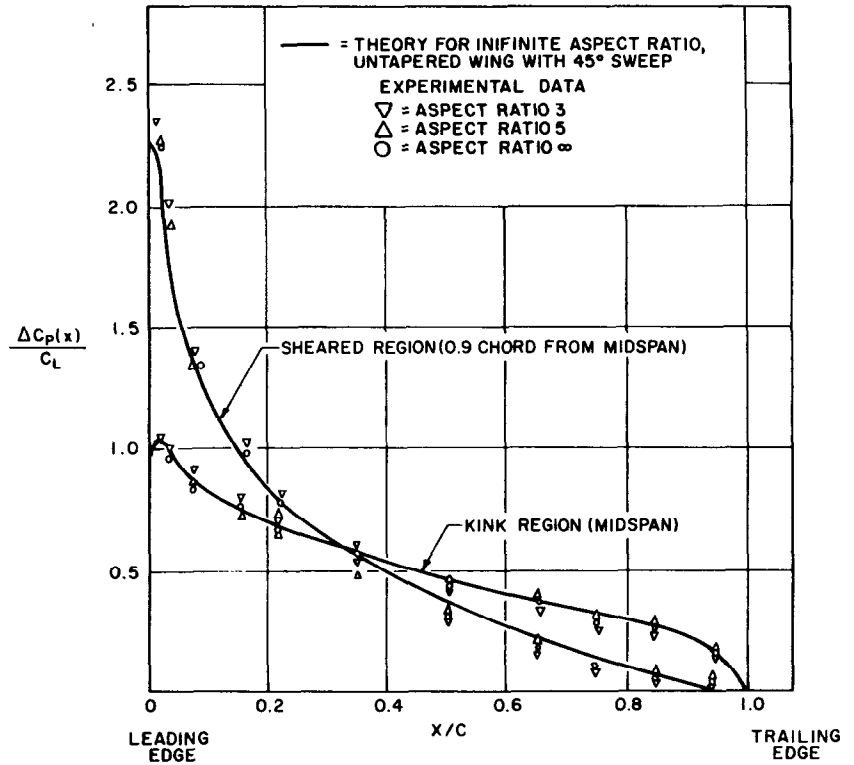


FIGURE 1.13 - PLOT OF PRESSURE COEFFICIENT OVER AVERAGE LIFT COEFFICIENT VERSUS CHORDWISE POSITION FOR THE KINK AND SHEARED REGIONS OF A 45° SWEEP WING. (REFERENCE 1.7)

5-5-

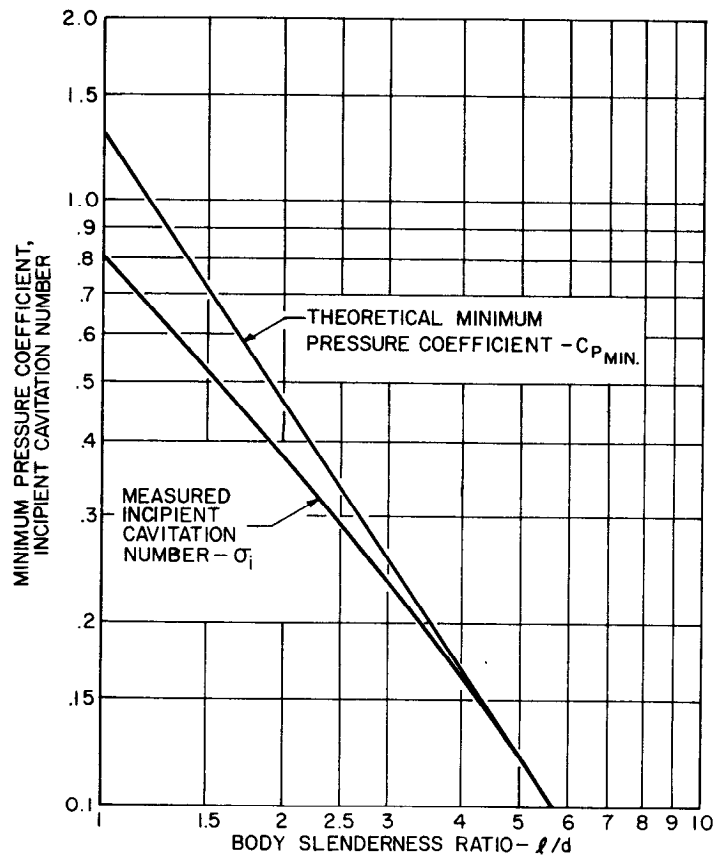


FIGURE 1.14 - COMPARISON OF MEASURED INCIPIENT CAVITATION NUMBER AND THEORETICAL MINIMUM PRESSURE COEFFICIENTS FOR ELLIPSOIDAL BODIES. (FROM I.18)

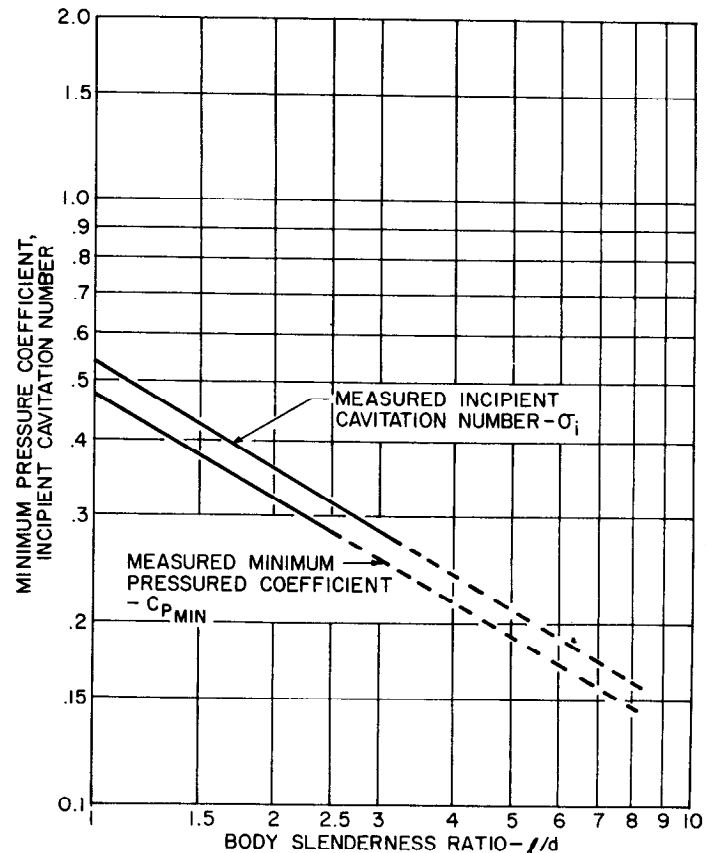


FIGURE 1.15 - COMPARISON OF MEASURED INCIPIENT CAVITATION NUMBER AND MINIMUM PRESSURE COEFFICIENT FOR OGIVAL BODIES. (FROM I.18)

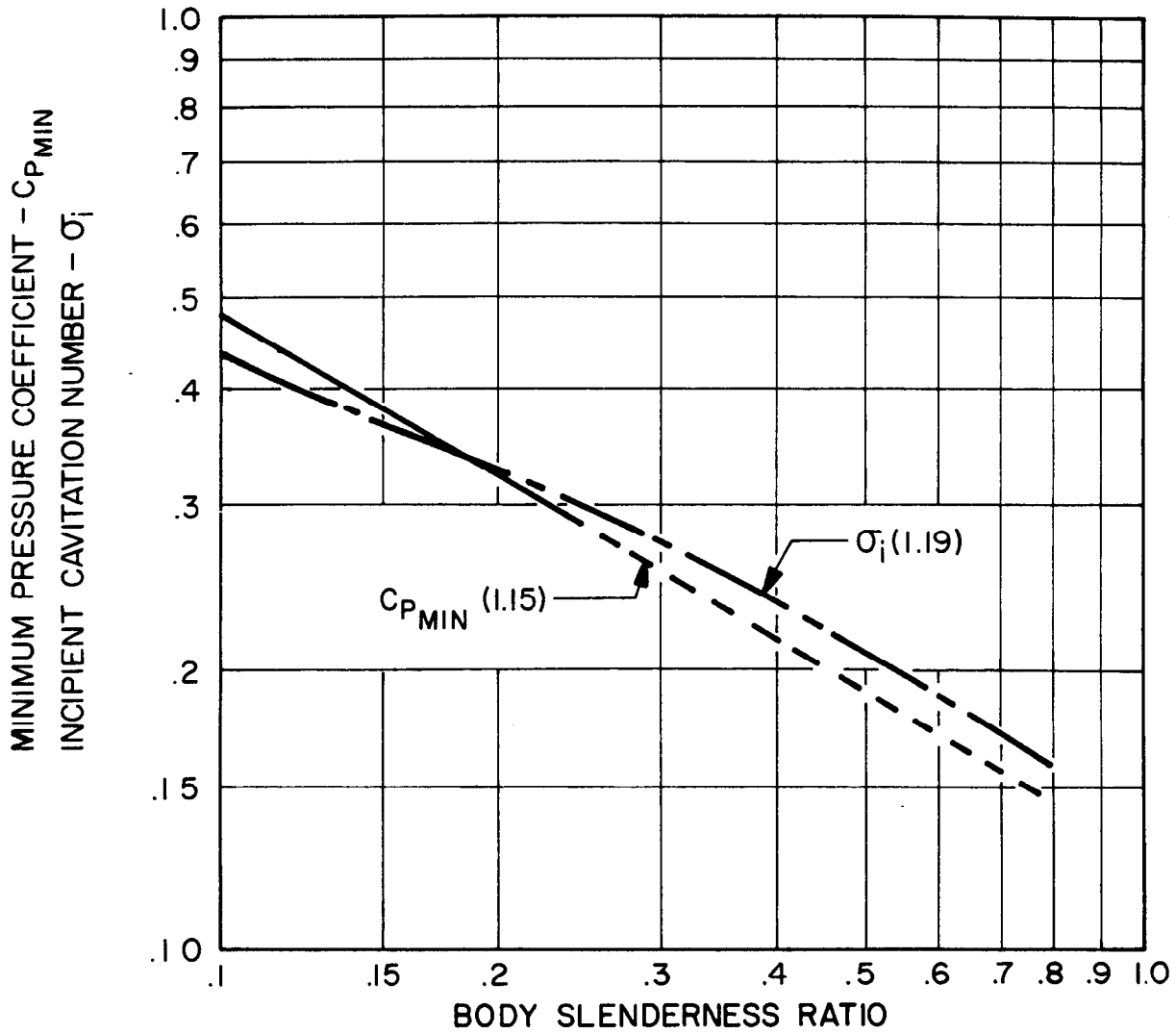


FIGURE I.16 - COMPARISON OF INCIPIENT CAVITATION NUMBER MEASURED BY KNAPP WITH MINIMUM PRESSURE COEFFICIENT MEASURED BY ROUSE AND McNOWN (FROM I.18)

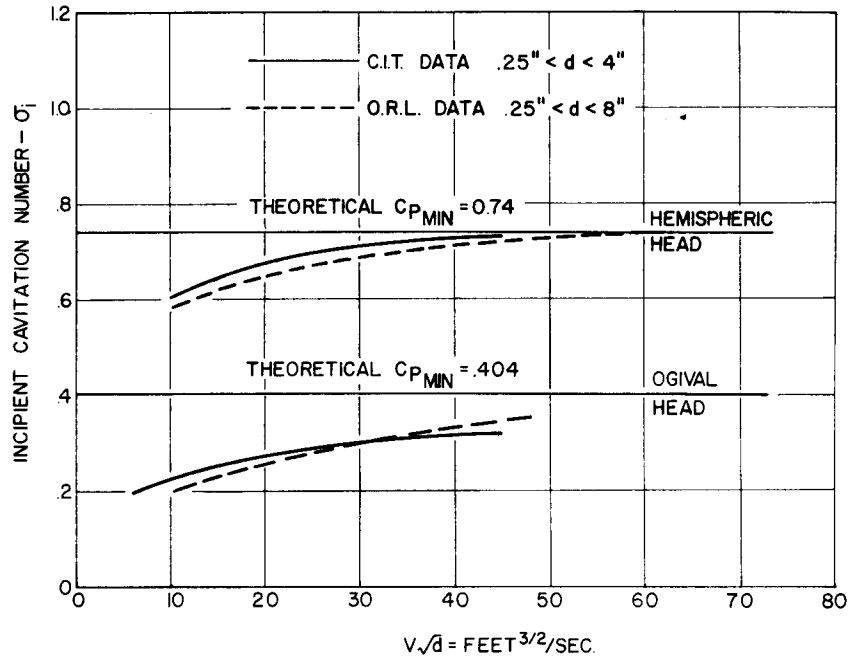


FIGURE I.17 COMPARISON OF MEASURED INCIPIENT CAVITATION NUMBER AND THEORETICAL MINIMUM PRESSURE COEFFICIENTS FOR AXISTMMETRIC BODIES SHOWING EFFECT OF PARAMETER $V\sqrt{d}$

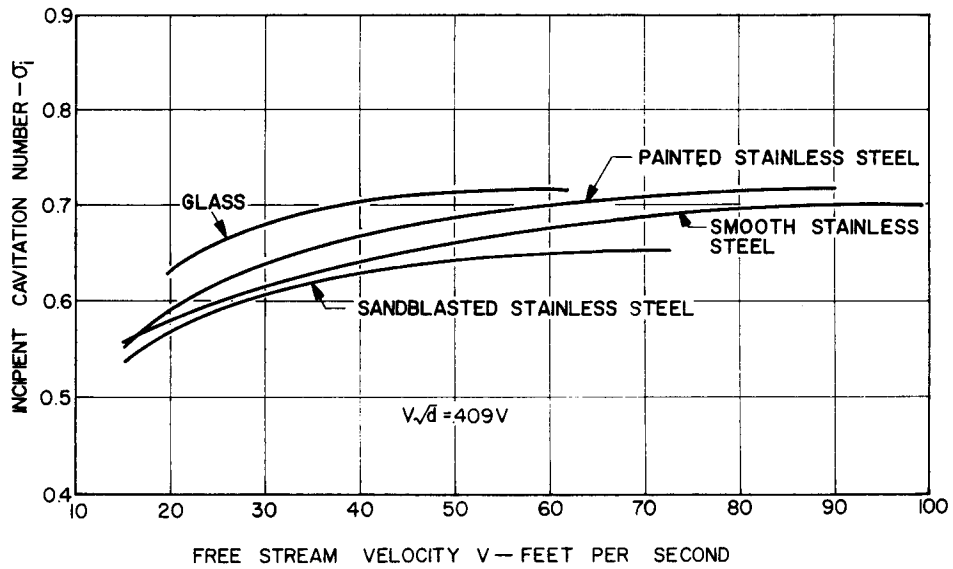


FIGURE I.18- EFFECT OF SURFACE FINISH ON CAVITATION INCEPTION FOR A TWO INCH DIAMETER HEMISPHERE (FROM I.20)

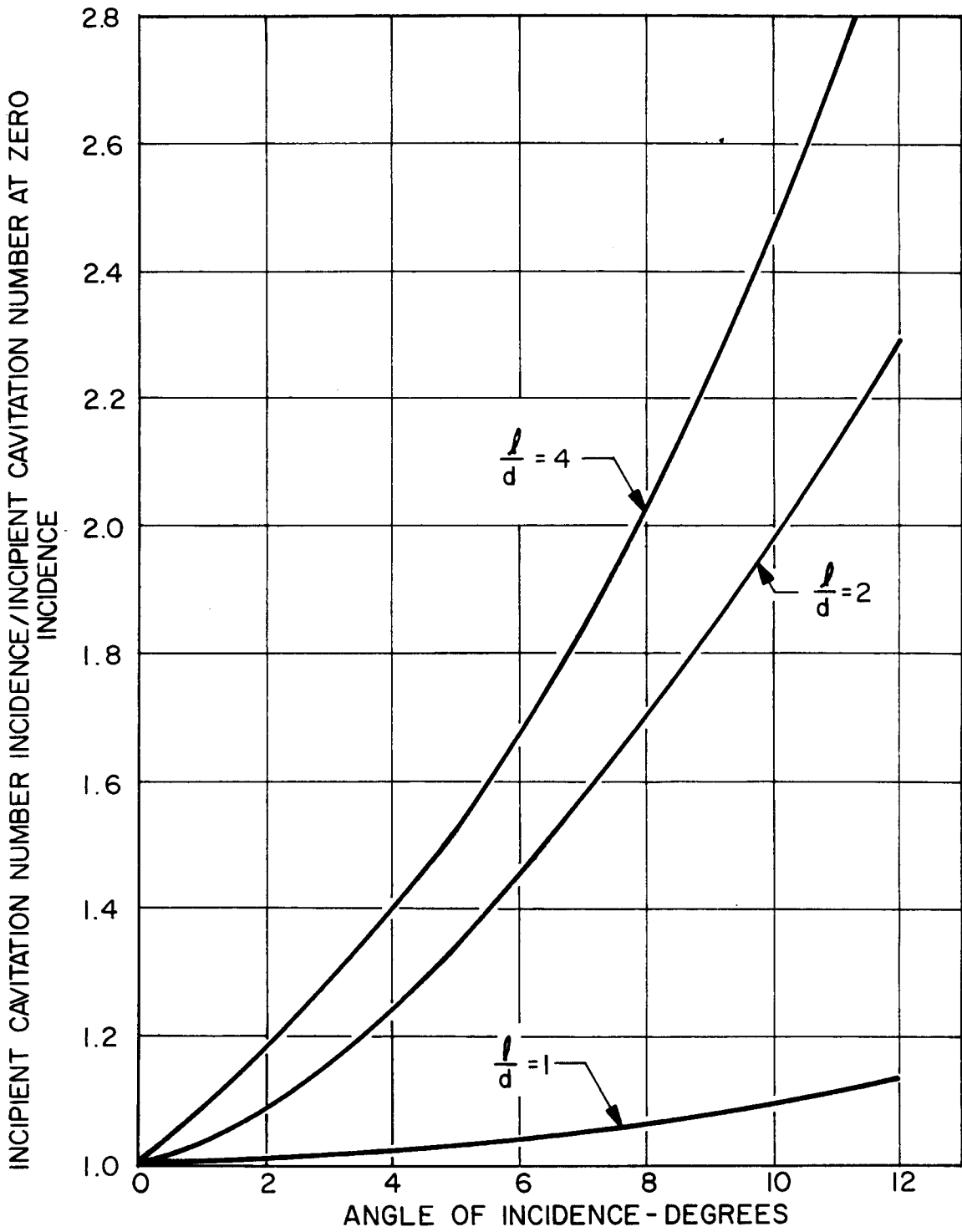


FIGURE 1.19-RATIO OF INCIPIENT CAVITATION NUMBER AT INCIDENCE TO THAT AT ZERO INCIDENCE AS A FUNCTION OF ANGLE OF ATTACK AND SLENDERNESS RATIO

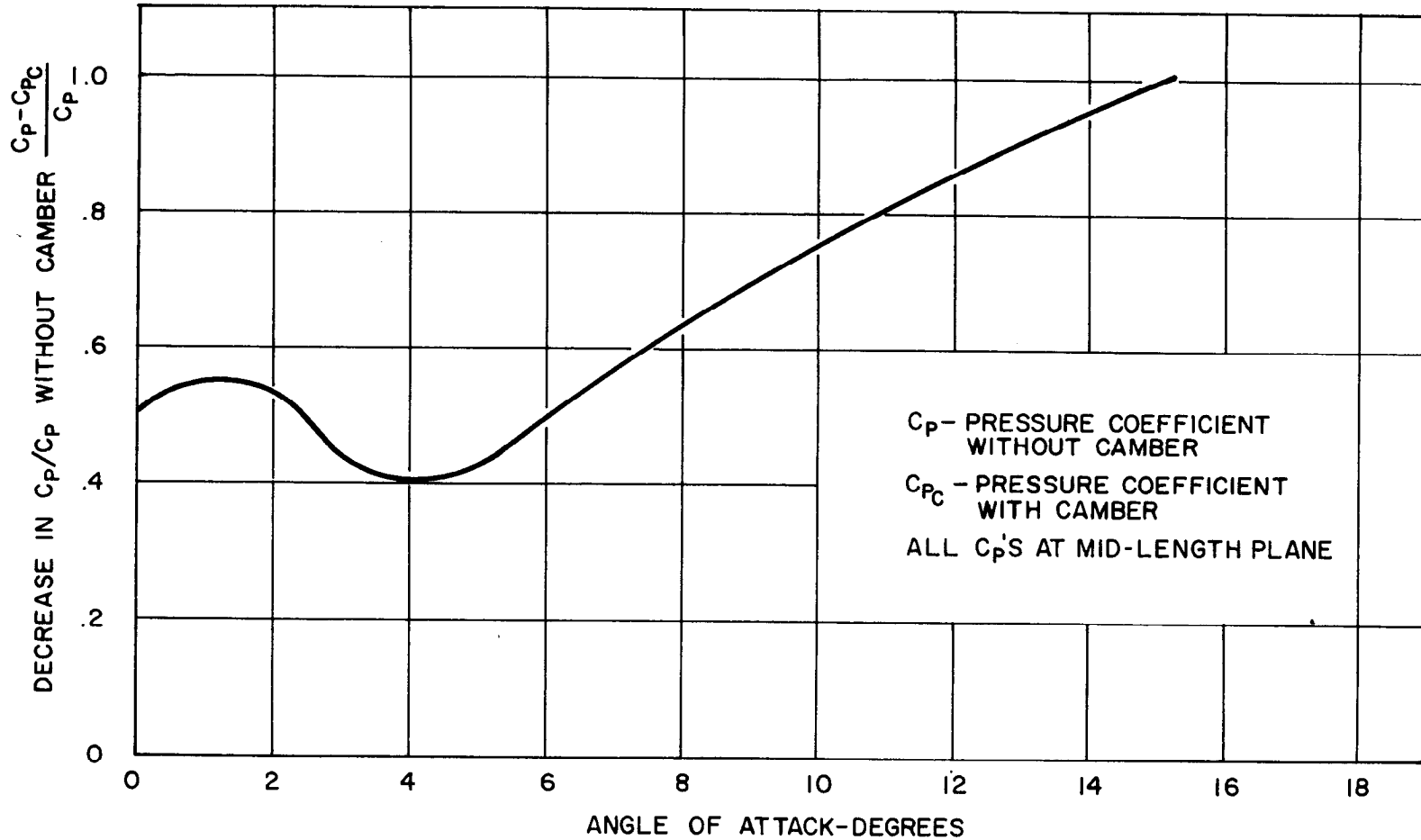


FIGURE I.20 -REDUCTION OF MINIMUM PRESSURE COEFFICIENT AT THE BODY MID-LENGTH ON THE SUCTION SIDE DUE TO CAMBERING FROM LANGE (I.17)

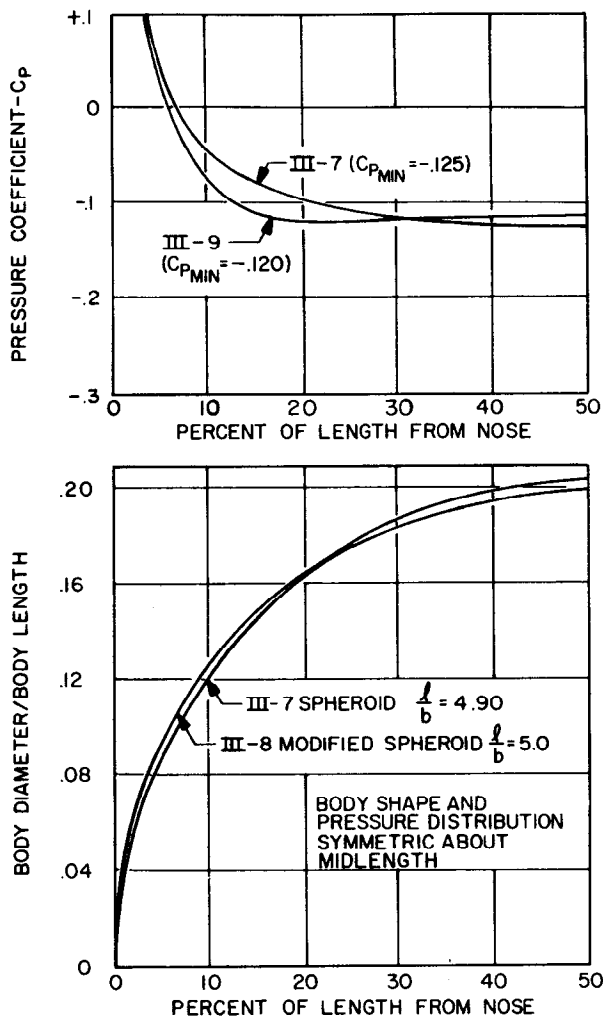


FIGURE 1.21-PRESSURE DISTRIBUTIONS AND SHAPES FOR BODIES III-7 AND III-8 FROM BRAND(I.15) SHOWING MINIMUM INCIPIENT CAVITATION NUMBERS FOR SYMMETRIC BODIES

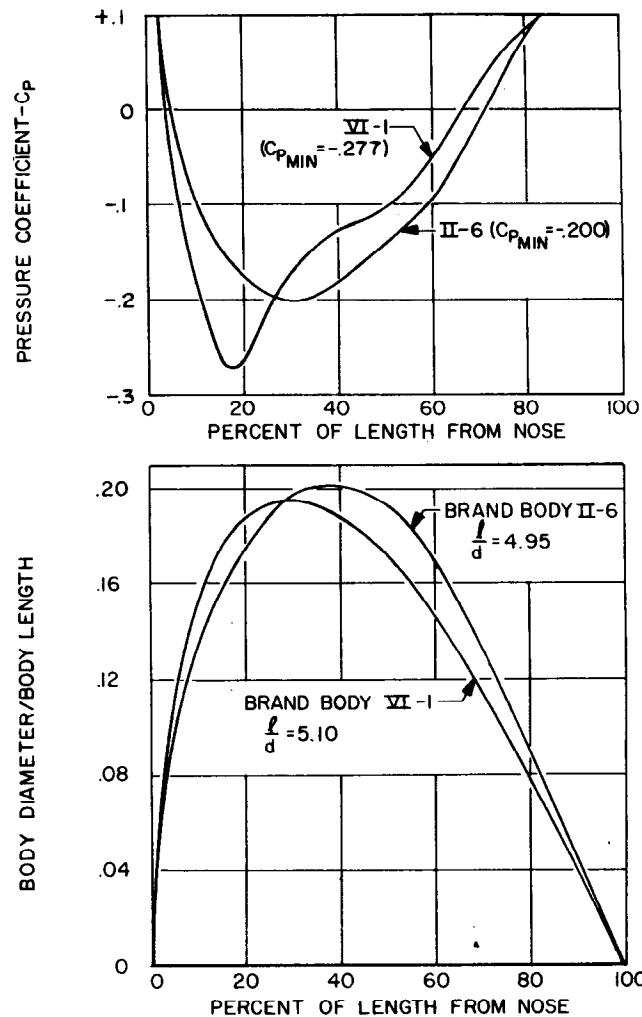


FIGURE 1.22-PRESSURE DISTRIBUTIONS AND SHAPES FOR BRAND BODIES II-6 AND VI-1 WITH HIGH PRESSURES AFT FOR AFT FOIL LOCATIONS (REFERENCE I.15)

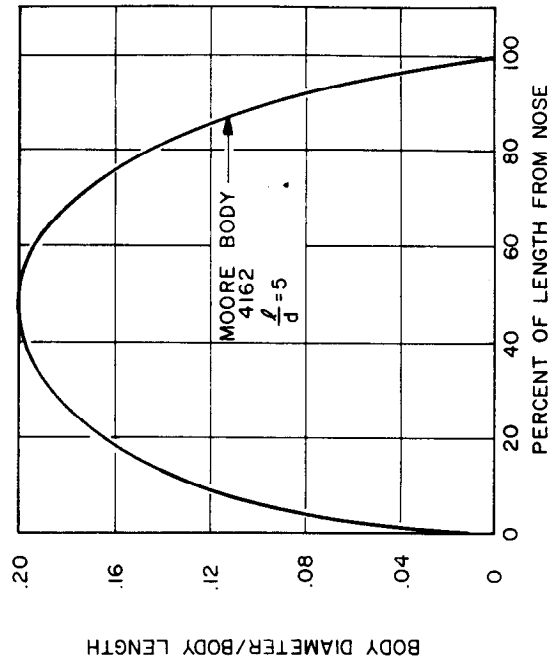
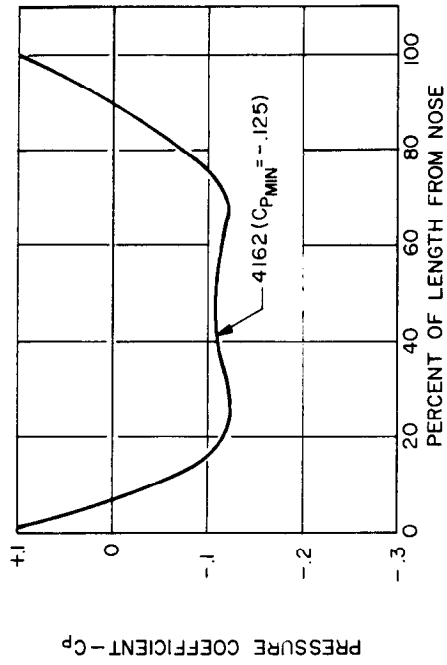


FIGURE 1.24 - PRESSURE DISTRIBUTION AND SHAPE FOR 4162 BODY GIVEN BY MOORE (REFERENCE 1.16)

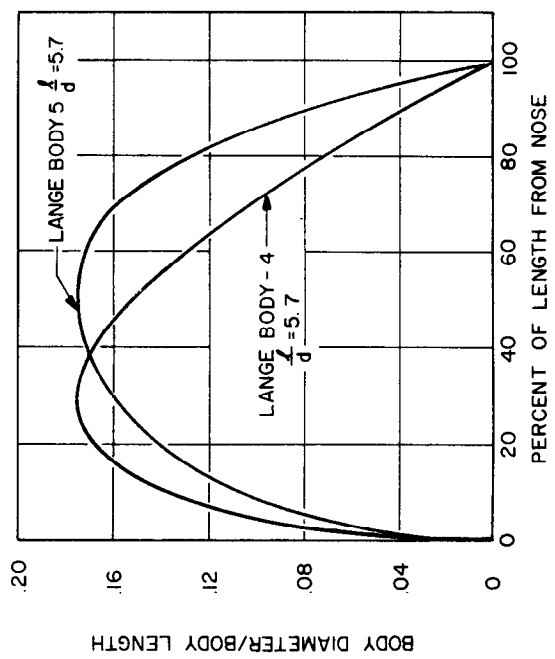
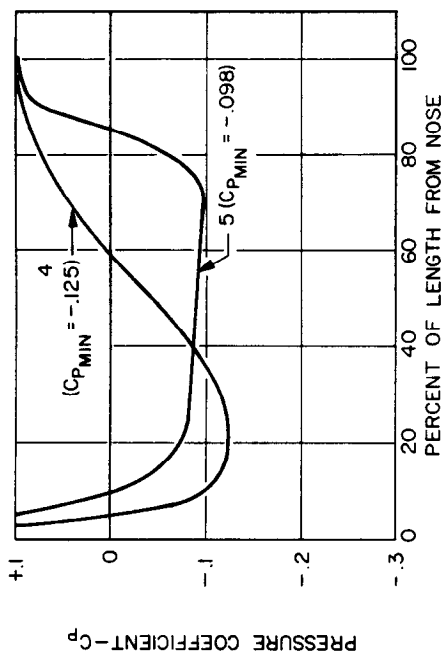


FIGURE 1.23 - PRESSURE DISTRIBUTIONS AND SHAPES FOR LANGE BODIES 4 AND 5 (REFERENCE 1.17)

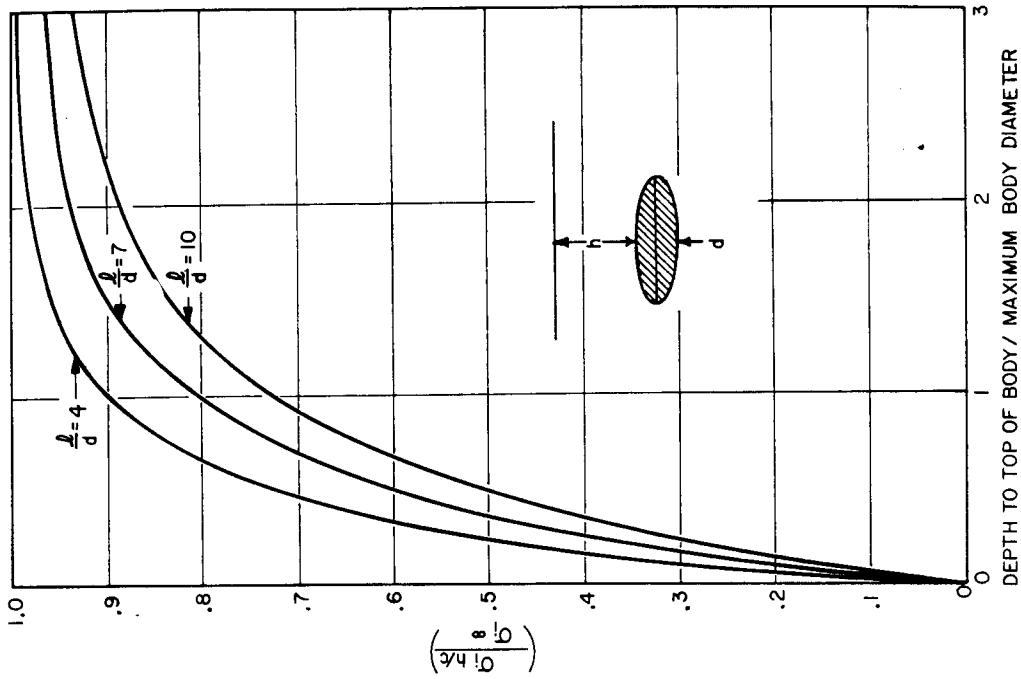


FIGURE 1.26 EFFECT OF DEPTH OF SUBMERGENCE ON THE INCIDENTAL CAVITATION NUMBER ON THE UPPER SURFACE OF AN AXISYMMETRIC BODY. (FROM REFERENCE 1.26)

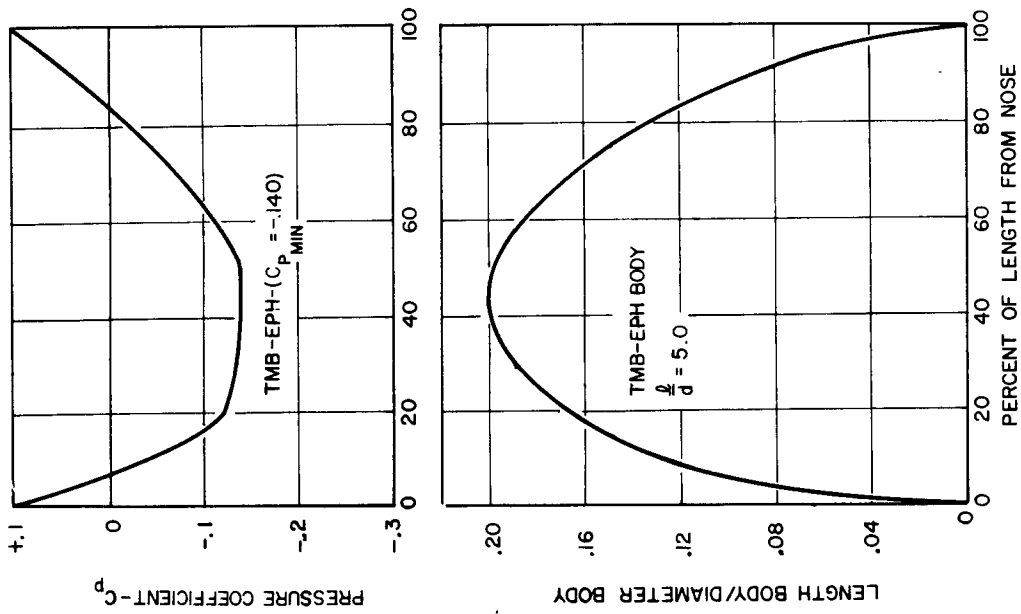


FIGURE 1.25 PRESSURE DISTRIBUTION AND SHAPE OF A TMB-EPH BODY FROM MOORE (REFERENCE 1.16)

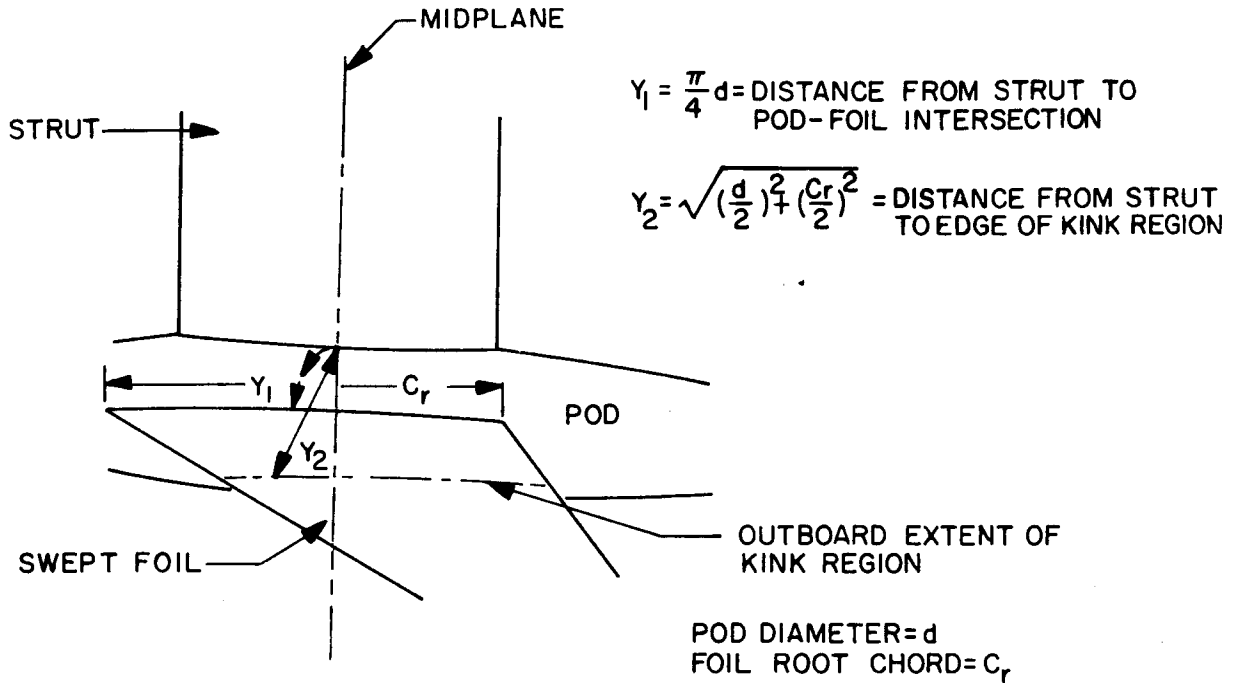


FIGURE 1.27 -FOIL-STRUT-POD INTERSECTION SHOWING DISTANCES FROM ONE COMPONENT TO THE CAVITATION INCEPTION POINT ON THE OTHER

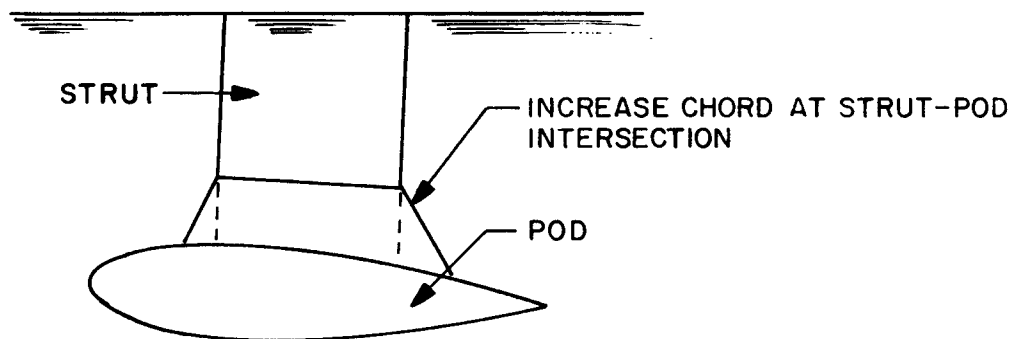


FIGURE 1.28 -INCREASE IN THE STRUT CHORD AT THE STRUT-POD INTERSECTION TO IMPROVE THE CAVITATION INCEPTION CHARACTERISTICS

HYDRONAUTICS, Incorporated

2.0

CHAPTER 2

CHOICE OF FOIL SYSTEM FOR
OPTIMUM PERFORMANCE

By

Roderick A. Barr

NOTATION

a	Constant defining the NACA rooftop camber distribution (see Chapter 1)
A	Foil aspect ratio
A_F	Foil planform area
A_S	Aspect ratio of submerged portion of strut
A_S	Area of submerged portion of strut
b	Factor defining end constraint of strut as a column
c	Foil chord
c_W	Strut chord at equilibrium waterline
c_f	Strut chord at foil or pod intersection
c_r	Midspan chord of foil
c_t	Tip chord of foil
C_c	Camber correction factor for section modulus
C_D	Drag coefficient based on planform area
C_{D_f}	Friction drag coefficient of foil or strut
C_{D_F}	Total drag coefficient of foil
C_{D_i}	Induced drag coefficient of foil
C_{D_I}	Interference drag coefficient of foil and strut
C_{D_P}	Profile drag coefficient of foil or strut

2.2

C_{D_S}	Spray drag coefficient of strut
C_{D_t}	Intersection drag factor of Reference 2.6
C_{D_T}	Tip loss drag coefficient of foil
C_f	Friction factor (usually Schoenherr)
C_F	Flap reduction factor for section modulus
C_H	Foil hollowing correction for section modulus
C_L	Section lift coefficient based on planform area
C_S	Foil thickness distribution factor for section modulus
C_t	Factor accounting for minimum pressure on a foil due to thickness distribution
C_α	Factor accounting for modification of incipient cavitation number due to angle of attack
E	Modulus of elasticity of strut material
f	Flap chordwise width
f/c	Flap-chord ratio
I_W	Moment of inertia of strut at undisturbed waterplane
K	Foil planform stress factor
K_f	Design columnar load of strut divided by critical load of strut
K_g	Acceleration of turn divided by the acceleration of gravity
K_i	Foil tip drag loss factor
$K_i \bar{c}_s$	Free surface correction for induced drag coefficient
	c_{D_i}

K_n	Percent of craft displacement Δ supported by a given strut
K_T	Factor to increase strut chord due to strut taper ratio
l_S	Length of submerged portion of the strut
m	Static margin of the craft
N	Number of struts per foil
P_c	Critical columnar load on strut
Re	Reynolds number based on foil or strut chord
s	Stress
\bar{s}	Non-dimensional stress - $\frac{s}{\frac{1}{2}\rho V^2}$
s_t	Stress in strut at equilibrium waterline
S	Planform area of foil
S_{ford}	Total planform area of all foils forward of CG
S_{aft}	Total planform area of all foils aft of CG
t	Foil thickness
t/c	Thickness-chord ratio of foil
(\bar{t}/c)	Average thickness-chord ratio of foil and strut at foil-strut intersection
$(t/c)_s$	Thickness-chord ratio of strut at equilibrium waterline
t_W	Wall or skin thickness of hollowed foil or strut section
V	Forward velocity of craft
X	Distance of foil from the craft center of gravity CG
z	Section modulus of foil or strut section
\bar{z}	Non-dimensional section modulus - z/c^3

Γ	Sweep angle of foil at the quarter chord line
Δ	Displacement of craft
δ_p	Planform correction factor for induced drag coefficient
λ	Taper ratio of foil - ratio of the midspan chord to the tip chord - c_r/c_t
λ_s	Taper ratio of strut
ν	Kinematic viscosity
ρ	Mass density of water
σ_i	Incipient cavitation number
σ_{i_f}	Incipient cavitation number of foil alone
σ_{i_p}	Incipient cavitation number of pod alone
σ_{i_s}	Incipient cavitation number of strut alone

INTRODUCTION

In undertaking the design of a hydrofoil craft, basic parameters such as displacement, maximum operating speed and operating environment will be known in advance. The designer is faced with the problem of producing, from these few numbers, a design which meets all requirements of speed, seaworthiness and stability while at the same time having the maximum possible efficiency (system lift-drag ratio).

Such a system must not only meet certain requirements for seaworthiness and stability, but must be free of unwanted cavitation and ventilation and have adequate behavior and performance throughout the entire operating range. To find the system meeting these requirements would seem a very difficult task, but it is nevertheless possible to approximately optimize a given system in each of these areas. In order to do this, however, the general features of the system must be chosen in advance. To begin with, then, the basis for the initial choice of the hydrofoil system (fully-wetted, surface-piercing, etc) must be decided upon.

In fully submerged foil systems, the stability and control characteristics of the foil are determined by the control surfaces (flaps and incidence) and the automatic control system. Because of the latter the stability and control characteristics of such systems are relatively insensitive to such parameters as foil aspect ratio, design lift coefficient and number of struts. The first consideration in the design of such a system can be that it have maximum efficiency while having adequate strength and cavitation free operation. Once the system is chosen, it can be modified,

as necessary, to meet the other requirements such as stability and control and ventilation inception, always keeping in mind the idea of maximizing the efficiency.

For systems where either the forward, or forward and aft foils are of surface piercing type, the choice becomes much more complicated. The shapes of such systems are generally chosen to provide certain favorable stability, control and motions parameters such as stiffness and damping ratio, etc. The problem becomes one of finding the system yielding these stability, control, and motion parameters and having the maximum efficiency and cavitation free operation. Here the designer's experience and cut and try procedures must be relied upon to facilitate the choice of the optimum system — for the number of independent variables becomes very large.

Both theory and experience have indicated that fully submerged foil systems with automatic control systems have smaller motions in a seaway than do comparable surface piercing foil systems. However, surface piercing systems have been somewhat favored in the past because of the greatly increased complexity associated with control systems. The Supramar hydrofoil boats (2.1) and the H.S. Dennison both employ surface piercing foils, although in the latter case automatic controls were added (2.2). Motions data for the Dennison are presented in Reference (2.3) where RMS vertical accelerations of .15 g are observed in 3 foot waves. The U.S. Navy hydrofoil ships PCH and AGEH utilize submerged systems with automatic control and there seems little question that such systems will be increasingly used in the future, especially for the higher design speeds.

FULLY SUBMERGED FOIL SYSTEMS

The results presented in the Grumman Handbook (2.4) indicate that a conventional (air-plane) configuration will always yield the maximum system efficiency (lift-drag ratios). Figure V.7 of (2.4) indicates the desirability of maximizing the loading on the forward foil, although there is little to be gained by increasing the loading on the forward foil over about 70 percent, particularly for split main foils. Practically, loadings between 60 and 90 percent on the forward foil are usually utilized to maximize the length between the forward and aft foils. The results presented in (2.4) are based on an assumed static margin of 0.05, although they are probably suitable for other practical static margins. Values of the static margin, which is given by

$$m \approx \frac{(S \times C_{L\alpha} \times X)_{\text{aft}} - (S \times C_{L\alpha} \times X)_{\text{ford}}}{S_{\text{aft}} + S_{\text{ford}}} \quad [2.1]$$

between 0.03 and 0.05 are probably acceptable.

Effect of Number of Struts and Aspect Ratio

The first step in choosing the foil system is to determine the number of struts and the allowable aspect ratio of the foil. These two parameters are interdependent and at the same time are functions of the allowable stress, the planform shape, the load distribution and the section modulus of the foil section. For a wing with straight taper as shown in Figure 2.1 the relationship between these parameters is given by

$$\bar{z} \bar{s} = K C_L A^2 \quad [2.2]$$

where

\bar{z} is the non-dimensional section modulus = $\frac{z}{c^3}$
at the centroid of the foil panel

\bar{s} is the non-dimensional stress coefficient = $\frac{s}{\frac{1}{2}\rho V^2}$

C_L is the lift coefficient

A is the foil aspect ratio

and K is a constant dependent on the number of struts, the taper ratio λ and the spanwise distribution of C_L . For the case of constant C_L , the value of K is given for one strut wing by Auslaender (2.5) as:

(a) Section modulus constant over the span:

$$K = \frac{(\lambda + 1)^2 (\lambda + 2)}{96 \lambda^3} \quad [2.3a]$$

(b) Stress constant over the span:

$$K = \frac{[(1 + \lambda)(1 + 2\lambda)(2 + \lambda)]^2}{384 (\lambda^2 + \lambda + 1)^3} \quad [2.3b]$$

2.9

For wings with two struts and constant taper as shown in Figure 2.1, the value of K for a wing with constant section modulus over the span is given by

$$K = \frac{(\lambda + 5)}{96(\lambda + 1)} \quad [2.4a]$$

For two strut wings it is not possible to design constant stress inboard of the struts because of the points of zero moment, but the outboard panels can be designed for constant stress in which case

$$K = \frac{[(\lambda + 2)(\lambda + 1)(\lambda + 5)]^2}{96[\lambda^2 + 4\lambda + 7]^3} \quad [2.4b]$$

where \bar{z} is the section modulus at the centroid of the outboard panel. Values of K for one strut and two strut wings are plotted in Figures 2.2a and 2.2b as a function of the taper ratio λ .

The advantage of a constant section modulus (\bar{z}) foil is the greater ease of construction which should result from making all foil sections similar. The major disadvantage of constant section modulus is the increased profile drag resulting from greater-thickness outboard of the struts.

The section moduli \bar{z} defined by the factors K of Equation [2.3b] and [2.4b] are at the centroid of area of the outboard panels of the foil. The section moduli at the strut or pod intersections are the same as given by the factors K of Equations [2.3a] and [2.4a]. For the two strut, constant stress foil with taper, the

section moduli inboard of the struts can be reduced from that at the struts or pods, further reducing the profile drag of the foil.

The cavitation inception characteristics of both constant \bar{z} and constant stress foils are the same at the intersections, as the sections are identical there. Away from the intersections, the reduced thicknesses of the constant stress section may lead to better or worse cavitation inception characteristics depending on the range of angles of attack likely. If the range of angles of attack is small, the constant stress foil will probably have better inception as well as drag characteristics. The only practical way to choose between the two types would seem to be to carry out calculations for both types and to choose the best type from cavitation inception, minimum drag and ease of construction. Where ease of construction is deemed a major consideration the constant section modulus foil is clearly indicated.

Determination of Section Modulus \bar{z}

The non-dimensional section modulus is a function of the section geometry and is given by

$$\bar{z} = C_s C_H C_f C_c \left(\frac{t}{c} \right)^2 \quad [2.5]$$

C_s is the factor accounting for the thickness distribution and is given in Table 2.1 for typical NACA sections. C_H is the factor accounting for hollowing and is given in Figure 2.3 as a

function of the section wall thickness t_w/t . C_f is the factor accounting for the loss in section modulus due to flaps and is given in Figure 2.4 as a function of flap-chord ratio λ_f for NACA 16 and 66 series sections. Figure 2.4 assumes that the flap contributes nothing to the section bending strength which is generally true. C_c accounts for the effect of camber and is given in Figure 2.5 as a function of the two-dimensional lift coefficient.

The thickness chord ratio t/c is determined from cavitation inception considerations. Chapter 1 gives the expression for the incipient cavitation number σ_1 , due to the wing alone:

$$\sigma_1 = \frac{C_L}{2a} + C_t \left(\frac{t}{c} \right) \cos \Gamma \quad [2.6]$$

where C_t is given for NACA sections in Table 1.1 and a describes the chordwise circulation distribution, see Chapter 1. The accurate prediction of σ_1 from theory is discussed in detail in Chapter 1 as is the probable conservative nature of that prediction.

The Grumman Handbook (2.4) indicates that a loading of 2000 pounds per square foot, corresponding to:

$$C_L = \frac{2000}{\frac{1}{2}\rho V^2}$$

should be used to avoid cavitation. Chapter 1 points out that this may be an oversimplification of the problem and that the particular operating conditions must be considered. Equation [2.6] can be modified to account for fluctuating angles of attack so that the incipient cavitation number on the foil, σ_{1_f} is given by

$$\sigma_{1_f} = C_\alpha \left(\frac{C_L}{2a} + C_t \left(\frac{t}{c} \right) \cos \Gamma \right) \quad [2.7]$$

where C_α accounts for the angles of attack expected in a seaway and is discussed in Appendix 1. Equations [2.2], [2.5] and [2.7] can now be combined to yield a relationship between the allowable aspect ratio and the lift coefficient:

$$A = \sqrt{\frac{C_s C_H C_f C_c \bar{s}}{K C_t^2 \cos^2 \Gamma}} \sqrt{C_L} \left[\frac{\sigma_{1_f}}{C_\alpha C_L} - \frac{1}{2a} \right] \quad [2.8]$$

The only problem arising in the solution of [2.8] is that the factor C_α is dependent on the thickness-chord ratio t/c . C_α can be approximated, however, and the relationship between A and C_L determined for several typical values of C_α . The result will be a series of curves, each for a constant value of C_α , of the type shown in Figure 2.6.

Calculation of Foil Drag

The optimum foil can only be determined by optimizing the whole foil system. For systems where most of the lift (say 80 percent or greater) is on the main foil it is probably adequate to optimize the main foil-strut system independently. The drag of the foils, strut and pods, can be calculated from the component drag coefficients given by Martin (2.6). The tail foil can then be optimized in the same manner, including the downwash drag from (2.6).

The foil drag is composed of: Induced drag, frictional drag, profile drag, wavemaking drag and tip loss drag. The strut drag is composed of frictional drag, profile drag and spray drag. In addition, there is a foil-strut interference drag or a pod drag. For foils operating in the downwash of other foils (as is the case with some tail foils), there is an additional induced drag.

The components of the foil drag (exclusive of downwash drag) are given by (2.6) as

$$\text{Induced drag } C_{D_i} = C_L^2 (1 + \delta_P) \left[\frac{1}{\pi A} + \frac{K_1 \bar{c}_s}{8\pi} \right]$$

$$\text{Friction drag } C_{D_f} = 2C_f$$

$$\text{Profile drag } C_{D_p} = 2C_f \left[1.2 \left(\frac{t}{c} \right) + 60 \left(\frac{t}{c} \right) \right]^4$$

Wavemaking drag - See Equation [58c] and Figure 10 of (2.6)

$$\text{Tip loss drag } C_{D_T} = K_1 \left(\frac{t}{c} \right)^2 \left(\frac{2}{T+1} \right)^2 \frac{1}{A}$$

The factors δ_P and $K_1 \bar{c}_s$ are planform and free surface corrections given by Figures 23 and 24 of (2.6). For wings of typical aspect ratios and taper ratios, δ_P is only a few percent and can be readily ignored. The factor $K_1 \bar{c}_s$ cannot be ignored generally, but is, for the range of interest, independent of aspect ratio and dependent only on the depth-chord ratio which can be estimated. The friction factor C_f is generally based on the Schoenherr friction line. The data of Figure 21 of (2.6) can be used to estimate the effect of surface roughness on the value of C_f . Standard ship practice allows for an increase in C_f due to roughness of 0.0004.

For the thickness ratios of interest here ($t/c \leq 0.12$) the term $60 (t/c)^4$ is much smaller than $1.2 (t/c)$ and can be readily ignored. The value of K_1 is given by (2.6), but for all practical foils the value of the tip loss drag becomes negligible and can be dropped. Figure 1 of Chen (2.7) indicates that for practical hydrofoil boats wavemaking drag should be negligible. This is borne out by Figure 10 of (2.6) which indicates that for practical aspect ratios the wavemaking drag is unlikely to be important. The total drag coefficient of the foil C_{D_F} can now be written, making these approximations:

$$C_{D_F} = \frac{C_L^2}{\pi} \left(\frac{1}{A} + \frac{K_1 \bar{c}_s}{8} \right) + 2(C_f + 0.0004) \left[1 + 1.2 \left(\frac{t}{c} \right) \right] .$$

[2.9]

It should be noted that the approximations inherent in Equation [2.9] are small, but are made only to facilitate the choice of an optimum foil system. Once a foil system has been chosen, the calculation of the performance should include all those terms omitted from [2.9] even though they be small. The same comments hold true for the calculation of strut and interference drag, the omission of small terms being designed to facilitate choice of an optimum foil system.

Estimation of Strut Size

The size, and consequently the drag, of the struts is determined by structural considerations and cavitation inception. The size is normally dependent on the bending loads occurring during turning although in some cases the columnar loading due to foil lift may become critical. A detailed analysis of strut loading and allowable stresses is beyond the scope of this chapter. Simple means of estimating the required strut geometry from structural considerations are, however, included.

For turning, a centrifugal load of 0.5 times the acceleration of gravity is often assumed. The Grumman Handbook recommends the use of 0.75 times gravity and this is probably a good design value, unless the value for the particular craft has been otherwise specified. Figure 2.7 indicates the loading of a strut during a turn and indicates those dimensions of importance. It is assumed that the loading on the strut is at the wetted center of area of the strut because of the effect of the free surface and foil. The stress in the strut at the equilibrium waterline is given by:

$$S_t = \frac{\Delta K_g}{3K_n} \frac{(2C_w + C_f)}{(C_w + C_f)} \cdot \frac{l_s}{C_w^3 \bar{z}} \quad [2.10]$$

where Δ is the displacement of the craft, K_g is the acceleration due to turning divided by the acceleration of gravity, K_n is the percent of the craft displacement supported by the strut and C_w and C_f are the strut chords at the equilibrium waterline and at the foil, and l_s is the submerged length of the strut. The stress is taken at the waterline because above this point the strut can generally be thickened by the amount required to keep the stress equal to or less than at the waterline.

The allowable section modulus \bar{z} can be found by combining Equation [2.5] and [2.7] and eliminating those terms peculiar to lifting foils

$$\bar{z} = C_s C_H C_F \left(\frac{\sigma_{1s}}{C_a C_t} \right)^2 \quad [2.11]$$

where C_F now refers to the reduction due to a flap type rudder, if this type is used for steering and σ_{1s} refers to the incipient cavitation number of the strut. The required chord at the equilibrium waterline can now be found from Equations [2.10] and [2.11]; the resulting equation is a quartic. If the center of load on the strut is assumed to be at the midlength, however the expression for the root chord becomes:

$$C_w = \sqrt[3]{\frac{\Delta K_g l_s}{2 K_n C_s C_H C_F} \left(\frac{C_a C_t}{\sigma_{i_s}} \right)^2 \frac{1}{S_f}} \quad [2.12]$$

Although Equation [2.12] is only exact for constant chord struts ($C_w = C_f$), the errors that will be introduced are small for all practical taper ratios. The exact value can be obtained by multiplying C_w by the factor K_T where K_T is given by Figure 2.8 as a function of the taper ratio C_w/C_f . The area of the strut is given by

$$A_s = \frac{(C_w + C_f)}{2} l_s$$

and the thickness chord ratio of the foil can be obtained from Equation [2.7].

If the strut is considered as a slender column the section at the waterline required to stay below the critical load can be calculated. For single strut foils the strut should be considered fixed at the waterline and pinned at the foil while for multi-strut foils the strut should be considered as fixed at the waterline and something between fixed and pinned at the foil end. In these cases the critical load P_c is given by

2.18

$$\begin{array}{l} \text{Single Strut foil} \\ \text{(foil end pinned)} \end{array} \quad P_c = \frac{\pi^2 E I_w}{(2l_s)^2} \quad [2.13a]$$

$$\begin{array}{l} \text{Multi-Strut Foil} \\ \text{(foil end fixed)} \end{array} \quad P_c = \frac{\pi^2 E I_w}{\left(\frac{1}{2}l_s\right)^2} \quad [2.13b]$$

where E is the modulus of elasticity and I_w is the moment of inertia of the strut section at the waterplane. The moment of inertia I_w is equal to

$$I_w = \frac{Z}{2} \left(\frac{t}{c}\right) C_w^4 \quad [2.14]$$

If the lift load on the strut ΔK_g is assumed to be some fraction K_f of the critical load P_c , then the required minimum chord which will be C_f is given by:

$$C_f = \left[\frac{2\Delta K_g (b l_s)^2}{\pi^2 K_f C_s C_H C_F E} \left(\frac{C_a C_t}{\sigma_{1s}} \right)^3 \right]^{\frac{1}{4}} \quad [2.15]$$

Although the loads applied to the strut will be greater, at times, than the steady lift, the strut should be adequate if a value of b lying between those for fixed and free lower ends and a reasonable factor of safety on the critical load P_c is used. A value of b of

one would seem to be a reasonable choice. Equation [2.14] is based on the assumption that the section modulus of the strut is everywhere greater than that at the foil intersection. The strut chord at the foil should be assumed equal to the foil chord or the value from [2.15], whichever is greater, and this value used in determining the strut area.

Calculation of the Strut and Interference Drag

The strut drag coefficient C_{D_F} can be obtained from Equation [2.9] by eliminating the induced drag term C_{D_i} and adding the interference drag C_{D_I} and Spray drag C_{D_S}

$$C_{D_F} = 2(C_f + 0.0004) \left[1 + 1.2 \left(\frac{t}{c} \right)_s \right] + C_{D_I} + C_{D_S} \quad [2.16]$$

The thickness chord ratio of the strut $(t/c)_s$ may vary so that an average value should be used. The thickness chord ratio at the vertical center of area is probably the most typical value.

Martin (2.6) gives an interference drag which accounts for the inter-action of the foil and strut:

$$C_{D_I} = C_{D_t} \left(\frac{\bar{t}}{c} \right)^2 \left(\frac{2}{\lambda+1} \right)^2 \frac{1}{A} \quad [2.17]$$

where (\bar{t}/c) is the average thickness of the foil and strut at the intersection. The factor C_{D_t} is given by Figure 26 of (2.6). For cases where the intersection is filleted and the value of \bar{t}/c is in the normal range ($\bar{t}/c \leq 0.15$) the interference drag becomes negligible.

For cases where pods are used at intersections, the pod drag replaces the interference drag. The pod drag is composed of frictional drag and separation or pressure drag. For slender bodies (say $l/d > 5$) the separation drag at zero incidence is very small. The friction drag is proportional to the pod surface area A_p , which is given approximately by

$$A_p = 3\pi d^2 (l/d) .$$

Assuming a ten percent increase in friction drag due to separation, the pod drag coefficient C_{D_I} , based on the pod cross-sectional area $\pi d^2/4$, is given by

$$C_{D_I} = 3.30 C_f (l/d) . \quad [2.18]$$

For a typical Reynolds number (say 10^7) the friction factor C_f is approximately 0.003 and the pod drag coefficient becomes approximately $0.01 l/d$, a value which is in agreement with tests of slender axisymmetric bodies.

Equation [2.18] gives good agreement with experiments such as those of Lange (2.18). Measured values of C_{D_I} from Lange, at $Re = 3 \times 10^6$ ($C_f = .0036$), are compared with Equation [2.18] in the following table:

Body	C_D measured	C_D calculated
2 - $l/d = 5.71$, d_{\max} at $.4l$.0685	.0677
3 - $l/d = 4.0$ d_{\max} at $.4l$.0450	.0472
4 - $l/d = 5.71$ d_{\max} at $.5l$.0685	.0677

The table above indicates good agreement, especially considering the approximation inherent in [2.18]. Where data for the particular body is unavailable, Equation [2.18] should give adequate results.

Reference (2.4) also gives an expression for the spray drag coefficient C_{D_s}

$$C_{D_s} = 0.24 \left(\frac{t_s}{c} \right)^2 \left(\frac{\lambda_s + 1}{2} \right)^2 \frac{1}{A_s} . \quad [2.19]$$

where λ_s is the taper ratio of the submerged portion of the strut, A_s is the aspect ratio of the submerged portion of the strut, and $(t/c)_s$ is taken at the free surface.

Determination of the System of Minimum Drag

With the aid of the equations presented above, the optimum foil-strut system can be chosen by parametric studies. Those parameters which must be varied in order to determine the optimum system are:

1. Fore and aft load distribution (loading on the forward foil usually 70 percent or greater).
2. Number of struts (usually one or two).
3. Main foil lift coefficient (usually in the range from 0.15 - 0.35).
4. Distribution of incipient cavitation number between foil, strut and pod at intersections. Reasonable ranges of values might be:

$$\sigma_{i_p} \leq \sigma_{i_s} \leq \sigma_{i_F} \leq 4 \sigma_{i_p} \quad (\text{with pod})$$

$$\sigma_{i_s} \leq \sigma_{i_F} \leq 3 \sigma_{i_s} \quad (\text{without pod})$$

Once the number of struts (2), foil lift coefficient C_L (3) and foil incipient cavitation number σ_{i_s} (4) are chosen, the aspect ratio is given by [2.8], the foil thickness chord ratio by [2.7] and the foil drag coefficient by [2.9]. The Reynolds number is based on the average chord and is given by:

$$Re = \frac{V_o c_{av}}{\nu} = \frac{V_o}{\nu} \sqrt{\frac{A_F}{A}}$$

where the foil planform area A_F is given by:

$$A_F = \frac{\Delta N}{KN^{\frac{1}{2}} \rho V_o^2 C_L}$$

and N is the number of struts per foil.

The strut size and drag can be determined once conditions (1), (2) and (4) are chosen. The chord and thickness of the strut at the waterline are determined from Equations [2.1] and [2.12]. The minimum chord of the strut at the foil intersection is given by [2.15]. In cases where it is desired to increase the chord C_f to that of the foil chord, the thickness can be reduced by keeping the same value of I_w as given by Equation [2.13].

APPENDIX 2.1

THE EFFECT OF THE SEAWAY ON FOIL DESIGN

Operation in a seaway will induce both positive and negative angles of attack on a foil. These changes in incidence will result in a change in the incipient cavitation number. In Equation [2.7] the factor C_α represents the ratio of the incipient cavitation number at finite incidence to that at zero incidence σ_1 . The values of C_α can be obtained from section cavitation buckets of the type shown in Figures 1.9 to 1.11. For initial calculations of the foil system characteristics, the section characteristics are not known, so that C_α cannot be found. One solution is to pick a wide enough range of values of C_α as illustrated in Figure 2.6 and determine by trial and error the foil aspect ratio and lift coefficient using Equations [2.8] and [2.9]. This process involves a considerable increase in the required labor, however.

An alternate scheme is to make as accurate an estimate of C_α as possible before using Equation [2.8]. This can be done if an optimum C_L (say 0.3) is assumed and the section thickness-chord ratio estimated from Equation [2.7] by iteration. In this case a t/c is assumed and the corresponding value of C_α estimated for the angle of attack range of interest. The process is repeated until the desired σ_1 is obtained. The corresponding value of C_α is then used in Equation [2.8]. If the resulting t/c and

C_L for optimum lift-drag ratio are different than the initial assumptions, the process can be repeated. Although several iterations may be necessary, this process should be much more efficient than the blind method of assuming a number of values of C_α .

For the preliminary estimate of C_α , Figure 2.9, which was obtained from data for a number of NACA sections, can be used. The angle of attack is the two-dimensional angle of attack which is given by

$$\alpha = \frac{C_{L_\alpha}}{2\pi} \alpha_{\text{seaway}}$$

where α_{seaway} is the angle of attack induced by the seaway and C_{L_α} is the lift curve slope from Equation 47.a of [2.4]. The angle of attack induced by the seaway can be obtained from Martin and Turpin (2.9) if the response is known or can be estimated. The nose radius can be obtained for a given section from (2.10). For the final estimate, the cavitation bucket of the assumed section should be calculated by methods given in Chapter 1.

REFERENCES

- 2.1 Schertel, H. Von, "Design and Operating Problems of Commercial Hydrofoils," Transactions of the Third Symposium on Naval Hydrodynamics, Office of Naval Research Publication ACR, 65, 1960.
- 2.2 Ask, H. R., "Stability Augmentation for Surface-Piercing Hydrofoil Craft," Proceedings of the Fourth Seminar on Ship Behavior at Sea, held at Stevens Institute of Technology, June 1962.
- 2.3 Sullivan, E. K., and Higgins, James A., "Tests and Trials of the H. S. Dennison," Hovering Craft and Hydrofoil Magazine, London, Volume 3, Numbers 3 and 4, December 1963 and January 1964.
- 2.4 Study of Hydrofoil Seacraft, Grumman Aircraft Engineering Corporation, October 1958.
- 2.5 Auslaender, Jakob, "Design Charts for One and Two-Strut Supercavitating Hydrofoil Wings (Wing Series A)," HYDRONAUTICS, Incorporated Technical Report 001-8, October 1961.
- 2.6 Martin, M., "The Stability Derivatives of a Hydrofoil Boat - Part I," HYDRONAUTICS, Incorporated Technical Report 001-10(I), January 1963.
- 2.7 Chen, C. F., "Optimum Wing-Strut Systems for High Speed Operation Near a Free Surface," HYDRONAUTICS, Incorporated Technical Report 001-1, June 1960.
- 2.8 Lange, G., "Forces and Pressure Distribution Measurements on Eight Fuselages," NACA Technical Memorandum No. 1194, October 1948.
- 2.9 Martin, Milton, and Turpin, Francis J., "The Effect of Surface Waves on Some Design Parameters of a Hydrofoil Boat," HYDRONAUTICS, Incorporated Technical Report 001-3, January 1961.
- 2.10 Abbott, I. H., von Doenhoff, A. E., and Stevens, L.S., "Summary of Airfoil Data," NACA Report No. 824, 1945.

TABLE 2.1

Tabulation of the Factor C_s Accounting for the Effect of Thickness Distribution on Section Modulus for Typical Hydrofoil Sections

Section	C_s
NACA 16 Series	.0890
NACA 65-A Series	.0775
NACA 66 Series	.0848
TMB-EPH Section	.0899

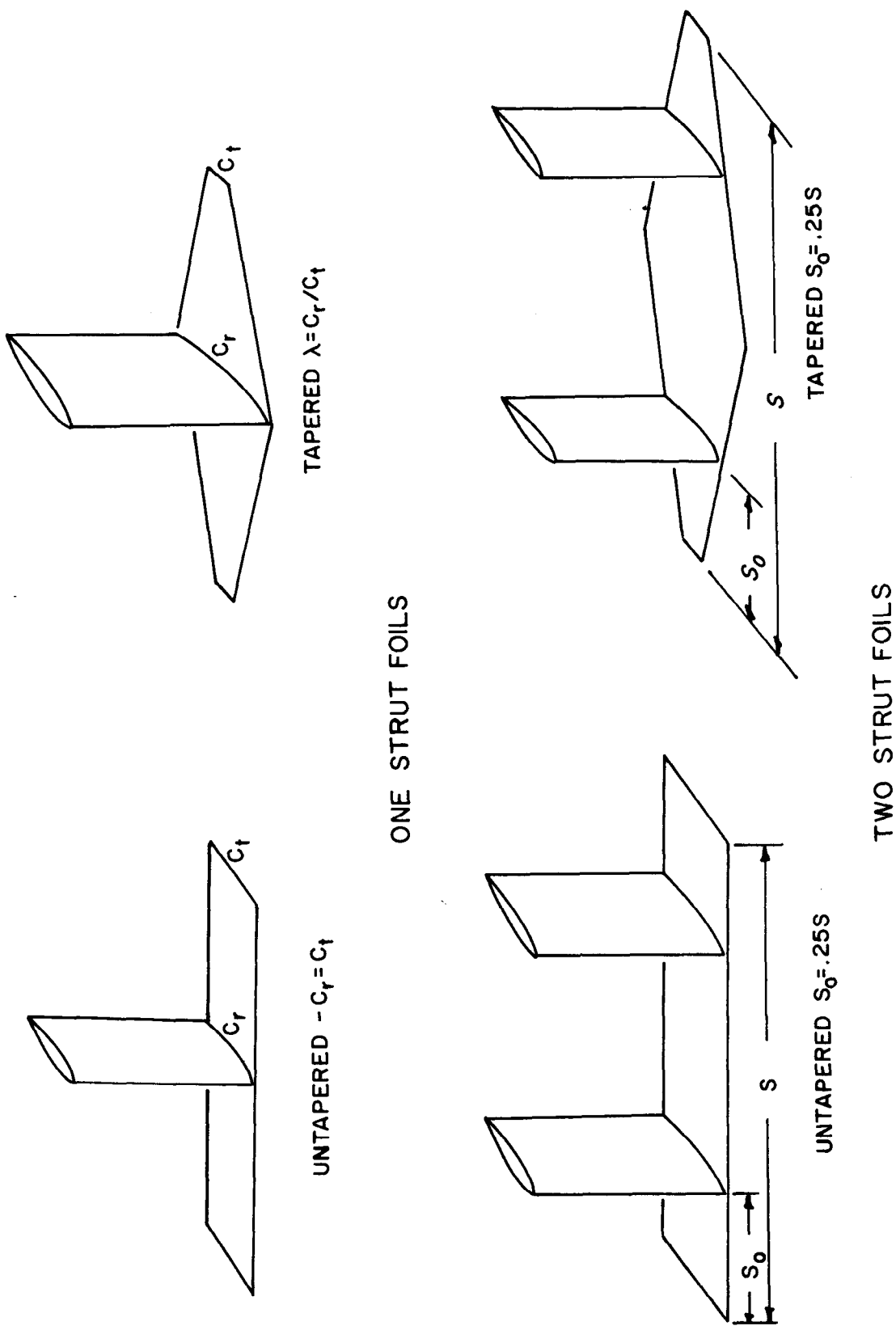


FIGURE 2.1 - VARIOUS HYDROFOIL CONFIGURATIONS CONSIDERED IN CHAPTER 2

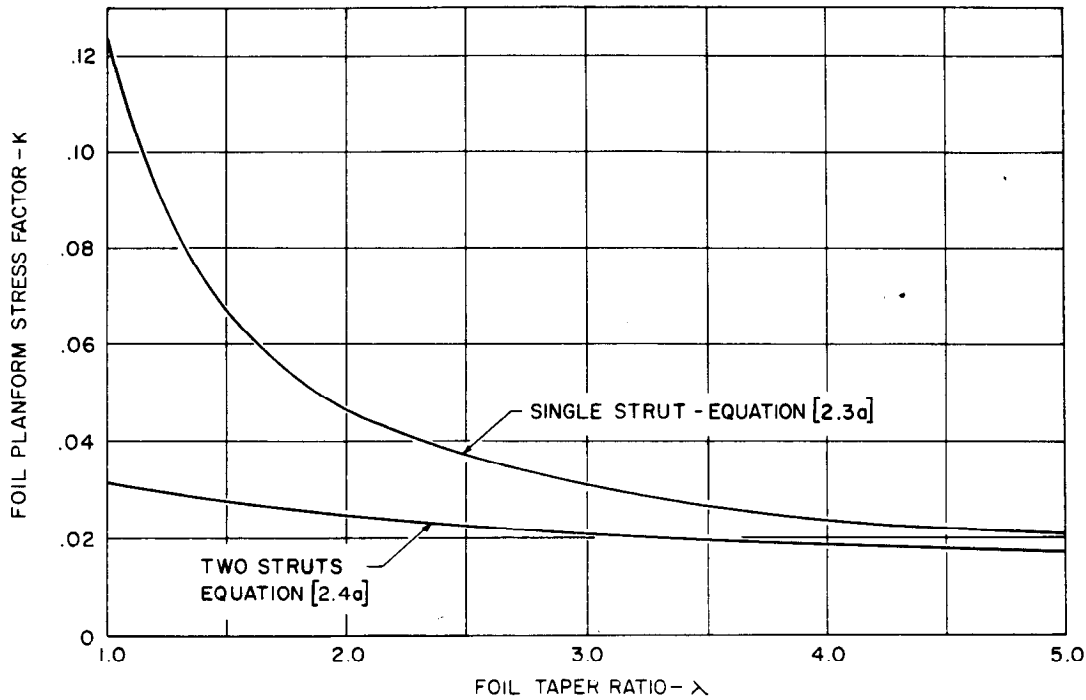


FIGURE 2.2a -FOIL PLANFORM STRESS FACTOR K FOR ONE AND TWO STRUT WINGS WITH CONSTANT SECTION MODULUS

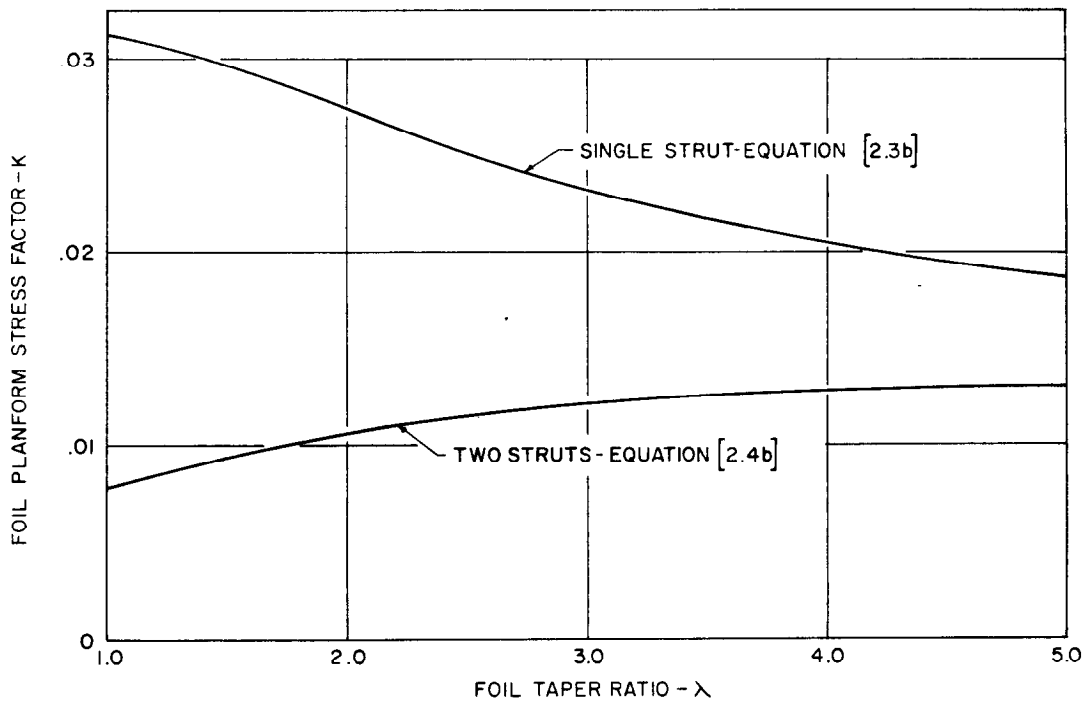


FIGURE 2.2b -FOIL PLANFORM STRESS FACTOR K FOR ONE STRUT AND TWO STRUT FOILS FOR DETERMINING THE SECTION MODULUS AT THE CENTROID OF CONSTANT STRESS FOILS

46

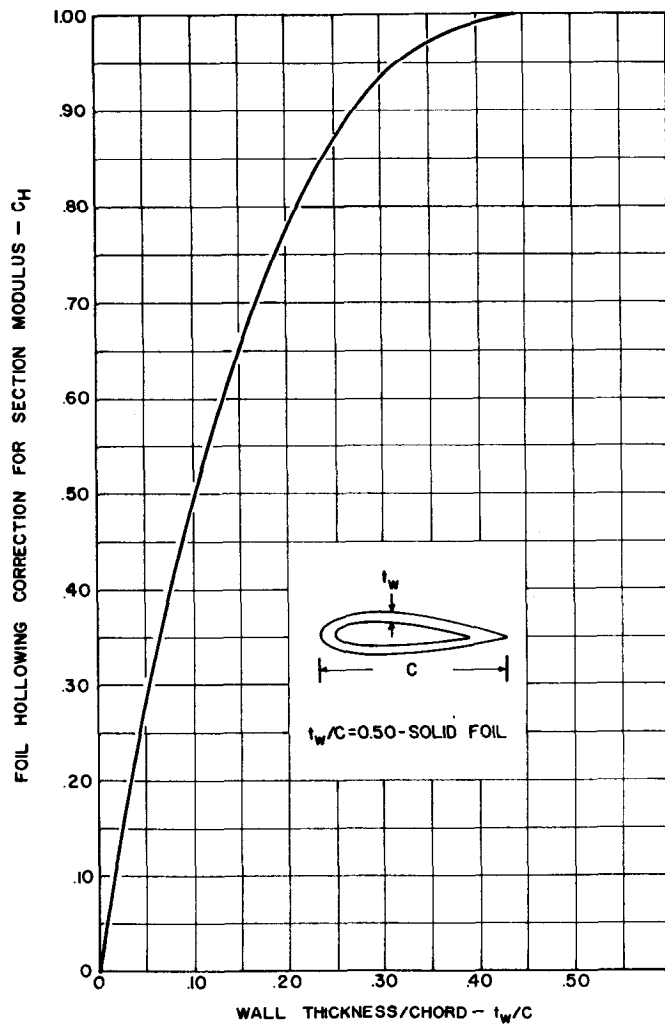


FIGURE 2.3—EFFECT OF WALL OR SKIN THICKNESS t_w/C - K ON FOIL HOLLOWING CORRECTION FACTOR - C_H

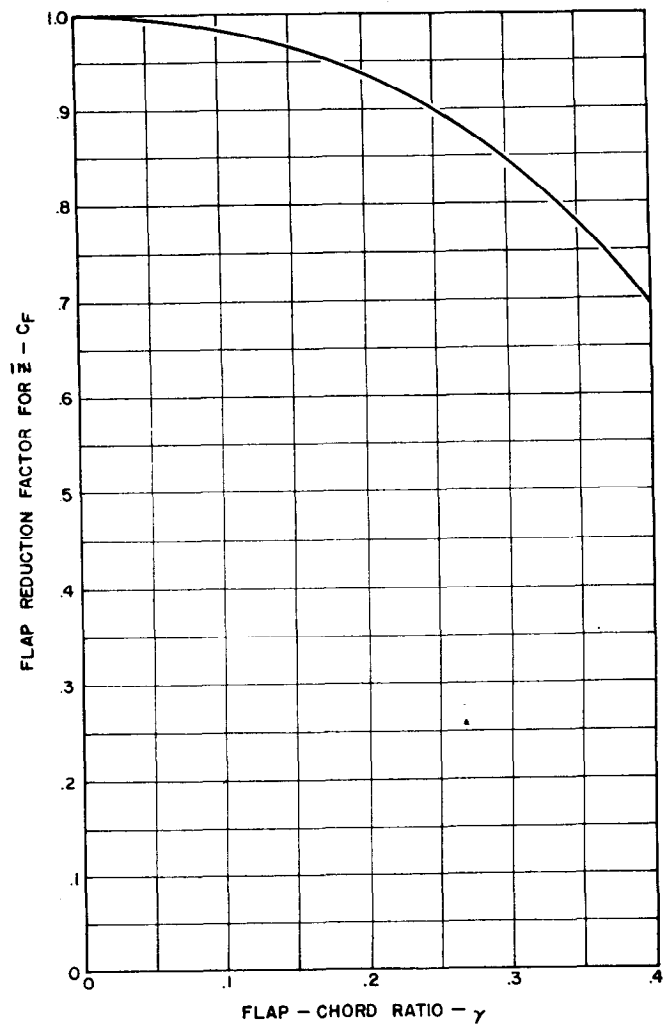


FIGURE 2.4—FLAP REDUCTION FACTOR FOR SECTION MODULUS - C_F , AS A FUNCTION OF FLAP-CHORD RATIO - γ

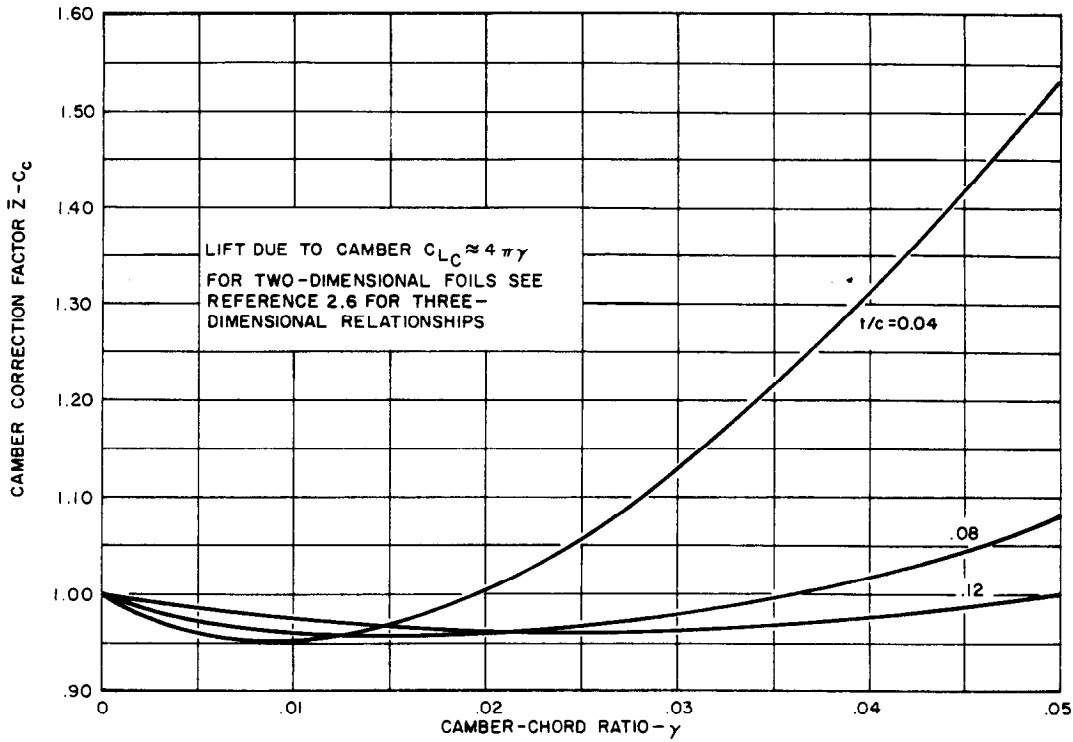


FIGURE 2.5a -CAMBER CORRECTION FACTOR FOR SECTION MODULUS FOR NACA 16 SERIES SECTIONS OF VARIOUS THICKNESS-CHORD RATIOS

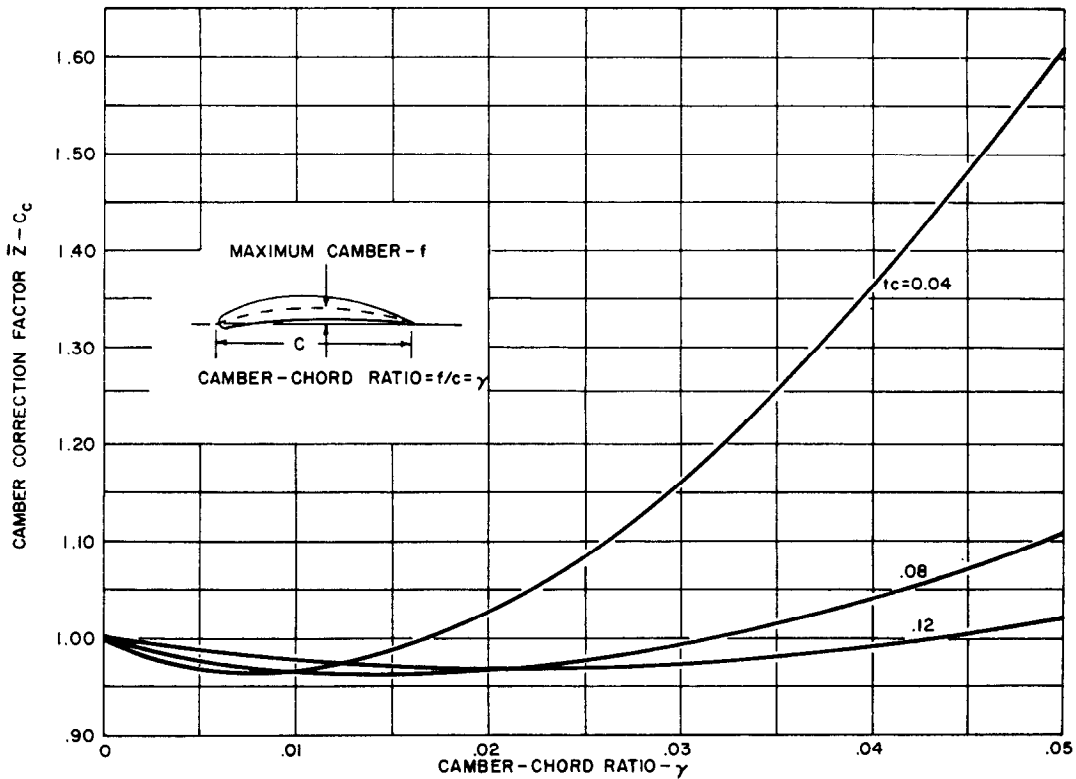


FIGURE 2.5b -CAMBER CORRECTION FACTOR FOR SECTION MODULUS FOR NACA 66 SERIES SECTIONS OF VARIOUS THICKNESS-CHORD RATIOS

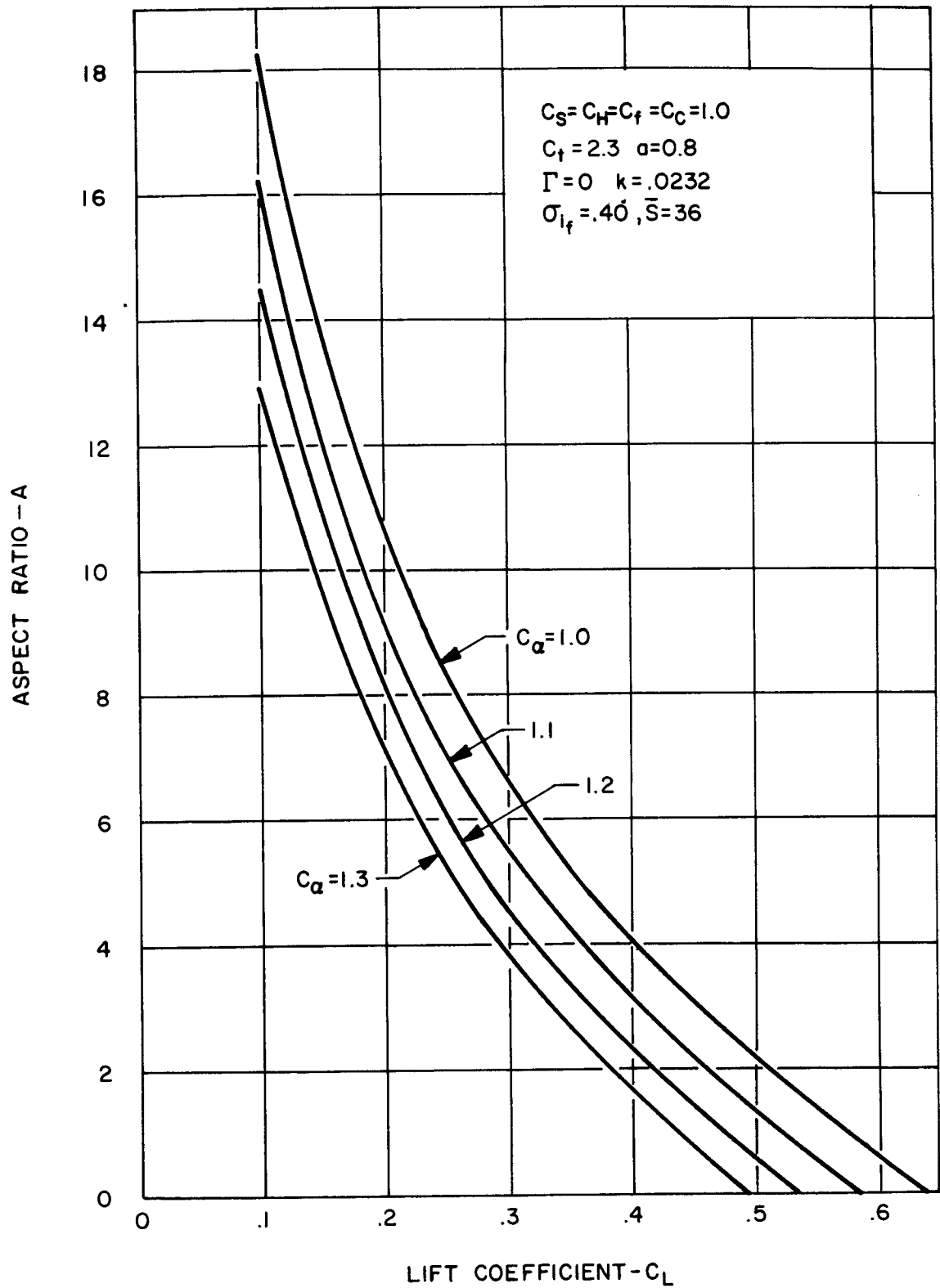


FIGURE 2.6 - TYPICAL CURVE SHOWING THE INFLUENCE OF LIFT COEFFICIENT AND CAVITATION PARAMETER C_α ON ALLOWABLE ASPECT RATIO

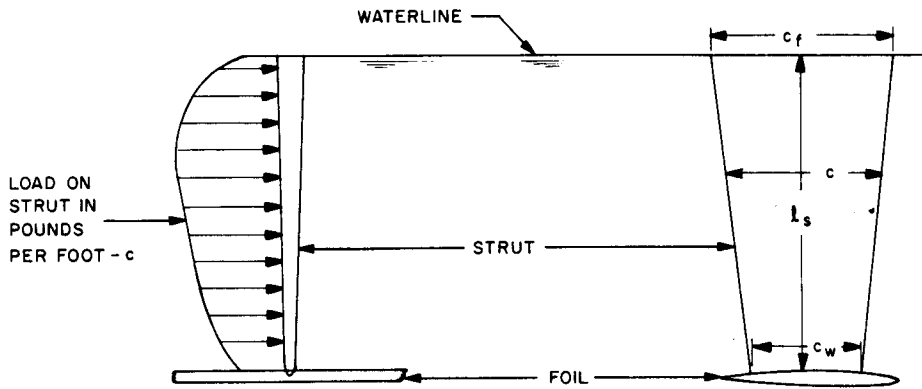


FIGURE 2.7-LOADING OF A STRUT DURING A TURN

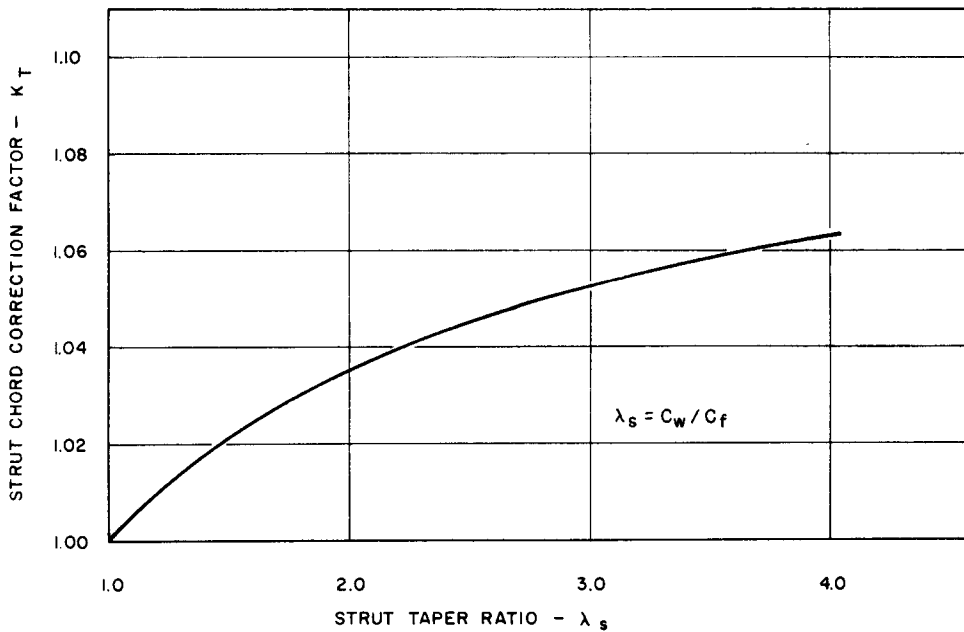


FIGURE 2.8 FACTOR FOR INCREASING STRUT CHORD CALCULATED USING EQUATION 2.12 WHEN THE STRUT IS TAPERED

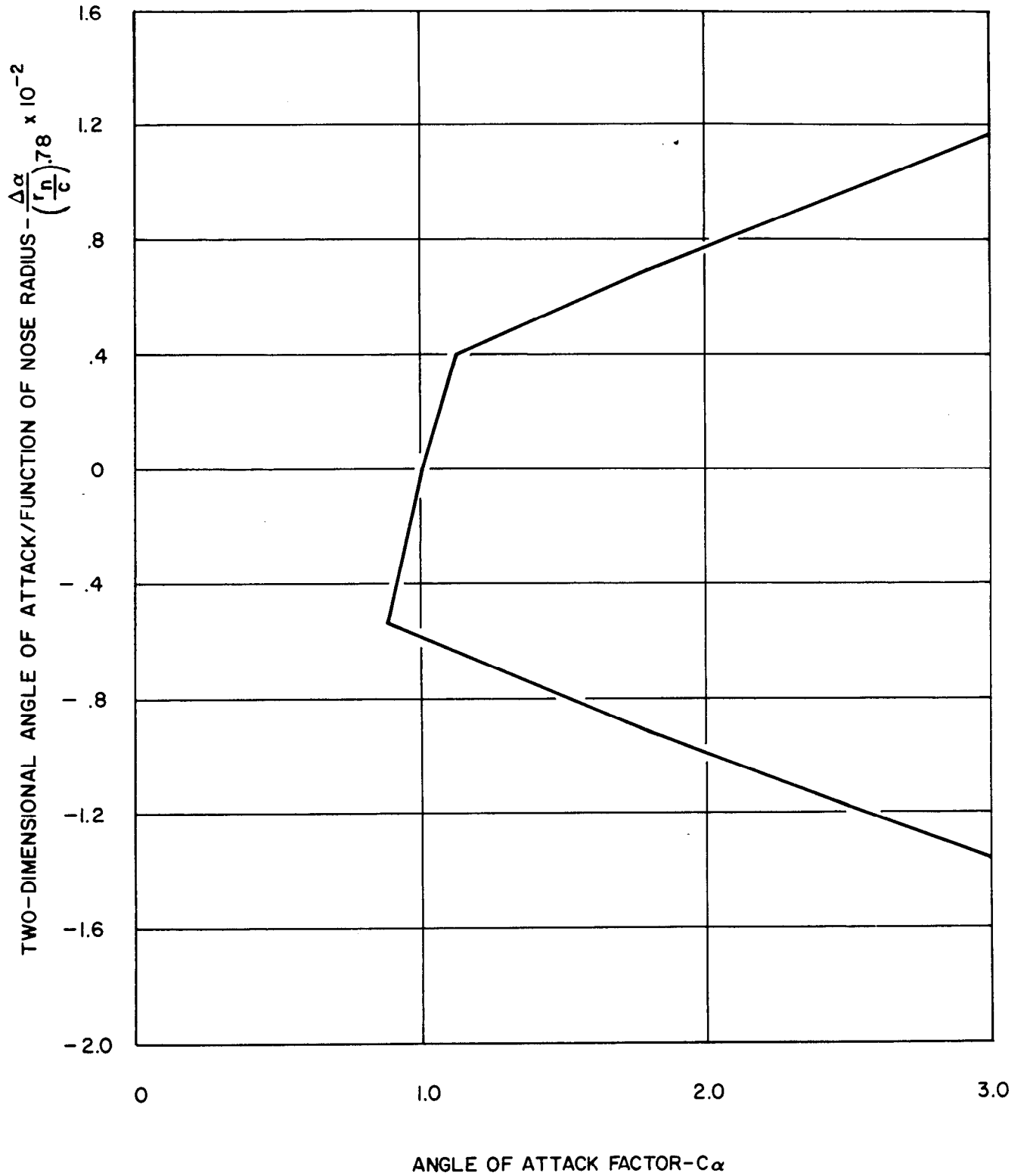


FIGURE 2.9—FACTOR C_α ACCOUNTING FOR THE EFFECT OF ANGLE OF ATTACK ON INCIPIENT CAVITATION NUMBER BASED ON DATA FOR NACA SECTIONS

HYDRONAUTICS, Incorporated

3.0

CHAPTER 3

VENTILATION INCEPTION OF SURFACE PIERCING
AND SUBMERGED FOILS AND STRUTS

By

Roderick A. Barr

NOTATION

AR	Effective aspect ratio of foil or strut
AR_g	Geometric aspect ratio of foil or strut
b	Width of reentrant jet
c	Foil or strut chord
C_p	Pressure coefficient
C_{pr}	Pressure coefficient at point of flow reattachment
C_{ps}	Pressure coefficient at point of flow separation
f_F	Ratio of inception angle of attack at finite Froude number to that at large Froude number
f_P	Correction to aspect ratio for end plate effect
F_c	Froude number based on chord V/\sqrt{gc}
F_d	Froude number based on depth $h - V/\sqrt{gh}$
g	Acceleration of gravity
h	Depth of submergence of bottom of strut or foil
h_w	Wave amplitude (flank to trough or crest)
h/c	Depth-chord ratio of bottom of strut or foil
l	Cavity length measured from foil trailing edge
l_F	Longitudinal distance from center of gravity (assumed pitch center) to point of interest
P_c	Pressure within cavity
P_o	Pressure at infinity at the same depth
P_r	Pressure at point of reattachment
P_s	Pressure at point of flow separation

3.2

Q	Quantity of air entrained in cubic feet per second
r	Craft response amplitude
r_F	Vertical distance from center of gravity to water surface
r_n	Nose radius of section
$r_{n/c}$	Ratio of nose radius to chord of section
Re	Reynolds number
t/c	Thickness-chord ratio of foil or strut
V	Forward velocity
V_j	Reentrant jet velocity - $V \sqrt{1 + \sigma}$
α	Angle of attack
α_E	Effective angle of attack
α_F	Angle of attack required for ventilation when Froude number effects are important
α_g	Geometric angle of attack
$\alpha_{h/c}$	Angles of attack required for inception at arbitrary depth-chord ratio
$\alpha_{h/c=1}$	Angle of attack required for inception at a depth-chord ratio of one
β	Side-slip angle of boat
Γ	Dihedral angle of foil
δ	Incidence angle of foil
ζ	Maximum heave amplitude
ν	Kinematic viscosity
ρ	Mass density of fluid
σ	Cavitation number $(P_o - P_c) / \frac{1}{2} \rho V^2$

τ	Trim angle of boat
ϕ	Maximum roll amplitude
ω	Frequency of wave encounter
θ	Maximum pitch amplitude
Σ	Pressure recovery factor

INTRODUCTION

In the past, much concern has been given to cavitation and the prediction of cavitation inception on hydrofoils and struts. Previous hydrofoil handbooks (3.1), (3.2) have devoted much space to cavitation while offering little of use concerning ventilation and ventilation inception. Although ventilation has been known to occur on struts and foils, little attention has been paid to its causes or to means of predicting ventilation inception.

Hydrofoil systems may be subject to ventilation of two types: Ventilation of struts and foils through a separated region on the panel; direct ventilation of fully submerged foils through the trailing tip vortices. The discussion here is concerned with ventilation of fully wetted foils and struts. Ventilation inception on foils, struts and propellers designed for ventilated operation has been covered in detail by Barr (3.3).

Because of the generally undesirable results of ventilation of foils and struts, it is desirable to know the conditions at which ventilation inception first occurs. The design of a foil system may have to be modified, or specially designed preventative devices such as ventilation fences provided, if ventilation appears to be a probability.

THE CAUSES OF VENTILATION

There are a number of possible causes leading to the conditions required for ventilation inception. These causes can be divided into three groups: Those leading to ventilation of struts;

those leading to ventilation of surface piercing foils; those leading to ventilation of fully submerged foils.

The primary cause of strut ventilation is turning. When a hydrofoil boat executes a turning maneuver the craft, and thus the strut, assumes an angle of heading to the direction of motion (side slip angle). The resulting angle of attack on the strut may be sufficient to cause separation and ventilation. Rolling motions of the craft will also result in an angle of attack on the strut, but this angle is probably never adequate to cause ventilation inception.

Ventilation inception on surface piercing foils can also result from turning, although this is less likely than in struts because of the effect of dihedral angle. The most likely cause of ventilation of surface piercing foils is the high angles of trim which may occur at or near takeoff. These large angles occur particularly when there are surface piercing foils forward only. A third possible cause of ventilation is the angles of attack induced by severe heave and pitch motions. These motions appear more likely than roll motions to induce ventilation. Ventilation of fully submerged foils can arise from either takeoff trim or from severe heave and pitch. For ventilation to occur on fully submerged foils an air supply must be present, necessitating the previous ventilation of a surface piercing foil or a strut. Ventilation inception can also occur if the tip of a fully submerged dihedral panel is very close to the free surface, as may occur during takeoff.

3.6

THE EFFECTS OF VENTILATION

The most important result of foil ventilation is the abrupt loss of lift caused by ventilation. This lift loss, which is illustrated for several typical foils in Figure 3.1, can result in hull crashing or nosing in of the boat caused by either loss of altitude or pitch or roll instability of the boat when one or more foils ventilate. These events can result in loss of foil-borne flight and in severe hull loadings and damage due to impact.

Ventilation can also result in vibrations and buffeting caused by periodic formation and collapse of the ventilated region. Although the collapse of the ventilated regions does not result in the damage caused by vapor cavity collapse, the vibrations and buffeting can be highly uncomfortable and structurally dangerous.

Ventilation of a strut may not be as serious as that of a foil but it may act as a prelude to foil ventilation. For this reason alone it should be avoided. It is certainly desirable to avoid ventilation of any type because of the possible damage and discomfort involved.

MECHANISMS OF VENTILATION INCEPTION

Ventilation inception can be defined as the condition where the flow over the hydrofoil changes from fully wetted or partially cavitating to one in which a stable, air-filled region or cavity is formed over the foil. The air inside the ventilated region or cavity must be continuously supplied from a source external to the flow, usually directly from the atmosphere, as it is being continuously removed by entrainment at the rear of the cavity.

3.7

There are two types of ventilation in which interest is concentrated. The first is the ventilation of a foil which is piercing the water surface, including both struts and surface piercing foils. The second type is that which occurs on a fully submerged foil panel.

There are four major physical conditions which must, as far as is known, exist for ventilation inception to occur: (1) a finite area of separated flow, due either to a separation of the boundary layer or the formation of a vapor-filled region (in which regions the flow is essentially stagnant) must exist continuously over the span of the foil; (2) the separated region or region of cavitating flow must be of sufficient size to allow passage of the air into this region; (3) the conditions must be such that after ventilation inception occurs a stable ventilated region is maintained at the operating conditions of the section for some finite period of time; and (4) the ventilating air pressure must be greater than the pressure within this region. Generally the satisfaction of condition (3) implies that condition (4) is well satisfied too.

The adequately sized separated region of low kinetic energy (stagnant) and relatively low pressure flow allows the ventilation air, which itself possesses low energy, freely to flow across the body and be driven downstream by its relatively high pressure to form a ventilated cavity. Air which might be introduced at a non-separated region, will not result in ventilation of the flow, for the air so introduced is rapidly swept aft by the flow in the form

3.8

of a streamer or string of bubbles, without seriously influencing the flow itself. The only case where ventilation inception may occur, other than through a separated air region on the foil, is on low aspect ratio foils at very shallow depth, where ventilation occurs through the tip vortices well aft of the foil.

Either boundary layer separation or cavitation can provide the conditions necessary to meet requirements (1) and (2), and either of these can be responsible in practice. Boundary layer separation is determined mainly by the section geometry (including incidence) and to a lesser extent by the flow Reynolds number. Cavitation is determined mainly by the section geometry and cavitation number. In general, ventilation inception by boundary layer separation is more probable as it can occur at considerably lower speeds than can reasonably sized areas of cavitation. Both types, as they effect ventilation inception, will be considered.

SEPARATION ON TYPICAL HYDROFOIL SECTIONS

Data on boundary layer separation on hydrofoils is almost nonexistent, and that which does exist, such as Chang and Dunham (3.4), is not applicable to the problem being considered here. Wadlin (3.5) has made experimental studies of boundary layer separation on surface piercing foils but no quantitative relations for the conditions for separation have been recorded. Airfoil data must be resorted to for a comprehensive view of the problem. Results for airfoil sections will be assumed applicable to the case of hydrofoil sections, a procedure which would seem valid. Unfortunately, while hydrofoils are generally of moderate aspect

ratio, the pertinent results for separation on airfoils are restricted to two-dimensional sections. Three dimensional effects are known, under certain circumstances, to have marked influence on boundary layer behavior. However, such three dimensional effects as may occur on hydrofoils are too complicated to be theoretically calculated at the present time. Fortunately, the three-dimensional effects may be expected to be strongest at the tip and near the trailing edge, and will probably be small very near the leading edge. As the leading edge will be the region of interest for ventilation inception, the effect of finite aspect ratio, other than on lift effectiveness, on separation characteristics of hydrofoils will be assumed very small and two-dimensional results (for separation near the leading edge) will be used.

Carrow (3.6) discusses five types of two-dimensional separation which have been observed by various investigators. McCullough and Gault (3.7) discuss the three types that have been observed in tests at the NACA. In general the types of separation discussed by the various investigators are similar, Carrow adding two less commonly observed types. These two references give the most comprehensive discussion of the subject available.

The first important type is long bubble separation (also called thin-airfoil separation). This occurs on thin sections and is shown in Figure 3.2a. At some small angle of attack (b) a separated region (bubble) first appears in the laminar boundary layer near the nose; as the angle of attack increases this "short bubble" which generally covers only a fraction of a percent of the chord (3.7) does not grow noticeably in length but moves toward the foil

leading edge (3.7) and (3.8). At some critical angle the bubble "bursts" and beyond this point the bubble begins to grow relatively rapidly with increasing incidence (c). At some incidence (d) the bubble has grown until it covers the entire upper surface of the foil. It is the bubble formed after "burst" that is referred to as the "long bubble." Due to the very small size of the bubble prior to "burst" (the bubble ranges in length from .2 percent of the chord (3.7) to about one percent of the chord (3.8)), its existence may or may not be adequate for ventilation inception.

A second type of separation known as leading edge stall is shown in Figure 3.2b. This type of separation occurs on foils of moderate thickness. At some small angle of attack (b) a short separation bubble forms. As the angle of attack is increased this bubble moves toward the leading edge (c) until suddenly, at some angle (d), the flow becomes separated over the entire chord from the nose aft. In this case the separation bubble does not grow continuously with increasing incidence as in the case of thinner foils, but rather suddenly assumes a length greater than the chord.

Whether long bubble or leading edge stall separation exists on a given foil actually depends on both the leading edge radius and the Reynolds number, and this dependency has not been thoroughly explored through experimentation. For this reason it is difficult to define precisely what is meant by thin or moderately thick sections. The following table will serve as a guide, however.

Foil	Reference	Nose Radius	Range of Long Bubble Separation	Range of Leading Edge Stall
63006	3.9	.00297	$Re < 10^7$	$Re > 10^7$
0006	3.9	.00400	$Re < 8 \times 10^6$	$Re > 8 \times 10^6$
0007	3.10	.00545	$Re \leq 6 \times 10^6$	$Re > 6 \times 10^6$

In general the differences in these types of separation is not important in the ventilation inception of sub-cavitating sections as the bubble size is not of great importance.

These data apply to hydraulically smooth foils, but the effects of roughness has been studied (3.9). It can be concluded that roughness generally has the effect of increasing effective Reynolds number and thus decreasing the Reynolds number required for the occurrence of leading edge stall.

A third important type of separation occurs on very thick sections ($t/c > .15$) and is shown in Figure 3.2c. This type of separation, known as trailing edge stall, starts as a separation of the turbulent boundary layer at the trailing edge, (b), the region of separation moving toward the leading edge, (c), as the section incidence is increased. On these very thick foils, a small separation bubble also forms near the leading edge at relatively small angles of attack, but trailing edge stall becomes serious before this bubble is able to expand and cause leading edge stall.

Two other types of separation are described by Carrow (3.6) but not by McCullough and Gault (3.7). The first of these, which occurs on thick sections, is separation of the laminar boundary

layer, starting at the trailing edge and progressing toward the leading edge. This type can only occur at very low Reynolds numbers. The second is separation of the turbulent boundary layer at the leading edge on very rough, very thick sections. Neither of these types will generally be of importance in connection with high speed underwater systems.

In the case of sections with blunt bases or sections with abrupt decreases in thickness at some point, the flow will readily separate at these discontinuities. In fact, separation at such points cannot be avoided at any practical Reynolds number. Such separation is not a function of the Reynolds number, the section thickness or the section incidence, and may be called discontinuity separation. This fourth important type of separation is illustrated in Figure 3.2d.

APPLICABLE TYPES OF SEPARATION

The type of separation leading to ventilation inception will be a function of the characteristics of the section being considered as well as the application (fully submerged foil, surface piercing foils or strut). As has been noted, the type of separation which actually occurs is a function of the geometry of the section. In particular, the mode of separation depends very much on the leading edge radius.

For sections with sharp leading edges (wedgelike), the separation has been found experimentally to be of the long bubble type (3.11). For sections with rounded noses the important geometric parameter determining leading edge behavior is probably the nose-radius rather than the section thickness. This is indicated by

Figure 3.3 which shows that the magnitude of the velocity peaks on the upper surface of a variety of airfoils of different thicknesses and shapes is proportional to incidence and is otherwise predominantly a function of nose radius alone.

For hydrofoil sections with nose-radii in the range of values $r_n/c < .0025$ leading to long bubble separation for Reynolds number up to about 10^7 , this mechanism should be assumed responsible for separation. For sections with thicker leading edges or for higher Reynolds numbers (see the previous table) leading edge stall occurs. Ventilation inception should be identical for these types of separation except for those cases where a large separated region is required. For long bubble separation, the bubble size is a function of incidence while for leading edge stall the bubble length should always be adequate for inception.

CONDITIONS REQUIRED FOR VENTILATION INCEPTION

Separation

Separation at the base of blunt based bodies and sections is not, for normal Reynolds numbers, a function of the velocity of flow or of any section incidence which may exist. As the flow passes the sharp corner formed by the blunt base it must by necessity separate, as the fluid cannot attain the infinite velocities required to turn the corner. Although the extent of this separated region may be a function of the Reynolds number it may always be assumed large enough to ensure ventilation inception, providing that the base pressure is low enough to pull air from some external source (see later section).

3.14

For lifting hydrofoils and streamlined struts, the occurrence of laminar bubble separation can be determined using a boundary layer calculation method such as the Karman and Pohlhausen method (3.12) or a simplification of this (3.13). Other and simpler methods such as that of Stratford (3.14) can also be used to predict the onset of separation. These methods provide, based on an iterative solution, the angle of attack and the point (on the foil surface) at which separation occurs. These methods do not, however, yield any information on the size of the separated region or on the angle of attack at which the small initial bubble bursts and becomes a "long" bubble.

Crabtree (3.15) has found that the pressure recovery factor Σ , pertaining to a short bubble can be used as a criteria for determining the angle at which the long bubble is formed. The pressure recovery factor which was first investigated by Norbury and Crabtree (3.16) is defined as:

$$\Sigma = (P_r - P_s) / \frac{1}{2} \rho V^2 = (C_{pr} - C_{ps}) / (1 - C_{ps}) \quad [3.1]$$

where C_{pr} and C_{ps} are respectively the pressure coefficients at the points of reattachment and separation of the short bubble. Crabtree has found from experiments that when the value of Σ reaches 0.35, the short bubble bursts.

It should be noted that this information cannot be used to predict short bubble bursting unless experimental pressure distributions for incidences right up to bursting are available.

This criterion is thus of limited value for prediction. In fact, experimental results must mainly be relied upon.

Experimental data pertaining to long bubble and leading edge stall is available from NACA and RAE tests. These data give bubble appearance and geometry (length and thickness) as a function of angle of attack for a number of sections. Of particular interest are the data for a thin double wedge of 4.23 percent thickness (3.11), and NACA 64A006 section (3.7), NACA 007.5 and 008 sections (3.10), and an RAE 101 section (3.15), all of which have thin noses. The angles of attack required for a separation bubble to form initially are available for all of these sections while extensive separation bubble geometry is available for the first two. Some results for bubble geometry of the other two foils is also available.

Figure 3.4 presents curves based on all the available applicable data mentioned above. The lowest of the four curves represents the boundary for formation of short laminar bubbles at the leading edge. The upper boundary curve corresponds to conditions where the short bubble bursts. In the shaded region the short bubble exists at the leading edge but does not grow in length with incidence. For angles greater than that for bubble bursting, a long bubble or leading edge stall bubble (full chord) has formed. The upper two curves represent, respectively, separation bubble lengths of ten and twenty percent where long bubbles exist. All of these data come directly from References (3.7), (3.9), and (3.10) with the exception of the data for the RAE 101 section on the ten percent chord length curve. This has been estimated from

3.16

the pressure distribution data presented in (3.15). Experimental results indicate that for thicker sections the angle of attack required for bubble bursting (about nine degrees in this case) is essentially the same as that required to produce a bubble whose length is twenty percent of the chord.

Figure 3.5, which is of particular interest for natural ventilation, presents the data of Figure 3.4 plus data for two thicker sections, 63012 and 66018. The upper and lower boundary curves have the same significance as in Figure 3.4. In the case of natural ventilation, particularly at the free surface, where air is available over the entire chord, the lower bound, representing the first appearance of a laminar bubble, probably represents the limit of ventilation inception. Figure 3.4 is of more interest where the location of the air supply is fixed, as in the case where ventilation is desired. For some fully submerged sections which are supplied indirectly, the air may not be present over the entire chord of the foil. In this case, it is likely that the upper curves of Figures 3.4 and 3.5 are of interest. The geometry of the foil system will dictate whether air will be supplied over the entire chord of the foil.

Extent of Separation and Experimental Results

At the smaller angles of attack, given by the long bubble boundary in Figure 3.4, separation has just begun and the bubbles are extremely small. In cases where the separation bubble required for ventilation inception must have a finite length and thickness, the angle of attack required to give a bubble of sufficient size can be estimated from data, Figures 3.6 and 3.7, which

show experimentally determined bubble shapes for a wedgelike leading edge (included angle = 4.9 degrees) and for a foil with a nose radius of .256 percent.

Only a small amount of experimental information on ventilation inception of fully submerged hydrofoils is available to serve in verifying the foregoing assumptions and results, and these are from tests at the University of Minnesota, (3.17), and HYDRONAUTICS (unreported). Other investigations of ventilated fully submerged hydrofoils have been made, such as (3.18), but these are for foils with forced ventilation from a series of holes distributed over the entire span which is of no interest here.

Approximate angles of attack required for ventilation inception on a six degree wedge and an 11.3 degree wedge hydrofoil are given by Shiebe and Wetzel (3.17). Experiments with small foils (a sharp leading edge flat plate and a wedge of 6 degrees) have been conducted at HYDRONAUTICS in order to determine the angles of attack required for ventilation inception. For the foils tested at Minnesota the measured angles of attack were: for the six degree wedge - eight degrees; for the 11.3 degree wedge - ten degrees. The tests conducted at HYDRONAUTICS, Incorporated showed: for the flat plate - four degrees and for the wedge - six degrees. In both cases these are the geometric angles of attack. The effective angles of attack α_e are less than the geometric angles because of finite span effects, and it is these effective angles which determine separation phenomena; they can be determined using the results of Wadlin (3.19) given in Equations [3.5] and [3.6]. When the geometric angles of attack are corrected for aspect ratio and

finite depth effects, the resulting effective angles of attack are found to be: for the Minnesota foils, 3.6 and 4.5 degrees, respectively. These results are shown in Figure 3.10 which presents the effective angles of attack required for separation, plotted as a function of the wedge angle.

It will be noted that two lines have been drawn through the data points in Figure 3.8. These curves represent different values of the location of the ventilating air ports. The inception air port on the foils tested at Minnesota was located at approximately nine percent of the chord aft of the leading edge, while in those tested at HYDRONAUTICS the port was located within two percent of the chord from the nose. For natural ventilation the air will not be supplied through a port but rather over some portion of the chord. In most cases the air will be present over the entire chord so that the lower curve of the figure would be applicable as it represents essentially the minimum angle for ventilation.

It can be seen that the results of Figure 3.8 are very much in agreement with the data presented in Figure 3.4, which indicates that effective angles of attack of approximately two and three degrees would be required for inception with bubble lengths of 2 and 10 percent of chord respectively; it should be recalled that Figure 3.4 corresponds to a wedge angle of 4.9 degrees.

Figure 3.8 also includes the inception angle for a surface piercing wedge foil of six degrees included angle as tested by Fridsma (3.20). In the case of the surface piercing foil the angle required for ventilation is a function of the Froude number F_c based on chord c :

$$F_c = \frac{V}{\sqrt{gc}} \quad [3.2]$$

For large Froude numbers ($F_c > 20$) the angle of attack becomes independent of the Froude number and it is this point that is shown in Figure 3.8. For the case where the Froude number is less than 20 the angle of attack α_F required is given by:

$$\alpha_F = \alpha f_F \quad [3.3]$$

where f_F is the ratio of the angle of attack required at small Froude number to that required at large Froude number ($F_c > 20$). The factor f_F is given in Figure 3.9, which is based on the data of (3.20). In the case of wedge foils the angle of attack α given by Figure 3.8 is measured from the face of the foil.

A comparison of the data of Fridsma (3.20) and the values of Figure 3.8 indicate that the depth-chord ratio of the foil of (3.20) appears to have little effect on the inception angle. This can be explained because the separated region behind a wedge, unlike that formed by an airfoil section, tends to be independent of the ventilating air pressure. Thus, even though the air pressure is decreased by increased airflow, the ventilated cavity is not subject to the choking off present with airfoil shaped foils. The upper curve of Figure 3.9 indicates that a stable ventilated cavity is maintained at an angle where theory would predict a

stable cavity for the wedge angle involved. For wedge shaped foils, then, it would appear that depth-chord ratio effects can be ignored for moderate depth-chord ratios (less than say 3.0).

The dependence of the inception angle on the wedge angle is borne out by theoretical considerations. As the wedge angle is increased, the magnitude of the adverse pressure gradient for a given angle of attack decreases, so that a larger angle of attack is required to reach the same pressure gradients and thus to achieve ventilation inception. Probably the most important conclusion that can be drawn from these data is that ventilation inception on wedges does, in fact, occur at angles of attack very close to those which might be deduced from boundary layer separation considerations and results.

A number of investigators have published data for ventilation inception on surface piercing struts. Breslin and Skalak (3.21) have tested struts of NACA 4412 section at various depth-chord ratios from 0.5 to 2.0. Wetzel has conducted tests for struts of NACA 0012 and 0024 sections for depth-chord ratios from 0.5 to 5.0. Kiceniuk (3.22) has tested a round nosed ogival strut, whose section shape approximates that of an airfoil, at one depth-chord ratio.

The tests of Breslin and Skalak indicate that ventilation inception can occur due to one or more causes. Figure 3.10 illustrates that, depending on the depth-chord ratio and the Froude number, the ventilation can result from either boundary layer separation or ventilation of the tip vortex. Figure 3.10 also illustrates that tip vortex ventilation is restricted to depth-chord ratios of 1.5 or less. Tests of a depth-chord ratio one

strut with a large end plate showed no tip vortex ventilation. It is thus likely that struts, which will terminate in a submerged foil, will not be subject to tip vortex ventilation. Thus, only boundary layer separation need be considered as a cause of ventilation inception.

Data from all of these tests indicates that there is a critical Froude number F_d based on depth, below which ventilation can never occur. Figure 3.11 shows that for depth-chord ratios of one or greater this critical Froude number is approximately 1.6. It is probable that surface piercing foils and struts will have Froude numbers greater than this limit so that ventilation will always be possible.

For surface piercing elements it is probable that ventilation inception can occur as soon as a small laminar bubble forms. Figure 3.5 indicates that for small nose radii the angle for formation of the laminar bubble is highly dependent on nose radii while for moderate nose radii ($r_n/c > 0.01$) the angle of attack becomes essentially independent of nose radii. This is borne out by the data of Figure 3.12 which indicates that the angle of attack required for ventilation is essentially independent of the section geometry and nose radii.

Figure 3.12 illustrates that the important parameter in determining the angle of attack required for inception appears to be the depth-chord ratio. This result can be explained in terms of the free surface closure discussed by Wadlin (3.22). Figure 3.13 illustrates the process which leads to choking of the

ventilated flow for large depth-chord ratios. As the angle of attack required for inception is reached, a ventilated region begins to form (a). As air progresses down the strut the volume of the ventilated region grows (b) causing an increase in the air-flow into the ventilated region. The reduction in pressure in the air resulting from increased air velocity causes the spray to close over the air passage through the free surface (c). This further reduces the air pressure, the process continuing until the air passage is completely closed over by the free surface. The ventilated region then disappears as the air is entrained away by the flow (d). When conditions required for inception are again met a new ventilated region will be formed and then choked off. A stable ventilated flow will only be achieved and maintained when the angle of attack is increased until the area of the ventilated region formed is adequate for passage of the air.

Figure 3.12 shows that at a depth-chord ratio of one, where the surface closure condition is probably not important, the data show effective angles of attack for inception of: from 5.5 to 6.5 degrees. This compares quite favorably with the angles of 6.2 to 6.4 degrees predicted by Figure 3.5 for the range of nose radii involved ($r_n/c \geq 0.0156$). It thus seems reasonable to assume that the short bubble curve of Figure 3.5 applies for surface piercing foils and struts where depth-chord ratio is small.

The effect of depth-chord ratio on the angle required for inception is basically a problem of the amount of air entrained per unit area of the ventilated region at the free surface. From the air entrainment result given by Barr (3.23) and the result of

Cuthbert (3.24) that

$$\frac{Q}{bV_J} \propto \frac{1}{\left(\frac{V\ell}{v}\right)^{1/5}} \quad [3.4]$$

where Q is the volume of air entrained, b is the reentrant jet width, V_J is the reentrant jet velocity and ℓ is the cavity length, it can be shown that

$$Q \propto \left(\frac{h}{c}\right) \alpha^{8/5} . \quad [3.5]$$

If it is assumed that the cavity closure effect is negligible at a depth-chord ratio of one, the angle of attack at another depth-chord ratio is given by

$$\alpha_{h/c} = (\alpha)_{h/c=1} \times \left(\frac{h}{c}\right)^{5/8} \quad [3.6]$$

where h/c is the depth-chord ratio. The dashed curve in Figure 3.12 was determined from this equation and is shown to be in very good agreement with the data. Although many other factors affect the relationship of [3.4], it is felt that Equation [3.6] represents a good working approximation for the effect of depth-chord ratio on inception angle.

Pressure Requirements

Ventilation inception cannot, of course, occur until the pressure of the ventilating air is greater than the pressure in the separation bubble. This will almost always be the case but it is of interest to summarize the situation regarding pressures in regions of boundary layer separation.

Before the separation bubble is formed, the pressure distribution on a section can be predicted with reasonable accuracy using theoretical results (3.25). Once the separation bubble forms, however, no adequate theoretical method for predicting the pressure distribution exists. Recourse to experimental data must again be made. These data give the pressure distributions on the surface of the sections both before and after separation occurs.

The important pressure is that within the separation bubble, rather than the pressure on the foil surface as reported in various NACA references. Very few measurements of pressure within the bubble are available, and no means of predicting pressures are available as the flow within the bubble is not well enough understood (3.26). However, the data of (3.8) shows that in general the pressure within the bubble is close to the pressure on the foil surface, the maximum variation in pressure coefficient being about 20 percent, and that the pressure within the bubble is lower than on the surface.

As the pressures of interest occur near the leading edge, they are, as previously mentioned, probably a function only of the nose radius or wedge angle. Based on this assumption, the pressure

distributions for the double wedge, 64A006, and 007.5 sections can again be used. Figures 3.14, 3.15 and 3.16 show the pressure distributions on these sections as a function of incidence. These pressures may not depend very strongly on Reynolds number for in Reference (3.7) it is shown that, although the pressure coefficients are functions of the Reynolds number, the dependency is limited to large negative pressures that occur at the leading edge before separation.

Figures 3.14 and 3.15 indicate that for sharp leading edge sections a pressure coefficient of about -1.0 likely occurs, while for sections with a finite nose radius a somewhat greater pressure coefficient exists but probably never exceeds -2.0.

Speeds Required

If the ventilating air pressure is known, the minimum speed at which ventilation inception can occur can be calculated. The speed at which ventilation inception occurs can be calculated from Equation [3.7] when the pressure coefficient C_p is known. The pressure coefficient C_p is given by:

$$C_p = \frac{P_c - P_o}{\frac{1}{2}\rho V^2} \quad [3.7]$$

where P_o is the ambient pressure at the foil and P_c is the cavity pressure which is equal to the air pressure less any losses occurring in transmitting the air to the foil. Some loss would be expected in the case where a fully submerged foil is ventilated by a strut or surface piercing foil.

Ventilation Resulting from Cavitation

Although ventilation inception probably results from boundary layer separation, it is possible for cavitation to lead to inception first. This would only be expected to occur at very high speeds where cavitation results primarily from thickness rather than incidence. In these cases, the angle of attack at which cavitation begins is inadequate for boundary layer separation.

Despite some difficulties in predicting theoretically the point of cavitation inception (see section on cavitation inception) it can usually be estimated with reasonable accuracy. However, the calculation of the point where cavitation becomes sufficient to allow ventilation inception would seem almost impossible, for there is no way of predicting when the bubble cavitation formed initially will become a continuous sheet. As in the case of boundary layer induced ventilation, inception can occur only when a continuous region of low pressure (cavitation) is present over the entire span of the foil or length of strut.

Experiments have indicated that for a typical surface piercing strut, cavitation appears to play no part in ventilation. Coffee and McKann (3.27) tested an unyawed 66.012 strut at speeds up to 70 feet per second. Although heavy cavitation was observed in many cases, no incidences of ventilation inception were recorded.

Until experimental observation of surface ventilation inception through cavitation can be obtained it would seem advisable to assume that boundary layer separation is the major cause of ventilation inception.

APPLICATIONS TO FULLY WETTED HYDROFOILS

In all cases the geometrical angle of attack must be determined from the operating conditions of the boat. The geometrical angle of attack α_g resulting from turning with a side slip angle β is given by

$$\alpha_g = \beta \sin \Gamma \quad [3.8]$$

where Γ is the dihedral angle and $\sin \Gamma = 1.0$ for struts. This angle of attack will be induced on all struts and dihedral foils. In the case of trim of the boat, the geometrical angle of attack of all fixed foils will be

$$\alpha_g = \tau \cos \Gamma \quad [3.9]$$

where τ is the trim angle. In the case where the foil also has some incidence δ the angle τ should be replaced by $(\tau + \delta)$.

In the case where the angles of attack are induced by motions, the calculation of α_g is more complex because the effect of orbital velocities must be taken into account. To estimate the exact angle of attack, it is necessary to know the phasing between the motion and orbital velocity. The worst possible case is that where the orbital velocity and craft velocity are 180 degrees out of phase. This should be used because this condition will probably be realized at some time. In this case the maximum geometrical angle of attack is given by

3.28

$$\alpha_g = \frac{\omega(r+h_w)}{U} \quad [3.10]$$

where h_w is the wave height of the significant wave, U is the forward velocity of the boat, ω is the frequency of encounter given by Martin and Turpin (3.28) and r is the craft response given by:

$$\begin{aligned} r &= \zeta \cos \Gamma \quad \text{heave (for foils)} \\ r &= \theta l_F \cos \Gamma \quad \text{pitch (for foils)} \\ r &= \phi r_F \sin \Gamma \quad \text{roll (for struts)} \end{aligned}$$

Here ζ is the maximum heave amplitude, θ is the pitch amplitude, ϕ is the maximum roll amplitude, l_F and r_F are the longitudinal and vertical distances of the point in question from the c.g.

Although these values represent the maximum angles of attack likely to be achieved, they are probably not unrealistic because of the highly variable nature of the flow conditions. It is likely that at some time in a realistic seaway these angles will be realized.

The effective angle of attack α_e which is the angle plotted in Figures 3.4 and 3.5 is given by:

$$\alpha_e = \frac{\alpha_g}{AR+3} \quad [3.11]$$

where AR is the geometrical aspect ratio of the submerged portion of the strut or foil. In cases where surface piercing foils terminate in fully submerged foils the aspect ratio should be the aspect ratio of the entire foil system. In cases where a strut or surface piercing foil terminates normal or nearly normal to another panel, the effective aspect ratio is greater than the geometric aspect ratio AR_g and is given by

$$AR = AR_g \times f_p \quad [3.12]$$

where f_p is given in Figure 3.16 from Riley (3.29). If the chord and span of the submerged panel are large compared with the chord of the surface piercing foil or strut, the factor f_p will approach 2.0.

Surface Piercing Foils and Struts

The basic angles of attack required for ventilation inception of sharp nose and round nose sections are given by Figures 3.8 and 3.5 respectively. These values represent a minimum value, and must be modified by free surface effects to obtain the actual effective angles of attack required for ventilation inception.

In the case of wedgelike sections the angle of attack α_e required for inception and given by Figure 3.8 must be modified by the factor F_c which gives the increase in angle required with decreasing Froude number. Equation [3.3] gives the required angle for low Froude numbers ($F_c < 20$). It has been concluded that no effect due to chokeoff is present for depth-chord ratios of three or less.

For round nose sections, Figure 3.5 can be used to obtain α_e . Here ventilation inception will only occur at Froude numbers based on depth F_d of approximately 1.6 or greater. If F_d is less than this value no ventilation should occur for any angle of attack. For depth-chord ratios greater than one, stable ventilated cavities will only result when the effective angle of attack α_e is greater than the value given by Equation [3.6]. It is probable, however, that highly undesirable unstable ventilated cavities will result at the angles predicted by Figure 3.5 so that the use of these angles is felt to be more realistic than the use of Equation [3.6]. For nose radii greater than those shown on Figure 3.5 ($r_n/c > 0.02$) an effective angle of attack of 6.5 degrees should be used as the inception angle α_e .

Fully Submerged Foils

For fully submerged foils the effective angles of attack required for inception are taken directly from Figures 3.5 and 3.8. No corrections are necessary unless it is known that air will not be introduced near the leading edge of the foil. In this case the curves of Figure 3.4 representing a separation bubble of finite length or the data on finite bubble sizes of Figures 3.6 and 3.7 can be used to find the required effective angle of attack.

It should be remembered that ventilation inception can only occur on a fully submerged foil when an air supply is available. This normally results from the ventilation of a surface piercing foil or strut. Conditions for simultaneous ventilation of both

the foil and a surface piercing element intersecting the foil must thus be present for ventilation inception of a fully submerged foil.

PREVENTION OF VENTILATION

Because of the undesirable effects of ventilation, it may be necessary to take steps to prevent it. This is especially true in a case where it is predicted that ventilation inception will occur.

Normal means of preventing ventilation inception involve the use of ventilation fences. A ventilation fence can be installed on either surface piercing foils or struts in order to prevent the passage of air beyond the fence. For maximum effectiveness, ventilation fences should be installed near the free surface, particularly in the case of surface piercing foils.

No data are available on the design of ventilation fences, so that the required dimensions must be estimated. The ventilation fence stops further progress of ventilation by forming a physical barrier which separates the separated regions on each side of the fence. When ventilation inception occurs, air passes through the separated region on the foil or strut until it reaches the fence. Further progress of the ventilating air is prevented unless the separated region is large enough to overlap the fence. The fence should thus be larger than any separated region expected.

The required size can be estimated from the separation bubble geometries given in Figures 3.6 and 3.7. From these figures it can be seen that a fence with a chord equal to the foil chord and

a width of about ten percent of the chord should give adequate insurance against spread of ventilation past the fence. In cases where large angles of attack are expected the fence should probably extend about one-half chord downstream of the trailing edge of the foil.

Base vented struts should be avoided in fully wetted foil systems as they form a natural path for ventilating air to reach the submerged foils. As noted earlier, separation will always occur on a base vented strut so that some ventilation of fully wetted foils is likely under many conditions.

In general, foil sections with large nose radii are less likely to ventilate than sections with nose radii less than one percent of the chord. As this is generally true of cavitation inception for all but the highest speeds, it is desirable to make the sections as thick as possible from a ventilation standpoint.

One way of avoiding ventilation of fully submerged foils is to provide streamlined pods or fairings at the intersection of fully submerged foils with struts and surface piercing foils. These pods inhibit ventilation inception by breaking the path of separated flow needed for ventilation of submerged foils; they may thus act as a fence.

REFERENCES

- 3.1 "Study of Hydrofoil Seacraft," Grumman Aircraft Engineering Corporation, October 1958.
- 3.2 Hydrofoil Handbook, Prepared for the Office of Naval Research by Gibbs and Cox, Inc., under Contract Nonr-507(00), 1954.
- 3.3 Barr, R. A., "Ventilation Inception," HYDRONAUTICS, Incorporated Technical Report 127-4, March 1963.
- 3.4 Chang, P. K., and Dunham, William H., "Laminar Separation of Flow Around Symmetrical Struts at Various Angles of Attack," DTMB Report 1365, January 1961.
- 3.5 Wadlin, Kenneth L., "Mechanics of Ventilation Inception," Proceedings of the Second Symposium on Naval Hydrodynamics, Office of Naval Research Publication ACR-38, 1958.
- 3.6 Carrow, D. D., "A Note on the Boundary Layer and Stalling Characteristics of Airfoils," Cambridge University Aeronautical Laboratory, C.P. 174, 1950.
- 3.7 McCullough, George B., and Gault, Donald E., "Examples of Three Representative Types of Airfoil-Section Stall at Low Speeds," NACA Technical Note 2502, September 1951.
- 3.8 Gault, Donald E., "An Experimental Investigation of Regions of Separated Laminar Flow," NACA Technical Note 3505, September 1955.
- 3.9 Loftin, Laurence K., Jr, and Bursnall, William J., "The Effect of Variations in Reynolds Numbers Between 3.0×10^6 and 25.0×10^6 Upon the Aerodynamic Characteristics of a Number of NACA 6-Series Airfoil Sections," NACA Report 964, 1950.

- 3.10 McCullough, George B., "The Effect of Reynolds Number on the Stalling Characteristics and Pressure Distributions of Four Moderately Thin Airfoil Sections," NACA Technical Note 3524, November 1955.
- 3.11 Rose, L. M., and Altman, J. M., "Low-Speed Faired, Double-Wedge Airfoil with Nose Flap," NACA Technical Note 2172, August 1950.
- 3.12 Schlichting, Hermann, Boundary Layer Theory, Translated by J. Kestin, McGraw Hill Book Company, New York, 1960.
- 3.13 Rott, Nicholas, and Crabtree, L. F., "Simplified Boundary-Layer Calculations for Bodies of Revolution and Yawed Wings," *Journal of the Aeronautical Sciences*, Volume 19, Number 8, 1952.
- 3.14 Stratford, B. S., "The Prediction of Separation of the Turbulent Boundary Layer," *Journal of Fluid Mechanics*, Volume 5, Part 1, 1959.
- 3.15 Crabtree, L. F., "Effects of Leading-Edge Separation on Thin Wings in Two-Dimensional Incompressible Flow," *Journal of the Aeronautical Sciences*, Volume 24, No. 8, August 1957.
- 3.16 Cooke, J. C., and Brebner, G. C., "Separation and its Prevention by Geometric Designs," *Boundary Layer and Flow Control*, Volume 1, Edited by G. V. Lachmann, Pergamon Press, New York, 1961.
- 3.17 Schiebe, F. R., and Wetzel, J. M., "Ventilated Cavities on Submerged Hydrofoils of Finite Span," St. Anthony Falls Hydraulic Laboratory Memorandum No. M-91, July 1961.
- 3.18 Lang, Thomas G., Daybell, Dorothy Argue, and Smith, Kenneth E., "Water-Tunnel Tests on Hydrofoils with Forced Ventilation," NAVORD Report 7008, November 1959.
- 3.19 Wadlin, Kenneth L., and Christopher, Kenneth W., "A Method for Calculation of Hydrodynamic Lift for Submerged and Planing Rectangular Lifting Surfaces," NASA Technical Report R-14, 1959.

- 3.20 Fridsma, Gerard, "Force and Moment Characteristics of a Surface Piercing, Fully Ventilated Dihedral Hydrofoil," Davidson Laboratory Report No. 795, November 1960.
- 3.21 Breslin, John P., and Skalak, Richard, "Exploratory Study of Ventilated Flows about Yawed Surface-Piercing Struts," NASA Memo 2-23-59W, April 1959.
- 3.22 Kiceniuk, Taras, "Preliminary Experimental Study of Vertical Hydrofoils of Low Aspect Ratio Piercing a Water Surface," CIT Report No. E-55.2, December 1954.
- 3.23 Barr, R. A., "Air Requirements for Ventilated Propellers," HYDRONAUTICS, Incorporated Technical Report 127-5, March 1963.
- 3.24 Cuthbert, Jerry W., "An Analysis of Air Entrainment in Cavity Flows," HYDRONAUTICS, Incorporated Technical Report 003-1, October 1960.
- 3.25 Patterson, Elizabeth W., and Braslow, Albert L., "Ordinates and Theoretical Pressure Distribution Data for NACA 6 and 6A Series Airfoil Sections with Thicknesses from 2 to 21 and from 2 to 15 percent Chord Respectively," NASA Technical Report R-84, 1961.
- 3.26 Twaites, Bryan, Editor, Incompressible Aerodynamics, Oxford at the Clarendon Press, 1960.
- 3.27 Coffee, Claude W., Jr and McKann, Robert E., "Hydrodynamic Drag of 12 - and 21-percent Thick Surface Piercing Struts," NACA Technical Note 3092, December 1953.
- 3.28 Martin, Milton, and Turpin, Francis J., "The Effect of Surface Waves on Some Design Parameters of a Hydrofoil Boat," HYDRONAUTICS, Incorporated Technical Report 001-3, January 1961.
- 3.29 Riley, Donald R., "Effect of Horizontal-Tail Span and Vertical Location on the Aerodynamic Characteristics of an Unswept Tail Assembly in Sideslip," NACA Technical Note 2907, February 1953.

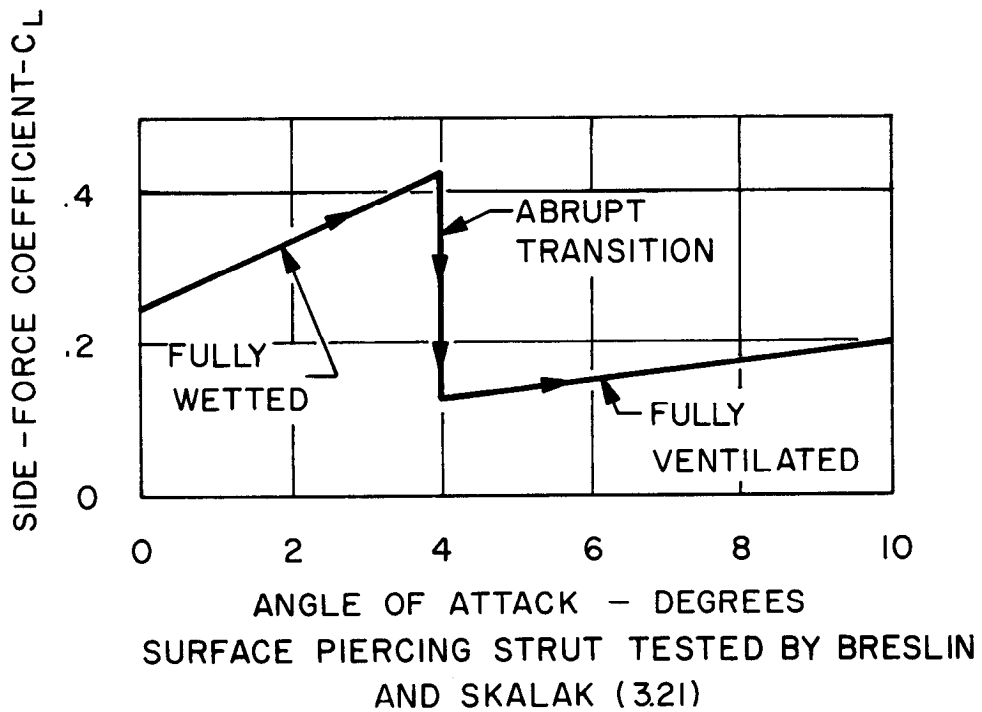
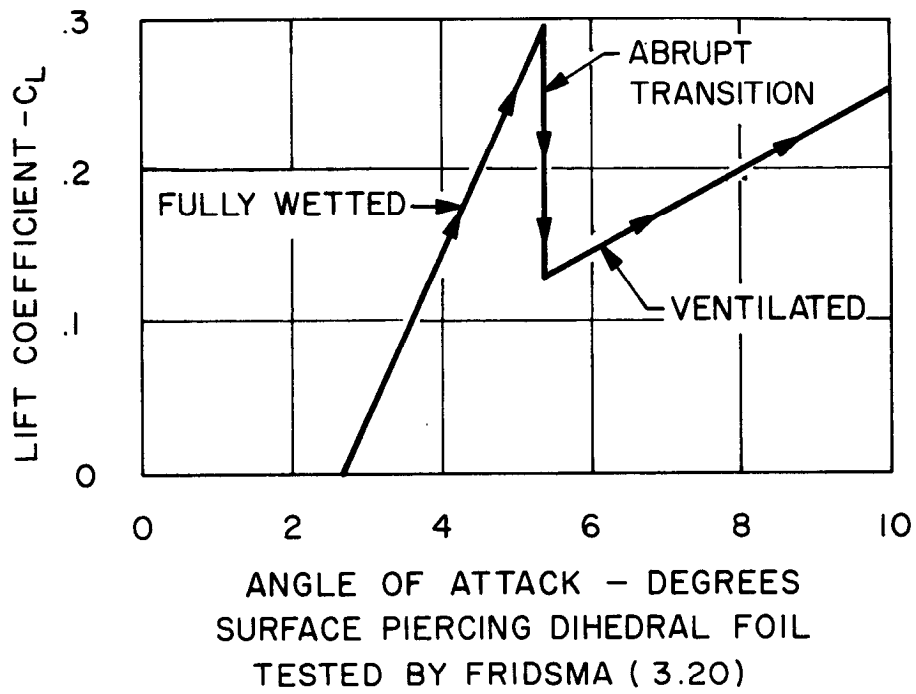
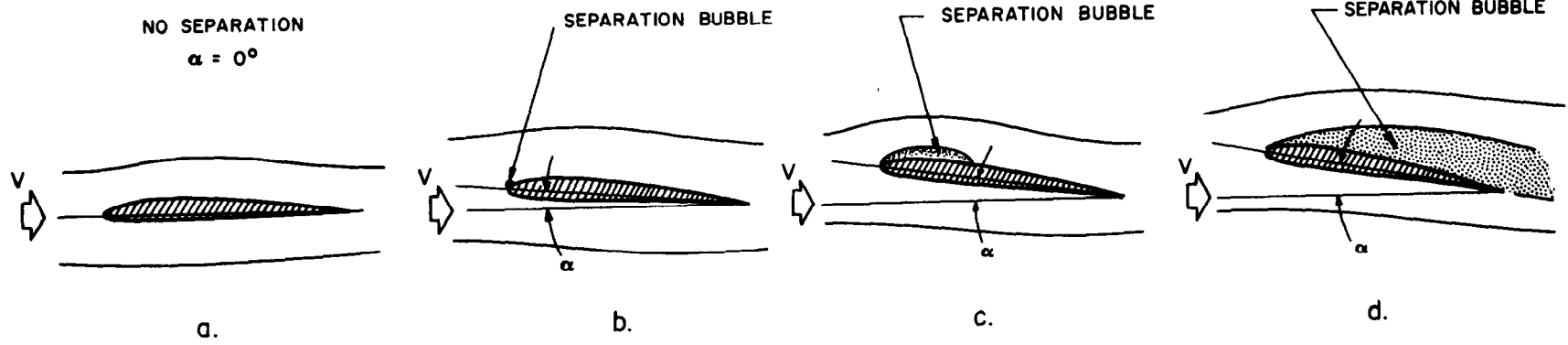
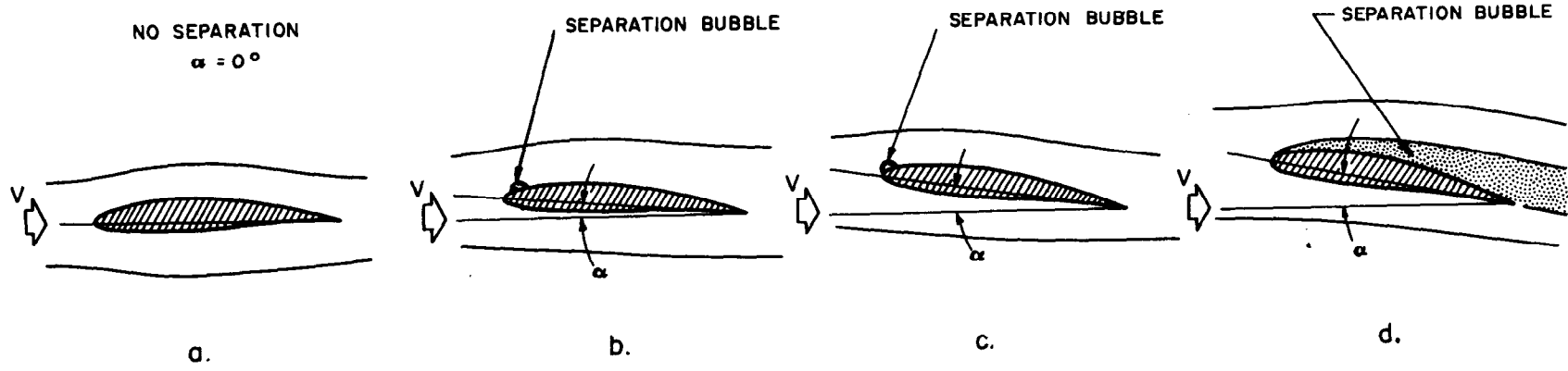


FIGURE 3.1 TYPICAL EXAMPLES OF ABRUPT FORCE CHANGES ASSOCIATED WITH VENTILATION INCEPTION FOR FOILS AND STRUTS

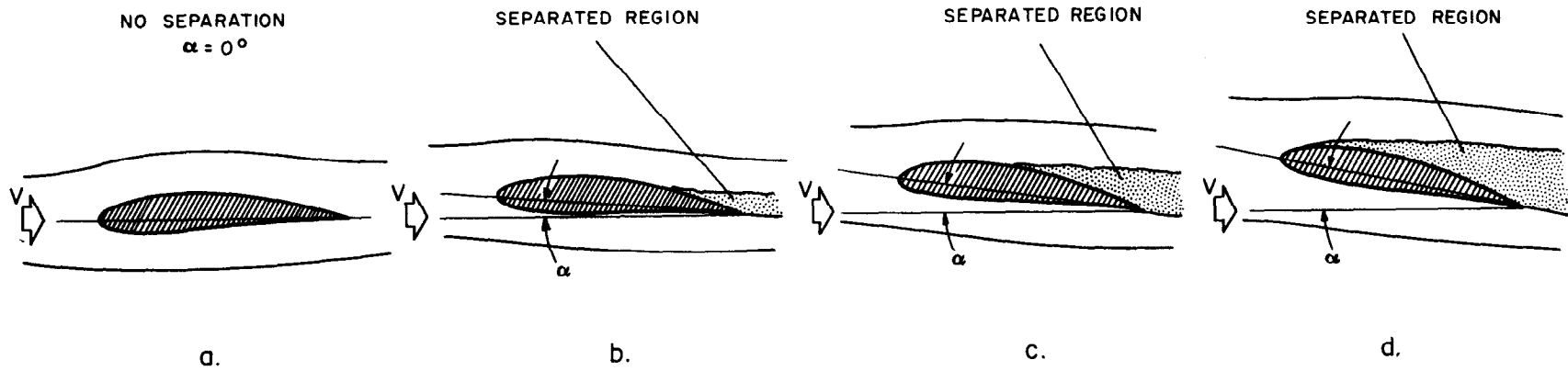


A. Long Bubble (Thin Airfoil) Type Separation
This Type Occurs On Very Thin Sections



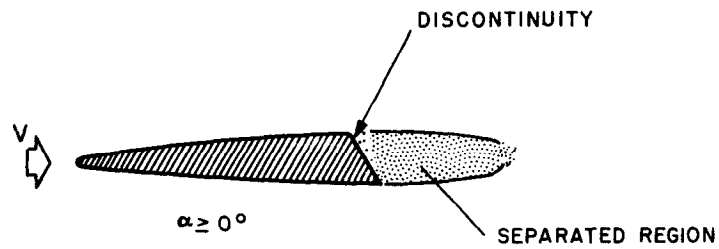
B. Leading Edge Stall
This Type Occurs On Sections Of Moderate Thickness

FIGURE 3.2- ILLUSTRATIONS OF THE VARIOUS TYPES OF SEPARATION OBSERVED ON FOILS



C. Trailing Edge Stall

This Type Occurs On Very Thick Sections



D. Discontinuity Separation

FIGURE 3.2 (CONT.)- ILLUSTRATIONS OF THE VARIOUS TYPES OF SEPARATION OBSERVED ON FOILS

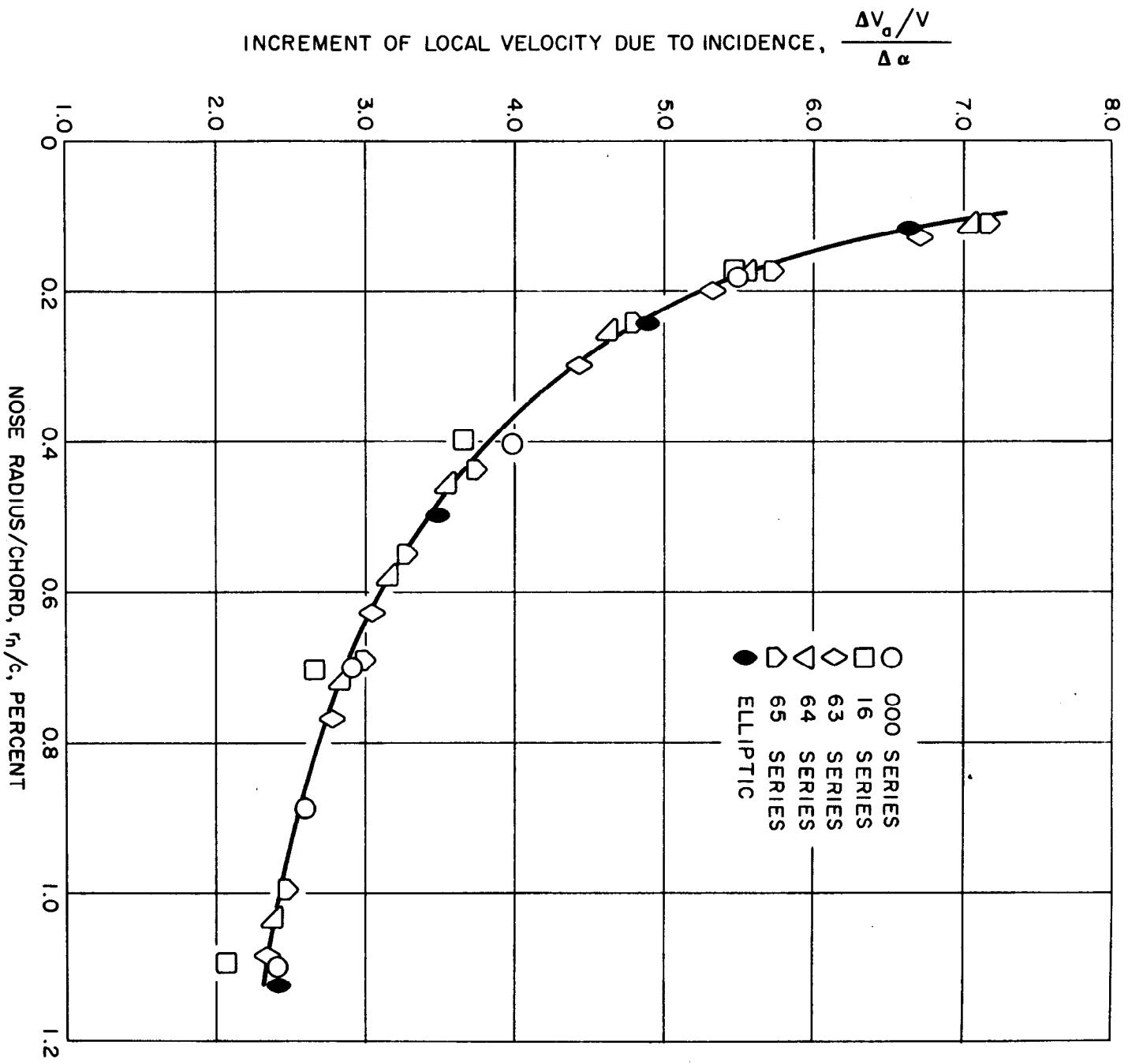


FIGURE 33-- INCREMENT OF LOCAL VELOCITY DUE TO INCIDENCE
VERSUS SECTION NOSE RADIUS

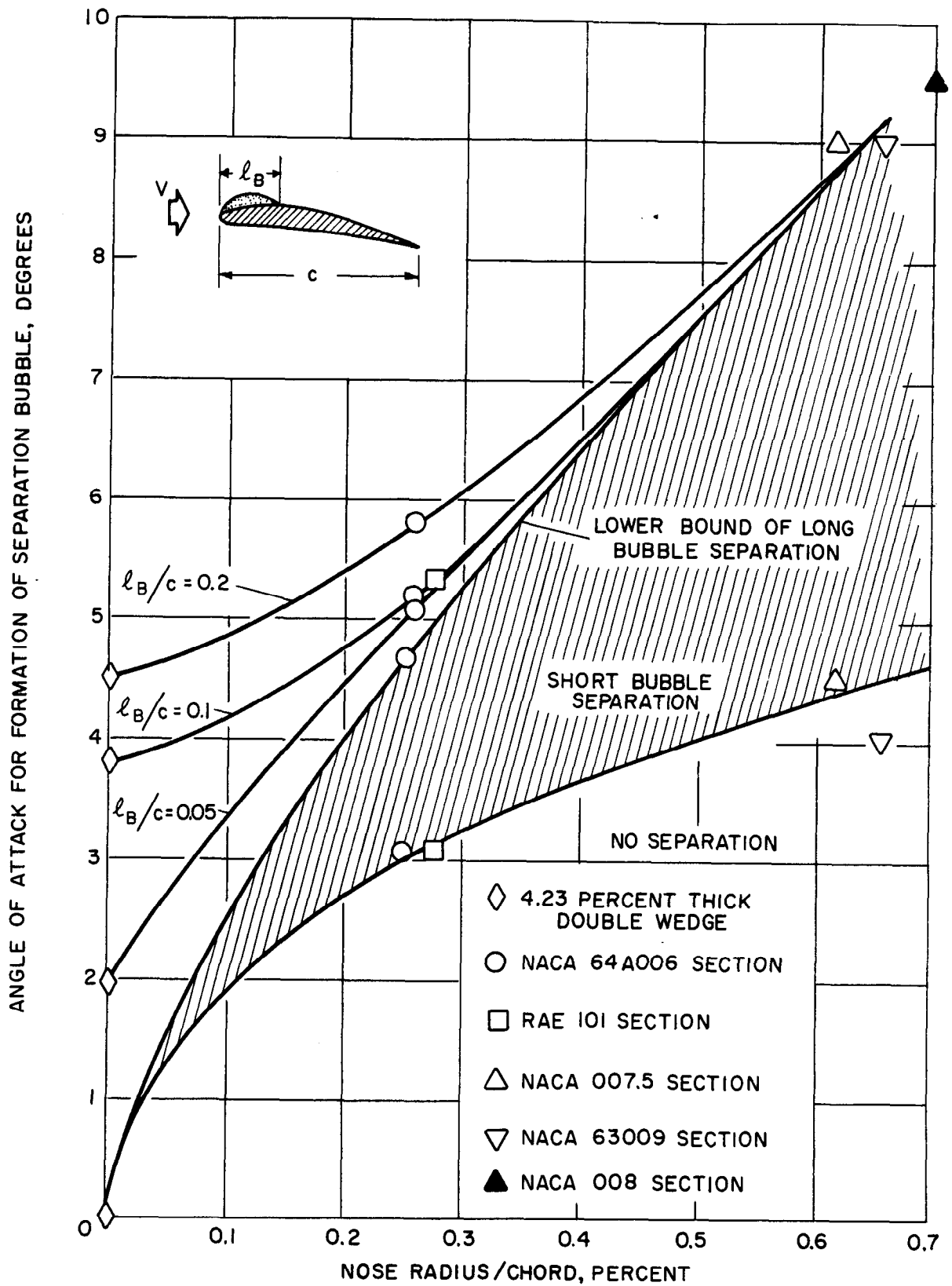


FIGURE 3.4- ANGLE OF ATTACK REQUIRED FOR FORMATION OF A SEPARATION BUBBLE AS A FUNCTION OF SECTION NOSE RADIUS

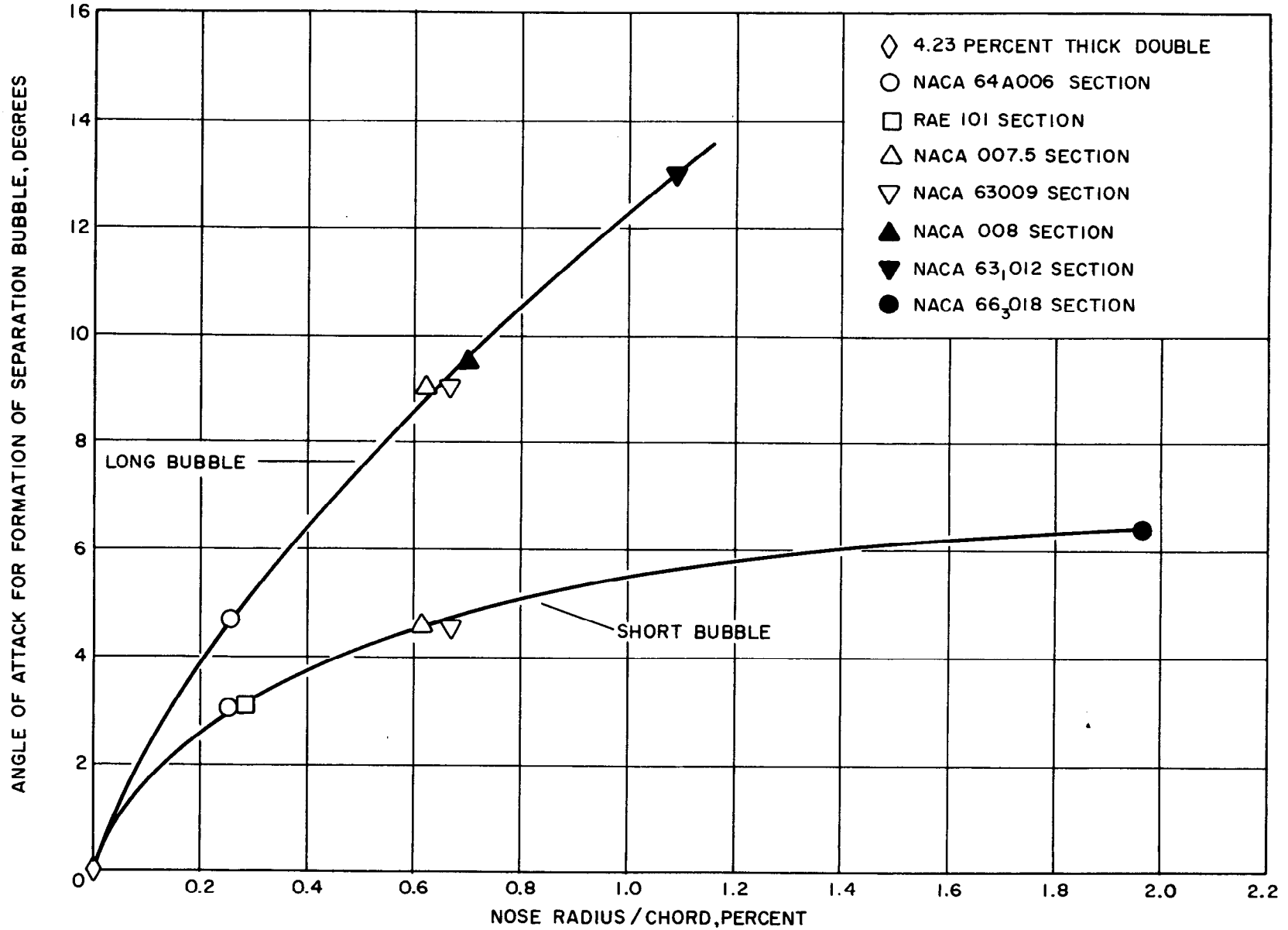


FIGURE 3.5- ANGLE OF ATTACK REQUIRED FOR FORMATION OF SEPARATION BUBBLES AS A FUNCTION OF NOSE RADIUS

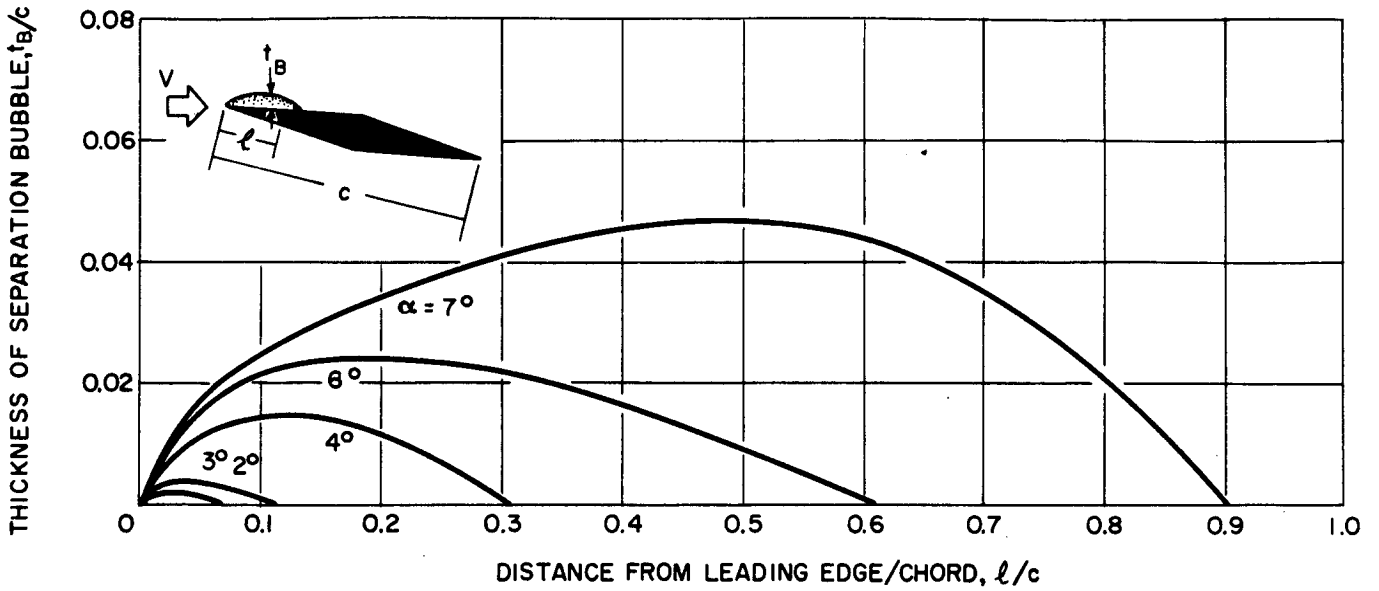


FIGURE 3.6— SIZE OF SEPARATION BUBBLE FOR A DOUBLE WEDGE SECTION ($t/c = 0.042$)
AT VARIOUS ANGLES OF ATTACK
(FOR USE WITH A SHARP LEADING EDGE SECTION)

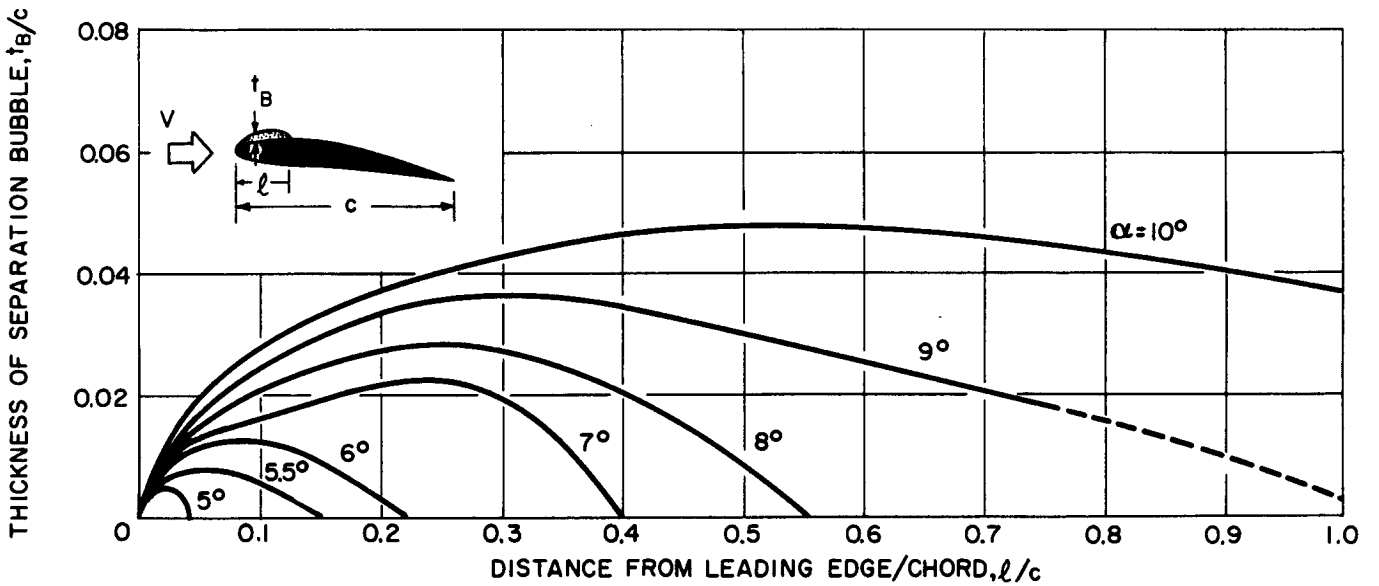


FIGURE 3.7— SIZE OF SEPARATION BUBBLES FOR AN NACA 64A006 SECTION FOR
VARIOUS ANGLES OF ATTACK

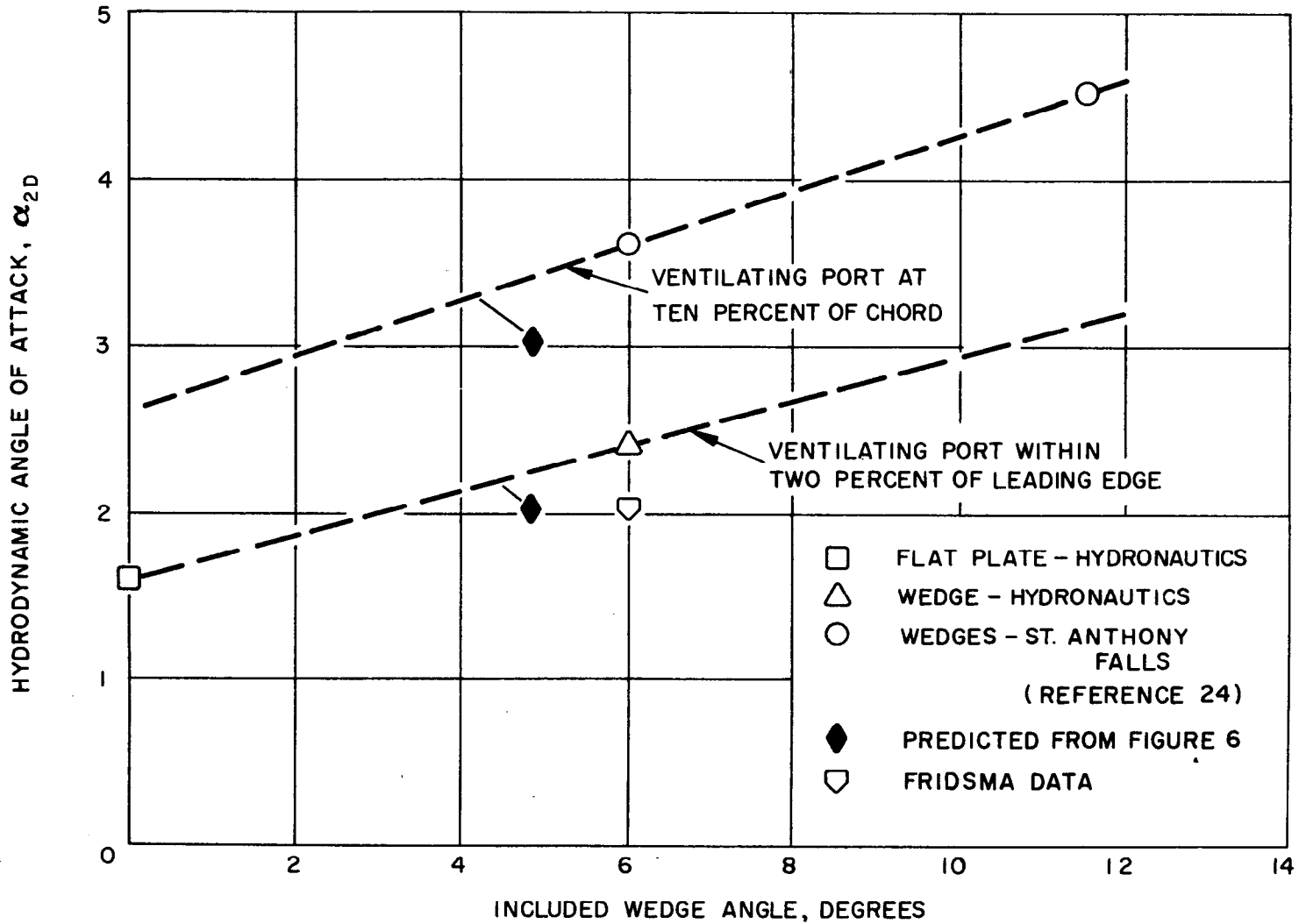


FIGURE 3.8- EXPERIMENTALLY DETERMINED ANGLES OF ATTACK REQUIRED FOR VENTILATION INCEPTION

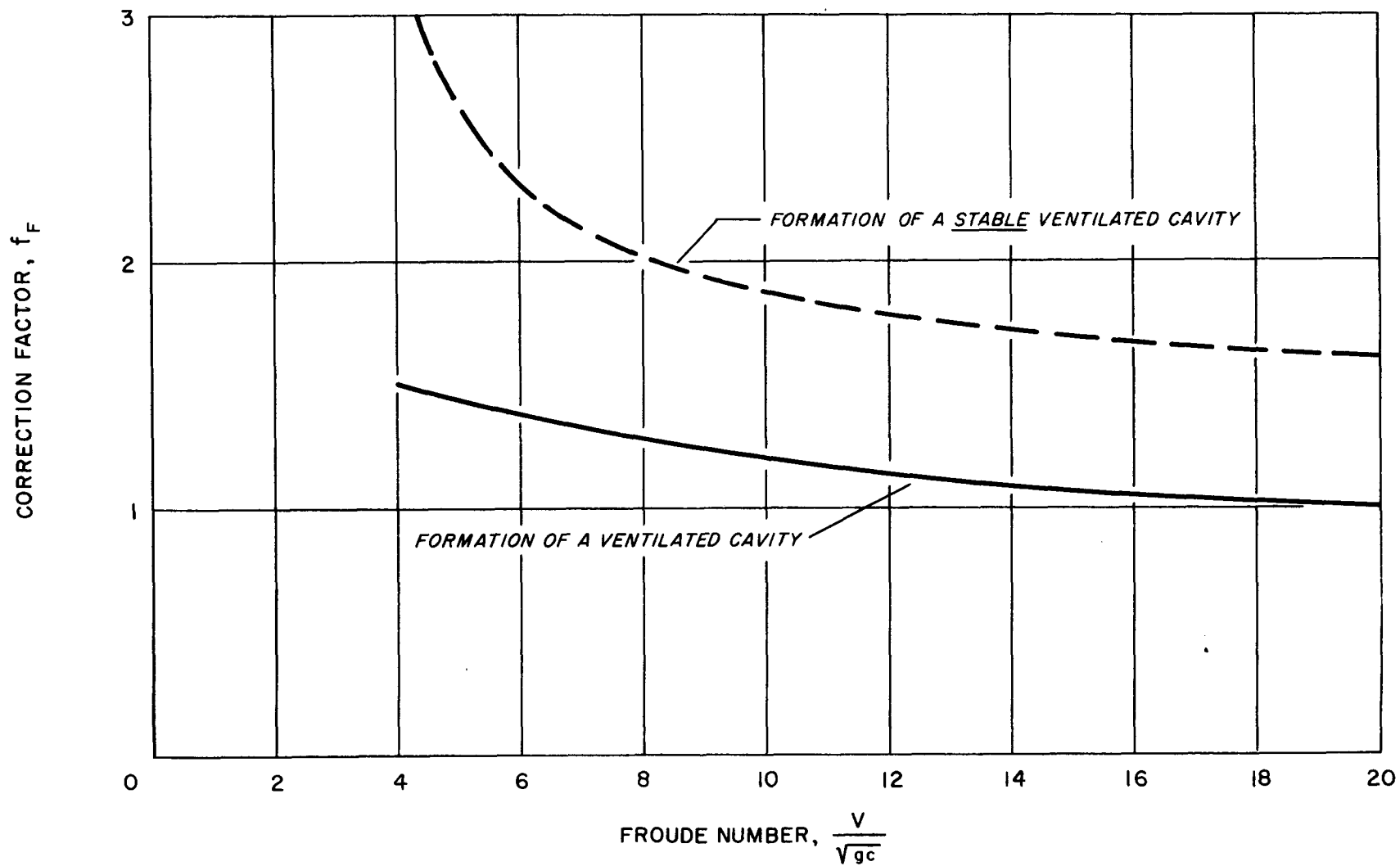


FIGURE 3.9— CORRECTION FACTOR f_F TO ACCOUNT FOR THE INFLUENCE OF THE FROUDE NUMBER ON ANGLE OF ATTACK FOR VENTILATION INCEPTION OF SURFACE PIERCING WEDGE FOILS (FROM [3.20])

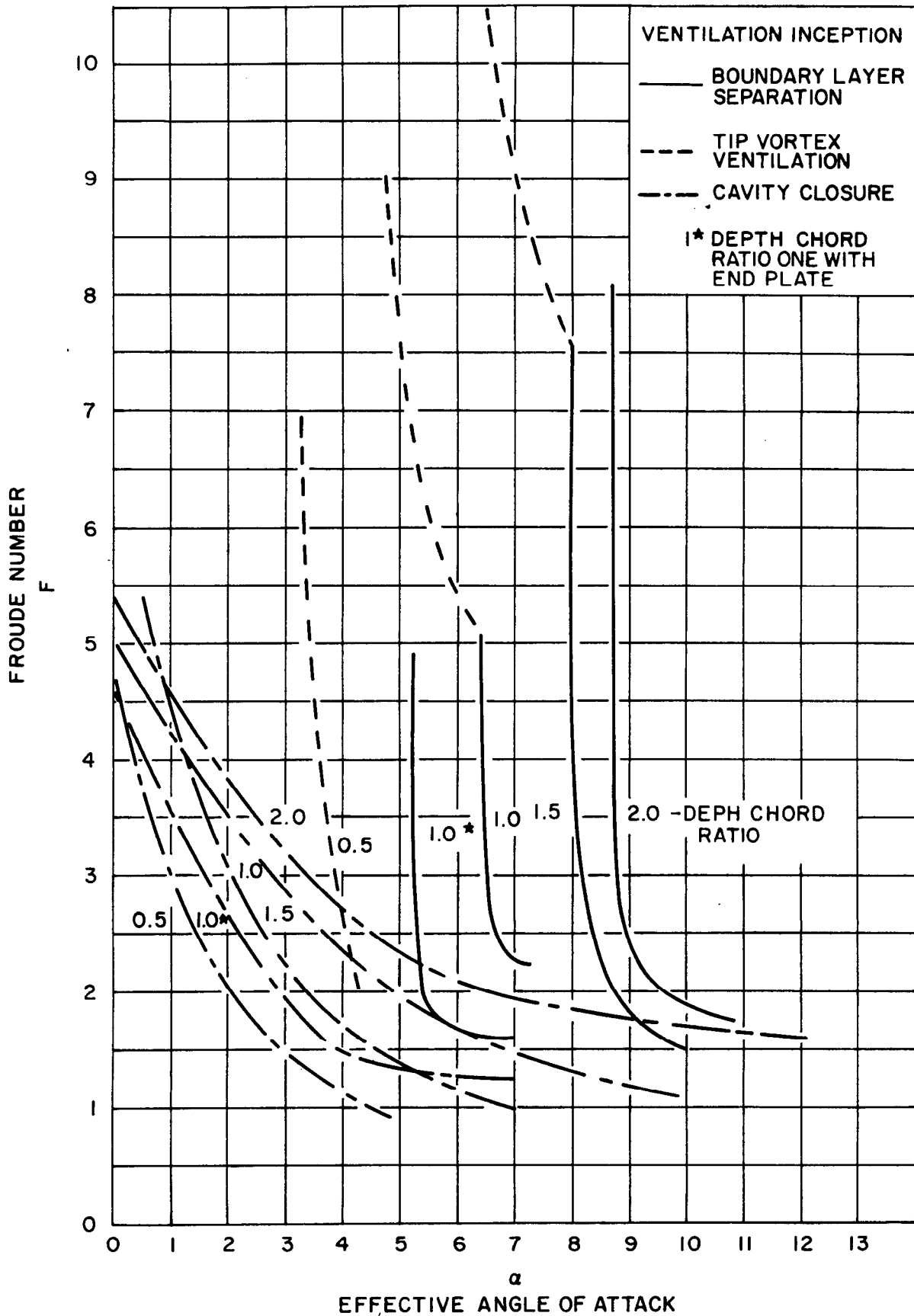


FIGURE 3.10 - TYPICAL VENTILATION INCEPTION RESULTS FOR SURFACE PIERCING STRUTS SHOWING DEPENDENCE ON DEPTH-CHORD RATIO AND FROUDE NO. FROM REFERENCE 3.20

145

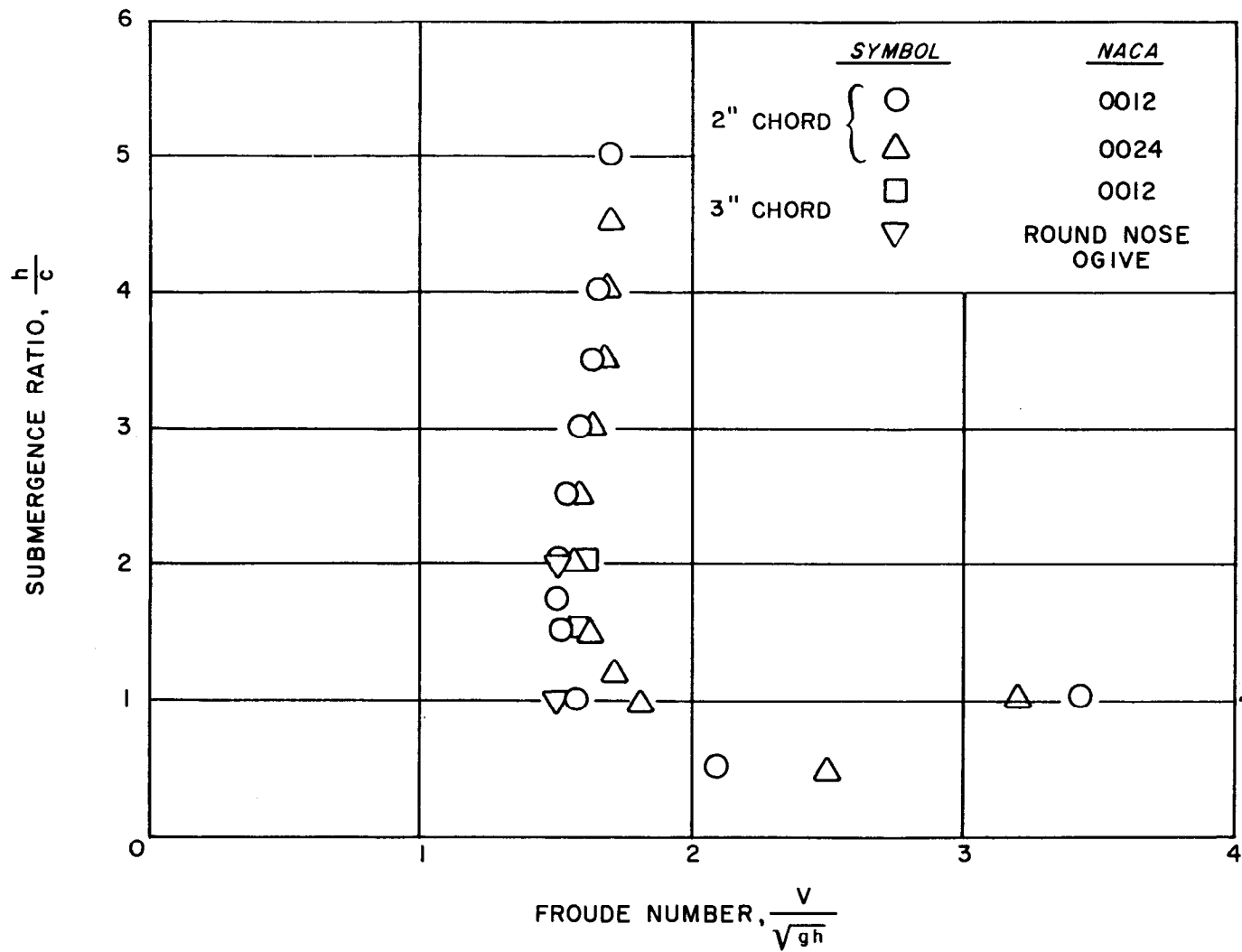


FIGURE 3.11- FROUDE NUMBER AT WHICH VENTILATION INCEPTION CAN OCCUR INDICATING MINIMUM VALUE OF APPROXIMATELY 1.6 FOR ALL DEPTH/CHORD RATIOS ABOVE

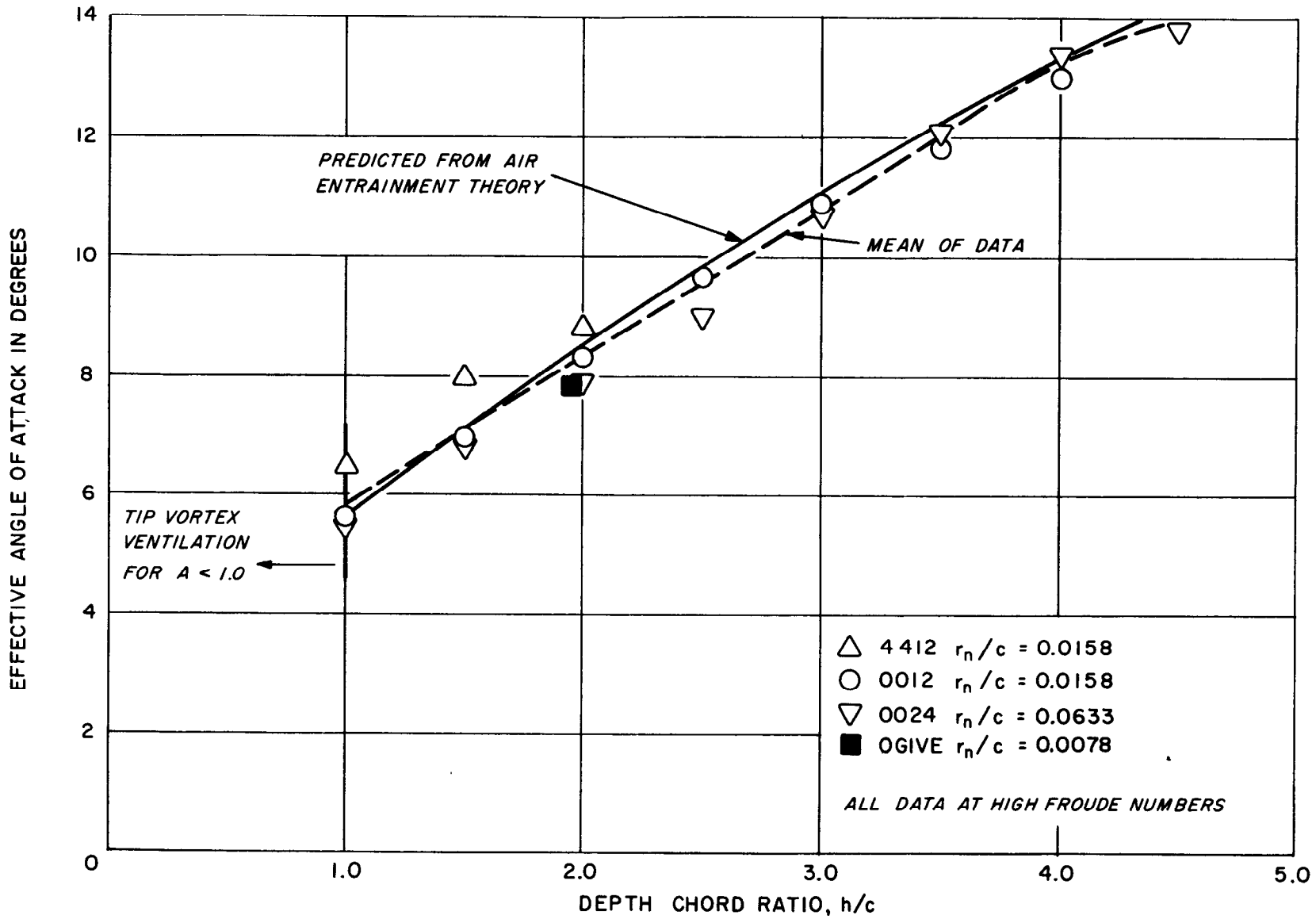
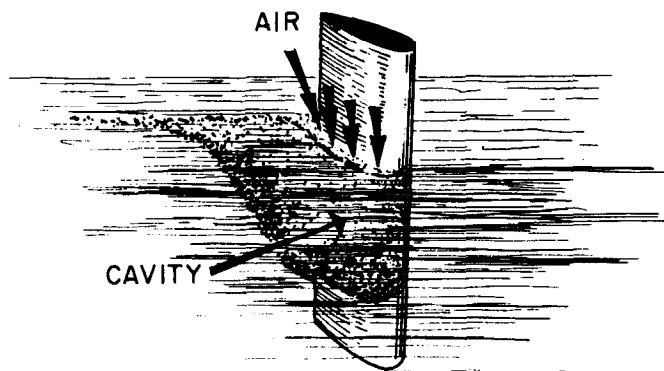
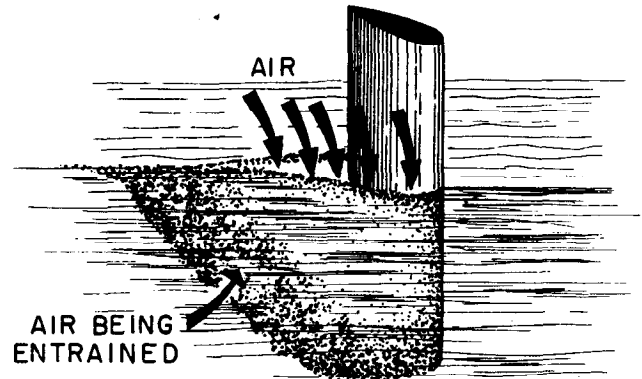


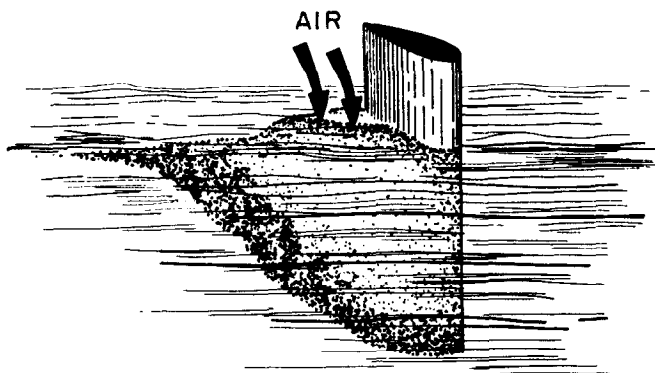
FIGURE 3.12— THE EFFECTIVE ANGLE OF ATTACK REQUIRED FOR VENTILATION OF SURFACE PIERCING STRUTS OF AIRFOIL SECTION AS A FUNCTION OF DEPTH/CHORD RATIO



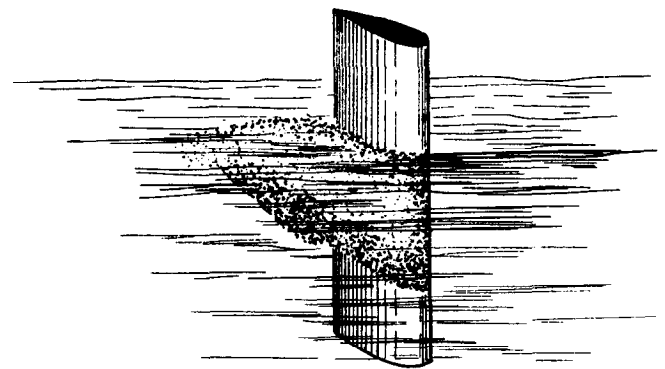
a. VENTILATED CAVITY FORMING AS SEPARATED BOUNDARY LAYER IS VENTILATED AT FREE SURFACE



b. VENTILATED CAVITY GROWS AND THE AIR REQUIRED INCREASES



c. SPRAY SHEET CLOSES UP THE CAVITY OPENING AS AIR PRESSURE DECREASES



d. CAVITY CLOSED OFF AT THE FREE SURFACE AND THE CAVITY DISAPPEARING

FIGURE 3.13— THE FORMATION AND DISAPPEARANCE OF AN UNSTABLE CAVITY ON A SURFACE PIERCING STRUT WHERE THE ANGLE OF ATTACK IS INADEQUATE

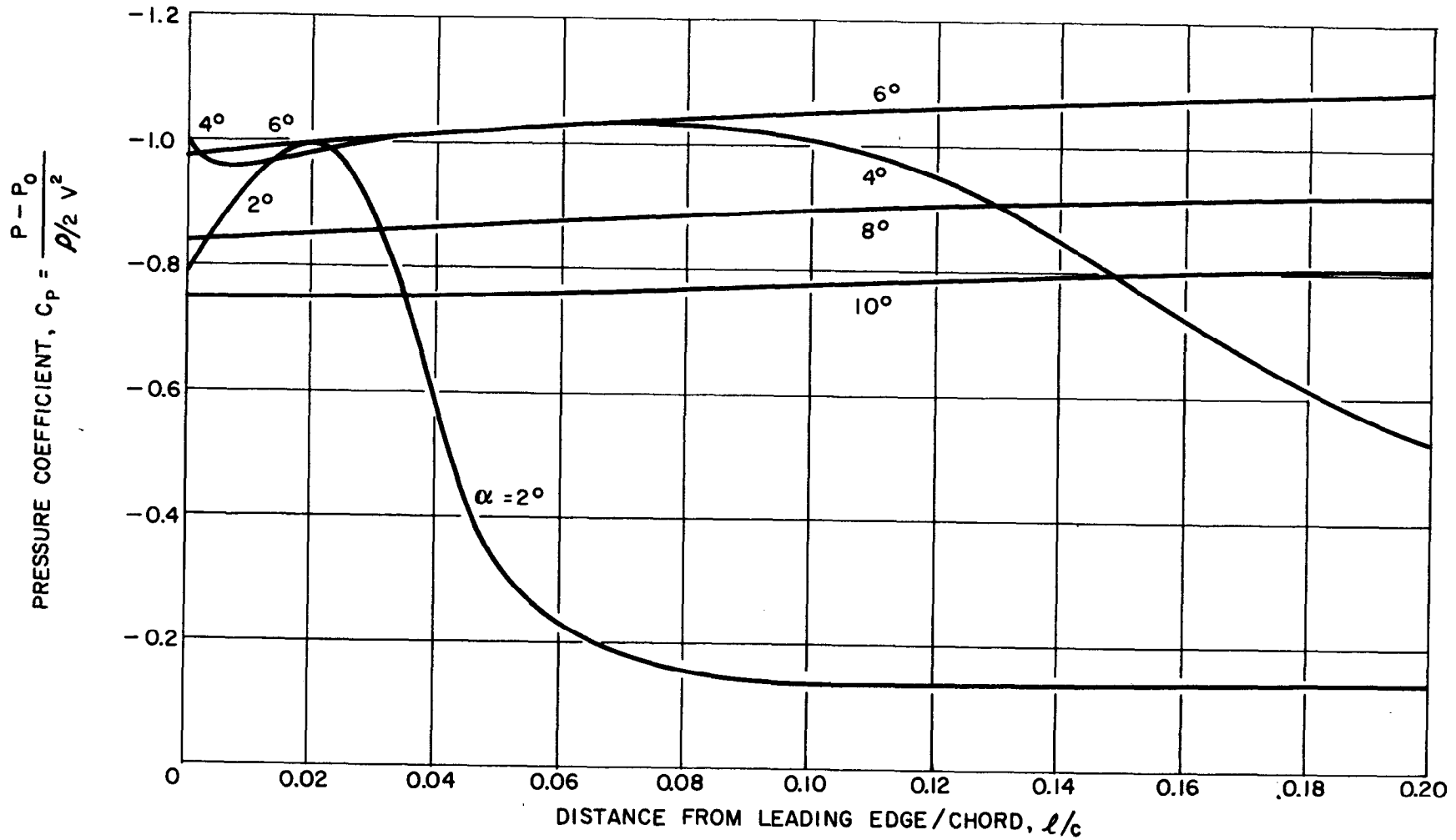


FIGURE 3.14- PRESSURE COEFFICIENTS ON FOIL UPPER SURFACE FOR A DOUBLE WEDGE SECTION
 ($t/c = 0.042$) FOR VARIOUS ANGLES OF ATTACK
 (FOR USE WITH SHARP LEADING EDGE SECTIONS)

bh1

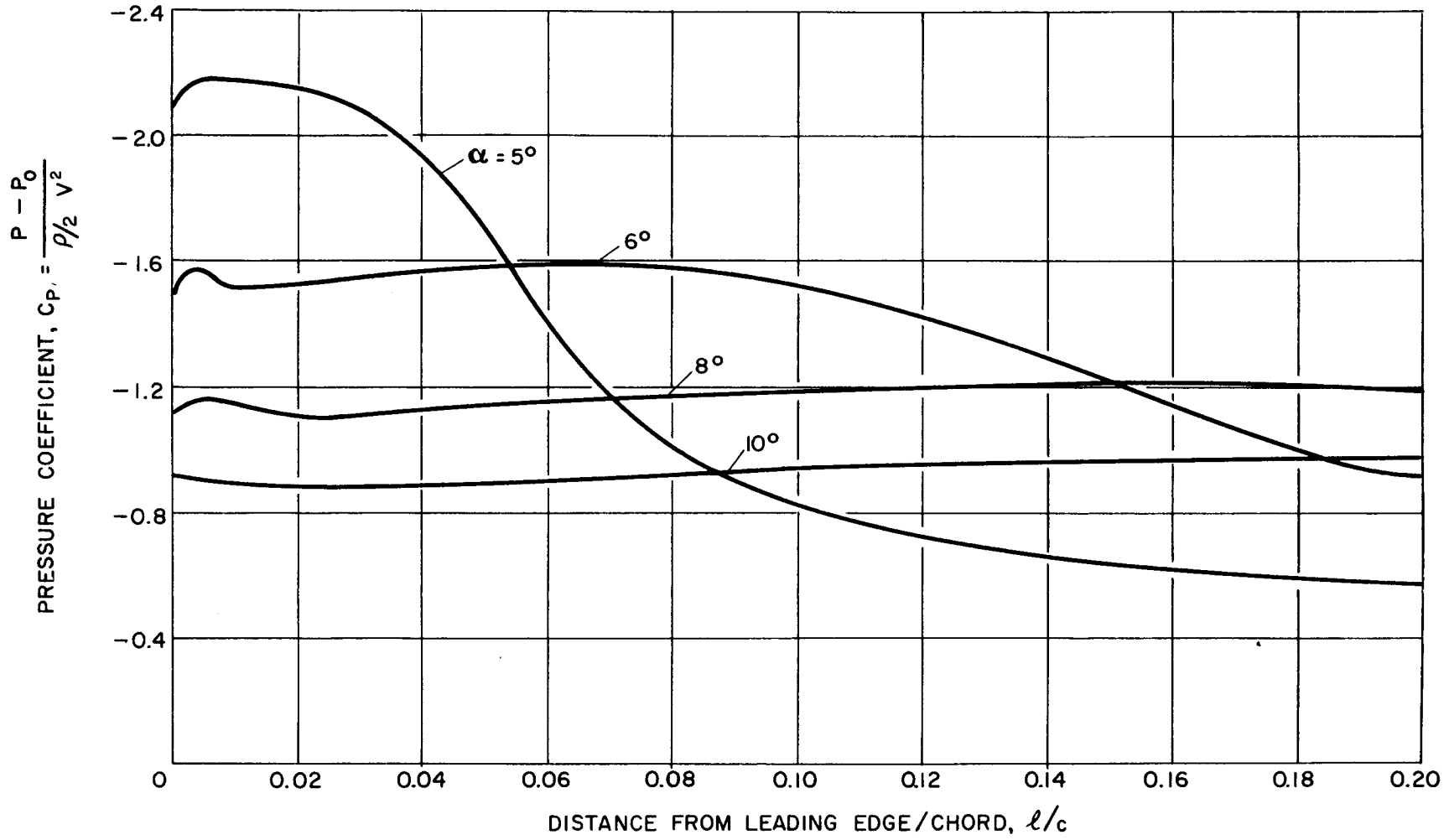


FIGURE 3.15- PRESSURE COEFFICIENTS ON FOIL UPPER SURFACE FOR AN NACA 64A006 SECTION FOR VARIOUS ANGLES OF ATTACK
(EQUIVALENT TO SECTIONS WITH PARABOLIC THICKNESS = 0.14)

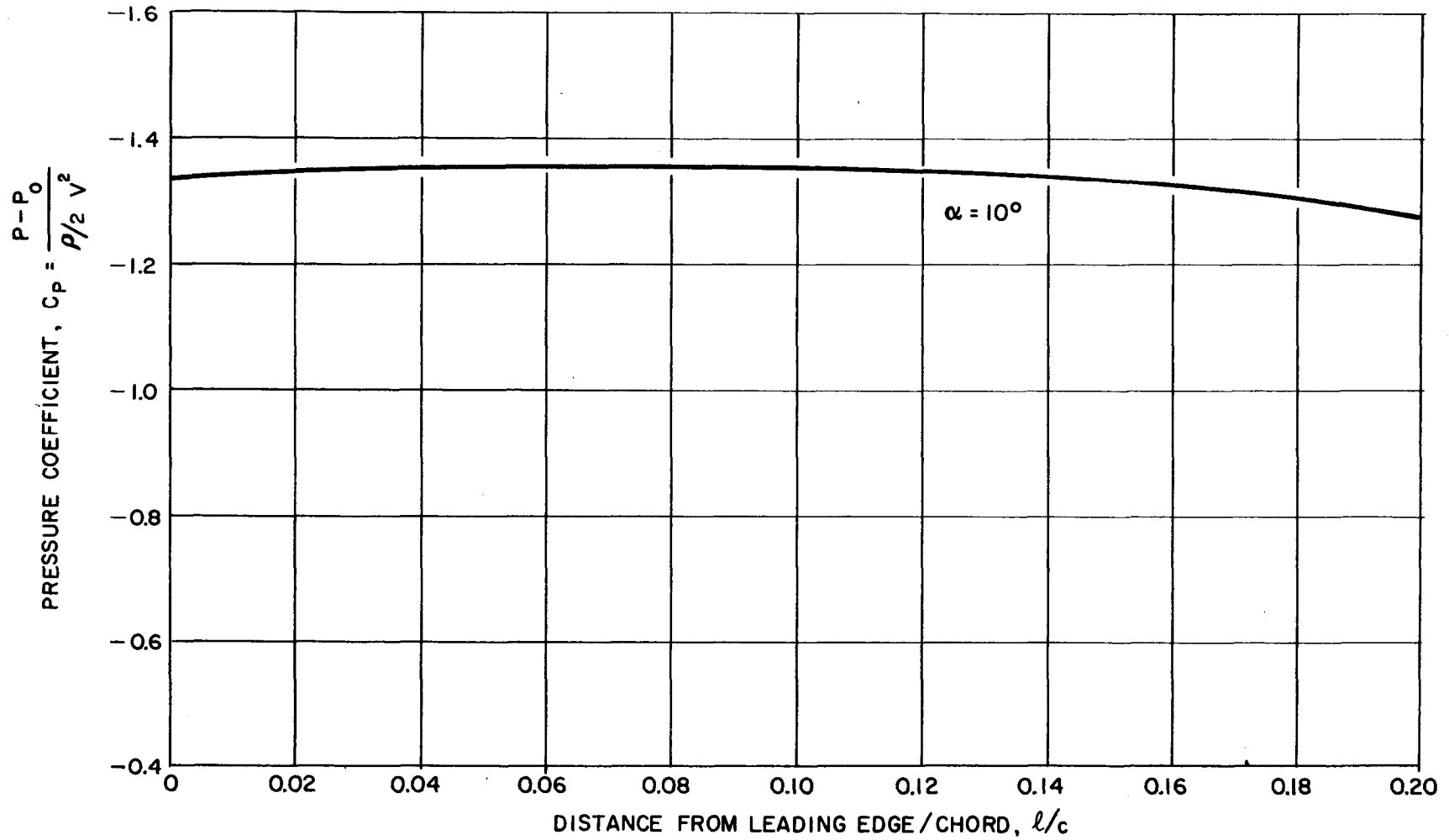


FIGURE 3.16 — PRESSURE COEFFICIENTS ON FOIL UPPER SURFACE FOR AN NACA 007.5 SECTION AT ANGLE OF ATTACK JUST AFTER SEPARATION
(EQUIVALENT TO SECTIONS WITH PARABOLIC THICKNESS=0.21)

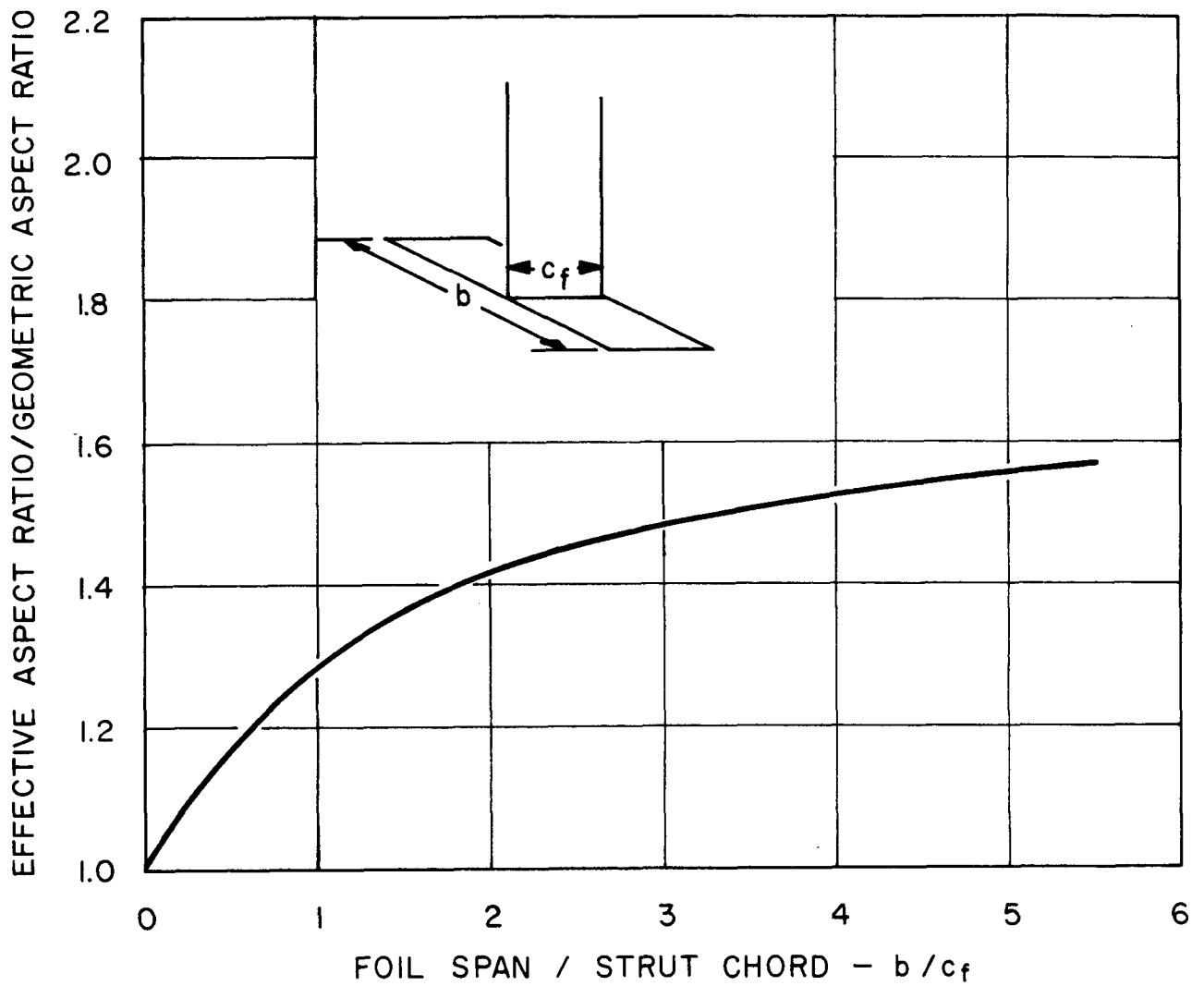


FIGURE 3.17 -THE EFFECT OF FOIL SPAN ON THE EFFECTIVE ASPECT RATIO OF A STRUT TERMINATING IN A NORMAL FOIL

HYDRONAUTICS, Incorporated

4.0

CHAPTER 4

TRIM, ALTITUDE AND PRE-TAKEOFF
RESISTANCE OF HYDROFOIL CRAFT

by

Roderick A. Barr

NOTATION

A	Characteristic area of foil or hull
A_f	Planform area of foil panel
A_h	Hull area wetted by solid water (not including spray)
AR	Aspect ratio of foil
AR_h	Aspect ratio of hull based on wetted area A_h
AR_s	Aspect ratio of surface piercing foil
$(A/\sqrt[3]{V})$	Hull loading factor defined as the hull area bounded by the chines divided by the displaced volume at rest to the $\frac{2}{3}$ power
a_o	Two-dimensional lift curve slope of a section including viscous effects
a_1, a_2	Empirical constants defining the lift force due to a surface piercing foil
B_M	Mean beam of the hull defined as the area bounded by the chines divided by the length between perpendiculars l
b	The half-beam of the idealized prismatic hull surface
C_L	Lift coefficient - $\frac{L}{\frac{1}{2}\rho Va^2 A}$
C_{L_d}	Design lift coefficient due to camber
C_{L_α}	Lift curve slope - $dC_L/d\alpha$ or $dC_L/d\tau$

C_{L_L}	Linear lift coefficient
$C_{L_{NL}}$	Non-linear lift coefficient
$(C_L)_\alpha$	Lift coefficient due to angle of attack (incidence or trim angle)
$C_{L_{\alpha_h}}$	Lift curve slope of hull
C_{L_δ}	Flap rate - $dC_L/d\delta$
$(C_L)_\delta$	Lift coefficient due to flap deflection
C_h	Hinge moment coefficient
C_{h_δ}	Hinge moment coefficient due to flap deflection - $dC_h/d\delta$
$(C_{h_\delta})_{\Lambda=0}$	Hinge moment coefficient due to flap deflection for unswept foil
c	Foil chord
c_r	Foil root chord
D	Total foilborne drag
d	Total vertical depth of surface piercing foil
F_z	Vertical force in the z direction
F_{N_∇}	Froude number for the hull based on the at rest displaced volume of the hull - $V/\sqrt{g\nabla^{1/3}}$
$F_{N_\nabla\mu}$	Froude number for the hull based on the unloaded displaced volume of the hull - $V/\sqrt{g[\nabla(1-\mu)]^{1/3}}$

f/c	Flap chord - foil chord ratio
g	Acceleration of gravity
h	Depth of submergence of a foil panel
K_b	Flap-span factor for $C_{L\delta}$
K_c	Flap-chord factor for $C_{L\delta}$
K_d	Three-dimensional biplane correction factor for $C_{L\alpha}$
K_{NL}	Non-linear lift correction factor
K_o	Two-dimensional biplane correction factor for $C_{L\alpha}$
K_2, K_3	Depth correction factor for $C_{L\alpha}$
L	Total lift of the foil system or of an individual foil
L_p	Length between perpendiculars of the hull
$L_{c.g.}$	Distance of the craft center of gravity from the hull transom
l_f	Distance between forward and after foil systems
l_M	Mean wetted length of the hull
l_s	Total strut length
l_{cb}	Distance between center of hull buoyancy and hull transom
l_{cp}	Distance between center of lift of hull and hull transom

M_b	Moment due to hull buoyancy
M_{DT}	Moment due to drag-thrust couple
M_h	Moment due to hull
M_n	Moment due to n'th component of the system
p	Percent of chord of the center of pressure from the quarter-chord line
R_H	Hull resistance
(R/W)	Hull resistance divided by boat weight
S	Foil span
s	Depth of submergence of keel of idealized hull at the transom
T	Propeller thrust
V	Velocity
V_K	Velocity in knots
V_M	Velocity in statute miles per hour
V_T	Takeoff velocity
ΔV	Change in velocity
X	Longitudinal distance measured from the center of gravity
X_b	Distance of the center of buoyancy from the center of gravity
X_c	Distance of center of pressure of foil lift due to camber from leading edge in percent of foil chord
X_f	Distance of foil center of pressure from center of gravity

4.5

X_h	Distance of the hull center of lift from center of gravity
$X_{\frac{c}{4}r}$	Distance of the foil center of pressure from the quarter-chord line at the foil root
X_{f_q}	Distance of the foil center of pressure from the foil quarter-chord line
Z_n	Vertical force due to the n'th component
Z_b	Vertical force due to the hull buoyancy
Z_h	Vertical force due to the hull dynamic lift
α	Angle of attack of the foil
α_A	Angle of attack or incidence of forward foils
α_F	Angle of attack or incidence of after foils
α_s	Angle of attack on struts with dihedral angle
$(\alpha_\delta)_{c_l}$	Flap effectiveness parameter
β	Hull deadrise angle
Γ	Foil dihedral angle
Δ	Displacement of craft in pounds
Δ'	Non-dimensional displacement ratio - $\Delta/\frac{1}{2}\rho V^2$
δ	Flap angle
δ'	Effective flap angle for swept foils - $\delta \cos \Lambda_h$
Λ	Sweep angle of the foil quarter-chord line
Λ_h	Sweep angle of the foil hinge line

4.6

- λ Taper ratio of the foil (root chord divided by tip chord)
- λ_o Sweep correction for lift-curve slope $C_{L\alpha}$
- μ Percent of craft weight supported by the foils before takeoff
- ρ Mass density
- τ Trim angle of boat relative to the hull base line
- τ_o Planform correction for lift-curve slope $C_{L\alpha}$

Subscripts

- A Referring to the foil systems aft of the center of gravity
- F Referring to the foil systems forward of the center of gravity
- h Pertaining to the hull
- n The n'th component of the system
- s Pertaining to the surface piercing foil systems

SUMMARY

The problem of calculating the trim and altitude of a hydrofoil boat as a function of forward speed is considered. Simultaneous equations in terms of these and other known variables are presented. Explicit solutions for a number of practical configurations are presented for the case of foilborne operation. These solutions are given in terms of the hydrodynamic coefficients of the foil systems, for which expressions are given. Expressions for the hydrodynamic coefficients of the hull are also presented for the solution of the equations for the pre-takeoff case. Methods of solution for the pre-takeoff case are indicated. The associated problem of craft resistance before takeoff is considered. The calculation of pre-takeoff drag is dependent on knowledge of trim and altitude as a function of speed. Contributions of the hull and foils to craft resistance are considered and means of estimating pre-takeoff resistance given.

INTRODUCTION

A knowledge of the trim and altitude history of a hydrofoil boat as a function of forward speed is of considerable interest and importance to the designer. The craft resistance prior to takeoff is particularly dependent on the instantaneous trim and rise of the craft and these values may vary widely from their design or cruise magnitudes. It is also desirable to know the trim and altitude of the craft in order to insure that foil control margins and geometries (in the case of surface piercing

systems) are properly chosen. The possibility of ventilation or cavitation inception is also dependent on these parameters. The general unavailability of methods for calculating the drag of hydrofoil craft before takeoff is largely due to lack of knowledge of trim and altitude.

Two problems are considered in this chapter: The solution of the basic force and moment equations for the trim and altitude of the craft, and the determination of the drag of the craft, particularly before takeoff occurs. Neither of these problems has been considered in the generally available literature.

THE BASIC EQUATIONS GOVERNING TRIM AND ALTITUDE

In general, operation of hydrofoil craft will be unsteady because of wave induced motions and variations in operating speed (such as occur during takeoff). The unsteadiness arising from acceleration of the craft is generally negligible and can be safely ignored in these calculations. Historically, operation of hydrofoil craft has been considered as a quasi-steady problem in order to make the problem more tractable. The unsteady forces on the foils, due to wave induced angles of attack, may be important but the resulting forces will generally be manifested as small perturbations of the quasi-steady trim and altitude. For these reasons, it is felt adequate to consider the steady force and moment equations in determining the average operating conditions of the craft.

The general vertical force equation and longitudinal moment equation governing the trim and altitude of the craft are

4.9

$$\sum_1^m Z_n = - \Delta \quad [4.1]$$

$$\sum_1^m M_n = 0$$

where:

- Z_n is the vertical force due to the n'th component of the system (foil or hull)
- M_n is the moment of the lift and drag forces of the n'th component about the y axis
- Δ is the craft weight
- m is the total number of foil and hull components.

The axis system upon which Equations [4.1] is based is the general one for hydrofoil craft and is shown in Figure 4.1. The origin of the axis system is at the center of gravity of the craft and Equations [4.1] refer to the fixed (x,y,z) coordinate system. Equations [4.1] must be satisfied at every speed for quasi-steady operation to occur.

The vertical forces Z_n are made up of the dynamic lift of each foil system, the dynamic lift of the hull (before takeoff), and the buoyancy of the hull (at low speeds before planing of the hull occurs). The moment M_n is composed of the moments of each of these vertical forces plus the moments arising from thrust and drag forces.

4.10

The most general expression for the vertical force due to a foil, Z_{f_n} , can be written in terms of the foil hydrodynamic coefficients:

$$Z_{f_n} = \frac{1}{2} \rho V_a^2 A_{f_n} \left[C_{L_{d_n}} + C_{L_{\alpha_n}} (\alpha_n + \tau) + C_{L_{\delta_n}} \delta_n \right] \quad [4.2]$$

where

- V_a is the forward speed
- A_f is the submerged area of the foil
- C_{L_d} is the design lift coefficient
- C_{L_α} is the lift-curve slope of the foil
- C_{L_δ} is the flap rate of the foil
- α is the incidence relative to the zero trim angle
- τ is the trim angle
- δ is the flap angle of the foil
- n denotes the n'th component of the foil system.

Equation [4.2] is written in most general terms including both incidence control and flaps, although most foils do not have both. For surface piercing foils, the area A_f will probably be a function of the altitude and trim.

The contribution to the total moment due to the n'th foil component, M_n , can be written

$$M_n = Z_{f_n} X_{f_n} \cos \tau \quad [4.3]$$

where

X_{f_n} is the distance from the center of gravity to the center of pressure of the foil panel in the body axis (X) coordinate system.

Because the trim angle will always be small ($\tau < 10$ degrees), the cos term in Equation [4.3] can be dropped and the moment M_n written

$$M_n = Z_{f_n} X_{f_n} \quad [4.4]$$

The force due to the dynamic lift of the hull, Z_h , can be written

$$Z_h = \frac{1}{2} \rho V_a^2 A_h C_{L_{\alpha_h}} (\tau + \alpha_h) \quad [4.5]$$

where

A_h is the wetted area (not including spray wetted area) of the hull projected on the X-Y plane

$C_{L_{\alpha_h}}$ is the lift curve slope of the hull

4.12

τ is the trim angle

α_h is the average angle of attack of the hull
at zero trim angle.

The corresponding moment due to the hull lift, M_h , is given by

$$M_h = Z_h X_h \quad [4.6]$$

where

X_h is the distance from the center of gravity
to the center of pressure of the hull measured
along the X axis.

The buoyancy force of the hull Z_b is given by

$$Z_b = \rho g \nabla \quad [4.7]$$

where

∇ is the submerged volume of the hull.

The corresponding moment of the buoyancy force about the center
of gravity is

$$M_b = Z_b X_b \quad [4.8]$$

where

X_b is the distance from the center of gravity
to the center of buoyancy of the hull
measured along the X axis.

It should be noted that the force and moment due to buoyancy act only at low speeds where true planing has not yet begun. The final contribution to the moment equation is the drag-thrust couple M_{DT} which will be discussed in a later section.

The most general vertical force and moment equations can now be written by substituting Equations [4.2] to [4.8] into Equations [4.1]. The general force and moment equations for the hydrofoil boat are then given by:

$$\frac{\Delta}{\rho/2V_a^2} = \Delta' = \sum_{n=1}^{n=m} A_{f_n} \left[C_{L_{d_n}} + C_{L_{\alpha_n}} (\alpha_n + \tau) + C_{L_{\delta_n}} \delta_n \right] + A_h C_{L_{\alpha_h}} (\tau + \alpha_h) + 2g\tau \quad [4.9]$$

$$0 = \sum_{n=1}^{n=m} A_{f_n} X_{f_n} \left[C_{L_{d_n}} + C_{L_{\alpha_n}} (\alpha_n + \tau) + C_{L_{\delta_n}} \delta_n \right] + A_h X_h C_{L_{\alpha_h}} (\tau + \alpha_h) + 2gX_b\tau + M_{DT} \quad [4.10]$$

Equations [4.9] and [4.10] represent simultaneous equations which are functions of the independent variables h and τ and the dependent variables Δ , V , δ_n and α_n . In some cases either h or τ may be constrained and become independent variables. In such cases

one of the other variables such as α_n or δ_n becomes a dependent variable. The drag-thrust couple is, in general, a function of all dependent and independent variables. The general procedure here is to eliminate one of the dependent variables between Equations [4.9] and [4.10], allowing a solution for the other dependent variables.

The Drag-Thrust Couple or Moment

The presence of a net couple or moment due to thrust and drag greatly complicates the determination of the trim and altitude of the craft. The magnitude of this moment is dependent on the drag which is, in turn, dependent on the trim and altitude. The solution for trim and altitude thus becomes an iterative process if the drag-thrust couple is considered. It is possible to eliminate or approximate this couple in a number of cases, thus eliminating this nonlinearity.

When a craft with fully submerged foil systems is operating foilborne, most of the drag is due to the foils which generally have the same elevation (relative to the craft coordinate system) as the propeller (thrust axis). The only drag producing a moment in such cases is the strut drag which is, typically, one third of the total drag. If the strut drag is assumed to act at the mid-length of the submerged portion of the strut or about one quarter of the total strut length above the foil, the drag-thrust couple M_{DT} can be written

4.15

$$M_{DT} = \frac{1}{12} D l_s \quad [4.11]$$

where

D is the total foilborne drag

l_s is the total strut length.

If the drag-lift ratio of the craft is assumed to be six, which is a typical conservative value for subcavitating foil systems, and the foil spacing is assumed to be ten times the total strut length, the value of M_{DT} becomes

$$M_{DT} = .0014 L l_f \quad [4.12]$$

where

L is the total foilborne lift

l_f is the longitudinal spacing between forward and aft foil systems.

Equation [4.11] ignores the effect of the air drag on the hull.

For a foil system with 75 percent of the load supported by the main foils, this moment is equivalent to a change in lift of one of the foil systems of 0.75 percent. For a boat with a static margin of 0.05 this would mean a change in lift of 2.8 percent due to additional trim. In both cases, it appears that the effect of drag-thrust couple on trim of a boat with fully submerged foils is small enough to be ignored.

4.16

For a foilborne, surface-piercing system, the foil drag is probably located about half-way between the thrust and the free surface so that the moment M_{DT} is three times the value given by Equation [4.12].

$$M_{DT} = .0042 L t_f \quad [4.13]$$

For a foil system with 75 percent of the load on the main foil, this represents an increase in the lift of the after foil or decrease in lift of the forward foil of 2.25 percent. If the vertical lift distribution of the surface piercing system is assumed proportional to the depth of submergence, this represents a change in submergence of the surface piercing foil of 2.25 percent, an amount which can probably be safely ignored. This would also represent a change in lift due to flaps or incidence of one of the foils of 2.25 percent, a negligible amount. It can thus be concluded that, for foilborne operation, the effect of the drag-thrust couple can be neglected for all normal foil systems.

Prior to takeoff, the contribution of the hull and struts to the drag will greatly increase the magnitude of the drag-thrust couple. It may be possible to make a reasonable approximation of the drag-thrust couple before takeoff, but the effect of this moment should be carefully considered during this period.

SOLUTION OF THE EQUATIONS

While Equations [4.9] and [4.10] apply to the case before takeoff has occurred, the solution of the equations for foilborne operation is obtained by first eliminating all hull terms. The

contributions due to the hull are usually non-linear so the solution cannot be obtained in explicit form. For the foilborne case, however, the equations are linear or can be readily linearized for a number of realistic foil systems. For this reason, solutions of Equations [4.9] and [4.10] for hullborne and foilborne cases are considered separately.

In finding the solutions presented here, certain assumptions have been made. These assumptions are all reasonable for the foil systems considered and introduce little or no approximation to the solutions. The assumptions are:

1. All foils are located at one of two longitudinal positions, these representing the center of the pressure of the foil system. This is true of almost all present designs such as the DENNISON, PCH and AGEH, and excludes only those systems with special auxiliary foils or hydroskis.

2. For foilborne operation, the performance of all foils lies within the linear range and can be characterized by a linear lift curve slope as in Equation [4.2]. Before takeoff, the foil lift coefficients may reach values where non-linear effects are important and should be considered. If non-linear effects appear to be important after takeoff, an accurate approximation of the non-linear effect can be made.

3. The change of the center of pressure of the foil system is small. For foilborne operation, the changes of location of center of pressure are probably negligible. Here again, the change in center of pressure can be estimated without introducing an unnecessary non-linearity into the equations.

Methods of Solution

There are several approaches open for solving the basic Equations [4.9] and [4.10] for the trim and altitude of the craft. These can be divided into those where the equations are linear or can be readily linearized and those where the equations are inherently non-linear.

In the first case, the equations can be solved by eliminating one of the dependent variables between Equations [4.9] and [4.10]. Several types of non-linearities occur which can be readily circumvented in determining such explicit solutions. The first is the change in center of pressure due to change in foil angle of attack or flap angle. A second is the non-linearity of foil lift. Explicit solutions can be obtained by assuming that the center of pressure is fixed and by using linear foil lift relationships as in Equation [4.2].

The shift in center of pressure, while it may be appreciable in terms of the foil chord, is generally small compared with the distance to the center of gravity. In such a case, an accurate solution can be obtained by using the exact center of pressure occurring at the last calculated point. This method is acceptable as long as reasonably small increments of velocity, and thus changes in center of pressure, are considered.

In cases where the foil lift coefficient is near the essentially linear range (say C_L less than 0.80) it is probably safe to ignore non-linear effects altogether. For larger lift coefficients, the non-linear effects can be approximated quite accurately

by using the magnitude of the non-linear effect at the previous point, or

$$C_L = C_{L_\alpha} K_{NL} \alpha \quad [4.14]$$

where

C_{L_α} is the linear lift-curve slope

α is the total equivalent angle of attack

K_{NL} is the non-linear correction.

The non-linear correction, as noted, can be determined from the non-linear and linear lift coefficient at the previous speed

$$\left(K_{NL} \right)_{V + \Delta V} = \left(\frac{C_{L_{NL}}}{C_{L_L}} \right)_V \quad [4.15]$$

where the subscripts V and $V + \Delta V$ denote the previous speed and the present speed. As with the shift in center of pressure, this method should be adequate if the increment in velocity ΔV is not too large. While the actual calculations will indicate acceptable values of ΔV , a value of one-tenth or less of the final velocity is probably acceptable.

For highly non-linear cases, such as exist before takeoff, this approach is probably unacceptable. Here some type of numerical solution of the simultaneous equations is indicated.

TRIM AND ALTITUDE AFTER TAKEOFF

The more tractable case of foilborne operation will be considered first. If the drag-thrust couple is assumed negligible, a number of explicit solutions can be obtained for practical foil configurations. Both fully submerged foil systems and surface piercing foil systems (surface piercing foils forward or aft only) lead to a number of explicit solutions. In cases where non-linearities exist, the expressions for lift can be multiplied by the appropriate factor K_{NL} discussed in the previous section to account for these non-linearities. The fully submerged foil systems can have either incidence control or flaps. Solutions for foils with both can also be obtained but these are felt to be unrealistic.

Fully Submerged Foils with Flaps and/or Incidence Control Forward and Aft.

This type of foil system is probably the most practical type for higher speed hydrofoil systems (see Chapter 3). All important Navy hydrofoil boats, including the PCH and AGEH (both with subcavitating foils) and the Navy Test Craft FRESH-1 (with supercavitating or ventilated foils), are of this type. For this type of foil system Equations [4.9] and [4.10] can be rewritten

$$\frac{\Delta}{\rho/2V^2} = A_F \left(C_{L_{\alpha_F}} (\alpha_F + \tau) + C_{L_{\delta_F}} \delta_F + C_{L_{d_F}} \right) + A_A \left(C_{L_{\alpha_A}} (\alpha_A + \tau) + C_{L_{\delta_A}} \delta_A + C_{L_{d_A}} \right) \quad [4.16]$$

$$0 = A_F X_f \left(C_{L_{\alpha_F}} (\alpha_F + \tau) + C_{L_{\delta_F}} \delta_F + C_{L_{d_F}} \right) + A_A X_A \left(C_{L_{\alpha_A}} (\alpha_A + \tau) + C_{L_{\delta_A}} \delta_A + C_{L_{d_A}} \right). \quad [4.17]$$

where the subscripts F and A refer to the forward and aft foil systems and the areas A_F and A_A refer to the total area if there are more than one forward or aft foils as in the case of the PCH and AGEH (two forward foils and one aft foil).

For most cases the foil submergence will be greater than one chord and the effect of depth on the lift curve slopes and flap rates $C_{L_{\alpha}}$ and $C_{L_{\delta}}$ can be ignored. Equations [4.16] and [4.17] thus become independent of the altitude h and a function only of the trim angle τ and foil incidence or flap angle α or δ .

These equations can be solved explicitly for a number of cases of interest. For these solutions it is assumed that there are either flaps or incidence forward and aft but not both. The cases considered here are: Angle of trim held fixed, solving for (a) aft incidence, (b) forward incidence, (c) aft flap angle, (d) forward flap angle; aft incidence held fixed solving for (e) forward flap angle or (f) trim angle; aft flap angle held fixed solving for (g) forward flap angle or (h) trim angle; forward incidence held fixed solving for (j) aft incidence or (k) trim

angle and; forward flap angle held fixed solving for (l) aft flap angle or (m) trim angle.

a., b., c. and d. Angle of trim held fixed or known

$$a. \quad \delta_A = \Delta' \left[\frac{X_F}{A_A C_{L\delta_A} (X_F - X_A)} \right] - \frac{C_{Ld_A}}{C_{L\delta_A}} - \frac{C_{L\alpha_A}}{C_{L\delta_A}} \tau \quad [4.18a]$$

$$b. \quad \delta_F = \Delta' \left[\frac{X_A}{A_F C_{L\delta_F} (X_A - X_F)} \right] - \frac{C_{Ld_F}}{C_{L\delta_F}} - \frac{C_{L\alpha_F}}{C_{L\delta_F}} \tau \quad [4.18b]$$

$$c. \quad \alpha_A = \Delta' \left[\frac{X_F}{A_A C_{L\alpha_A} (X_F - X_A)} \right] - \frac{C_{Ld_A}}{C_{L\alpha_A}} - \tau \quad [4.18c]$$

$$d. \quad \alpha_F = \Delta' \left[\frac{X_A}{A_F C_{L\alpha_F} (X_A - X_F)} \right] - \frac{C_{Ld_F}}{C_{L\alpha_F}} - \tau \quad [4.18d]$$

e. f. Aft incidence fixed

$$e. \quad \tau = \Delta' \left[\frac{X_F}{A_A C_{L\alpha_A} (X_F - X_A)} \right] - \frac{C_{Ld_A}}{C_{L\alpha_A}} - \alpha_A \quad [4.18e]$$

$$f. \quad \alpha_F = \Delta' \left[\frac{C_{L\alpha_A} A_A X_A + C_{L\alpha_F} A_F X_F}{C_{L\alpha_A} C_{L\alpha_F} A_F A_A (X_A - X_F)} \right] + \frac{(C_{L\alpha_F} C_{Ld_A} - C_{L\alpha_A} C_{Ld_F})}{C_{L\alpha_A} C_{L\alpha_F}} + \alpha_A \quad [4.18f]$$

g. h. Aft flap angle fixed

$$g. \quad \tau = \Delta' \left[\frac{X_F}{A_A C_{L\alpha_A} (X_F - X_A)} \right] \frac{C_{Ld_A}}{C_{L\alpha_A}} - \frac{C_{L\delta_A}}{C_{L\alpha_A}} \delta_A \quad [4.18g]$$

$$h. \quad \delta_F = \Delta' \left[\frac{C_{L\alpha_A} A_A X_A + C_{L\alpha_F} A_F X_F}{C_{L\alpha_A} C_{L\delta_F} A_F A_A (X_A - X_F)} \right] + \frac{(C_{L\alpha_F} C_{Ld_A} - C_{L\alpha_A} C_{Ld_F})}{C_{L\alpha_A} C_{L\delta_F}} + \frac{C_{L\alpha_F} C_{L\delta_A}}{C_{L\alpha_A} C_{L\delta_F}} \delta_A \quad [4.18h]$$

j.k. Forward incidence fixed

$$j. \quad \tau = \Delta' \left[\frac{X_A}{A_F C_{L\alpha_F} (X_A - X_F)} \right] - \frac{C_{Ld_F}}{C_{L\alpha_F}} - \alpha_F \quad [4.18j]$$

$$k. \quad \alpha_A = \Delta' \left[\frac{C_{L\alpha_A} A_A X_A + C_{L\alpha_F} A_F X_F}{C_{L\alpha_F} C_{L\alpha_A} A_A A_F (X_F - X_A)} \right] - \frac{(C_{L\alpha_F} C_{Ld_A} - C_{L\alpha_A} C_{Ld_F})}{C_{L\alpha_F} C_{L\alpha_A}} + \alpha_F \quad [4.18k]$$

l. m. Forward flap angle fixed

$$l. \quad \tau = \Delta' \left[\frac{X_A}{A_F C_{L\delta_F} (X_A - X_F)} \right] - \frac{C_{Ld_F}}{C_{L\delta_F}} - \frac{C_{L\delta_F}}{C_{L\alpha_F}} \delta_F \quad [4.18l]$$

$$m. \quad \delta_A = \Delta' \left[\frac{C_{L\alpha_A} A_A X_A + C_{L\alpha_F} A_F X_F}{C_{L\alpha_F} C_{L\delta_A} A_A A_F (X_F - X_A)} \right] - \frac{(C_{L\alpha_F} C_{Ld_A} - C_{L\alpha_A} C_{Ld_F})}{C_{L\alpha_F} C_{L\delta_A}} + \frac{C_{L\alpha_A} C_{L\delta_F}}{C_{L\alpha_F} C_{L\delta_A}} \delta_F \quad [4.18m]$$

Surface Piercing Foils Forward and Fully Submerged Foils Aft

Next to the fully submerged foil system this type is probably the most popular type of foil system. The H.S. DENNISON is of this type. For this type of foil system Equations [4.9] and [4.10] can be rewritten

$$\begin{aligned} \Delta' = & A_S \left(C_{L_{\alpha_S}} \tau + C_{L_{d_S}} \right) \\ & + A_F \left(C_{L_{\alpha_F}} (\alpha_F + \tau) + C_{L_{\delta_F}} \delta_F + C_{L_{d_F}} \right) \\ & + A_A \left(C_{L_{\alpha_A}} (\alpha_A + \tau) + C_{L_{\delta_A}} \delta_A + C_{L_{d_A}} \right) \end{aligned} \quad [4.19]$$

$$\begin{aligned} 0 = & A_S X_S \left(C_{L_{\alpha_S}} \tau + C_{L_{d_S}} \right) + A_F X_F \left(C_{L_{\alpha_F}} (\alpha_F + \tau) + C_{L_{\delta_F}} \delta_F + C_{L_{d_F}} \right) \\ & + A_A X_A \left(C_{L_{\alpha_A}} (\alpha_A + \tau) + C_{L_{\delta_A}} \delta_A + C_{L_{d_A}} \right) \end{aligned} \quad [4.20]$$

where the subscript s denotes the forward surface piercing foil or foils.

As in the case of the fully submerged foil system, the lift and moment of the forward and aft fully submerged foils are assumed to be independent of depth. It is assumed that there are no flaps or incidence control on the surface piercing foils, although

there may be fully submerged panels forward with either flaps or incidence control. The DENNISON has fully submerged panels with flaps.

While as many solutions can be obtained here as for the case of all fully submerged foils, only a few are given. These are felt to be the more realistic cases. Solutions for less general cases, such as those with no fully submerged foils forward, can be readily obtained by elimination of the appropriate terms in Equations [4.21]. The cases for which solutions are given are: flaps on forward and aft submerged foils fixed solving for (a) trim angle and (b) depth of submergence; forward and aft submerged foil incidence fixed solving for (c) trim angle; trim angle and forward submerged flap angle fixed solving for (d) after the flap angle or (e) depth of submergence. All of these solutions are based on the slight simplification that X_S and X_F are equal, but solutions can be readily obtained when $X_S \neq X_F$.

a. b. Forward and aft flap angles fixed

$$a. \quad \tau = \Delta' \left[\frac{X_F}{A_A C_{L\alpha_A} (X_F - X_A)} \right] - \frac{(C_{L\delta_A} \delta_A + C_{Ld_A})}{C_{L\alpha_A}} \quad [4.21a]$$

$$b. \quad A_S C_{Ld_S} - A_S C_{L\alpha_S} \left[C_{Ld_A} + C_{L\delta_A} \delta_A - \Delta' \left[\frac{X_F}{A_A (X_F - X_A)} \right] \right]$$

$$= f(a_1 h + a_2) = - \Delta' \left[\frac{C_{L\alpha_A} A_A X_A + C_{L\alpha_F} A_F X_F}{(X_F - X_A) A_A} \right]$$

$$+ A_F \left[C_{L\alpha_F} (C_{Ld_A} + C_{L\delta_A} \delta_A) - C_{L\alpha_A} (C_{Ld_F} + C_{L\delta_F} \delta_F) \right] \quad [4.21b]$$

c. Forward and aft foil incidence fixed

$$\tau = \Delta' \left[\frac{X_F}{A_A C_{L\alpha_A} (X_F - X_A)} \right] - \frac{C_{Ld_A}}{C_{L\alpha_A}} - \alpha_A \quad [4.21c]$$

d. e. Trim angle and forward flap angle fixed

$$d. \quad \delta_A = \Delta' \left[\frac{X_F}{A_A C_{L_{\delta_A}} (X_F - X_A)} \right] - \frac{C_{L_{d_A}}}{C_{L_{\delta_A}}} - \frac{C_{L_{\alpha_A}}}{C_{L_{\delta_A}}} \tau \quad [4.21d]$$

$$e. \quad A_S C_{L_{d_S}} + A_S C_{L_{\alpha_S}} \tau = f(a_1 h + a_2)$$

$$= \Delta' \left(\frac{X_A}{X_A + X_F} \right) - A_F \left(C_{L_{\alpha_F}} \tau + C_{L_{\delta_F}} \delta_F + C_{L_{d_F}} \right) \quad [4.21e]$$

It can be seen that the right hand sides of Equations [4.21b] and [4.21e] are equated to the term $f(a_1 h + a_2)$. This denotes that the right hand sides of the equation, while apparently non-linear, may in fact be linear functions of the depth. This result is discussed in detail in the section on hydrodynamic coefficients.

Solutions of the Equations Before Takeoff

The solution of the equations are greatly complicated by the addition of the hull terms. For the case of a boat with only fully submerged foils, the non-linearities introduced by the hull are those due to hull buoyancy, hull center of buoyancy and drag-thrust couple. As these terms, particularly the hull buoyancy

and drag-thrust couple, decrease rapidly as takeoff speed is approached, it is possible to make simplifying approximations for these terms. These approximations allow the determination of solutions for the case where all foils are submerged.

For the fully submerged foil system, foil lift forces are assumed to be linear functions of the trim angle and to be independent of the foil submergence. Thus, only the hull terms are functions of the submergence and these can be eliminated to determine solutions.

As the craft velocity approaches takeoff velocity, the buoyancy terms and the drag-thrust couple become negligible and Equations [4.9] and [4.10] can be considerably simplified. For this condition, Equations [4.9] and [4.10] can be written in the form

$$\Delta' = A_F(f) + A_A(a) + H(k_1 + s)\tau \quad [4.22]$$

$$0 = A_F X_F(f) + A_A X_A(a) + H(k_1 + s)[m\tau + k_2 + s] \quad [4.23]$$

where

$$f = C_{L\alpha_F}(\tau + \alpha_F) + C_{Ld_F} \quad \text{or} \quad C_{L\alpha_F}\tau + C_{L\delta_F}\delta_F + C_{Ld_F}$$

$$a = C_{L\alpha_A}(\tau + \alpha_A) + C_{Ld_A} \quad \text{or} \quad C_{L\alpha_A}\tau + C_{L\delta_A}\delta_A + C_{Ld_A}$$

H and k_1 are constants defined by Equation [4.42]

k_2 is a constant defined by Equations [4.45] and [4.46]

m is the distance from the transom to the center of gravity of the craft (negative) and $X_h = m + l_{cp}$.

The abbreviated notation of Equations [4.22] and [4.23] is introduced in order to make the solution more manageable. Equations [4.22] and [4.23] can be solved simultaneously for either the trim angle or the transom submergence. If the value of l_{cp}/l_M is assumed to be constant (such as .775) the solution will be a cubic in either τ or s . As the solution for τ is less complex, this form is presented here:

$$\begin{aligned}
 & \tau^3 \left[(X_F - m) A_F C_{L\alpha_F} + (X_A - m) A_A C_{L\alpha_A} \right] \\
 & + \tau^2 \left\{ A_F (X_F - m) (f') + A_A (X_A - m) (a') + A_F^2 C_{L\alpha_F}^2 + A_A^2 C_{L\alpha_A}^2 \right. \\
 & \quad \left. + 2A_A A_F C_{L\alpha_A} C_{L\alpha_F} \right\} \\
 & + \tau \left\{ k_2 - [k_1 + 2(\Delta' + A_F (f') + A_A (a'))] \left(A_F C_{L\alpha_F} + A_A C_{L\alpha_A} \right) \right\} \\
 & + \Delta'^2 + \Delta' [2A_F (f') + 2A_A (a') - k_1] + k_1 [A_F (f') + A_A (a')] \\
 & + A_F^2 (f')^2 + A_A (a')^2 + 2A_F A_A (f')(a') = 0 \quad [4.24]
 \end{aligned}$$

H and k_1 are constants defined by Equation [4.42]

k_2 is a constant defined by Equations [4.45] and [4.46]

m is the distance from the transom to the center of gravity of the craft (negative) and $X_h = m + l_{cp}$.

The abbreviated notation of Equations [4.22] and [4.23] is introduced in order to make the solution more manageable. Equations [4.22] and [4.23] can be solved simultaneously for either the trim angle or the transom submergence. If the value of l_{cp}/l_M is assumed to be constant (such as .775) the solution will be a cubic in either τ or s. As the solution for τ is less complex, this form is presented here:

$$\begin{aligned}
 & \tau^3 \left[(X_F - m)A_F C_{L\alpha_F} + (X_A - m)A_A C_{L\alpha_A} \right] \\
 & + \tau^2 \left\{ A_F(X_F - m)(f') + A_A(X_A - m)(a') + A_F^2 C_{L\alpha_F}^2 + A_A^2 C_{L\alpha_A}^2 \right. \\
 & \quad \left. + 2A_A A_F C_{L\alpha_A} C_{L\alpha_F} \right\} \\
 & + \tau \left\{ k_2 - [k_1 + 2(\Delta' + A_F(f') + A_A(a'))] \left(A_F C_{L\alpha_F} + A_A C_{L\alpha_A} \right) \right\} \\
 & + \Delta'^2 + \Delta' [2A_F(f') + 2A_A(a') - k_1] + k_1 [A_F(f') + A_A(a')] \\
 & + A_F^2 (f')^2 + A_A^2 (a')^2 + 2A_F A_A (f')(a') = 0 \qquad [4.24]
 \end{aligned}$$

where

$$(f') = C_{L\alpha_F} \alpha_F + C_{Ld_F} \quad \text{or} \quad C_{L\delta_F} \delta_F + C_{Ld_F}$$

$$(a') = C_{L\alpha_A} \alpha_A + C_{Ld_A} \quad \text{or} \quad C_{L\delta_A} \delta_A + C_{Ld_A}$$

While the form of Equation [4.24] is very complex, the only terms that change with speed are Δ' , X_F and X_A and only the first changes significantly. Thus, once a solution is obtained for one forward velocity, the solutions for other velocities will be greatly simplified. As Equation [4.24] is a cubic, there will be three solutions. It is probable that two of these solutions will be imaginary, leaving only one real solution. If all solutions are real, the positive solution is the correct one, as the trim angle always increases from zero as the craft gains speed. It is probable that Equation [4.24] holds for velocities down to at least 70 percent of the takeoff velocity.

For lower velocities, where buoyancy terms predominate, other approximations must be employed. For relatively low speeds, say less than half the takeoff velocity, the hull lift terms are probably quite small?. As the distance between the center of hull pressure and craft center of gravity is also small, the hull lift moment M can be eliminated from Equation [4.10]. Because of the small magnitude of the hull lift force, the effect of submergence, s , on hull lift can probably be estimated from the value of submergence at the previous speed, thus eliminating the dependence

4.32

of hull lift on submergence. As the change of center of buoyance is rather slow with submergence, the location of center of buoyancy X_{cb} can also be estimated from the previous speed. Making use of the assumptions, Equations [4.9] and [4.10] take the form

$$\Delta' = A_F(f) + A_A(a) + H\tau + Bs^3/\tau \quad [4.25]$$

$$0 = A_F X_F(f) + A_A X_A(a) + Bk_3 s^3/\tau \quad [4.26]$$

where

(f) and (a) are as defined before

H is determined from Equation [4.42] estimating s from the previous velocity

B and k_3 are determined from Equations [4.48] and [4.50] estimating s from the value at the previous velocity.

As Equations [4.25] and [4.26] are functions of s only in the last terms, the equations can be readily solved for τ :

$$\tau = \frac{(k_3 - X_F)A_F(f') + (k_3 - X_A)A_A(a')}{A_F C_{L\alpha_F} (X_F - k_3) + A_A C_{L\alpha_A} (X_A - k_3) - Hk_3} \quad [4.27]$$

where

$$(f') = C_{L\alpha_F} \alpha_F + C_{Ld_F} \quad \text{or} \quad C_{L\delta_F} \delta_F + C_{Ld_F}$$

$$(a') = C_{L\alpha_A} \alpha_A + C_{Ld_A} \quad \text{or} \quad C_{L\delta_A} \delta_A + C_{Ld_A}$$

It should be noted that Equation [4.27] is more approximate than any of the other solutions presented in this chapter, and its use should not be extended to velocities greater than about one half takeoff velocity without careful consideration. In both Equations [4.24] and [4.27] it is assumed that flap angles or foil incidences are known.

There is probably a region, extending at least from fifty to seventy percent of the takeoff velocity, in which neither Equation [4.24] nor [4.27] is of acceptable accuracy. The best means of avoiding this difficulty is probably to use these equations to calculate the trim angles and submergences for velocities above and below this range and to interpolate the values in this range ($.5 V_{T_0} \lesssim V \lesssim .7 V_{T_0}$). Generally the trim angle is not changing appreciably within this range so that it may be possible to solve either Equation [4.8] or [4.9] for the submergence s using an interpolated trim angle.

HYDRODYNAMIC COEFFICIENTS

In order to evaluate, numerically, the solutions presented in the last section, it is necessary to express the foil and hull hydrodynamic coefficients in terms of the known geometry. The one basic assumption made in evaluating these hydrodynamic coefficients is that all coefficients are steady or independent of time. The results presented by Martin (4.1) indicate that unsteady effects should be negligible for the slow accelerations associated with takeoff and acceleration of a hydrofoil craft.

Foil Hydrodynamic Coefficients

The lift curve slope, C_{L_α} , for an untapered and unswept foil can be obtained from Equation [47a] of Reference 4.1. If only the linear term is considered,

$$C_{L_\alpha} = \frac{a_0 K_2 K_3 AR}{1 + AR + 2K_2} \quad [4.28]$$

where

K_2 and K_3 are depth correction factors given in Figures 12 and 13 of (4.1)

AR is the foil aspect ratio

A_0 is the two-dimensional lift curve slope including viscous effects (2π for very thin sections).

For foils with taper and/or sweep, the less exact expression, given by Equation [49a] of (4.1) can be used:

$$C_{L_\alpha} = \frac{K_0 a_0 \cos \Gamma}{1 + \frac{K_0 a_0}{\pi AR} K_d (1 + \lambda_0)(1 + \tau_0)} \quad [4.29]$$

where

K_0 is the two-dimensional biplane correction given by Figure 14 of (4.1)

K_d is the three-dimensional biplane correction given by Figure 16 of (4.1)

- τ_o is the planform correction given by Figure 17
of (4.1)
- λ_o is the sweep correction given by Figure 15
of (4.1)
- Γ is the dihedral angle.

In both Equations [4.28] and [4.29], depth effects are important only for shallow depths and the factors K_2 , K_3 , K_o and K_d become essentially one for depth-chord ratios (h/c) of two or greater. As most fully submerged foils are designed to operate at such depths ($h/c \geq 2$), the lift curve slopes can usually be assumed to be independent of depth for fully submerged foils. This is especially true before takeoff, when foil submergence is almost twice the design foilborne value. The aspect ratio of fully submerged foils is, of course, independent of depth.

The flap rate, $C_{L\delta}$, can be obtained from Equation [77] of Martin (4.1) by noting that, for the range of flap angles δ and hinge line sweep angles Λ_h of interest,

$$\delta' = \tan^{-1}(\tan \delta \cos \Lambda_h) = \delta \cos \Lambda_h. \quad [4.30]$$

Making use of Equation [4.30], the flap rate becomes

$$C_{L\delta} = C_{L\alpha} (\alpha_\delta)_c K_c K_b \cos \Lambda_h \quad [4.31]$$

where

- $C_{L\alpha}$ is the lift curve slope given by Equation [4.28] or [4.29]
- $(\alpha_{\delta})_{c\lambda}$ is the flap effectiveness parameter given by Figure 39 of (4.1)
- K_b is the flap-span factor given by Figure 40 of (4.1)
- K_c is the flap-chord factor given by Figure 35 of (4.1)
- Λ_h is the hinge line sweep angle

As noted by Martin (4.1), the flap rate $C_{L\delta}$ is dependent on depth only through the term $C_{L\alpha}$. Thus, $C_{L\delta}$ is probably independent of depth for most fully submerged foils.

The sweep angle of the hinge line Λ_h can be expressed in terms of the quarter-chord sweep angle Λ and the foil geometry by

$$\Lambda_h = \Lambda - \tan^{-1} \left[\frac{4(\lambda - 1)(.75 - f/c)}{AR(\lambda + 1)} \right] \quad [4.32]$$

where

- λ is the foil taper ratio
- f/c is the flap-chord ratio.

The chordwise location of the center of pressure of the foil is determined by the relative contributions to lift of camber, incidence and flap angle. The center of pressure due to camber

(the design lift coefficient of the foil) is given by the Airfoil Summary (4.2). The center of pressure due to angle of attack is usually taken as the quarter-chord line. Experimental results presented in (4.2) indicate that the quarter-chord line is very good until stall occurs (usually at $C_L > 1.0$). As stall is avoided in all normal foil operation, the quarter-chord line can be use for all cases. Thus, for foils without flaps, the center of pressure is given by

$$p = \frac{(X_c - .25)}{1 + \frac{(C_L)_\alpha}{C_{L_d}}} \quad [4.33]$$

where

- p is the percent of chord of the center of pressure aft of the foil quarter-chord line
- X_c is the location of the center of pressure due to camber in percent of chord aft of the leading edge
- $(C_L)_\alpha$ is the lift coefficient due to incidence (not C_{L_α})
- C_{L_d} is the design lift coefficient or lift coefficient due to camber.

Expressions for the center of pressure of lift due to flaps are not generally given in the literature. The center of pressure can, however, be deduced from the flap hinge moment. For this purpose, the results of Dods as presented in Equation [92] of

Martin (4.1) are suggested. For the range of interest this equation can be greatly simplified, yielding for the flap moment coefficient $C_{h\delta}$

$$C_{h\delta} = \left(C_{h\delta} \right)_{\Lambda=0} \cos \Lambda \cos \Lambda_h \quad [4.34]$$

where

$\left(C_{h\delta} \right)_{\Lambda=0}$ is the hinge moment coefficient for unswept wings given by Figure 45 of (4.1)

Λ is the quarter-chord sweep angle

Λ_h is the hinge line sweep angle given by Equation [4.32].

Making use of the definitions of $C_{h\delta}$ and $C_{L\delta}$ given in (4.1) the location of the center of pressure due to flap lift can be readily shown to be

$$X_{f_q} = \left(.75 - \frac{f}{c} \right) + \left(\frac{C_{h\delta}}{C_{L\delta}} \right) \left(\frac{f}{c} \right)^2 \quad [4.35]$$

where

X_{f_q} is the distance of the center of pressure due to flap lift from the quarter-chord line in percent of chord

$\frac{f}{c}$ is the flap-chord ratio.

4.39

For foils with flaps, the chordwise location of the center of pressure p in percent of chord is given by

$$p = \frac{(X_c - .25) + \frac{(C_L)_\delta}{C_{L_d}} X_{f_q}}{1 + \frac{(C_L)_\alpha}{C_{L_d}} + \frac{(C_L)_\delta}{C_{L_d}}} \quad [4.36]$$

The value of p is given by either Equations [4.33] or [4.36] depending on whether the foil has flaps which are producing lift or not.

The expressions for p given by Equations [4.33] and [4.36] introduce non-linearities into the solutions because of the dependence on the lift terms $(C_L)_\alpha$ and $(C_L)_\delta$. For the case of a foil without flaps (Equation [4.33]), the maximum possible value of p is, for practical camber types, about .25. If an average value of p of say .15 is used, the maximum probable error is about one-tenth of the chord. While this is large compared to the chord, it may be quite small compared with the distance of the foil center of pressure from the craft center of gravity. For foils with operating flaps, it is probably not possible to find an acceptable average value of p . One means of avoiding this problem is outlined in the previous section. Basically, it consists of estimating p from the value calculated at the previous speed.

For a swept and tapered foil, the location of the center of pressure behind the quarter-chord point at the foil root $X_{\frac{c}{4}r}$ is given by

$$X_{\frac{c}{4}r} = \frac{S}{6(\lambda + 1)} \left[(2\lambda + 1) \tan \Lambda + \frac{4p(\lambda^2 + 4\lambda + 1)}{AR(\lambda + 1)} \right] \quad [4.37]$$

where

S is the foil span

Λ is the quarter-chord sweep angle

λ is the foil taper ratio.

Using Equations [4.32] or [4.36] and [4.37], the distance of the foil center of pressure from the craft center of gravity X_{fn} can be determined.

Surface Piercing Foil Characteristics

In the case of surface piercing foils, the foil aspect ratio, foil area and depth correction factors in Equations [4.28] and [4.29] are functions of the foil submergence or craft altitude. It would thus appear that the term Z_{fn} of Equation [4.2] is highly non-linear with altitude for surface piercing foils.

The foil area, aspect ratio and average depth of submergence can be defined in terms of the submergence z_s of the foil. The foil area A_s can be expressed as

$$A_s = \frac{c_r z_s \left[2 - \left(1 - \frac{1}{\lambda} \right) \frac{z_s}{d} \right]}{2 \tan \Gamma} \quad [4.38]$$

where

c_r is the chord at the lower end or root of the foil

z_s is the depth of submergence of the lower end of the foil

d is the total vertical depth of the foil from root to tip

Γ is the dihedral angle

λ is the taper ratio of the foil.

Equation [4.38] is based on the assumption that the foil chord tapers linearly from the root to the tip. The area is the area projected on the X-Z plane.

The foil aspect ratio AR_s is given by

$$AR_s = \frac{2 z_s}{c_r \left[2 - \left(1 - \frac{1}{\lambda} \right) \frac{z_s}{d} \right] \frac{z_s}{d} \sin \Gamma} \quad [4.39]$$

The effective depth-chord ratio should be based on the depth of submergence at the foil center of pressure. Because of the foil taper, and the loss of lift at the free surface, the center of pressure probably lies about 40 percent of the span from the root to the free surface. Based on this assumption, the effective

4.42

depth-chord ratio h/c of the foil is

$$\frac{h}{c} = \frac{.6 z_s}{c_r \left[1 - .4 \left(1 - \frac{1}{\lambda} \right) \frac{z_s}{d} \right]} \quad [4.40]$$

Because of the rather weak dependence of the lift curve slope on depth-chord ratio, the error resulting from the assumption of a center of pressure is probably very small.

It can be readily seen from Equations [4.38] through [4.40] that the forces and moments due to surface piercing foils will be highly non-linear with depth of submergence z_s . It may be possible, however, to adequately represent the total lift force of the surface piercing foil by a linear expression such as

$$Z_s = C_{L_{\alpha_s}} A_s \tau = (a_1 + a_2 z_s) \tau \quad [4.41]$$

where

a_1 and a_2 are constants depending on the foil system geometry.

If such a relationship holds for the range of submergences of interest, explicit solution of Equations [4.19] and [4.20] can be readily obtained as indicated by Equations [4.21]. Calculation of the term $C_{L_{\alpha_s}} A_s$ for a typical tapered surface piercing foil have been carried out using Equations [4.29] and [4.38] - [4.40]. The assumed characteristics of this typical foil are

4.43

Taper ratio $\lambda = 2.0$ Dihedral angle = $\sin^{-1} .60 = 36.8^\circ$ Total foil depth = c_r .

The calculated results are presented in Figure 4.3. This figure indicates that an expression of the form of Equation [4.41] will give excellent results within the probable range of operating depths ($0.5 \leq z_s/d \leq 1.0$). The maximum error using such an expression for $C_{L_{\alpha_s}} A_s$ would be about five percent. Once a surface piercing foil has been chosen, a calculation of this type can be carried out to see if an expression of the type given by Equation [4.41] can be used in calculation of trim and altitude.

Hull Hydrodynamic Forces

The forces and moments due to the hull before takeoff can be divided into those due to hydrodynamic forces (lift) and hydrostatic (buoyancy) forces. The forces and moments due to hull lift force will be considered first.

The actual hull form is likely to be of a complex nature, with twist, keel rock, varying beam and curved chines. The analysis of the lift force on such a hull form is greatly complicated by the non-linearities resulting from these characteristics. It is possible in many cases, however, to adequately represent the hull by a simplified prismatic form. Figure 4.4 shows such an idealized hull form based on the following assumptions:

(a) The beam of the submerged portion of the hull is constant.

(b) The keel line of the submerged portion of the hull is straight (no rocker).

(c) The chine line is parallel to the keel line (zero angle of twist) for the submerged portion.

(d) The bottom of the hull is a straight vee (no concavity or convexity).

In general, the preceding assumptions will be quite good for the after 50 percent of the hull length. For the range of speeds of greatest interest (the planing regime), it is probable that only the after portion of the hull will be submerged, so that the errors introduced by the preceding assumptions should be small. If the actual hull varies seriously from these assumptions, say in large variation of beam or large twist, average values as shown in Figure 4.5 can be used. While the large changes in beam of the H. S. DENNISON (4.3) probably make such an idealization of questionable value, the hull of the PCH would appear to fit these assumptions adequately. The designer must decide if the hull in question can be so represented in order to allow use of the greatly simplified results presented here.

The wetted area and the aspect ratio of the hull can be defined in terms of the parameters of the idealized hull form. The projection of the wetted area on the X-Y plane, A_h , is given by

4.45

$$A_h = \frac{(2s - b \tan \beta)b}{\tan \tau} \approx \frac{(2s - b \tan \beta)b}{\tau} \quad [4.42]$$

where

s is the depth of submergence of the keel at the transom

b is the half-beam

τ is the trim angle of the keel with respect to the x-y plane

β is the hull deadrise angle.

The aspect ratio of the hull AR_h is given by

$$AR_h = \frac{4 b \tau}{(2s - b \tan \beta)} \quad [4.43]$$

In both Equations [4.42] and [4.43] the tangent of the trim angle is replaced by the trim angle. For the trim angle range of interest ($0 \leq \tau \leq 5^\circ$) this introduces a negligible error.

The lift coefficients for prismatic planing surfaces or planing hulls of the type considered here have been determined by investigators at NACA and DTMB for a number of deadrise angles (4.4), (4.5) and (4.6). Results of these tests have been used by Shuford (4.7) to determine expressions for the lift coefficient and center of pressure of such planing surfaces. The expression for the hull lift curve slope can be obtained from these

4.46

results and is given by

$$C_{L_{\alpha_h}} = \frac{.5\pi AR_h}{1 + AR_h} (1 - \sin \beta)\tau + \frac{4}{3} \cos \beta \tau^2. \quad [4.44]$$

The expression $(AR_h/1 + AR_h)$ complicates the solution because it is a non-linear function of the submergence and trim angle. For small values of AR such as considered here ($0.2 \leq AR \leq 0.5$) the following approximation can be introduced

$$\frac{AR_h}{1 + AR_h} \approx \frac{AR_h}{1.35} \quad [4.45]$$

The introduction of this approximation into Equation [4.44] greatly reduces non-linearity and results in a maximum possible error of eleven percent in the lift force. Although this would appear to be a sizable error, the decreasing importance of hull lift as takeoff is approached makes it less serious. Making use of such an approximation, Equation [4.44] can be rewritten

$$C_{L_{\alpha_h}} = 1.26 AR_h \tau (1 - \sin \beta) + \frac{4}{3} \cos \beta \tau^2. \quad [4.46]$$

It can now be shown that the total hull lift force is a linear function of the craft trim angle τ and a linear function of the keel depth of submergence s . Substituting the expression for AR_h from [4.43] into [4.46] and multiplying by the hull area from Equation [4.42], we have

4.47

$$L_h = C_{L\alpha_h} A_h \tau = [5.04b^2 (1 - \sin \beta) + 1.33b(2s - b \tan \beta) \cos \beta] \tau. \quad [4.47]$$

While Equation [4.47] involves the approximation of Equation [4.45], it greatly simplifies solution of the hullborne equations by making the hull lift force a linear function of the submergence s and trim angle τ .

The center of dynamic lift or pressure for a planing surface is given by (4.7) as:

$$\frac{l_{cp}}{l_M} = \frac{\frac{.437\pi AR_h \tau}{1 + AR_h} (1 - \sin \beta) + \frac{2}{3} \tau^2 \cos \beta}{\frac{.500\pi AR_h \tau}{1 + AR_h} (1 - \sin \beta) + \frac{4}{3} \tau^2 \cos \beta} \quad [4.48]$$

where

l_{cp} is the distance of the center of lift or pressure forward of the transom

l_M is the mean wetted length of the hull

AR_h is the aspect ratio of the hull

β is the hull deadrise angle.

The approximation for the term $(AR/1 + AR)$ given by Equation [4.45] can be used here. In this case, however, the introduced error is much smaller because the first terms of both the

numerator and denominator predominate and both are equally in error. It is therefore expected that the maximum error will be less than five percent. Equation [4.48] can now be rewritten

$$\frac{l_{cp}}{l_M} = \frac{.874 AR_h (1 - \sin \beta) + .529 \tau \cos \beta}{AR_h (1 - \sin \beta) + 1.058 \tau \cos \beta} \quad [4.49]$$

Substituting the value of AR_h from Equation [4.43], the expression for l_{cp}/l_M becomes independent of trim angle τ :

$$\frac{l_{cp}}{l_M} = \frac{.874 b (1 - \sin \beta) + .132 (2s - b \tan \beta) \cos \beta}{b (1 - \sin \beta) + .264 (2s - b \tan \beta) \cos \beta} \quad [4.50]$$

The mean length L_M is given, for the idealized hull form, by

$$l_M = \frac{2s - b \tan \beta}{2\tau} \quad [4.51]$$

The distance of the center of pressure from the transom and from the center of gravity is thus inversely proportional to the trim angle. The moment due to hull lift, obtained from Equations [4.46], [4.50] and [4.51] is thus a linear function of trim angle, but a non-linear function of submergence s . For the expected range of aspect ratios ($.25 \leq AR \leq .50$) and the range of trim angles of interest ($0.05 \leq \tau \leq 0.10$) a constant value of l_{cp}/l_M of .775 will give the location of the center of pressure

within five percent. For takeoff calculations it is probably acceptable to use this value, together with l_M from Equation [4.51]. The hull lift moment will then be a linear function of both trim angle and submergence.

Hull Hydrostatic Forces

The hull hydrostatic forces can be readily determined for the idealized hull form discussed in the previous section. The submerged portion of the hull, as shown in Figure 4.4, is a truncated pyramid. The submerged volume of the hull can be shown to be

$$V_h = \frac{l}{3 \tan \beta \sin \tau} [s^3 - (s - b \tan \beta)^3] \quad [4.52]$$

where

- V_h is the submerged volume of the hull
- β is the hull deadrise angle
- τ is the trim angle of the keel
- s is the submergence of the keel at the transom
- b is the half-beam of the hull.

As the hull trim angle τ is generally small, $\sin \tau \approx \tau$. The displacement of the hull can thus be expressed as

$$\Delta_h = \frac{\rho g}{3 \tan \beta \tau} [s^3 - (s - b \tan \beta)^3] \quad [4.53]$$

where

- ρ is the fluid density
- g is the acceleration of gravity.

4.50

The lift force due to hull buoyancy is thus a highly non-linear function of hull submergence s and trim angle τ . Fortunately, the hull buoyancy force and moment decrease rapidly with increasing speed so that approximations can be introduced. At low speeds the terms s and $b \tan \beta$ are probably about equal so that the displacement can probably be approximated by

$$\Delta_h = \frac{\rho g s^3}{3 \tan \beta \tau} \quad [4.54]$$

Once the planing regime has been reached the vertical force and moment due to buoyancy can be eliminated from Equations [4.9] and [4.10].

The distance of the center of buoyancy from the hull transom is given by

$$\frac{l_{cb}}{l_M} = \frac{[s^4 - (s - b \tan \beta)^4]}{4(s - \frac{b}{2} \tan \beta) [s^3 - (s - b \tan \beta)^3]} \quad [4.55]$$

where

- l_{cb} is the distance of the center of buoyancy of the transom
- l_M is the mean length given by Equation [4.46]
- s is the depth of submergence of the hull at the transom
- b is the half-beam of the hull.

Again noting that, (for low speeds) $s \sim b \tan \beta$, Equation [4.50] can be approximated for low speeds by

$$\frac{l_{cb}}{l_M} = \frac{s}{4(s - \frac{b}{2} \tan \beta)} . \quad [4.56]$$

The value of l_{cb}/l_M as a function of the parameter $s/b \tan \beta$ is plotted in Figure 4.8. This figure indicates that the value of l_{cb}/l_M assumes an asymptotic value of one third for values of $s/b \tan \beta$ of two or greater. Unfortunately, however, such large values of this parameter will occur, if at all, only at very low speeds.

It can thus be seen that it is not possible to find linear expressions for hull vertical force and moment due to buoyancy, even when simplifying assumptions are made. The expressions given by Equations [4.54] and [4.56] will, however, considerably simplify the solution of the pre-takeoff problem. As the speed increases, the contribution of the buoyant terms becomes negligible and can be ignored.

Resistance of Hydrofoil Craft Before Takeoff

One of the most important reasons for determining the trim and altitude history of a hydrofoil craft before takeoff is to allow calculation of the craft resistance before takeoff. Because of the serious problems associated with propulsion of hydrofoil

craft just prior to takeoff (at the so-called hump speed), it is essential to have an accurate estimate of the resistance during the preliminary design phase.

The theoretical analysis of planing craft drag has reached a state of development far in advance of that for displacement craft. Clement and Pope (4.8) and (4.9) have presented methods for calculating the resistance of planing craft. These results are based on the planing surface data (4.4) to (4.6) referred to earlier. These results are for the fully planing region. The fully planing region is typically that where the Froude number $F_{N_{\nabla}}$ is greater than three. For lower Froude numbers these results are not applicable.

Unfortunately, the operating Froude number of the hydrofoil craft $F_{N_{\nabla}}$, is given by

$$F_{N_{\nabla}} = \frac{V}{\sqrt{g \nabla^{\frac{1}{3}}}} \quad [4.57]$$

where

- V is the forward speed in feet per second
- g is the acceleration of gravity
- ∇ is the displaced volume of the craft at rest.

is generally less than the critical value (of approximately three) before takeoff. The significance of the Froude number before takeoff can be seen if we consider typical planing craft characteristics. If we consider hull 3668 of Clement and Blount (4.10), with a length-beam ratio L_P/B_M of 5.5 which is typical

for hydrofoil boat hulls, and assume a typical value of hull loading (say $A/\nabla^{2/3} = 8.5$) the speed-length ratio is related to FN_{∇} by

$$\frac{V_k}{\sqrt{L}} = 1.13 F_{N_{\nabla}} \quad [4.58]$$

where

V_k is the forward speed in knots

L is the length of the craft between perpendiculars.

The speed-length ratio corresponding to $F_{N_{\nabla}} = 3$ would be 3.39, a value usually not reached before takeoff occurs.

As hydrofoil boats gain speed, however, the foils support an increasing percentage of the craft displacement. The displacement supported by the hull is reduced by the factor $(1 - \mu)$ where μ represents the percent of the craft displacement supported by the foils. As hull unloading occurs, the effective Froude number becomes

$$F_{N_e} = \frac{F_{N_{\nabla}}}{(1 - \mu)^{1/8}} \quad [4.59]$$

where

F_{N_e} is the effective Froude number based on volume

$F_{N_{\nabla}}$ is the Froude number based on total displaced volume.

Similarly the effective hull loading factor is increased over the normal value:

$$\left(\frac{A}{V}\right)_e^{\frac{2}{3}} = \frac{\left(\frac{A}{V}\right)^{\frac{2}{3}}}{(1 - \mu)^{\frac{2}{3}}} \quad [4.60]$$

where

$\frac{A}{V}^{\frac{2}{3}}$ is the hull loading factor based on projected area of the hull and displaced volume at rest

$\left(\frac{A}{V}\right)_e^{\frac{2}{3}}$ is the effective hull loading factor.

In calculating the hull resistance of a hydrofoil craft, the effective Froude number and loading given by [4.59] and [4.60] should always be used. The variation of μ with forward velocity is a function of the system geometry and cannot be estimated accurately beforehand. It is thus not possible to estimate, beforehand, the speed at which the hull can be considered to be fully planing.

The results of Clement and Pope (4.8) and (4.9) can thus be used to calculate hull resistance for $F_{Ne} > 3.0$. The only drawback to the use of the results of this method is the restriction of the hull deadrise angles to 15 degrees or less. Because of the severity of the hull impact problem, the deadrise angles of hydrofoil craft are likely to be greater than 15 degrees. There are several means of circumventing this difficulty. The first is to make calculations for several of the deadrise angles given by Clement and Pope and extrapolate to the required angle. A second method involves determination of the increase in resistance

with deadrise angle from available model data. Figure 4.9 from (4.11) gives an indication of the increase in resistance with deadrise angle for angles from zero to 20 degrees.

J. F. Stoltz, in his discussion of the paper by Clement and Blount (4.8), gives an empirical expression for the resistance:

$$\frac{R}{W} = 0.0175 \left[\frac{25 \Delta}{V_M^2 B_M^2} + \frac{\beta}{15} \right] + \frac{V_M^2 B_M^2}{100 \Delta} \quad [4.61]$$

where

- Δ is the displacement in pounds
- V_M is the velocity in statute miles per hour
- B_M is the mean wetted beam
- β is the deadrise angle in degrees.

Equation [4.61] has been shown to be in excellent agreement with the data of Clement and Blount (4.8) for the fully planing regime ($F_{N\triangledown} > 3.5$) and can therefore be used to make rapid estimates of the effect of deadrise angle on resistance. Figure 4.8 presents a plot of R/W as a function of $V_M^2 B_M^2 / \Delta$, for various deadrise angles, based on Equation [4.61]. These curves can be used to estimate the increase in resistance at any velocity. The lower limit of applicability of these curves, corresponding to a Froude number of three for a typical hull, is also shown in Figure 4.8. The parameter $V_M^2 B_M^2 / \Delta$ can be readily related to the Froude number $F_{N\triangledown}$ for a given hull.

For the range of speeds where buoyancy effects are important ($F_{N_e} < 3.0$), the resistance data presented by Clement and Blount (4.10) can be used for estimating the hull resistance. Figures 14-18 and 21-25 of (4.10) present the resistance as a function of F_{N_v} , $A/\sqrt{3}$ and location of the center of gravity l_{cg}/l_p . From these figures it can be seen that the principal influence of l_{cg}/l_p is on the craft trim angle and that any variation in resistance with l_{cg}/l_p is due to the change in trim angle. Thus, if the trim angle of the hydrofoil craft is known, the equivalent value of l_{cg}/l_p can be chosen to give the correct resistance. As in the case for fully planing resistance, the equivalent value of the hull loading $(A/\sqrt{3})_e$ and F_{N_e} should be used. The resulting resistance of the hull R_H is given by

$$R_H = \left(\frac{R}{W}\right) \Delta (1 - \mu) \quad [4.62]$$

where

- $\left(\frac{R}{W}\right)$ or $\left(\frac{R}{\Delta}\right)$ is the resistance-displacement ratio given by Figures 14-18 and 21-25 of Reference 4.10.
- Δ is the total craft displacement
- μ is the percent of the displacement supported by the foils

The results of Clement and Blount (4.10) cover a range of parameters which is likely to encompass most practical hydrofoil boat hulls. The range of parameters covered is:

$$\begin{aligned} L_P / B_M &= 2.0 - 7.0 \\ \Delta / \sqrt{V^3} &= 4.0 - 8.5 \\ L_{cg} / L_P &= 0.0 - 0.12. \end{aligned}$$

The low twist angles of these hulls are desirable because of the excellent resistance characteristics that result and because of the reduced length of struts required by the forward foil systems. Comparison of the hulls described in Reference 4.10 with test of a number of previous planing craft indicate that the hulls described in Reference 4.10 have excellent resistance characteristics for $F_{N_\nabla} > 1.5$. As takeoff will normally occur at Froude numbers greater than one and one half, these hulls should be very good for minimizing the resistance at the so-called "hump" speed.

The only drawback of the Clement-Blount hulls is the low deadrise angle (12.5 degrees). While this low deadrise contributes to the excellent resistance characteristics, it may be unacceptable in view of structural loadings resulting from impact or crashing. It is probable that deadrise angles of approximately 20 degrees are likely to be selected for purely structural reasons. If deadrise angles greater than 12.5 degrees are used, the hull resistance will certainly increase. Figure 4.9 from Reference 4.11 shows the effect of deadrise angle on resistance down to a Froude number of about 2.4. This figure indicates that

the increase in resistance with deadrise angle is essentially independent of Froude number. While the effect of deadrise angle probably tends to disappear at very low Froude number, it is suggested that the increase in the fully planing range as given by Figures 4.8 or 4.9 or Equation [4.61] be used. As deadrise angles greater than 12.5 degrees are anticipated this procedure should be conservative.

The resistance of the foil system is calculated in essentially the same manner before and after takeoff. Certain additional factors may be needed before takeoff, however. In particular, the large separation drag associated with large foil incidence and flap angle must be considered, as must any additional drag terms arising from the surface piercing foil systems. Otherwise, the foil system resistances are calculated by the method outlined in Chapter 2.

The increased profile drags of the foils associated with large trim, incidence or flap angles can be estimated from either the Airfoil Summary (4.2) or data in Martin (4.1). It should be noted that the data in the Airfoil Summary is for two dimensional sections. To determine the profile drag of a section at incidence the operating lift coefficient given by

$$C_L = C_{L_d} + C_{L_\alpha} (\alpha + \tau) \quad [4.63]$$

should be used.

The resistance due to struts is generally little effected by the trims that occur before takeoff. The effective thickness chord ratio of the strut sections decreases by the factor $\cos \tau$, but for the trim angles occurring before takeoff, this decrease is negligible. In some surface piercing foil systems there are so-called struts (non-cambered members) which are oriented at a dihedral angle less than 90 degrees. As the boat trims, these struts will develop lift because of the angle of attack given by

$$\alpha_s = \tau \cos \Gamma \quad [4.64]$$

where

α_s is the angle of attack of the dihedral strut.

Unless the dihedral angle is large ($\Gamma > 45$ degrees) these members are more properly considered as foils. In any case, the drag of these members is calculated as for any foil.

The drag of the pods, if any are used, will be increased appreciably, only if larger trim angles result. In general it can be assumed that the pod drag coefficient does not increase during takeoff.

Factors Influencing Hull Resistance

Clement (4.11) presents general considerations for choosing the hull characteristics leading to minimum resistance. Figure 4.10 from (4.11) indicates an optimum value of L/B_A of 5.65 for craft with a displacement greater than 100,000 pounds. This

value would seem to be a good choice for hydrofoil boats, offering a good compromise between hull weight, resistance and impact loads.

Figure 4.11 presents a plot of hull loading coefficient $\Delta/\frac{1}{2}\rho LBV^2$ as a function of craft displacement for a number of existing hydrofoil craft. This figure indicates a value of 0.013 as average for all craft displacements.

Figure 4.12, also from (4.11) presents the relationship between L/B_A and the hull loading factor $A/\sqrt{V^2}$ for minimum resistance. For an L/B_A of 5.65, the value of $A/\sqrt{V^2}$ is eight. These results are based, however, on fully planing results. At low speeds, the resistance appears to decrease continuously with increased hull loading. The values indicated by Figures 4.10 and 4.12 are probably reasonable for hydrofoil use.

The deadrise angle is generally chosen from structural considerations. These indicate the maximum possible deadrise angle, and some compromise between structural and resistance considerations must be made. Ideally, takeoff resistance calculations should be made for several deadrise angles to determine the relative sacrifices in hull weight and pre-takeoff resistance. The twist angle should be minimized, at least over the after 60-70 percent of the hull length, in order to minimize hull resistance. The shape of the buttocks in the forward 30 to 40 percent of the hull length should have little effect on resistance as this area is submerged only at low speeds. It is anticipated that the type of twist incorporated in the Series 62 hulls (4.8) should have little or no effect on the hull resistance.

REFERENCES

- 4.1. Martin, M., "The Stability Derivatives of a Hydrofoil Boat - Part I," HYDRONAUTICS, Incorporated Technical Report 001-10(I), January 1963.
- 4.2. Abbott, I. H., von Doenhoff, A. E., and Stivers, L. S., "Summary of Airfoil Data," NACA Report Number 824, 1945.
- 4.3. Sullivan, E. K., and Higgins, James A., "Test and Trials of the H. S. Dennison," Hovering Craft and Hydrofoil Magazine, Volume 3, Numbers 3 and 4, December 1963 and January 1964.
- 4.4. Weinstein, Irving, and Kapryan, Walter J., "The High-Speed Planing Characteristics of a Rectangular Flat Plate Over a Wide Range of Trim and Wetted Length," NACA Technical Note 2981, 1953.
- 4.5. Kapryan, Walter J., and Boyd, George M., Jr., "Hydrodynamic Pressure Distributions Obtained During a Planing Investigation of Five Related Prismatic Surfaces," NACA Technical Note 3477, 1955.
- 4.6. Chambliss, Derrill B., and Boyd, George M., Jr., "The Planing Characteristics of Two V-Shaped Prismatic Surfaces Having Angles of Dead Rise of 20° and 40° ," NACA Technical Note 2876, 1953.
- 4.7. Shuford, Charles L., Jr., "A Theoretical and Experimental Study of Planing Surfaces Including the Effect of Cross Section and Plan Form," NACA Report 1355, 1958.
- 4.8. Clement, E. P. and Pope, J. D., "Graphs for Predicting the Resistance of Large Stepless Planing Hulls at High Speeds," David Taylor Model Basin Report 1318, April 1959.
- 4.9. Clement, Eugene P., and Pope, James D., "Stepless and Stepped Planing Hulls - Graphs for Performance Prediction and Design," DTMB Report 1490, January 1961.

- 4.10 Clement, Eugene P., and Blount, Donald S., "Resistance Tests of a Systematic Series of Planing Hull Form," Transactions of the Society of Naval Architects and Marine Engineers, Volume 71, 1963.
- 4.11 Clement, Eugene P., "Analyzing the Stepless Planing Boat," DTMB Report 1093, November 1956.

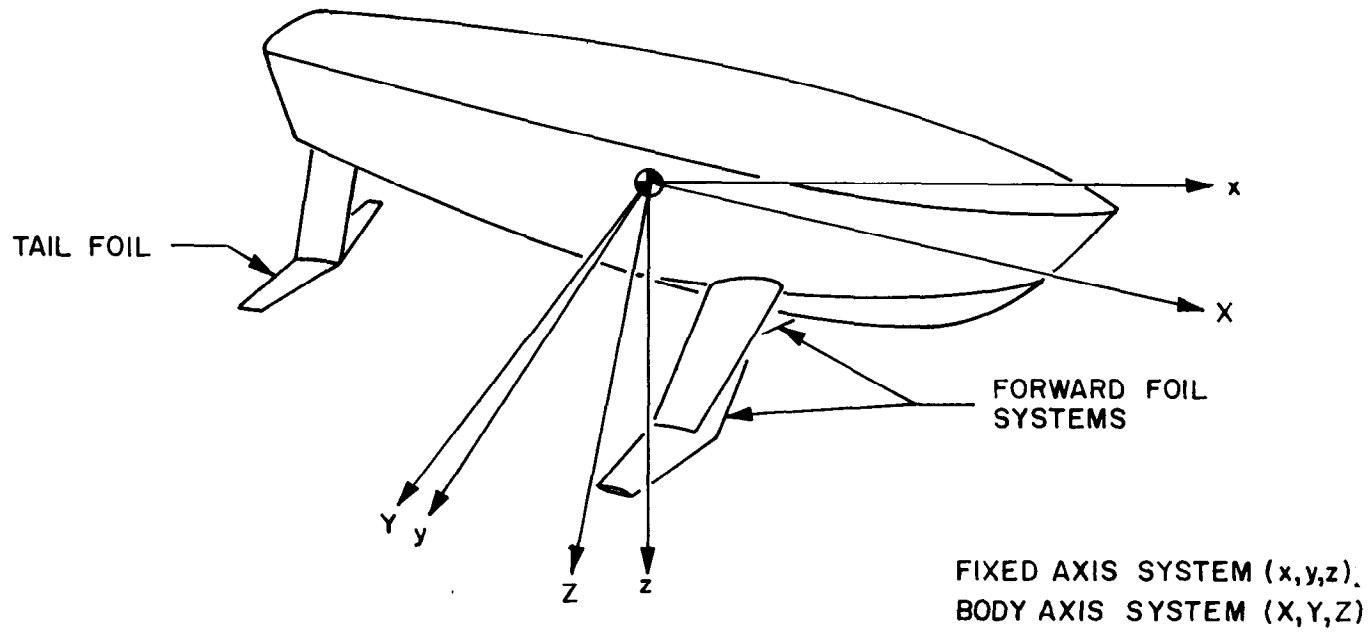


FIGURE 4.1

-COORDINATE SYSTEMS USED IN THIS CHAPTER FOR A HYDROFOIL CRAFT

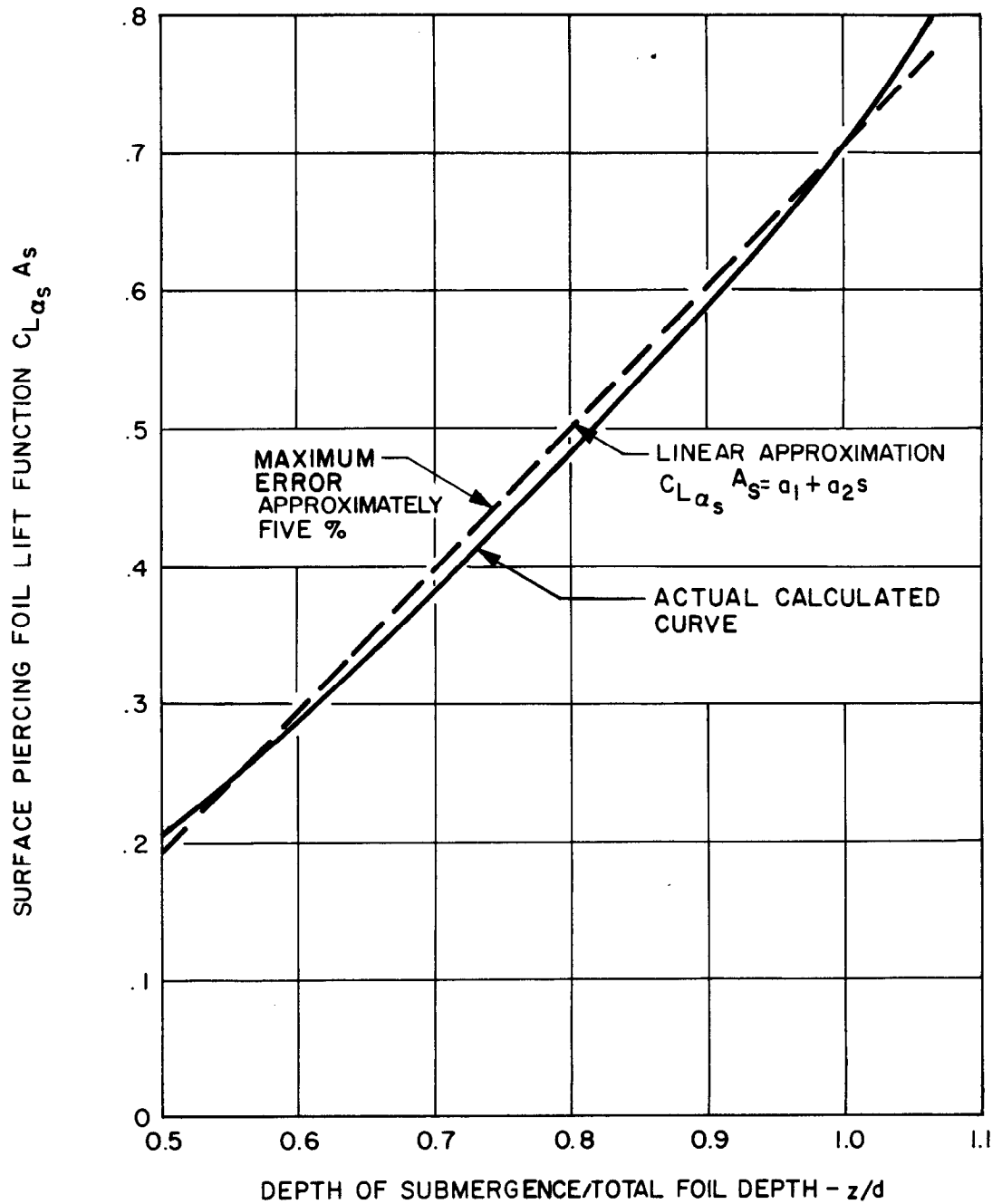


FIGURE 4.3-VARIATION OF SURFACE PIERCING LIFT FUNCTION $C_L \alpha_s A_s$ WITH FOIL SYSTEM SUBMERGENCE

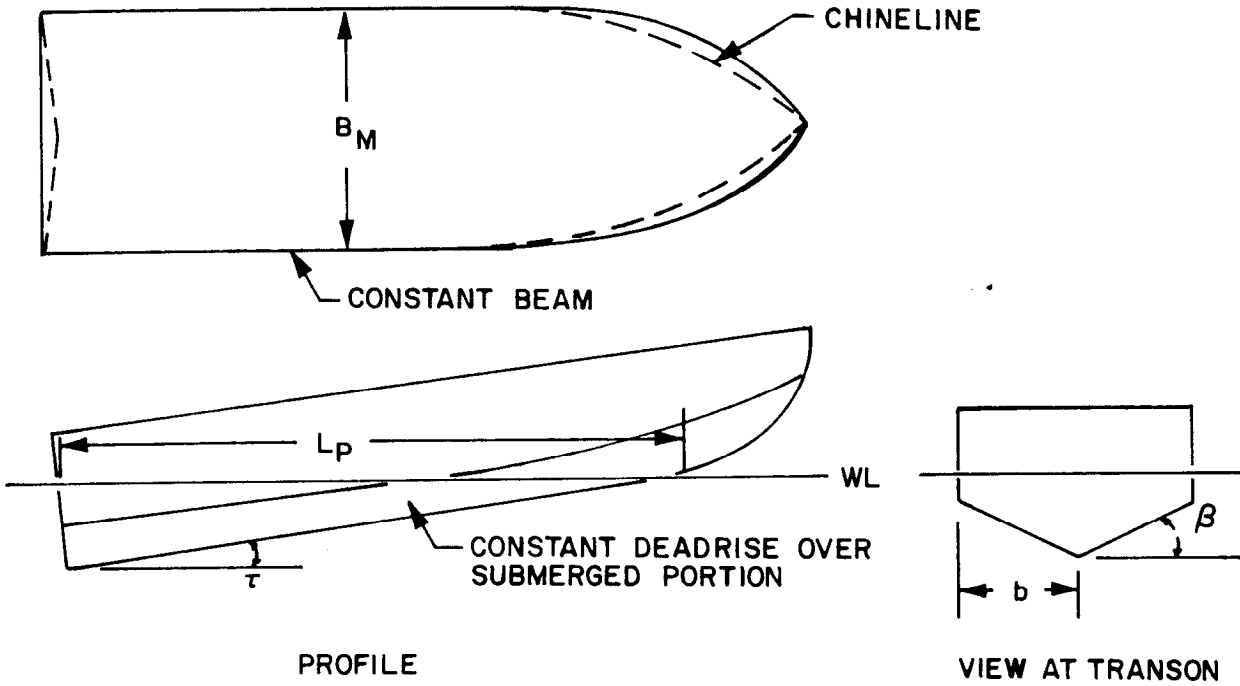


FIGURE 4.4 - IDEALIZED HULL FORM

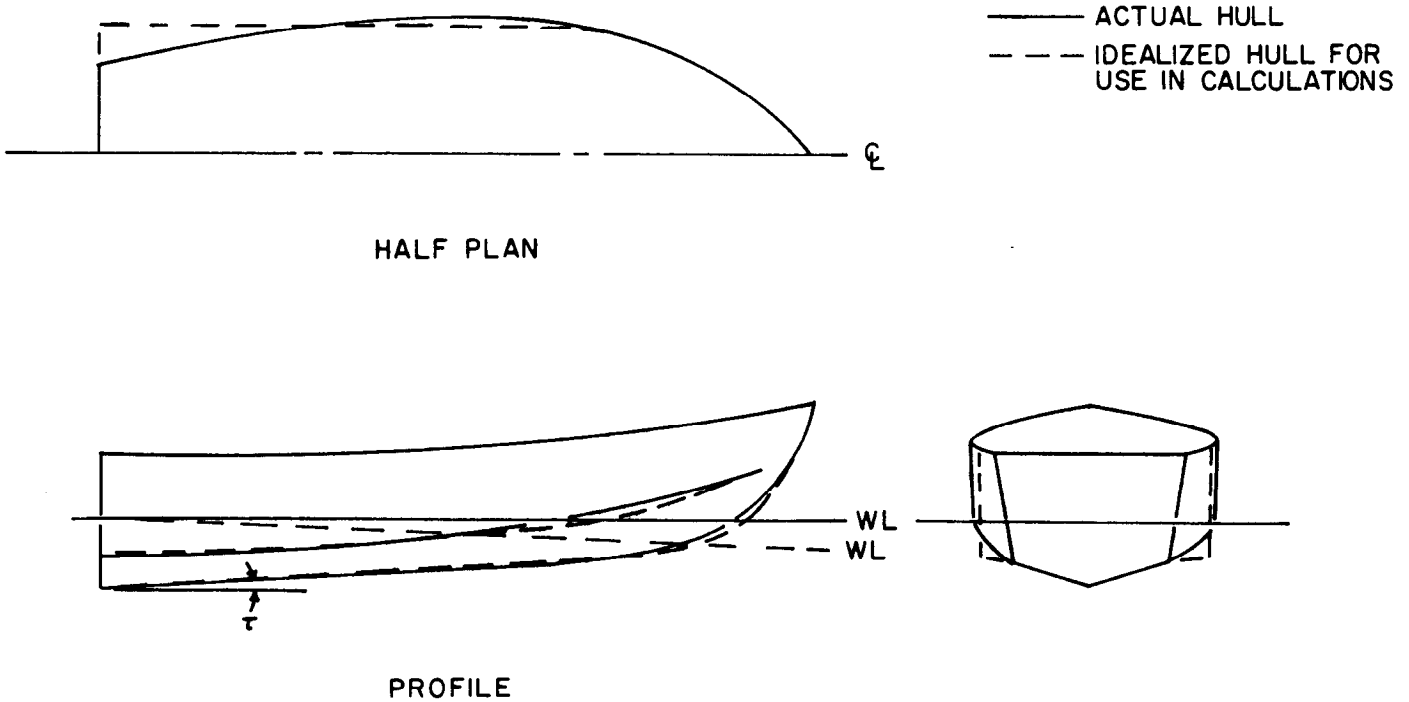


FIGURE 4.5 - IDEALIZATION OF HULL FORM

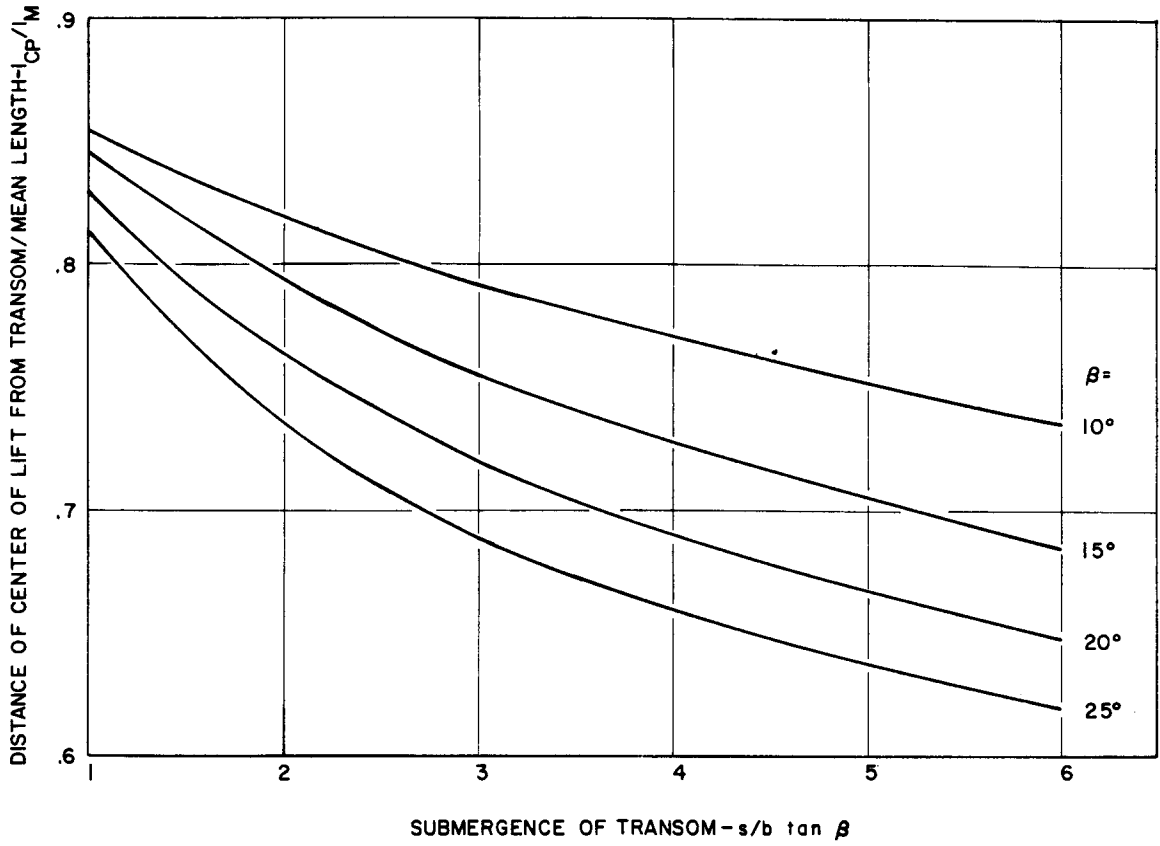


FIGURE 4.6 CENTER OF HULL LIFT AS A FUNCTION OF SUBMERGENCE AND DEADRISE ANGLE

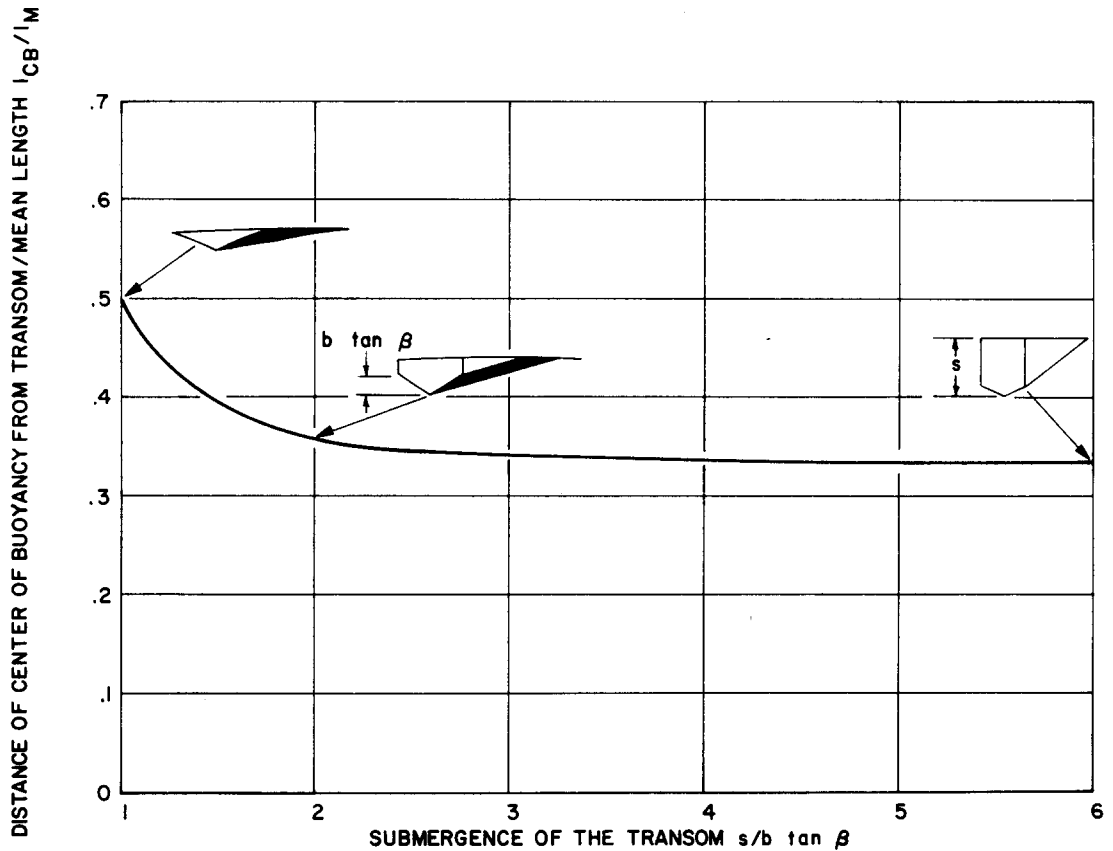


FIGURE 4.7 VARIATION OF THE LOCATION OF THE CENTER OF BUOYANCY OF THE SUBMERGED PORTION OF HULL AS A FUNCTION OF SUBMERGENCE

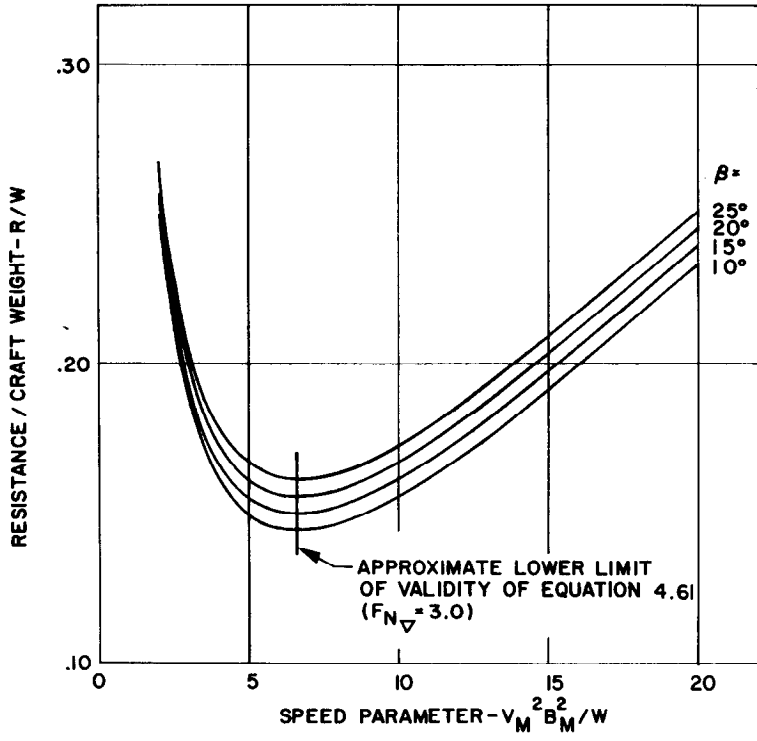


FIGURE 4.8 EFFECT OF SPEED PARAMETER AND DEADRISE ANGLE ON PLANING HULL RESISTANCE FROM THE FORMULA OF STOLTZ (4.61)

RESISTANCE / RESISTANCE FOR 10 DEGREE DEADRISE ANGLE

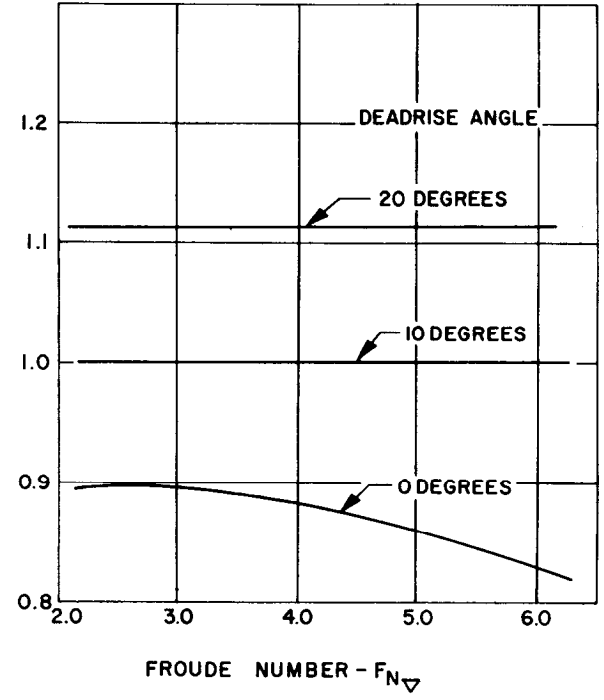


FIGURE 4.9 VARIATION OF HULL RESISTANCE WITH DEADRISE ANGLE AS A FUNCTION OF HULL FROUDE NUMBER

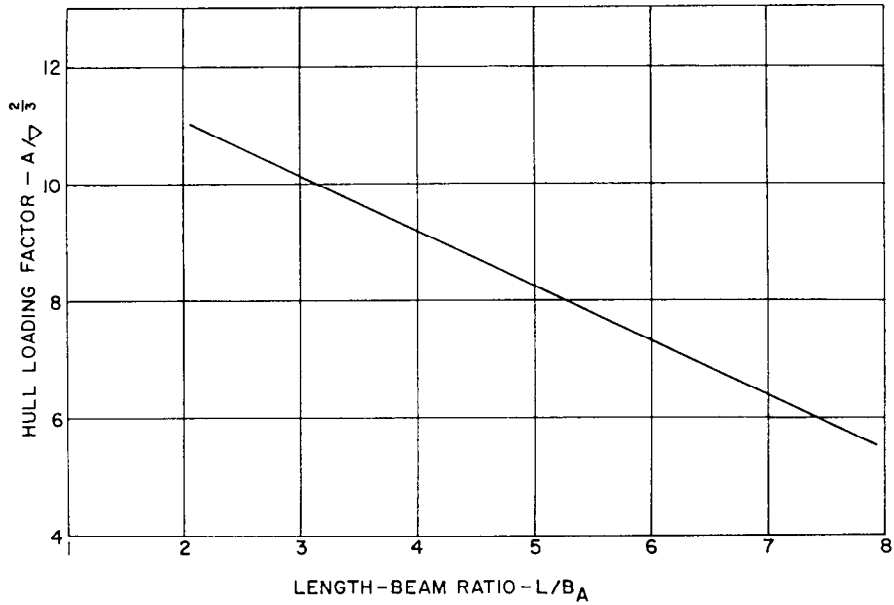


FIGURE 4.10 HULL LOADING FACTOR FOR MINIMUM HULL RESISTANCE AS A FUNCTION OF LENGTH-BEAM RATIO

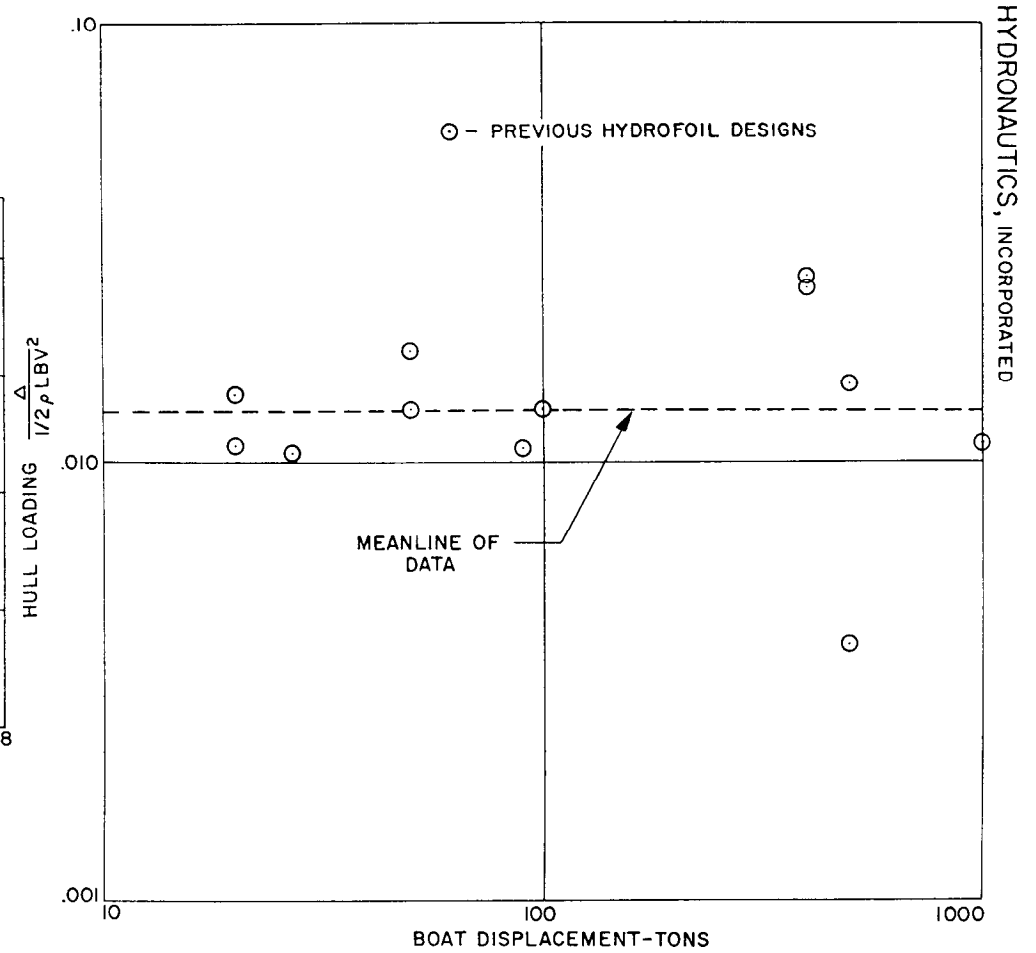


FIGURE 4.11 TYPICAL HULL LOADINGS FOR HYDROFOIL BOAT DESIGNS

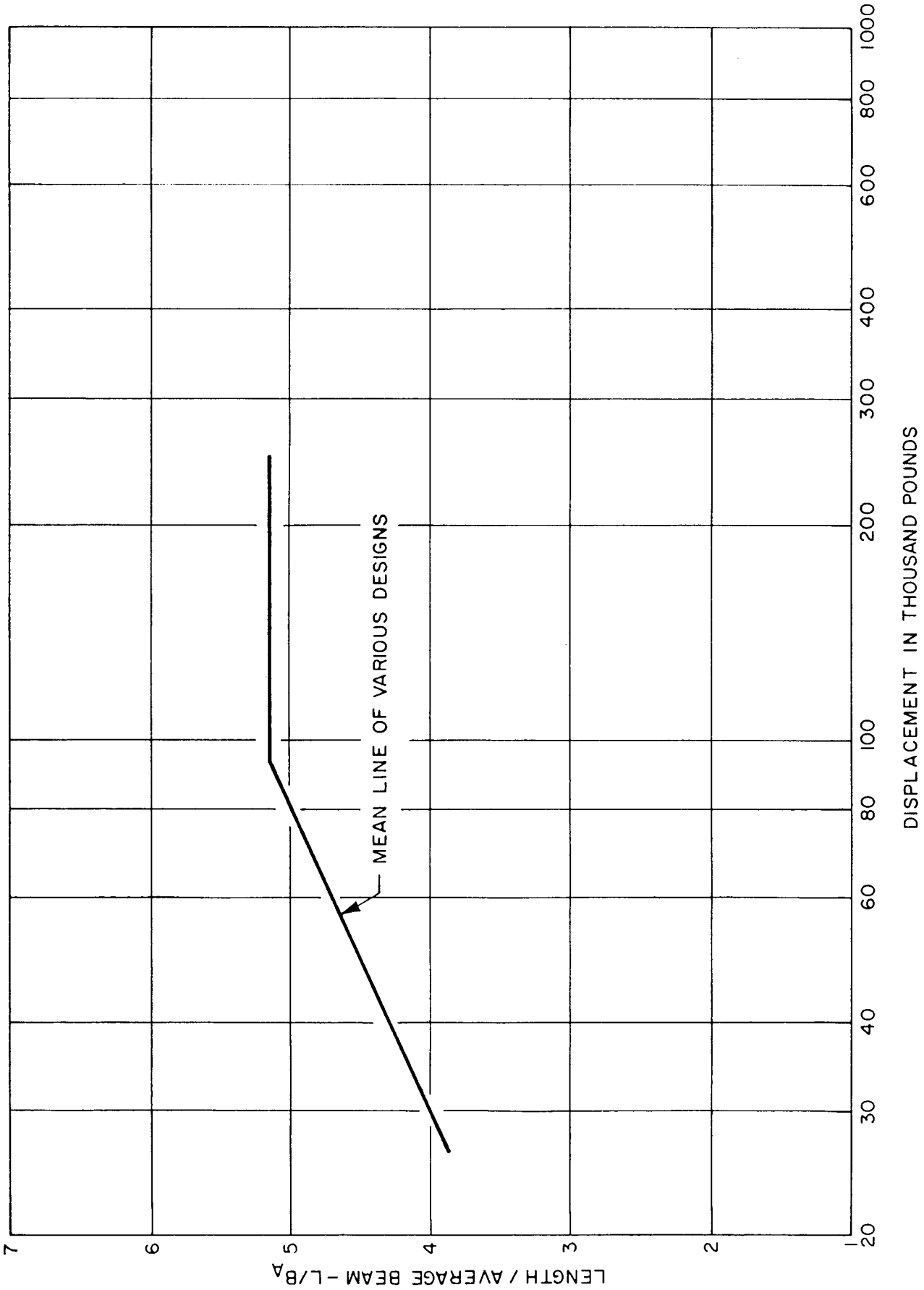


FIGURE 4.12-VARIATION OF LENGTH-BEAM RATIO FOR TYPICAL PLANING CRAFT DESIGNS FROM CLEMENT (4.11)

HYDRONAUTICS, Incorporated

5.0

CHAPTER 5

LONGITUDINAL STABILITY (CONTROLS FIXED)

By

Milton Martin

NOTATION

A_a sum of the horizontal projected area of the two aft surface piercing panels (see Figure 5.5).

A_f sum of the horizontal projected area of the two forward surface piercing panels (see Figure 5.5)

A_r reference area - usually $\bar{S}_a + \bar{S}_f$ at design conditions

b_a stiffness factor due to depth change of aft dihedral panel (see Equation 5.34, 5.35 et seq.)

C_{L_a} = $\frac{\sum (C_L)_f S_f \cos \Gamma}{\bar{S}}$ mean lift coefficient at the aft foils

C_{L_f} mean lift foils coefficient at the forward foils

$(C_L)_f$ = $L_f / \frac{1}{2} \rho U_f^2 S_f$ panel lift coefficient

$(C_{L_h})_f$ = $\frac{\partial C_L}{\partial \left(\frac{h}{c_s} \right)}$ is the effective lift-depth coefficient of the forward surface piercing panel

\bar{c}_s mean chord of the surface piercing panel

c_w chord of the surface piercing panel measured at the free surface

$C_{L_{\alpha a}}$ = $\frac{\sum (C_{L_{\alpha}})_f S_f \cos^2 \Gamma_f}{\bar{S}_f}$ mean effective lift-curve slope coefficient at the aft foils

$C_{L_{\alpha f}}$ mean effective lift-curve slope coefficient at the forward foils

$\left(C_{L_{\alpha}} \right)_f = \frac{\partial (C_L)_f}{\partial \alpha_f}$ rate of change of lift coefficient with panel angle of attack of hydrofoil panel in panel axis system (for a V-foil with dihedral Γ , $\alpha_f = \alpha \cos \Gamma$)

$D = \frac{d}{dt}$ derivative with respect to time

d_a depth of aft foil

d_f depth of forward foil (see Figure 5.5)

$F = \frac{U}{\sqrt{gl}}$ Froude number

g acceleration of gravity

h perturbation in position of c.g. relative to horizontal water reference level (positive downward)

\dot{h} time rate of change of h

$I = mk^2$ boat moment of inertia about c.g.

\bar{K}' gain factor

k boat radius of gyration for rotation about the c.g.

$L = (L)_f \cos \Gamma_f$ vertical lift on foil panel

L_a vertical lift on aft foil system

L_f vertical lift on forward foil system

$(L)_f$	hydrodynamic lift on foil panel, normal to panel
l	$= x_f + x_a$ horizontal distance between center of lift of forward and aft foils
M	hydrodynamic moment component about the stability y-axis (positive from z to x) - pitch moment
m	mass of craft
$N_{\frac{1}{2}}$	number of cycles required to decay to half-amplitude
p	stability root
q	rate of change of pitch angle
\dot{q}	time rate of change of q
R_a	stiffness factor due to depth change of horizontal aft panel (See Equations 5.34, 5.35 et seq.)
S_f	true plan form area (not projected area) of panel
\bar{S}_a	$= \sum_a S_f \cos \Gamma_f$ total horizontal projected area of aft foils.
\bar{S}_f	$= \sum_f S_f \cos \Gamma_f$ total horizontal projected area of forward foils
s.m.	static margin (see Equation 5.52)
$T_{\frac{1}{2}}$	time required to decay to half-amplitude
t	time
U	forward boat speed
u	x-component of perturbation of velocity of the boat at its c.g. (also written du)

5.4

\dot{u}	time rate of change of u
w	z -component of perturbation of velocity of the boat at its c.g. (also written dw)
\dot{w}	time rate of change of w
X	hydrodynamic component of force in the positive direction of the stability x -axis-longitudinal force
x_a	horizontal distance from c.g. to center of lift of aft foils
x_f	horizontal distance from c.g. to center of lift of forward foils
Z	hydrodynamic force in the positive direction of the stability z -axis (positive downward) vertical force
α	angle of attack of boat with respect to its stability axes ($= \tan^{-1} w/U$)
α_f	$= \alpha \cos \Gamma_f$ angle of attack on foil panel
Γ_f	dihedral angle of panel
γ	$= \tan^{-1} \left \frac{\sigma_i}{\sigma_r} \right $
ζ	damping ratio ($= \cos \gamma$ for $\zeta \leq 1$)
θ	pitch angle of boat
κ_1	$= \frac{C_{L_{\alpha a}}}{C_{L_{\alpha f}}}$
κ_2	$= \frac{C_{L_a}}{C_{L_f}}$

σ_i	imaginary part of stability root, damped natural frequency of the mode
σ_r	real part of stability root
ϕ	angle between a root and a pole
ψ	angle between a root and a zero
ω_n	undamped natural frequency

Static Derivatives

X_u, X_w, X_h Rate of change of X hydrodynamic force with u, w or h at steady state equilibrium condition; the partial derivative $\frac{\partial X}{\partial u}$, $\frac{\partial X}{\partial w}$ or $\frac{\partial X}{\partial h}$.

Z_u, Z_w, Z_h

M_u, M_w, M_h

Rotary Derivatives

X_q, X_θ Rate of change of X hydrodynamic force with q or θ at steady state equilibrium condition; the partial derivative; $\frac{\partial X}{\partial q}$, $\frac{\partial X}{\partial \theta}$.

Z_q, Z_θ

M_q, M_θ

Added Mass Derivatives

$X_{\dot{u}}$, $X_{\dot{w}}$ Rate of change of X hydrodynamic force with \dot{u} ,
 or \dot{w} ; $\frac{\partial X}{\partial \dot{u}}$ $\frac{\partial X}{\partial \dot{w}}$

$Z_{\dot{u}}$, $Z_{\dot{w}}$

$X_{\dot{q}}$, $Z_{\dot{q}}$

Added Moment of Inertia Derivatives

$M_{\dot{q}}$, $M_{\dot{u}}$, $M_{\dot{w}}$ Rate of change of M hydrodynamic moment with \dot{u} , \dot{q}
 or \dot{w} ; the partial derivative $\frac{\partial M}{\partial \dot{q}}$, $\frac{\partial M}{\partial \dot{u}}$ or $\frac{\partial M}{\partial \dot{w}}$

Subscripts

- a aft foil system
- f forward foil system
- H uncoupled heave mode
- P uncoupled pitch mode

Superscripts

- dot, . derivative with respect to time
- prime, ' represents non-dimensional quantity (see Table 5.4)
- double prime, '' represents non-dimensional force and moment divided by non-dimensional mass and moment of inertia respectively.

INTRODUCTION

The stability of a hydrofoil boat may depend on a large number of factors in addition to those considered in the familiar rigid boat equations of motion (Equations [5.1]-[5.3]). The effect of waves, non-linearities, structural flexibility and lag in the build-up of hydrodynamic forces will affect the stability of the hydrofoil boat, to varying degrees depending on the specific application. Kaplan (5.2) found that in general the longitudinal stability of hydrofoil boats can be affected by the presence of surface waves. The inclusion of the effects of waves resulted in a set of stability equations which had time-dependent coefficients so that numerical methods of analysis had to be used. These equations were applied to the investigation of the motion of a completely submerged foil system in head and following waves. The conclusions of this study, based on the limited data and analysis performed, were that the appropriate equations of motion (for a linear analysis at least) should probably have constant coefficients since the additional information obtained by the use of the time-dependent coefficients did not appear to be worth the great amount of additional computational effort required.

The results of limited investigations on specific configurations indicate that the effects of non-linearities on the calm sea longitudinal stability of hydrofoil boats is also small as long as the motions are moderate. For example, Ogilvie (5.3) found that for a tandem surface piercing foil system the computed non-linear transient responses to moderate perturbations were quite similar to the linear responses. This does not mean however that the effects of non-linearities on motions in a seaway are not

5.8

important. Ogilvie (5.3) and others have demonstrated that these effects can be quite significant.

The effect of structural flexibility on the dynamic stability of a hydrofoil boat depends to a great extent on the relative value of the lowest natural frequency of the elastic modes. If this is much higher than the rigid body modes, the deflections of the elastic structure are essentially in phase with the perturbation loads and the rigid body stability derivatives need be corrected only for the static elastic deflection produced by the loads. If, on the other hand, it is close to one of the rigid body modes, significant coupling forces can occur, and it is necessary to include these, together with the additional equations of motion corresponding to the added significant elastic degrees of freedom, in the determination of the boat stability. Although, in some cases, the flexibility can have an appreciable effect on the stability (5.4), since its inclusion greatly increases the difficulties of determining configurations with desirable response characteristics, its dynamic effect is usually disregarded in the preliminary stages of design. Once a preliminary design has been established for the "rigid boat" then more detailed calculations, considering the effects of flexibility, should be made. Methods of deriving the equations of motion in the elastic degrees of freedom and for determining the hydroelastic stability derivatives are given in Reference (5.1) and (5.5).

It has been found (5.6) that, in a seaway where there exist frequencies of wave encounter which are relatively high compared to the natural frequency of the craft, the hydrodynamic lag of

hydrofoils produce some effect on the response, especially for the higher aspect ratio foils. However, in calm water, the rates of divergence or convergence and the frequencies of motion are usually sufficiently small so that the effects of unsteadiness may be neglected.

THE LONGITUDINAL STABILITY EQUATIONS

If, in the nondimensional longitudinal equation of motion (Equations 56a,b,c of Reference 5.1) we made the elevator angle, η , equal to zero, we obtain the controls fixed stability equations

$$\left(m'D' - X_u'\right)u' - \left(X_w'D' + X_h'\right)h' - \left(X_q'D' + X_w' + X_\theta' - C_{L_o}\right)\theta' = 0 \quad [5.1]$$

$$-Z_u'u' + \left[\left(m' - Z_{\dot{w}}'\right)D'^2 - Z_w'D' - Z_h'\right]h' - \left[Z_{\dot{q}}'D'^2 + \left(Z_q' + Z_{\dot{w}}'\right)D' + Z_w' + Z_\theta'\right]\theta' = 0 \quad [5.2]$$

$$-M_u'u' - \left(M_{\dot{w}}'D'^2 + M_w'D' + M_h'\right)h' + \left[\left(I_y' - M_{\dot{q}}'\right)D'^2 - \left(M_q' + M_{\dot{w}}'\right)D' - \left(M_w' + M_\theta'\right)\right]\theta' = 0 \quad [5.3]$$

which are the equilibrium equations in surge, heave and pitch respectively. Since these equations are linear their solutions are linear and may be expressed as the sum of exponentials

5.10

$$u' = \sum u_i' e^{\sigma_i' t'} \quad [5.4]$$

$$h' = \sum h_i' e^{\sigma_i' t'} \quad [5.5]$$

$$\theta' = \sum \theta_i' e^{\sigma_i' t'} \quad [5.6]$$

where u_i' , h_i' and θ_i' are determined from the initial conditions and σ_i' , the stability roots, are obtained by substituting these equations into Equations [5.1] - [5.3]. In order for non-trivial solutions to exist σ_i' must have only those values which will make the determinant of the resulting equations equal to zero; i.e.

$$\begin{vmatrix} (m' \sigma' - X_u') & -(X_w' \sigma' + X_h') & -(X_q' \sigma' + X_w' + X_\theta' - C_{L_o}) \\ -Z_u' & \bar{m}' \sigma'^2 - Z_w' \sigma' - Z_h' & -\left[(Z_q' + Z_w') \sigma' + Z_w' + Z_\theta' \right] \\ -M_u' & -(M_w' \sigma' + M_h') & \bar{I}_y' \sigma'^2 - M_q' \sigma' - (M_w' + M_\theta') \end{vmatrix} = 0 \quad [5.7]$$

where

$$\bar{m}' = m' - Z_{\dot{w}}'$$

$$\bar{I}_y' = I_y' - M_{\dot{q}}'$$

and $Z_{\dot{q}}'$ and $M_{\dot{w}}'$ have been neglected since they have a negligible effect on the stability. Equation [5.7] is known as the characteristic equation of the hydrofoil boat in longitudinal motion and the determinant is called the corresponding stability determinant. Expansion of this determinant leads to the following fifth degree equation for σ'

$$A\sigma'^5 + B\sigma'^4 + C\sigma'^3 + D\sigma'^2 + E\sigma' + F = 0 \quad [5.8]$$

where

$$A = 1$$

$$B = -M_q'' - Z_w'' - X_u''$$

$$C = Z_w''M_q'' - M_w'' - M_\theta'' - Z_h'' - M_w''(Z_q'' + Z_{\dot{w}}'') + M_q''X_u'' + Z_w''X_u'' \\ - X_w''Z_u'' - M_u''X_q''$$

$$\begin{aligned}
D = & Z_w'' M_\theta'' - M_w'' Z_\theta'' + M_q'' Z_h'' - M_h'' \left(Z_q'' + Z_{\dot{w}}'' \right) \\
& + X_u'' \left[M_w'' + M_\theta'' - Z_w'' M_q'' + Z_h'' + M_w'' \left(Z_q'' + Z_{\dot{w}}'' \right) \right] \\
& - Z_u'' \left[X_h'' + M_w'' X_q'' - X_w'' M_q'' \right] - M_u'' \left[X_w'' + X_\theta'' - C_{L_o}'' - X_q'' Z_w'' \right. \\
& \left. + X_w'' \left(Z_q'' + Z_{\dot{w}}'' \right) \right]
\end{aligned}$$

$$\begin{aligned}
E = & Z_h'' \left(M_w'' + M_\theta'' \right) - M_h'' \left(Z_w'' + Z_\theta'' \right) - X_u'' \left[Z_w'' M_\theta'' + M_q'' Z_h'' \right. \\
& \left. - M_w'' Z_\theta'' - M_h'' \left(Z_q'' + Z_{\dot{w}}'' \right) \right] - Z_u'' \left[M_w'' \left(X_\theta'' - C_{L_o}'' \right) \right. \\
& \left. + M_h'' X_q'' - X_w'' M_\theta'' - M_q'' X_h'' \right] - M_u'' \left[X_w'' Z_\theta'' \right. \\
& \left. + X_h'' \left(Z_q'' + Z_{\dot{w}}'' \right) - X_q'' Z_h'' - Z_w'' \left(X_\theta'' - C_{L_o}'' \right) \right]
\end{aligned}$$

$$\begin{aligned}
F = & X_u'' \left[M_h'' \left(Z_w'' + Z_\theta'' \right) - Z_h'' \left(M_w'' + M_\theta'' \right) \right] - Z_u'' \left[M_h'' \left(X_w'' + X_\theta'' - C_{L_o}'' \right) \right. \\
& \left. - X_h'' \left(M_w'' + M_\theta'' \right) \right] + M_u'' \left[Z_h'' \left(X_w'' + X_\theta'' - C_{L_o}'' \right) - X_h'' \left(Z_w'' + Z_\theta'' \right) \right]
\end{aligned}$$

Note that the primes in Equations [5.1] - [5.7] indicate the non-dimensional quantity as defined in the nomenclature section. The double primed terms, defining the coefficients of Equation [5.8], are obtained by dividing the primed force derivatives in Equation [5.1] by m' , in Equation [5.2] by \bar{m}' , and the primed moment derivatives in Equation [5.3] by \bar{I}' . The solution of Equation [5.8] yields five values of the non-dimensional stability roots σ_i' which can be real or complex. The complex roots occur in conjugate pairs. The part of the solution corresponding to the sum of two terms with these roots represents a convergent or divergent oscillation. Thus if $\sigma_1' = \sigma_r' + i\sigma_i'$ and $\sigma_2' = \sigma_r' - i\sigma_i'$ then part of the right hand side of Equation [5.4] for example may be written as

$$u_1' e^{(\sigma_r' + i\sigma_i')t'} + u_2' e^{(\sigma_r' - i\sigma_i')t'}$$

which is readily reduced to

$$e^{\sigma_r' t'} (a' \cos \sigma_i' t' + b' \sin \sigma_i' t')$$

where

$$a' = u_1' + u_2'$$

$$b' = i(u_1' - u_2')$$

since

$$e^{\pm i\sigma_1't'} = \cos \sigma_1't' \pm i \sin \sigma_1't'$$

Since a' and b' are always real u_1' and u_2' must be conjugate complex. Clearly if σ_r' is negative the oscillation is convergent or damped and if σ_r' is positive the oscillation is divergent or unstable. The contribution to the motion of purely real roots are non-oscillatory and result in a divergent or convergent contribution to the total motion depending on the sign of σ_1' . Thus if the real part of each of the roots is negative the motion is stable and if any of these roots has a positive real part the motion is unstable. The motion corresponding to each real value of σ' and each complex pair are called the normal modes of motion. Although it is possible in theory to excite a single mode, in practice normal disturbances excite all of the modes to varying degrees. The handling qualities of a hydrofoil boat depends not only on whether the craft is stable or not but also on the degree of stability and on the characteristics of the modes.

In the field of aircraft the requirement on dynamic stability generally takes the form of a specification on the time for a disturbance to damp to half amplitude or the degree of damping in one cycle. The damping required for good flying qualities varies with the period. Typical of such requirements is the graph given by Figure 1 from Reference (5.7) which until recently applied to the lateral oscillation, or "Dutch roll" of aircraft. The non-dimensional time to damp to $\frac{1}{2}$ amplitude $T_{\frac{1}{2}}'$ for a given mode is

obtained from the following equation

$$e^{\sigma_r' t_2'} = \frac{1}{2} e^{\sigma_r' t_1'}$$

where

$$t_2' - t_1' = T_{\frac{1}{2}}'$$

σ_r' = real part of the stability root for the short period mode

which gives

$$T_{\frac{1}{2}}' = \frac{\ln 2}{|\sigma_r'|} = \frac{.69}{|\sigma_r'|} \text{ lengths of travel} \quad [5.9a]$$

or in seconds

$$T_{\frac{1}{2}} = \frac{.69}{|\sigma_r|} = \frac{.69}{|\sigma_r'|} \frac{l}{U} \text{ seconds} \quad [5.9b]$$

While the requirements specified in Reference (5.8) on the longitudinal stability of the phugoid mode of aircraft (the long period oscillation) allow a slight amount of instability for very long natural oscillation periods and neutral stability for periods below 15 seconds. The requirements on the short-period oscillation (periods < 6 seconds) are that the normal acceleration (from elevator pulse) shall damp to at least 1/10 amplitude in 1 cycle and the residual oscillations shall not be of objectionable magnitude.

5.16

This latter requirement is related to the stability index through the following equation

$$e^{\sigma_r' t_2'} < \frac{1}{10} e^{\sigma_r' t_1'}$$

where $t_2' - t_1'$ is the non-dimensional period T' .

σ_r' is the real part of the short-period mode stability root.

Thus

$$\frac{\sigma_r'}{\sigma_i'} = \frac{\sigma_r}{\sigma_i} < - \frac{\ln 10}{2\pi} = - .366$$

where $\sigma_i' \left(= \frac{2\pi}{T'} \right)$ is the non-dimensional damped oscillation frequency or imaginary part of the stability root. This corresponds

to an effective minimum damping ratio $\zeta \left(= \frac{\sigma_r}{\sqrt{\sigma_r^2 + \sigma_i^2}} \right)$ of 0.34.

Since the period is less than 6 seconds the dimensional damped frequency is given by

$$\sigma_i > \frac{2\pi}{6} \approx 1 \text{ rad./sec.}$$

Sometimes the above specification is given in terms of number of cycles to damp to half amplitude. This is readily seen to be, for $\zeta < 1$

$$N_{\frac{1}{2}} = \frac{.69}{2\pi} \frac{|\sigma_1|}{|\sigma_r|} = \frac{.69}{2\pi} \frac{\sqrt{1-\zeta^2}}{\zeta} \text{ cycles} \quad [5.9c]$$

For an oscillation to dampen to 1/10 in one cycle it will dampen to 1/2 in .30 cycles.

Numerous other specifications on stability and handling qualities are described in Reference (5.8) where an attempt is made to apply knowledge acquired from experiments with airplanes and helicopters to V/STOL vehicles. The difficulty of this task is great since motion studies and pilot and passenger reactions (see References (5.9) - (5.11) for example) in full scale vehicles are needed for the complete story. In many respects the stability requirements for hydrofoil boats, even in calm seas, are more severe than for aircraft since the flying altitude is more severely restricted before failure due to "crash landing" on the hull or foil broaching. When the requirements of operating without crashing, broaching or excessive accelerations in a seaway are added the criteria for dynamic stability as applied to aircraft has even less direct application to hydrofoil boats. In the absence of a large background of experience it is necessary to rely on experimental and theoretical determinations of seaway response in evaluating the suitability of a given boat design. This in turn is related to the forcing spectrum of the seaway, the stability of the craft and, in the case of hydrofoil boats with automatic controls, on the characteristics of the control system as well. With reference to the latter case a recent study (5.12) on a boat with an aircraft type

completely submerged foil system, employing automatic controls, found that with the gains selected for good stability and response in a calm sea, the craft response in sinusoidal waves was unsatisfactory. On the other hand Kaplan and Jacobs (5.13) found for a series of five 40 knot boats with various surface piercing foil configurations the most stable also gave the best performance in a following sea. The five configurations studied are described in Table 5.1 and their stability roots and damping ratios of the dominant roots are given in Table 5.2. It is seen that all the configurations have one large negative real root, another much smaller one, and a pair of small complex conjugate roots. This is a typical root configuration of many surface piercing foil configurations. The roots that mainly control the response in these examples are the complex conjugate pair since the modes corresponding to the larger negative real roots damp out quickly. These systems thus behave approximately like second order systems. Configurations 3 and 4 which had the greatest degree of stability (damping ratio $\zeta = .67$ and $.50$ respectively and time to one-half amplitude $T_{\frac{1}{2}} = .57$ seconds and $.51$ seconds respectively) broached the least and had the least rms motion in a following sea (see Table 5.3). Configuration 5, which had the smallest damping ratio and longest time to one-half amplitude, broached the most and had the largest rms motion. Although the wave forcing spectrum also has a very important effect on the degree of broaching it was found, in this case at least, that the influence of the damping ratio and time to one-half amplitude, which are determined entirely from the stability roots, were the dominating factors. Since a good description of the seaway is given in terms of a sum

of sine waves of wave lengths and frequencies with various spectral distributions, depending on the sea state, the frequency response characteristics of the boat are obviously of great importance. For the above examples this was predominantly determined by the pair of complex conjugate roots and may therefore be approximated by that of a second order system, which, in turn, depends entirely on the damping ratio ζ of the complex pair. The effect of ζ on the frequency response of second order systems is shown in Figure 5.2. It is clear that, in order to avoid the large motions associated with sharp resonances it is desirable to maintain ζ large. On the other hand it is necessary to keep ζ from becoming too large in order to avoid sluggishness and excessive values of $T_{\frac{1}{2}}$ (see Equations [5.9], [5.24b] and Figure 5.3). In any case, the determination of optimum stability characteristics required for satisfactory behavior in a seaway should always take into account the forcing spectrum of the seaway.

ROUTH'S STABILITY CRITERION

Although with modern high speed computers it is relatively easy to determine the stability roots from Equation [5.8] it is sometimes desired to know only if the system is stable or unstable. For this purpose a mathematical technique developed by Routh, applicable to any characteristic equation of the form of Equation [5.8], may be used.

The Routh stability criterion is presented here without proof. The reader is referred to Reference (5.14) for further details. Let the characteristic equation for a system be

$$a_n \sigma^n + a_{n-1} \sigma^{n-1} + a_{n-2} \sigma^{n-2} + \dots + a_1 \sigma + a_0 = 0 \quad a_n > 0^* \quad [5.10]$$

where the a's are real. If any of the a's are zero or if all of the a's are not of the same sign then there are imaginary roots or roots with positive real parts and the system is unstable. To determine if the system is stable when all of the a's exist and are of the same sign, the following procedure is followed. The coefficients of the characteristic equation are arranged in the first two rows of the following array as shown below. The remaining rows are then evaluated from these.

$$\begin{array}{cccc}
 a_n & a_{n-2} & a_{n-4} & a_{n-6} \dots\dots \\
 a_{n-1} & a_{n-3} & a_{n-5} & a_{n-7} \dots\dots \\
 F_{n-2} & b_2 & b_3 & \dots\dots \\
 F_{n-3} & c_2 & \dots\dots & \\
 \vdots & & & \\
 F_1 & \dots & & \\
 F_0 & \dots & &
 \end{array}$$

* $a_n > 0$ is not restrictive since this is readily achieved by multiplying Equation [5.10] by -1.

The constants F_{n-2} , b_2 , b_3 etc., are evaluated as follows

$$F_{n-2} = a_{n-1}a_{n-2} - a_n a_{n-3}$$

$$b_2 = a_{n-1}a_{n-4} - a_n a_{n-5}$$

Similarly the constants F_{n-3} , c_2 etc., are given by

$$F_{n-3} = F_{n-2}a_{n-3} - a_{n-1} b_2$$

$$c_2 = F_{n-2}a_{n-5} - a_{n-1} b_3$$

The same pattern is followed for the remaining rows. The complete array is triangular ending with the F_0 term. Routh's criterion states that if any of the terms in the first column, a_n , a_{n-1} , F_{n-2} , F_{n-3} , \dots , F_1 , F_0 becomes negative the system is unstable. The last of these terms, F_0 , is of special interest. This term always contains the product $a_0 F_1$. Duncan (5.15) has shown that for an otherwise stable system, if by varying some design parameter so that only a_0 changes sign from plus to minus then one real root goes from negative to positive and a divergence appears in the solution. On the other hand if only F_1 goes from plus to minus then the real part of a complex pair of roots

becomes positive and a divergent oscillation appears in the solution.

If we apply the above test to a cubic equation given by

$$A\sigma^3 + B\sigma^2 + C\sigma + D = 0 \quad A > 0 \quad [5.11]$$

then the necessary and sufficient conditions for stability are that

$$A, B, D, (BC - AD) > 0$$

These conditions imply that $C > 0$.

For a quartic equation given by

$$A\sigma^4 + B\sigma^3 + C\sigma^2 + D\sigma + E = 0 \quad A > 0 \quad [5.12]$$

The necessary and sufficient conditions for stability are that

$$A, B, D, E > 0$$

and

$$D(BC - AD) - B^3E > 0 \quad [5.12a]$$

The conditions imply that $C > 0$. The quantity on the left hand side of Equation [5.12a] is known as Routh's discriminant.

For a quintic equation given by

$$A\sigma^5 + B\sigma^4 + C\sigma^3 + D\sigma^2 + E\sigma + F = 0 \quad A > 0 \quad [5.13]$$

The system will be stable if

$$A, B, D, F > 0$$

$$BC - AD > 0$$

$$D(BE - AF)(BC - AD) - B(BE - AF)^2 - F(BC - AD)^2 > 0$$

These conditions imply that $C, E > 0$.

SOLUTIONS OF THE CHARACTERISTIC EQUATION

Methods for solving the characteristic equation are described in the literature (5.16), (5.17) and (5.18). Furthermore, programs for use on various electronic computers are also available. It is clear that the characteristic equation for longitudinal motion of a hydrofoil boat as given in Equation [5.8] involves the interaction of so many hydrodynamic coefficients that it sometimes becomes extremely difficult to interpret the effect of parameter changes on the stability. Some attempt to simplify these equations was made by Chuck, Luke and Scroggs (5.12) with only limited success.

For hydrofoil boats with fully submerged foils Chuck et al obtained an approximate factorization of Equation [5.8] as follows:

$$\begin{aligned} & \left(\sigma' - Z_w'' \right) \left(\sigma' - M_q'' \right) \left[\sigma'^3 + \left(\frac{M_\theta''}{M_q''} + \frac{Z_h''}{Z_w''} - X_u'' \right) \sigma'^2 \right. \\ & \left. + \frac{E}{Z_w'' M_q''} \sigma' + \frac{F}{Z_w'' M_q''} \right] = 0 \quad \text{(for fully submerged foils)} \end{aligned} \quad [5.14]$$

They found that this equation gave roots which closely approximated those of the more exact equation for the range of craft configurations considered in their study. The first two factors are obtained when one discards the terms in the equations of motion resulting from changes in speed and depth. Equation [5.7] then becomes

$$\begin{vmatrix} \bar{m}' \sigma'^2 - Z_w' \sigma' & - Z_q' + Z_{\dot{w}}' \sigma' - Z_w' \\ - M_w' \sigma' & I_y' \sigma'^2 - M_q' \sigma' - M_w' \end{vmatrix} = 0$$

yielding

$$\left(\sigma' - \frac{Z_w'}{\bar{m}'} \right) \left(\sigma' - \frac{M_q'}{I_y'} \right) \approx 0$$

since the product $M_w' (Z_q' + Z_{\dot{w}}' + \bar{m}')$ is much smaller than $Z_w' M_q'$.

Although Equation [5.14] relates two of the roots directly to the craft dimensions in a simple way they are of limited usefulness since they give the two most negative roots. The craft performance depends almost entirely on the values of the three low frequency roots.

For craft with surface piercing foils fore and aft the same reference found the following approximate form for the characteristic equation

$$\begin{aligned} \sigma'^5 + \left(-Z_w'' - M_q'' \right) \sigma'^4 + \left(-M_\theta'' - Z_h'' + Z_w'' M_q'' \right) \sigma'^3 + \left(Z_w'' M_\theta'' \right. \\ \left. + M_h'' + Z_h'' M_q'' \right) \sigma'^2 + E\sigma' + F = 0 \end{aligned} \quad [5.15]$$

It was found that in most cases $\sigma' = -\frac{F}{E}$ was a root of this equation. This root was also usually much smaller than the other roots.

Although the foregoing simplifications are useful and convenient they do not furnish sufficient insight to be of great value in interpreting the effect of parameter changes on the stability. In many cases the effect of surge may be neglected as is often done in the stability analysis of aircraft and underwater vehicles. When this is done the X' equation (Equation [5.1]) and the terms $Z_u'u'$ and $M_u'u'$ are dropped from the equations of motion. This leads to the following quartic equation in σ' obtained from Equation [5.7] where the term Z_w has also been dropped as small.

$$\left(\sigma'^2 - \frac{M_q'}{I'} \sigma - \frac{M_\theta' + M_w'}{I'} \right) \left(\sigma'^2 - \frac{Z_w'}{m'} \sigma' - \frac{Z_h'}{m'} \right) - \frac{Z_q' M_w'}{m' I'} \left(\sigma' + \frac{M_h'}{M_w'} \right) \left(\sigma' + \frac{Z_w' + Z_\theta'}{Z_q'} \right) = 0 \quad [5.16]$$

which may also be written in the usual form as

$$A\sigma'^4 + B\sigma'^3 + C\sigma'^2 + D\sigma' + E = 0 \quad [5.17]$$

where

$$A = 1$$

$$B = -\frac{Z_w'}{m'} - \frac{M_q'}{I'}$$

$$C = -\frac{Z_h'}{m'} + \frac{Z_w' M_q'}{m' I'} - \frac{M_\theta' + M_w'}{I'} - \frac{Z_q' M_w'}{m' I'}$$

$$D = \frac{Z_q' Z_h'}{m'^2} + \frac{Z_w' (M_\theta' + M_w')}{m' I'} - \frac{M_w' (Z_w' + Z_\theta')}{m' I'} - \frac{Z_q' M_h'}{m' I'}$$

$$E = \frac{1}{m' I'} \left[Z_h' (M_\theta' + M_w') - M_h' (Z_w' + Z_\theta') \right]$$

Setting the first two terms in the parentheses of Equation [5.16] equal to zero yield the characteristic equations for the uncoupled pitch and heave motion respectively. The last two terms are the coupling terms. When these terms are zero or small the stability roots are simply the roots of the characteristic equations for uncoupled motions. The values of the uncoupled non-dimensional stability roots are thus given by

$$p_{1,2}' = \frac{Z_w'}{2m'} \pm \sqrt{\left(\frac{Z_w'}{2m'}\right)^2 + \frac{Z_h'}{m'}} = p_{1,2} \frac{l}{U} \quad [5.18]$$

$$p_1' + p_2' = \frac{Z_w'}{m'} = (p_1 + p_2) \frac{l}{U} \quad [5.18a]$$

$$p_{3,4}' = \frac{M_q'}{2I_y'} \pm \sqrt{\left(\frac{M_q'}{2I_y'}\right)^2 + \frac{M_\theta' + M_w'}{I_y'}} = p_{3,4} \frac{l}{U} \quad [5.19]$$

$$p_3' + p_4' = \frac{M_q'}{I_y'} = (p_3 + p_4) \frac{l}{U} \quad [5.19a]$$

The two roots given by $p_{1,2}'$ describe the uncoupled stability of the heave degree of freedom and those for $p_{3,4}'$ the pitch degree of freedom. The uncoupled motion in each degree of freedom has the properties of a simple harmonic oscillator (linear second order system) and can therefore be described in terms of the well known

properties of linear oscillators. Thus the undamped natural frequency in the uncoupled heave and pitch degrees of freedom are given by

$$\left(\omega_n'\right)_H = \left(-\frac{Z_h'}{m'}\right)^{\frac{1}{2}} = \left(\omega_n\right)_H \frac{l}{U} \quad [5.20]$$

$$\left(\omega_n'\right)_P = \left(-\frac{M_\theta' + M_w'}{I'}\right)^{\frac{1}{2}} = \left(\omega_n\right)_P \frac{l}{U} \quad [5.21]$$

respectively. The damping ratios in heave and pitch are correspondingly

$$\zeta_{H'} = \frac{-Z_w'}{2m' \left(\omega_n'\right)_H} = \zeta_H \quad [5.22]$$

$$\zeta_{P'} = \frac{-M_q'}{2I' \left(\omega_n'\right)_P} = \zeta_P \quad [5.23]$$

It can be seen from the above equations that the roots can also be expressed in terms of ζ and ω_n as follows

$$p_{1,2} = -\omega_n \zeta \left(1 \pm \frac{\sqrt{1 - \zeta^2}}{\zeta} \right) \quad [5.24a]$$

For $0 < \zeta < 1$ the roots are a complex pair ($p_{1,2} = \sigma_r \pm i\sigma_i$)

where

$$\sigma_r = -\omega_n \zeta = -\omega_n \cos \gamma$$

$$\sigma_i = \pm \omega_n \sqrt{1 - \zeta^2} = \pm \omega_n \sin \gamma$$

$$\gamma = \tan^{-1} \left| \sigma_i / \sigma_r \right|$$

For $\zeta > 1$ the roots are real and the smallest one $\sigma_{r(\min)}$ is given by

$$p_2 = -\omega_n \left(\zeta - \sqrt{\zeta^2 - 1} \right) = \sigma_{r(\min)} \quad [5.24b]$$

It is seen that for a given value of ω_n this root approaches zero rapidly as ζ is increased. Figure 5.3 is a plot of this root versus ζ for $\omega_n = 1$.

Equations [5.18] - [5.24] are simple enough relations to furnish considerable insight to the designer in determining the effect of parameter changes on the uncoupled stability roots since estimates of M_q' , M_θ' , M_w' , Z_w' and Z_h' can be related to the boat geometry in a fairly simple manner. In any practical case however the effect of the coupling term on the values of the stability roots must be taken into account. In this connection, solution of the characteristic equation, as given in the form of Equation [5.16], by the root-locus method can be of value to the designer. In this method the uncoupled roots are first plotted on graph paper and the variation in their values are traced by a simple graphical construction as the magnitude of the coupling term is gradually increased from zero to its design value. By this method it becomes possible to trace the role of each derivative in the determination of the stability roots of the coupled equations of motion. This can serve as a valuable aid to the designer in assessing, in a graphical manner, the effects of parameter changes on the stability roots.

ROOT-LOCUS METHOD

Equation [5.16] may be rewritten in the following form

$$\frac{\bar{K}' (\sigma' - z_1') (\sigma' - z_2')}{(\sigma' - p_1') (\sigma' - p_2') (\sigma' - p_3') (\sigma' - p_4')} = -1 \quad [5.25]$$

where p_1' , p_2' , p_3' , p_4' are the roots of the uncoupled motion in heave and pitch respectively as determined from Equations [5.18]

and [5.19] and for $|Z_q'| > 0$ and $|M_w'| > 0$

$$z_1' = -\left(\frac{M_h'}{M_w'}\right)$$

$$z_2' = -\left(\frac{Z_w' + Z_\theta'}{Z_q'}\right)$$

$$\bar{K}' = -\frac{Z_q' M_w'}{m' I'} \quad [5.25a]$$

The p' 's are called the poles and the z' 's are called the zeros of the left hand side of Equation [5.25].

For $\left|\frac{M_h'}{M_w'}\right| \gg |\sigma_d'|$, where $|\sigma_d'|$ is the modulus of the largest

dominant root, one of the zeros may be removed since the numerator of Equation [5.25] can be approximated by

$$\bar{K}' (\sigma' - z_2')$$

where

$$\bar{K}' \approx -\frac{Z_q' M_h'}{m' I'} \quad [5.25b]$$

If $\frac{Z_w' + Z_\theta'}{Z_q'} \gg |\sigma_d'|$ then the other zero may be removed since

the numerator of Equation [5.25] can be approximated by

5.32

$$\bar{K}' (\sigma' - z_1')$$

where

$$\bar{K}' \approx - \frac{M_w' (Z_w' + Z_\theta')}{I' m'} \quad [5.25c]$$

If both of the above conditions are satisfied then both zeros may be removed since the numerator of Equation [5.25] is simply \bar{K}' where

$$\bar{K}' \approx - \frac{M_h' (Z_w' + Z_\theta')}{I' m'} \quad [5.25d]$$

The roots of the coupled equations are the values of σ' that satisfy Equation [5.25]. As the root locus method is ordinarily used, in the synthesis of automatic control systems, the term \bar{K}' is a control gain constant which can, for most control systems, be set at various values without changing the values of the poles and zeros. A graph of the locus of solutions of an equation such as Equation [5.25] is thus found for various values of \bar{K}' in order to determine a desirable value of this gain constant. As used here, however it is seen from Equation [5.25] and the subsequent definitions of \bar{K}' that, of the locus of roots for an arbitrarily selected range of values of \bar{K}' , the only applicable solutions of the coupled characteristic equation are the points on the locus at which \bar{K}' is given by one of Equations [5.25a] - [5.25d] and for which the poles and zeros either remained unchanged or changed only slightly. Although this severely

restricts the usefulness of the method situations exist in which this approach can furnish insight into the effect of various parameters on stability not as readily obtainable by conventional methods. Some examples will be discussed in a later section of this chapter.

W. R. Evans (5.19) has developed a technique for the graphical construction of the locus of roots of an equation such as Equation [5.25]* for various values of \bar{K}' provided the poles and zeros remain fixed. An example of such a locus is shown in Figure 5.4 where

$$\begin{aligned} z_1' &= +0.5 & p_3' &= -2.0 \\ z_2' &= -7.0 & p_4' &= -5.0 \\ p_1' &= -2.5 + i \\ p_2' &= -2.5 - i \end{aligned}$$

and \bar{K}' varies over a wide range of positive and negative values. It is seen from Equation [5.25] that for $K = 0$ the roots are simply the poles p_1' , p_2' , p_3' , p_4' . As \bar{K}' is increased or decreased four loci of roots are generated, one passing through each pole at $\bar{K}' = 0$. For any particular root σ' the terms $\sigma' - z_1'$, $\sigma' - z_2'$, $\sigma' - p_1'$, etc., are in general complex numbers designating directed line segments with modulus $|\sigma' - z_1'|$, etc., and amplitude ψ_1 , etc., (see Figure 5.4) so that Equation [5.25] may be written as the following two equations

* The method is applicable to equations with any number of poles and zeros as long as the number of zeros does not exceed the number of poles.

5.34

$$\psi_1 + \psi_2 - \phi_1 - \phi_2 - \phi_3 - \phi_4 = \begin{cases} (1 + 2m) 180^\circ & \text{for } \bar{K}' > 0 \\ (2m) 180^\circ & \text{for } \bar{K}' < 0 \end{cases} \quad [5.26a]$$

$$\frac{\bar{K}' \left| \sigma' - z_1' \right| \left| \sigma' - z_2' \right|}{\left| \sigma' - p_1' \right| \left| \sigma' - p_2' \right| \left| \sigma' - p_3' \right| \left| \sigma' - p_4' \right|} = 1 \quad [5.26b]$$

for $m = 0 \pm 1, \pm 2, \dots$

and where the angles ψ and ϕ are defined in Figure 5.4. Equation [5.26a] says that the locus of possible values of σ' must be such that the left hand side of this equation is real and negative for $\bar{K}' > 0$ and real and positive for $\bar{K}' < 0$. From each of the roots p_1' , p_2' , p_3' and p_4' a locus can be drawn which satisfies this equation. Simple rules have been devised [see for example References (5.19), (5.20)] to aid in drawing these loci and once these have been mastered it is sometimes possible to sketch in the loci roughly by inspection. For greater accuracy and for the more complicated root loci the use of an integrating protractor* is very helpful. Once the loci of the roots of interest are drawn it is possible to find the value of σ' corresponding to any value of \bar{K}' from a plot of σ' versus \bar{K}' obtained with the aid of Equation [5.26b]. This procedure is further simplified with the aid of the Spirule.

*A commercially available instrument for use in constructing root-locus plots, called the Spirule, has this as one of its features.

PRELIMINARY ANALYSIS FOR LONGITUDINAL STABILITY

In designing for a given degree of stability, the selection of parameters based on the uncoupled motion in pitch and heave is generally a good starting point. Furthermore, it is helpful in the preliminary analysis to use simplifying approximations as much as possible and to make more precise calculations in the final stages. On this basis we investigate solutions of Equation [5.16] where the coefficients are approximated by the following expressions which are based on the more exact ones derived in Reference (5.5). All summations are taken over all the submerged hydrofoil panels and struts. It is assumed that the thrust couple is zero. Some of the expressions will be seen to be generalizations of results obtained by Weinblum (5.21).

Uncoupled Heave Damping

With the aid of Reference (5.5) we approximate the heave damping term of Equation [5.16], but in dimensional form, by

$$\begin{aligned}
 -Z_w &\approx \frac{1}{2}\rho U \sum C_{L_\alpha} S \cos^2 \Gamma \\
 &= \frac{1}{2}\rho U C_{L_{\alpha f}} \bar{S}_f \left[1 + \frac{C_{L_{\alpha a}} \bar{S}_a}{C_{L_{\alpha f}} \bar{S}_f} \right] \\
 &= \frac{1}{2}\rho U C_{L_{\alpha f}} \bar{S}_f \left[1 + \frac{\kappa_1}{\kappa_2} \frac{x_f}{x_a} \right] \quad [5.27]
 \end{aligned}$$

where

$$C_{L_{\alpha f}} \left(= \frac{\sum C_{L_{\alpha}} \cos \Gamma S \cos \Gamma}{\sum S \cos \Gamma} \right)_f \text{ is the mean effective}$$

lift-curve slope coefficient at the forward foils,

$$\bar{S}_f \left(= \sum S \cos \Gamma \right)_f \text{ is the horizontal projected area}$$

of the forward foils,

x_f distance from c.g. to center of lift of forward foils,

f, a subscripts referring to the fore and aft foils respectively,

$$k_1 = \frac{C_{L_{\alpha a}}}{C_{L_{\alpha f}}}$$

$$k_2 = \frac{C_{L_a}}{C_{L_f}}$$

$$C_{L_f} \left(= \frac{\sum C_L S \cos \Gamma}{\bar{S}} \right)_f \text{ is the mean lift coefficient at}$$

the forward foils.

The mass of the boat may be written in terms of the lift on the foil system as

$$m = \frac{\rho U^2 C_{L_f} \bar{S}_f}{2g} \left[1 + \frac{x_f}{x_a} \right] = \frac{\rho U^2 C_{L_f} \bar{S}_f}{2g x_a'} \quad [5.28]$$

so that on dividing m into Equation [5.27] we obtain, the sum of the stability roots for uncoupled heave motion

$$\frac{Z_w}{m} \approx -\frac{g}{U} \frac{C_{L_{\alpha f}}}{C_{L_f}} \left(x_a' + \frac{\kappa_1}{\kappa_2} x_f' \right) = p_1 + p_2 \quad [5.29]$$

By multiplying Equation [5.29] by l/U we obtain the non-dimensional form

$$\frac{Z_w'}{m'} = -\frac{1}{F^2} \frac{C_{L_{\alpha f}}}{C_{L_f}} \left(x_a' + \frac{\kappa_1}{\kappa_2} x_f' \right) = p_1' + p_2' \quad [5.30]$$

where

F is the Froude number based on the length l

l is a reference length. In this case

$$l = x_f + x_a$$

A likely value for $C_{L_{af}}/C_{L_f}$ for a subcavitating foil system at maximum speed is somewhere between 10 and 25. A reasonable maximum Froude number is of the order of $F = 1.5$ to 2.0 . Using these values in Equation [5.30] gives an approximate range for $p_1' + p_2'$, assuming the value κ_1/κ_2 is close to unity, of

$$\frac{Z_w'}{m'} = p_1' + p_2' \approx -2.5 \text{ to } -11 \quad [5.31]$$

In dimensional form this is

$$\frac{Z_w}{m} = p_1 + p_2 \approx -2.5 \frac{U}{l} \text{ to } -11 \frac{U}{l} \text{ sec.}^{-1} \quad [5.32]$$

Effect of Speed - If the submerged foil area does not change with speed then the value of Z_w'/m' will not change with speed since F^2 times the lift coefficient and lift curve slope will remain practically constant. On the other hand if the submerged foil area changes with speed in a way such that C_L remains constant (as may be possible with area stabilized craft) then the value of Z_w'/m' will vary as $1/U^2$ and that of Z_w/m as $1/U$ provided

$C_{L_{\alpha f}}$ and $C_{L_{\alpha a}}$ remain constant.

Uncoupled Heave Stiffness

Using Reference (5.5) we approximate the heave stiffness term of Equation [5.16], but in dimensional form, by

$$- Z_h = \frac{1}{2} \rho U^2 \sum \left(C_L c_w \cot \Gamma + C_{L_h} \frac{S \cos \Gamma}{\bar{c}_s} \right) \quad [5.33]$$

In order to express Z_h in terms of the foil geometry we idealize the foil area distribution as shown in Figure 5.5. We consider the foil to have two principal panels, a horizontal flat panel and a surface piercing panel set at a dihedral angle Γ . If we consider the lift developed on the dihedral panel separately from that on the horizontal one we may approximate Equation [5.33] by

$$\begin{aligned} - Z_h = \frac{1}{2} \rho U^2 & \left\{ \frac{C_{L_f} \bar{S}_f}{d_f} \frac{A_f}{\bar{S}_f} \left[\left(\frac{c_w}{\bar{c}_s} \right)_f + \frac{1}{C_{L_f}} \left(\frac{C_{L_h}}{\bar{c}_s/d} \right)_f \right] + R_f \right. \\ & \left. + \frac{C_{L_a} \bar{S}_a}{d_a} \frac{A_a}{\bar{S}_a} \left[\left(\frac{c_w}{\bar{c}_s} \right)_a + \frac{1}{C_{L_a}} \left(\frac{C_{L_h}}{\bar{c}_s/d} \right)_a \right] + R_a \right\} \quad [5.34] \end{aligned}$$

where

d_f is the depth of the forward foil (see Figure 5.5),

A_f is the sum of the horizontal projected area of the two forward surface piercing panels,

$\left(\frac{c_w}{c_s}\right)_f$ is the chord of the surface piercing panel measured at the free surface,

$\left(\bar{c}_s\right)_f$ is the mean chord of the forward surface piercing panel,

$\left(C_{L_h}\right)_f \left(= \frac{dC_L}{d\left(\frac{h}{\bar{c}_s}\right)} \right)$ is the effective lift-depth coefficient of the forward surface piercing panel,

R_f represents a small remainder which may be thought of as the contribution of the horizontal panel.

The term R_f is normally determined together with the term containing $\left(C_{L_h}\right)_f$ as described in Reference (5.5) but is shown separately

here for convenience. As A_f goes to zero R_f becomes the value for a completely submerged foil, while for $A_f = S_f$ it becomes equal to zero. Equation [5.34] may be written

$$- Z_h = \frac{L_f}{d_f} \frac{A_f}{S_f} \left(\frac{c_w}{c_s} + b_f \right)_f + \frac{L_a}{d_a} \frac{A_a}{S_a} \left(\frac{c_w}{c_s} + b_a \right)_a + \frac{1}{2} \rho U^2 (R_f + R_a) \quad [5.35]$$

where

$$L_f \quad \left(= \frac{1}{2} \rho U^2 C_{L_f} \bar{S}_f \right) \text{ is the lift at the forward foils,}$$

$$b_f = \left(\frac{C_{L_h}}{\bar{c}_s/d} \right)_f \frac{1}{C_{L_f}},$$

$$L_a = m_g - L_f.$$

The heave stiffness at the forward and aft foils is seen to be approximately inversely proportional to d_f and d_a respectively.

For a given value of d_f and d_a the stiffness is largest when

$A_f/\bar{S}_f = A_a/\bar{S}_a = 1$; i.e., the horizontal panel area is zero. Increasing the ratio c_w/\bar{c}_s also increases the heave stiffness. The

value of b depends on a number of factors but principally on the dihedral angle depth-chord ratio and aspect ratio, as described in Reference (5.5). According to this reference b has a magnitude which usually lies between about $\frac{1}{2}$ and 2^* .

According to Equation [5.20] the square of the undamped natural frequency for the uncoupled heave motion is given by

* Values in the vicinity of five have been estimated in Reference (5.12) and (5.19) but details of the method of determination are not given. On the other hand this term has been assumed to be negligible in References (5.3) and (5.13).

$$\begin{aligned} \left(w_n \right)_H^2 = - \frac{Z_h}{m} = \frac{g}{l} & \left[\frac{x_a'}{d_f'} \frac{A_f}{\bar{S}_f} \left(\frac{c_w}{\bar{c}_s} + b_f \right)_f + \frac{x_f'}{d_a'} \frac{A_a}{\bar{S}_a} \left(\frac{c_w}{\bar{c}_s} + b_a \right)_a \right] \\ & + \frac{1}{2} \rho U^2 \left(\frac{R_f + R_a}{m} \right) \end{aligned} \quad [5.36]$$

Multiplying through by l^2/U^2 we obtain the non-dimensional form

$$\begin{aligned} \left(w_n' \right)_H^2 = - \frac{Z_h'}{m'} = \frac{l}{F^2} & \left[\frac{x_a'}{d_f'} \frac{A_f}{\bar{S}_f} \left(\frac{c_w}{\bar{c}_s} + b_f \right)_f + \frac{x_f'}{d_a'} \frac{A_a}{\bar{S}_a} \left(\frac{c_w}{\bar{c}_s} + b_a \right)_a \right] \\ & + \frac{1}{2} \rho l^2 \left(\frac{R_f + R_a}{m} \right) \end{aligned} \quad [5.37]$$

For V-foils fore and aft we have $A/\bar{S} = 1$. If in addition

$d_a = d_f = d$, $b_a = b_f = b$ and $(c_w/\bar{c}_s)_a = (c_w/\bar{c}_s)_f$ we get, since

$$x_a' + x_f' = l$$

$$\left(w_n \right)_{H2}^2 = \frac{lg}{d} \frac{c_w}{\bar{c}_s} + b \quad [5.38]$$

$$\left(\omega_n'\right)_{H2}^2 = \frac{1}{F^2} \frac{\ell}{d} \left(\frac{c_w}{\bar{c}_s} + b \right) \quad [5.39]$$

For completely submerged foils aft and V-foils forward Equations [5.36] and [5.37] become respectively

$$\left(\omega_n\right)_{H1}^2 = \frac{g}{\ell} \frac{x_a}{d_f} \left(\frac{c_w}{\bar{c}_s} + b_f \right) + \frac{1}{2} \rho U^2 \left(C_{L_h} \bar{S}_a / m \bar{c}_s \right)_a \quad [5.40]$$

$$\left(\omega_n'\right)_{H1}^2 = \frac{1}{F^2} \frac{x_a}{d_f} \left(\frac{c_w}{\bar{c}_s} + b_f \right) + \frac{1}{2} \rho \ell^2 \left(C_{L_h} \bar{S}_a / m \bar{c}_s \right)_a \quad [5.41]$$

The contribution from the term for the completely submerged foil (the second term on the right) is generally very small at depth-chord ratios near unity or greater.

Effect of Speed - It is seen from Equation [5.36] that $\left(\omega_n\right)_H^2$ is inversely proportional to d and will vary with speed approximately as d is allowed to vary with speed. For constant foil depths $\left(\omega_n\right)_H$ is practically independent of speed.

Uncoupled Heave Damping Ratio

The uncoupled heave damping ratio is, from Equation [5.22]

$$\zeta_H = \frac{-Z_w'/m'}{2\left(\omega_n'\right)_H}$$

which gives with the aid of Equations [5.30] and [5.37]

$$\zeta_H = \frac{\frac{C_{L_{\alpha f}}}{C_{L_f}} \left(x_a' + \frac{\kappa_1}{\kappa_2} x_f' \right)}{2F \left[\frac{x_a'}{d_f'} \frac{A_f}{S_f} \left(\frac{c_w}{\bar{c}_s} + b_f \right)_f + \frac{x_f'}{d_a'} \frac{A_a}{S_a} \left(\frac{c_w}{\bar{c}_s} + b_a \right)_a + \frac{1}{2} \rho t^3 \left(\frac{R_f + R_a}{m} \right)^{\frac{1}{2}} \right]} \quad [5.42]$$

For the case of two V-foils as represented in Equation [5.38] and [5.39]; i.e., $b_f = b_a = b$, $d_f = d_a = d$ and $(c_w/\bar{c}_s)_f = (c_w/\bar{c}_s)_a$.

$$\zeta_H = \frac{1}{2F} \frac{C_{L_{\alpha f}}}{C_{L_f}} \sqrt{\frac{d}{t(c_w/\bar{c}_s + b)}} \left(x_a' + \frac{\kappa_1}{\kappa_2} x_f' \right) \quad [5.43]$$

For the case of submerged foils aft and V-foils forward we have, on neglecting the small contribution of the aft foil in Equation [5.41]

$$\zeta_H \approx \frac{1}{2F} \frac{C_{L_{\alpha f}}}{C_{L_f}} \sqrt{\frac{d_f'}{x_a' (c_w/\bar{c}_s + b)}} \left(x_a' + \frac{\kappa_1}{\kappa_2} x_f' \right) \quad [5.44]$$

It will be seen later that it is generally desirable not to allow this quantity to become much greater than unity nor less than about

.70. However, this depends on the uncoupled pitch mode and the coupling term which are discussed subsequently.

It can be seen that for completely submerged foils Equation [5.42] reduces to

$$\zeta_H = \frac{\frac{C_{L_{\alpha f}}}{C_{L_f}} \left(\dot{x}_a' + \frac{\kappa_1}{\kappa_2} \dot{x}_f' \right)}{2F \left\{ \frac{\rho \ell^2}{2m} \left[\left(C_{L_h} \bar{S}_f / \bar{c}_s \right)_f + \left(C_{L_h} \bar{S}_a / \bar{c}_s \right)_a \right] \right\}^{\frac{1}{2}}} \quad [5.45]$$

Due to the small magnitude of C_{L_h} for the usual fully wetted submerged foil systems the value of ζ_H in these cases is generally much greater than unity. This leads to two real roots given by

$$p_{1,2}' = \left(\omega_n \right)_H' \zeta_H \left(1 \pm \frac{\sqrt{\zeta_H^2 - 1}}{\zeta_H} \right) \quad \text{for } \zeta_H > 1$$

The term dependent on ζ_H given by $\zeta_H^{-1} \sqrt{\zeta_H^2 - 1}$ and plotted in Figure 5.3 becomes small very rapidly with increasing ζ_H so that the smaller of the roots p_1' , p_2' usually shows only a very

slight stability in the uncoupled heave.

Effect of Speed - For the case given by Equation [5.42], if d is held constant then C_L will be proportional to $1/U^2$, ζ_H will increase directly with speed and, since $(\omega_n)_H$ is practically constant, the damped natural frequency will decrease with increasing speed. On the other hand, if C_L is to be held constant, the \sqrt{d} is proportional to $1/U$ and ζ_H varies inversely with the speed squared provided the remaining terms do not change very much.

Uncoupled Pitch Damping

From Reference (5.5) we approximate the pitch damping term of Equation [5.16], but in dimensional form, by

$$-M_q \approx \frac{1}{2}\rho U C_{L_{\alpha f}} x_f \bar{S}_f \left(\dot{x}_f + \frac{\kappa_1}{\kappa_2} x_a \right) \quad [5.46]$$

If we put $I = mk^2$ then we have, on combining Equation [5.28] and [5.46]

$$\frac{M_q}{I} \approx -\frac{g}{U} \frac{x_a' x_f'}{k'^2} - \frac{C_{L_{\alpha f}}}{C_{L_f}} \left(\dot{x}_f' + \frac{\kappa_1}{\kappa_2} x_a' \right) = p_3 + p_4 \quad [5.47]$$

which according to Equation [5.19a] is the sum of the two roots for uncoupled pitch. By multiplying through by l/U we obtain the

non-dimensional form

$$\frac{M_q'}{I'} = - \frac{1}{F^2} \frac{x_a' x_f'}{k'^2} \frac{C_{L_{\alpha f}}}{C_{L_f}} \left(x_f' + \frac{\kappa_1}{\kappa_2} x_a' \right) = p_3' + p_4' \quad [5.48]$$

By comparing these expressions with Equations [5.29] and [5.30] it is seen that

$$\frac{M_q}{I} = \frac{Z_w}{m} \frac{x_a' x_f'}{k'^2} \frac{\left(x_f' + \frac{\kappa_1}{\kappa_2} x_a' \right)}{\left(x_a' + \frac{\kappa_1}{\kappa_2} x_f' \right)}$$

$$\frac{M_q'}{I'} = \frac{Z_w'}{m'} \frac{x_a' x_f'}{k'^2} \frac{\left(x_f' + \frac{\kappa_1}{\kappa_2} x_a' \right)}{\left(x_a' + \frac{\kappa_1}{\kappa_2} x_f' \right)}$$

Representative values for a tandem foil system are $x_f' \approx 1/2$ and $k' = 1/3$. This gives

$$\frac{x_a' x_f'}{k'^2} = 9/4$$

Thus, for $\kappa_1 \approx \kappa_2$, the sum of the stability roots in uncoupled pitch may be as large as about twice that for heave. As x_f' or x_a' becomes smaller this ratio becomes smaller becoming equal to unity when x_f' or x_a' equals 0.13.

Uncoupled Pitch Stiffness

From Reference (5.5) the pitch stiffness term of Equation [5.16] may be approximated, in dimensional form, by the following expression

$$-(M_\theta + M_w U) = -\sum \left[x^2 Z_h - x Z_w U \right] \quad [5.49]$$

For the first part of this term we have, with the aid of Equation [5.35]

$$-M_\theta = \frac{mg x_f' x_a'}{l} \left[\frac{x_f'}{d_f'} \frac{A_f}{S_f} \left(\frac{c_w}{c_s} + b_f \right)_f + \frac{x_a'}{d_a'} \frac{A_a}{S_a} \left(\frac{c_w}{c_s} + b_a \right)_a \right] + \frac{\rho U^2}{2} \left(x_f'^2 R_f + x_a'^2 R_a \right).$$

[5.50]

It is clear that $-M_{\theta}$ is always positive and therefore produces a restoring moment. For the second part of this term we have

$$\begin{aligned} -M_w &= -\frac{1}{2}\rho U C_{L_{\alpha f}} \left(x_f \bar{S}_f - \kappa_1 x_a \bar{S}_a \right) \\ &= \frac{1}{2}\rho U C_{L_{\alpha f}} x_f \bar{S}_f \left(\frac{\kappa_1}{\kappa_2} - 1 \right) \end{aligned} \quad [5.51]$$

In order for $-M_w$ to be positive it is necessary that $\frac{\kappa_1}{\kappa_2} > 1$. In order to achieve this it may become necessary to operate one of the hydrofoils at a non-optimum condition, since it is usually necessary to operate the aft foil either at a lesser loading, a greater depth, a higher aspect ratio, with less sweep or in some other appropriate way [see Reference (5.5)] different from the forward foils. The effect of downwash from the forward foil on the aft foil should also be taken into account in the determination of $C_{L_{\alpha}}$ on the aft foil [see Reference (5.5)]. The stabilizing effect of $-M_w$ is sometimes expressed in terms of the dimensionless distance aft of the c.g. at which $-Z_w$ acts. This has sometimes been called the static margin* of the boat and is given by

* Static margin in aircraft is usually non-dimensionalized with respect to the mean chord of the main lifting surface whereas here it is with respect to the distance between foils l .

$$\text{s.m.} = \frac{M_w}{Z_w \ell} = x_a' x_f' \frac{\left(\frac{\kappa_1}{\kappa_2} - 1 \right)}{\left(x_a' + \frac{\kappa_1}{\kappa_2} x_f' \right)} \quad [5.52]$$

Solving this equation for κ_1/κ_2 we obtain

$$\kappa_1/\kappa_2 = \frac{x_a'}{x_f'} \left(\frac{x_f' + \text{s.m.}}{x_a' - \text{s.m.}} \right) \quad [5.53]$$

Although the static margin is of primary importance in the stability of the short period longitudinal mode of aircraft its influence on the longitudinal stability of hydrofoil boats is usually of less importance. This is especially true for boats with surface piercing hydrofoils fore and aft since $-M_\theta$ is usually a relatively large factor. (See also Equations [5.56] and [5.58] and related discussion). For boats with completely submerged foils, where $-M_\theta$ is small Reference (5.12) shows that, for a conventional configuration with $\bar{S}_f/\bar{S}_a = 3/2$, the effect of increasing the static margin from $-.10$ to $+.30$, though increasing the longitudinal stability of the boat, did not improve the stability sufficiently to eliminate the need for stability augmentation. Similar results for a canard configuration with $\bar{S}_f/\bar{S}_a = 2/3$

are reported in Reference (5.22). When it is realized that this static margin variation corresponded to a variation of κ_1/κ_2 of from 2/3 to 6 or a movement of the c.g. from mid-ships to 10 percent aft of the forward foils it is clear how difficult it is to adequately stabilize a completely submerged foil system of this type without automatic controls. Nevertheless, some static margin may be desirable in order to allow for some shift in the longitudinal c.g. location without substantial adverse changes in the transfer function of the uncontrolled boat and to provide some pitch stability in case of failure of the automatic control system.

According to Equation [5.21] the square of the undamped natural frequency for the uncoupled pitch motion is given by

$$\begin{aligned}
 (\omega_n)_P^2 &= -\frac{M_\theta + M_w U}{mk^2} = \frac{g}{l} \frac{x_f' x_a'}{k'^2} \left\{ \left[\frac{x_f'}{d_f'} \frac{A_f}{S_f} \left(\frac{c_w}{\bar{c}_s} + b_f \right) \right]_f \right. \\
 &\quad \left. + \frac{x_a'}{d_a'} \frac{A_a}{S_a} \left(\frac{c_w}{\bar{c}_s} + b_a \right) \right]_a + \frac{\rho U^2 l}{2mg} \left(\frac{x_f}{x_a} R_f + \frac{x_a}{x_f} R_a \right) \\
 &\quad \left. + \frac{C_{L\alpha f}}{C_{L_f}} \left(\frac{\kappa_1}{\kappa_2} - 1 \right) \right\} \quad [5.54]
 \end{aligned}$$

where the last term is the contribution due to static margin. In non-dimensional form Equation [5.54] becomes

$$\left(w_n'\right)_P^2 = - \frac{M_\theta' + M_w'}{m' k'^2} = \left(w_{n_P}\right)^2 \frac{l^2}{U^2} \quad [5.55]$$

For the case of V-foils fore and aft we have $\frac{A}{S} = 1$. If in addition $d_a = d_f = d$, $b_a = b_f = b$ and $(c_w/\bar{c}_s)_f = (c_w/\bar{c}_s)_a$ then

$$\left(w_n'\right)_{P2}^2 = \frac{g}{d} \frac{x_f' x_a'}{k'^2} \left[\left(\frac{c_w}{\bar{c}_s} + b \right) + \frac{d}{l} \frac{C_{L_{\alpha f}}}{C_{L_f}} \left(\frac{\kappa_1}{\kappa_2} - 1 \right) \right] \quad [5.56]$$

$$\left(w_n'\right)_{P2}^2 = \frac{1}{F^2} \frac{l}{d} \frac{x_f' x_a'}{k'^2} \left[\left(\frac{c_w}{\bar{c}_s} + b \right) + \frac{d}{l} \frac{C_{L_{\alpha f}}}{C_{L_f}} \left(\frac{\kappa_1}{\kappa_2} - 1 \right) \right] \quad [5.57]$$

For completely submerged foils aft and V-foils forward Equation [5.54] becomes

$$\begin{aligned} (\omega_n)_{Pl}^2 &= \frac{g}{d_f} \frac{x_a' x_f'}{k'^2} \left[x_f' \left(\frac{c_w}{\bar{c}_s} + b \right) + d_f' \frac{C_{L_{\alpha f}}}{C_{L_f}} \left(\frac{\kappa_1}{\kappa_2} - 1 \right) \right] \\ &+ \frac{1}{2} \rho U^2 \frac{x_a'^2}{k'^2} \left(C_{L_h} \bar{S}_a / m \bar{c}_s \right)_a = (\omega_n)_{Pl}^2 \frac{U^2}{l^2} \end{aligned} \quad [5.58]$$

where the contribution from the last term is usually small for depth-chord ratios near unity or greater. It is seen from Equation [5.56] that, since $d/l \ C_{L_{\alpha f}}/C_{L_f}$ is of the order of 1 or 2 the value of κ_1/κ_2 must be of the order of 1.5 or greater to begin to have a significant effect on ω_{n_p} . According to Equation [5.52] this corresponds to a s.m. of about 0.1 (for $x_a/l = \frac{1}{2}$). On the other hand, for the completely submerged aft foil case it is seen from Equation [5.58] that the relative importance of static margin becomes increasingly great as the value of x_f' becomes smaller.

Effect of Speed - It may be seen from Equation [5.54] that the contribution of $-M_\theta/mk^2$ to $(\omega_n)_p^2$ is inversely proportional to the depth of the surface-piercing foils, d_f and d_a and will depend on speed only insofar as d_f and d_a are permitted to vary with speed. On the other hand the contribution of the last term in

5.54

Equation [5.54] $(-M_w U/mk^2)$ to $(\omega_n)_P^2$ is directly proportional to the velocity squared for a constant value of d_f and d_a .

Uncoupled Pitch Damping Ratio

The uncoupled pitch damping ratio is from Equation [5.23]

$$\zeta_P = \frac{-M_q/I}{2\omega_n P}$$

which gives, with the aid of Equations [5.48], [5.54] and [5.55]

$$\zeta_P = \frac{\sqrt{\frac{x_a' x_f'}{k'^2}} \frac{C_{L\alpha f}}{C_{L_f}} \left(x_f' + \frac{\kappa_1}{\kappa_2} x_a' \right)}{2F \left[\frac{x_f'}{d_f'} \frac{A_f}{S_f} \left(\frac{c_w}{\bar{c}_s} + b_f \right)_f + \frac{x_a'}{d_a'} \frac{A_a}{S_a} \left(\frac{c_w}{\bar{c}_s} + b_a \right)_a \right.}$$

$$\left. + \frac{\rho U^2 \ell}{2mg} \left(\frac{x_f}{x_a} R_f + \frac{x_a}{x_f} R_a \right) + \frac{C_{L\alpha f}}{C_{L_f}} \left(\frac{\kappa_1}{\kappa_2} - 1 \right) \right]^{\frac{1}{2}} \quad [5.59]$$

For the case of two V-foils for which $b_f = b_a = b$, $d_f = d_a = d$

and $(c_w/\bar{c}_s)_a = (c_w/\bar{c}_s)_f$ we have

$$\zeta_P = \frac{\sqrt{\frac{x_a' x_f'}{k'^2}} \frac{C_{L_{\alpha f}}}{C_{L_f}} \left(x_f' + \frac{\kappa_1}{\kappa_2} x_a' \right)}{2F \left[\frac{l}{d} \left(c_w / \bar{c}_s + b \right) + \frac{C_{L_{\alpha f}}}{C_{L_f}} \left(\frac{\kappa_1}{\kappa_2} - 1 \right) \right]}^{\frac{1}{2}} \quad [5.60]$$

For the case of submerged foils aft and V-foils forward we have, on neglecting the small contribution of the aft foil due to the depth effect (the R_a term in Equation [5.54])

$$\zeta_P = \frac{\sqrt{\frac{x_a' x_f'}{k'^2}} \frac{C_{L_{\alpha f}}}{C_{L_f}} \left(x_f' + \frac{\kappa_1}{\kappa_2} x_a' \right)}{2F \left[\frac{x_f'}{d_f'} \left(c_w / \bar{c}_s + b \right) + \frac{C_{L_{\alpha f}}}{C_{L_f}} \left(\frac{\kappa_1}{\kappa_2} - 1 \right) \right]}^{\frac{1}{2}} \quad [5.61]$$

Comparing Equations [5.60] with the uncoupled heave damping ratios given by Equations [5.43] we see that the uncoupled damping ratio in pitch is roughly given by

$$\zeta_P \approx \sqrt{\frac{x_f' x_a'}{k'^2}} \zeta_H \quad [5.62]$$

when $\kappa_1 \approx \kappa_2$. ζ_P is seen to get smaller as x_f' or x_a' become smaller. Representative values for a tandem foil system are $x_f' \approx 1/2$ and $k' \approx 1/3$. Thus the damping ratio in pitch may be as large as about $3/2$ that in heave. The effect of static margin will be to reduce this ratio. If we compare Equations [5.61] and [5.44] for the case where the aft foil is completely submerged we have for the case $\kappa_1 = \kappa_2$

$$\zeta_P \approx \frac{x_a'}{k'} \zeta_H \quad [5.63]$$

For the case of $x_a' = 1/2$ this gives the same result as above, i.e., $\zeta_P/\zeta_H \approx 3/2$. However, in this case ζ_H is $\sqrt{2}$ times as large as for the same case but with V-foils fore and aft. The ratio of ζ_P/ζ_H is seen to get larger as the ratio x_a' is increased. The relative effect of static margin in keeping the magnitude of ζ_P/ζ_H from becoming excessive is greater in these cases than for the case of V-foils fore and aft.

The Coupling Terms

The stability derivatives that account for the principal coupling effects are given in the last term of Equation [5.16]. From Equation [5.60] we have

$$\frac{M_w}{I} = - \frac{g}{U\ell} \frac{x_f'(1 - x_f')}{k'^2} \frac{C_{L_{\alpha f}}}{C_{L_f}} \left(\frac{\kappa_1}{\kappa_2} - 1 \right) \quad [5.64]$$

and

$$\frac{M_w'}{I'} = - \frac{1}{F^2} \frac{x_f'(1 - x_f')}{k'^2} \frac{C_{L_{\alpha f}}}{C_{L_f}} \left(\frac{\kappa_1}{\kappa_2} - 1 \right) \quad [5.65]$$

From Reference (5.5) we find that $Z_q \approx M_w$ so that

$$\frac{Z_q}{m} = - \frac{g\ell}{U} x_f'(1 - x_f') \frac{C_{L_{\alpha f}}}{C_{L_f}} \left(\frac{\kappa_1}{\kappa_2} - 1 \right) \quad [5.66]$$

and

$$\frac{Z_q'}{m'} = \frac{1}{F^2} x_f'(1 - x_f') \frac{C_{L_{\alpha f}}}{C_{L_f}} \left(\frac{\kappa_1}{\kappa_2} - 1 \right) \quad [5.67]$$

From Equations [5.29] and [5.30] we have

$$\frac{Z_w}{m} = - \frac{g}{U} \frac{C_{L_{\alpha f}}}{C_{L_f}} \left(x_a' + \frac{\kappa_1}{\kappa_2} x_f' \right) \quad [5.68]$$

and

$$\frac{Z_w'}{m'} = - \frac{1}{F^2} \frac{C_{L_{\alpha f}}}{C_{L_f}} \left(x_a' + \frac{\kappa_1}{\kappa_2} x_f' \right) \quad [5.69]$$

From Reference (5.5) we make the following approximation for M_h

$$M_h \approx \frac{1}{2} \rho U^2 \sum \left[x \left(C_L c_w \cot \Gamma + C_{L_h} \frac{S \cos \Gamma}{\bar{c}_s} \right) - z \left(C_D \frac{c_w}{|\sin \Gamma|} + C_{D_h} \frac{S}{\bar{c}_s} \right) \right] \approx \sum \left[-x Z_h + z X_h \right] \quad [5.70a]$$

The drag on the struts and surface piercing foils usually accounts for the principal contribution to $\sum z X_h$. Since $\sum z X_h$ is always negative it is clear from the role of M_h in E of Equation [5.17] that $\sum z X_h$ tends to be destabilizing. For completely submerged foil systems this term is a major component of M_h . With the aid

of Equation [5.34] we obtain

$$\begin{aligned} \frac{M_h}{I} \approx \frac{Z_\theta + \Sigma z X_h}{mk^2} \approx \frac{g}{l^2} \frac{x_a' x_f'}{k'^2} \left[\frac{1}{d_f'} \frac{A_f}{S_f} \left(\frac{c_w}{\bar{c}_s} + b_f \right)_f - \frac{1}{d_a'} \frac{A_a}{S_a} \left(\frac{c_w}{\bar{c}_s} + b_a \right)_a \right] \\ + \frac{\rho U^2}{2k^2} \left(\frac{x_f R_f - x_a R_a}{m} \right) + \frac{\Sigma z X_h}{I} \end{aligned} \quad [5.70b]$$

and

$$\begin{aligned} \frac{M_h'}{I'} \approx \frac{Z_\theta' + \Sigma z' X_h'}{m' k'^2} \approx \frac{1}{F^2} \frac{x_a' x_f'}{k'^2} \left[\frac{1}{d_f'} \frac{A_f}{S_f} \left(\frac{c_w}{\bar{c}_s} + b_f \right)_f - \frac{1}{d_a'} \frac{A_a}{S_a} \left(\frac{c_w}{\bar{c}_s} + b_a \right)_a \right] \\ + \frac{\rho l}{2k'^2} \left(\frac{x_f R_f - x_a R_a}{m} \right) + \frac{\Sigma z' X_h'}{I'} \end{aligned} \quad [5.71]$$

since according to Reference (5.5) we also find the following relationships

$$M_h = Z_\theta + \Sigma z X_h \quad \text{and} \quad M_h' = Z_\theta' + \Sigma z' X_h' \quad [5.72]$$

For the case of fore and aft V-foils with $\left(\frac{c_w}{c_s} + b_f\right)_f = \left(\frac{c_w}{c_s} + b_a\right)_a$
we have

$$\begin{aligned} Z_\theta &= M_h - \Sigma z X_h = 0 && \text{when } d_f = d_a . \\ Z_\theta &= M_h - \Sigma z X_h > 0 && \text{when } d_f < d_a . \\ Z_\theta &= M_h - \Sigma z X_h < 0 && \text{when } d_f > d_a . \end{aligned} \quad [5.73]$$

For the case of completely submerged foils aft and a V-foil forward we have, on neglecting the small contribution due to R_a

$$\frac{M_h - \Sigma z X_h}{I} = \frac{g}{\ell d_f} \frac{x_f'(1-x_f')}{k'^2} \left(\frac{c_w}{c_s} + b_f\right)_f = \frac{M_h' - \Sigma x' X_h'}{I'} \frac{U^2}{\ell^3} \quad [5.74]$$

and

$$\frac{Z_\theta}{m} = \frac{g\ell}{d_f} x_f'(1-x_f') \left(\frac{c_w}{c_s} + b_f\right)_f = \frac{Z_\theta'}{m'} \frac{U^2}{\ell} \quad [5.75]$$

It is thus clear that the coupling terms M_h/I and Z_θ/m tend to be largest for tandem systems with submerged foils aft and V-foils forward. From Equation [5.74] and [5.75] it is seen that this varies inversely as d_f .

When the static margin is zero or very small the zeros in the coupling term become very large and are effectively eliminated. By combining Equations [5.67], [5.69], [5.71] and [5.72] we obtain

$$\frac{Z_w' + Z_\theta'}{Z_q'} = \frac{-\frac{C_{L\alpha f}}{C_{L_f}} \left(x_a' + \frac{\kappa_1}{\kappa_2} x_f' \right) + \frac{x_a' x_f'}{d_f'} \left[\frac{A_f}{S_f} \left(\frac{c_w}{\bar{c}_s} + b_f \right)_f - \frac{d_f}{d_a} \frac{A_a}{S_a} \left(\frac{c_w}{\bar{c}_s} + b_a \right)_a \right] + \frac{\rho U^2}{2} \left(\frac{x_f R_f - x_a R_a}{m} \right)}{-x_a' x_f' \frac{C_{L\alpha f}}{C_{L_f}} \left(\frac{\kappa_1}{\kappa_2} - 1 \right)} \quad [5.76a]$$

$$= \left\{ \frac{1}{(s.m.)} - \frac{\left[\frac{A_f}{S_f} \left(\frac{c_w}{\bar{c}_s} + b_f \right)_f - \frac{d_f}{d_a} \frac{A_a}{S_a} \left(\frac{c_w}{\bar{c}_s} + b_a \right)_a \right]}{d_f' \frac{C_{L\alpha f}}{C_{L_f}} \left(\frac{\kappa_1}{\kappa_2} - 1 \right)} - R \right\} \quad [5.76b]$$

The absolute value of this term for s.m. $\ll 1$ is clearly much greater than unity for $Z_\theta' \leq 0$. The maximum positive value that

the numerator of the second term in Equation [5.76a] can achieve is $1/4 d_f' (c_w/\bar{c}_s + b_f)_f$. With the representative values of $d_f' = 1/18$ and $c_w/\bar{c}_s + b_f = 2.5$ this gives for this term a value of 1. which is less than $C_{L_{af}}/C_{L_f} \left(x_a' + \frac{\kappa_1}{\kappa_2} x_f' \right)$ so that the numerator is usually negative or slightly positive in such cases also. Thus for small values of static margin $(Z_w' + Z_\theta')/Z_q'$ is usually much greater than the modulus of the dominant roots $|\sigma_d'|$. For these cases the effect of Z_q' , in Equation [5.16], on the dominant roots is small. This results in the elimination of one of the zeros in Equation [5.24]. Thus

$$\frac{\sigma' Z_q'}{m'} + \frac{Z_w' + Z_\theta'}{m'} \approx \frac{Z_w' + Z_\theta'}{m'}$$

and is usually less than zero.

The other zero in the coupling term of Equation [5.24] can be eliminated in the same manner when $|M_h'/M_w'| \gg |\sigma_d'|$. For these cases we have

$$\frac{\sigma' M_w'}{I'} + \frac{M_h'}{I'} \approx \frac{M_h'}{I'}$$

Thus the numerator of Equation [5.25] for small M_w' reduces to the case given by Equation [5.25d]

$$- \frac{M_h' (Z_w' + Z_\theta')}{m' I'} = - \bar{K}' \quad [5.77]$$

If in addition M_h'/I' or $(Z_w' + Z_\theta')/m'$ is also very small then the coupling is correspondingly small and the stability roots are then essentially those of the uncoupled equations of motion. From Equations [5.70] and [5.71] it is clear that M_h'/I' and hence Z_θ'/m' can be made to take on values varying from large positive (submerged foils aft only) to large negative (submerged foils forward only). Thus a considerable amount of control over this coupling term can be exercised.

EXAMPLE

The following example is selected to illustrate a possible application of the root locus method to stability analysis. The hydrofoil configuration was selected so that variations in the coupling term had a minimal influence on the uncoupled roots. Although this condition makes the stability design problem straightforward it is not a requisite for obtaining useful results by this method.

We consider an area stabilized tandem hydrofoil configuration which has negligible static margin so that the coupling term is given by Equation [5.77]. In addition we assume the c.g. is midway between the center of lift of the forward and aft foil systems. It can be seen by comparing Equations [5.29], [5.38], [5.47] [5.56] and [5.71] that it is possible to make large changes in M_h'/I' by varying the ratio

$$\frac{\frac{1}{d_f'} \frac{A_f}{S_f} \left(\frac{c_w}{\bar{c}_s} + b_f \right)_f}{\frac{1}{d_a'} \frac{A_a}{S_a} \left(\frac{c_w}{\bar{c}_s} + b_a \right)_a}$$

between almost zero (submerged foils forward only) to very much greater than unity (submerged foils aft only) without appreciably affecting Z_w'/m' , Z_h'/m' , M_q'/I' , M_θ'/I' , which determine the uncoupled stability roots. Thus, for this case, a root locus plot will show how the stability roots are affected by the ratio of the degree of area stabilization forward to that aft for various selected sets of uncoupled stability roots. The maximum value of M_h/I under these conditions is, from Equation [5.70] for completely submerged foils aft only, and on neglecting the term in R

$$\left(\frac{M_h}{I}\right)_{\max} \approx \frac{g}{\ell d_f} \frac{\left(\frac{c_w}{c_s} + b_f\right)_f}{4k'^2} + \frac{\Sigma z X_h}{I} = \left(\frac{Z_\theta}{mk^2}\right)_{\max} + \frac{\Sigma z X_h}{mk^2} \quad [5.78]$$

By interchanging the fore and aft foils we have for the minimum value

$$\left(\frac{M_h}{I}\right)_{\min} \approx -\left(\frac{M_h}{I}\right)_{\max} + \frac{2 \Sigma z X_h}{I} = -\left(\frac{Z_\theta}{mk^2}\right)_{\max} + \frac{\Sigma z X_h}{mk^2} \quad [5.79]$$

To non-dimensionalize we multiply through by ℓ^3/U^2

$$\left(\frac{M_h'}{I'}\right)_{\max} = \frac{1}{F^2 d_f'} \frac{\left(\frac{c_w}{c_s} + b_f\right)_f}{4k'^2} + \frac{\Sigma z' X_h'}{m' k'^2} = \frac{Z_\theta' + \Sigma z' X_h'}{m' k'^2} \quad [5.80]$$

From Equations [5.40] and [5.58] we have for the undamped, uncoupled natural frequencies

$$\left(\omega_n\right)_H^2 = \frac{g}{2d_f'} \left(\frac{c_w}{c_s} + b_f\right) \quad ; \quad \left(\omega_{n_H}'\right)^2 = \frac{1}{2F^2 d_f'} \left(\frac{c_w}{c_s} + b\right) \quad [5.81]$$

$$\left(\omega_n\right)_P^2 = \frac{g}{8d_f' k'^2} \left(\frac{c_w}{c_s} + b_f\right) \quad ; \quad \left(\omega_{n_P}'\right)^2 = \frac{1}{4k'^2} \left(\omega_{n_H}'\right)^2 \quad [5.82]$$

From Equations [5.44] and [5.63] we have for the uncoupled damping ratios

$$\zeta_H = \frac{1}{2F} \frac{C_{L_{\alpha f}}}{C_{L_f}} \sqrt{\frac{2d_f'}{\left(\frac{c_w}{c_s} + b_f\right)}} \quad [5.83]$$

5.66

$$\zeta_P = \frac{1}{2k'} \zeta_H \quad [5.84]$$

From Equations [5.18], [5.19] and [5.24] we have for the uncoupled stability roots

$$p_{1,2}' = -\zeta_H \omega_{n_H}' \left[1 \pm \sqrt{\frac{\zeta_H^2 - 1}{\zeta_H}} \right] \quad [5.85]$$

$$p_{3,4}' = -\zeta_P \omega_{n_P}' \left[1 \pm \sqrt{\frac{\zeta_P^2 - 1}{\zeta_P}} \right] \quad [5.86]$$

We take as an example of an application of the foregoing, a boat with the following data

$$F = 1.8 \quad d_f' = 1/16 \quad \frac{c_w}{c_s} + b = 2.5$$

$$\frac{C_{L\alpha}}{C_L} = 15 \quad k' = 1/3 \quad \kappa_1 = \kappa_2 = 1$$

and $\Sigma z'X_h'/m'k'^2$ assumed negligible. From Equations [5.81] and

[5.82] we obtain for the non-dimensional frequencies

$$\omega_{n_H}' = \left[\frac{16 \times 2.5}{2(1.8)^2} \right]^{\frac{1}{2}} = 2.48$$

$$\omega_{n_P}' = \frac{3}{2} \times 2.48 = 3.72$$

From Equations [5.83] and [5.84] we get for the damping ratios

$$\zeta_H = \frac{15}{2 \times 1.8} \sqrt{\frac{2}{16 \times 2.5}} = .93$$

$$\zeta_P = \frac{3}{2} \times .93 = 1.40$$

From Equations [5.85] and [5.86] we get for the stability roots for the uncoupled heave and pitch modes

$$p_{1,2}' = - .93 \times 2.48 \left[1 \pm i \frac{\sqrt{.14}}{.93} \right] = -2.31 \pm .93 i$$

$$p_{3,4}' = -1.40 \times 3.72 \left[1 \pm \frac{\sqrt{.96}}{1.40} \right] = -1.56 \text{ and } -8.8$$

5.68

From Equations [5.77] and [5.80] we get for the coupling constant when M_h'/I' is maximum

$$\begin{aligned}\bar{K}' &= -\left(\frac{M_h'}{I'}\right)_{\max} \left[\frac{Z_w' + Z_\theta'}{m'} \right] = -\frac{2.5 \times 16 \times 9}{(1.8)^2 \times 4} \left[\frac{-15}{(1.8)^2} + \frac{2.5 \times 16}{(1.8)^2 \times 4} \right] \\ &= -27.8 [-4.63 + 3.09] = 43\end{aligned}$$

Since Z_w'/m' is a negative constant, a possible maximum exists for some value of M_h'/I' between zero and 27.8. If r is the ratio between this value and 27.8 we have for the equation for r , since $M_h' \approx Z_\theta'$

$$\frac{d}{dr} \left\{ -27.8r \left[-4.63 + 3.09r \right] \right\} = 0$$

which yields

$$r = \frac{4.63}{2(3.09)} = .75$$

The maximum value of the coupling term is then

$$\bar{K}'_{\max} = -.75(27.8) [-4.63 + .75(3.09)] = 48.3$$

The minimum value for the coupling term is obtained by reversing the sign of M'_h and Z'_θ , thus

$$\bar{K}'_{\min} = 27.8 [-4.63 - 3.09] = -214$$

The locus of the stability roots for this range of coupling values is shown in Figure 5.6. The points marked by crosses (x) represent the stability roots for the uncoupled heave mode and the points marked by triangles (Δ) represent the roots for the uncoupled pitch mode.

The construction of the root locus plot is facilitated by making the following observations: *

1. For $\bar{K}' > 1$ the real axis locus must lie between the two real roots. For $\bar{K}' < 1$ the real axis locus lies outside the two real roots.

2. There are four loci and four asymptotes to infinity since there are four roots and no zeros.

3. The asymptotes are as follows: For $\bar{K}' > 1$ they lie along lines given by $\frac{(1 + 2m)180^\circ}{4}$. These are given by angles

* More details on the method, are contained in standard texts. See References 5.19 or 5.20 for example.

of $\pm 45^\circ$ and $\pm 135^\circ$. For $\bar{K}' < 1$ they lie along lines given by $\frac{(2m)180^\circ}{4}$. These are given by 0° , $\pm 90^\circ$ and 180° .

4. The intersection point of the asymptotes lies at the center of gravity of the poles since there are no zeros. This point is given by

$$\sigma_0' = \frac{-(2.31 + 2.31 + 1.56 + 8.8)}{4} = -3.75$$

5. The breakaway point σ_1' on the real axis between -1.56 and -8.8 is found from

$$-\frac{1}{\ell_2} - \frac{1}{\ell_1} - \frac{2b}{b^2 + \omega_1'^2} = 0$$

where the ℓ 's, ω_1' , b are defined on Figure 5.4. By trial and error $\sigma_1' = -7.0$ corresponding to $\ell_1 = 5.4$, $\ell_2 = -1.8$ and $b = 4.7$.

6. The angle of departure from the pole $-2.31 + .93j$ is obtained from Φ_4 in the following equation

$$\Phi_1 + \Phi_2 + \Phi_3 + \Phi_4 = (1 + 2m)180^\circ$$

$$8^\circ + 90^\circ + 129^\circ + \Phi_4 = (1 + 2m)180^\circ$$

$$\therefore \Phi_4 = -47^\circ$$

7. The frequency at which the oscillatory root becomes unstable was not computed separately in this case. However it is readily found by setting Routh's discriminant equal to zero and solving for \bar{K}' . The desired frequency is then obtained by putting $\sigma' = i\omega'$ in Equation [5.12] and solving the imaginary equation

$$\omega' = \sqrt{\frac{D}{B}}$$

where the above found value of \bar{K}' is substituted in the expression for D.

8. Since Z_w'/m' and M_q'/I' are held constant the sum of the roots must remain constant. Thus the real parts of the smallest roots tend to move in opposite directions as the coupling term changes in magnitude.

The above relationships were sufficient guides in this case so that with the aid of the Spirule the root-locus plot on Figure 5.6 was readily drawn. The arrow is drawn in the direction of increasing value of M_h'/I' . It is seen that for the case of the completely submerged foil aft and V-foil forward ($\bar{K} = +43$) the dominant stability roots are the complex pair which have a value of $\sigma_c' = -1.3 \pm 1.5i$ and a damping ratio $\zeta = 0.65$. As the value of M_h'/I' is decreased it is seen that this root first becomes less stable and then reverses at a value of $\bar{K}' = 48.3$ becoming again more stable. At a value of $\bar{K}' = +3$ it is seen that the real part of this root is equal to the minimum real root. At this point the complex root is $\sigma_c' = -2.1 \pm 0.75i$ and the

least stable real root has a value of about -2.1 also. This is the point at which the least stable mode has the maximum rate of decay. Furthermore, it is seen that the value of ζ is 0.94 thus indicating negligible overshoot and apparent desirable frequency response characteristics. As \bar{K}' is decreased further the value of ζ for the complex root becomes smaller and the root approaches the 90° asymptote with a real part of -3.75. The smallest real root continues to move to the right leading to a divergence type of instability at $\bar{K}' = -88$. This is the condition for $E = 0$ in the characteristic equation [Equation 5.12]. The portion of the root-locus plot shown by the broken lines gives the stability roots for values of \bar{K}' beyond the range obtainable in this example. Familiarity with root-locus plots enables the designer to determine the effect of changing the uncoupled roots quite readily.

Figure 5.6 reveals a considerable amount of information about the stability of the boat. It indicates that a relatively small amount of coupling, obtained by making the area stabilization forward slightly greater than aft would maximize the stability of the least stable mode. Since this result leads to values of A_f/\bar{S}_f and A_a/\bar{S}_a which are less than unity it is possible to increase the foil depth if desired since the degree of area stabilization is essentially determined by the product

$\frac{1}{d'} \frac{A}{\bar{S}} \left(\frac{c_w}{c_s} + b \right)$ at the forward and aft foils respectively. Figure

5.6 also shows the sensitivity of the stability to variations in

the distribution of area stabilization. It reveals, graphically, the manner in which the coupling alters the uncoupled stability roots.

Effect of Speed - The effect of changing speed on the uncoupled stability roots is readily determined from Equations [5.81] - [5.86]. It is apparent that as the speed changes and for d_f' constant, $\zeta_H(\omega_n')$ and $\zeta_P(\omega_n')$ remain approximately constant. While ζ_H and ζ_P increase directly with speed. Thus with decreasing speed the real part of the complex roots remain constant but the imaginary part increases. Simultaneously the roots due to uncoupled pitch move closer together and eventually form a complex pair when $\zeta_P = 1$; at which point the real part remains constant while the imaginary part increases with further reduction in speed. This pattern of behavior is clearly illustrated in Figure 4 of Reference (5.22) and Figure 49 of Reference (5.12) (in dimensional form), for the case where the coupling terms are small, i.e., surface piercing foils fore and aft. For increasing speed the complex roots move together, while maintaining a constant real part, and split into two real roots after joining on the real axis. Since ζ_P increases while $\zeta_P(\omega_n')$ does not the two real roots due to the uncoupled pitch move further apart. The effect of positive coupling ($\bar{K}' > 0$), when all the uncoupled roots are real, is to cause the two least negative roots (uncoupled pitch and heave roots) to move toward each other and for large enough \bar{K}' form a complex pair. The behavior of the two most negative roots is similar. For negative coupling the least negative root

moves in the direction of the positive real axis toward $+\infty$ while the most negative real root moves in the opposite direction. The remaining real roots move together to form a complex pair and eventually move out toward the 90° and 270° asymptotes for large enough negative values of \bar{K}' .

It is clear from the foregoing example that the application of the root locus method in the determination of the stability of area-stabilized hydrofoil boats can furnish considerable insight to the designer. Familiarity and experience with the general construction of such plots is of course important, especially in applications where there is a zero or two and a given parameter variation changes more than one variable at a time. However only four loci are involved and the root loci of most hydrofoil boats have a good deal of similarity. Undoubtedly the root locus method will not be of practical use in all stability studies of area-stabilized craft. However, it can be an extremely useful tool in some problems in stability analysis and design of area-stabilized boats and its use should always be considered.

CONCLUDING REMARKS

The first part of this chapter presents a derivation of the characteristic equation of the hydrofoil boat together with a discussion of some of the simplifications possible and methods of determining the stability. Since the coefficients of the characteristic equation are given in terms of the stability derivatives it is necessary to obtain these derivatives preferably from model data or by the use of detailed estimating procedures such as those described in Reference 5.5. Although this procedure is feasible

once a design is reasonably well established it may be expensive and time consuming in the preliminary stages of design. Therefore simplifying approximations have been derived for many of the formulas for the stability derivatives given in Reference 5.5 and methods of relating these to the uncoupled stability roots have been given. Furthermore, the effects of coupling on the uncoupled stability roots has been treated in conjunction with the application of Evans root locus method of solving characteristic equations. It is felt that this procedure offers a useful additional tool to the designer in the preliminary synthesis of area stabilized hydrofoil systems. It should be emphasized that once a desirable arrangement is found by the approximate formulas referred to above more exact calculations should be made.

REFERENCES

- 5.1. Martin M., "Equations of Motion for Hydrofoil Craft," HYDRONAUTICS, Incorporated Report 001-9, 1962.
- 5.2. Kaplan, Paul, "Longitudinal Stability and Motions of a Tandem Hydrofoil System in a Regular Seaway," Davidson Laboratory Report No. 517, December 1959.
- 5.3. Ogilvie, T.F., "The Theoretical Predictions of the Longitudinal Motions of Hydrofoil Craft," David Taylor Model Basin Report 1138, November 1958.
- 5.4. French, H.R., Holgate, T.A. and Jamieson, J.J., "System Dynamics for a Craft with Submerged Hydrofoils," Proc. Hydrofoils and Air Cushion Vehicles, Washington, D. C., September 1962 (published by IAS).
- 5.5. Martin, M., "The Stability Derivatives of a Hydrofoil Boat"-Part I and II, HYDRONAUTICS Report 001-10(I) and 001-10(II), 1963.
- 5.6. Connors, J. L., Mass. Inst. Tech. Flight Control Lab., Report FCL-7203-R11, May 1955, Confidential.
- 5.7. "Flying Qualities of Piloted Aircraft, USAF Spec. 1815-B, 1948.
- 5.8. Anderson, Seth B., "An Examination of Handling Qualities Criteria for V/STOL Aircraft, NASA TN D-331, July 1960.
- 5.9. Eisenberg, P., "Considerations of Hydrofoil Boat Handling and Motions Qualities," HYDRONAUTICS Report 001-4, October 1960.

- 5.10. Newell, F., and Rhoads, D.W., "Flight Evaluations of the Effect of Variable Phugoid Damping in a JTB-26B Airplane," WADC Tech. Report 56-223, ASTIA Document No. 118103, December 1956.
- 5.11. Chalk, C.R., "Additional Flight Evaluations of Various Longitudinal Handling Qualities in a Variable-Stability Jet Fighter," WADC Tech. Report 57-719, Part I, ASTIA Document No. 142184, January 1958.
- 5.12. Chuck, G., R.K.C. Luke and S. J. Scroggs, "Study of Hydrofoil Stability and Control," Hughes Aircraft Report No. SRS-399, Eng. Div., Aerospace Group, December 1960.
- 5.13. Kaplan, P., and Jacobs, W.R., "Dynamic Performance of Scaled Surface-Piercing Hydrofoil Craft in Waves," Davidson Laboratory Report No. 704, June 1959.
- 5.14. Routh, E.J., "Dynamics of a System of Rigid Bodies," 6th ed., Macmilland and Co., London, 1905.
- 5.15. Duncan, W.J., "Control and Stability of Aircraft," Cambridge University Press, 1952.
- 5.16. Lin, Chek-Nge, "Method of Successive Approximations of Evaluating the Roots of Cubic and Higher Equations," Journal of Mathematics and Physics, vol. 20, 1941.
- 5.17. Friedman, B., "Note on Approximating Complex Zeros of a Polynomial," Communications on Pure and Applied Mathematics, v. 2, n. 2, June 1949.
- 5.18. Zimmerman, C.H., "An Analysis of Longitudinal Stability in Power-Off Flight, With Charts for Use in Design," NACA Report 521, 1935.
- 5.19. Evans, W.R., "Control System Dynamics," McGraw-Hill Book Company, Inc., New York, 1954.

- 5.20. D'Azzo, J.J., and Houppis, C. H., "Control System Analysis and Synthesis," McGraw-Hill Book Company, Inc., New York, 1960.
- 5.21. Weinblum, Georg P., "Approximate Theory of Heaving and Pitching of Hydrofoils in Regular Shallow Waves," David Taylor Model Basin Report C-479, October 1954.
- 5.22. Chuck, G., and Luke, R.K.C., "Longitudinal Stability and Control of Canard Hydrofoil Craft," Hughes Aircraft No. SRS-440, Eng. Div., Aerospace Group, June 1961.

TABLE 5.1
Summary of Craft Characteristics
(Velocity = 40 knots)

Symbol	Characteristic	Configuration				
		1	2	3	4	5
D	Displacement, lbs	30,000	30,000	30,000	29,450	27,422
LOA	Length overall, ft	40.0	40.0	40.0	34.4	37.0
k	Long.rad.of gyr.,ft	9.21	9.21	9.21	7.93	8.50
x_f	C.G. to fwd foil,ft	9.63	9.63	9.63	14.49	7.94
x_a	C.G. to aft foil,ft	19.26	19.26	19.26	17.01	15.88
\bar{S}_f	Area fwd.foil,ft ²	22.00*	22.00*	22.00*	11.70*	21.62*
\bar{S}_a	Area aft foil,ft ²	10.23	15.00	13.10	12.13*	11.68
C_{L_f}	Lift coef.fwd.foil	0.200	0.200	0.200	0.298	0.185
C_{L_a}	Lift coef.aft foil	0.215	0.147	0.168	0.244	0.171
$C_{L_{\alpha f}}$	Lift slope fwd foil	3.13	3.13	3.13	3.02	3.23
$C_{L_{\alpha a}}$	Lift slope aft foil	3.83	3.81	2.94	3.24	3.92
Γ_f	Dihedral fwd., deg	38	38	38	42	38
Γ_a	Dihedral aft, deg	0	0	45	56	0
\bar{c}_f	Mean chord fwd.,ft	3.00*	3.00*	3.00*	2.17*	2.91*
\bar{c}_a	Mean chord aft,ft	--	--	1.75	2.17*	--
d_f	Submergence fwd.,ft	2.54	2.54	2.54	2.09	2.57
d_a	Submergence aft,ft	2.50	2.50	3.75	2.09	3.34

* Includes factor of 2 to account for number of foils.

Note: The effect of C_{L_h} was not taken into account in these calculations.

TABLE 5.2

Stability Constants of Five Area Stabilized Boats

Stability Constant	Configuration				
	1	2	3	4	5
σ_1	-16.71	-22.22	-15.75	-19.28	-16.74
σ_2	- 8.01	- 9.44	- 7.21	- 5.63	-11.00
Re $\sigma_{3,4}$	- 0.44	- 0.47	- 1.20	- 1.35	- 0.37
$\pm \text{Im } \sigma_{3,4}$	1.86	1.78	1.33	2.34	2.89
$\zeta_{3,4}$.23	.26	.67	.50	.13
$(T_{\frac{1}{2}})_{3,4}$ sec.	1.55	1.45	.57	.51	1.85
$(N_{\frac{1}{2}})_{3,4}$.45	.41	.12	.19	.85

Table 5.3(a) - Comparison of Amplitudes of Vertical Displacement on the Basis of Root Mean Square
 U = 40 knots - Following Seas

Configuration	Forward Foil Wind Speed knots			Aft Foil Wind Speed knots		
	18	14	10	18	14	10
1	5.4	3.0	.85	4.9	2.8	.77
2	5.1	2.8	.74	4.7	2.6	.71
3	4.1	2.1	.53	3.5	1.8	.49
4	3.6	1.8	.51	2.8	1.4	.44
5	5.5	3.1	.88	5.1	3.0	.86

Table 5.3 (b) - Probability of Foil Emergence

1	.080	.017	--	.058	.007	--
2	.080	.013	--	.047	.004	--
3	.036	.001	--	--	--	--
4	.017	--	--	--	--	--
5	.098	.017	--	.027	.001	--

TABLE 5.4

The Non-Dimensional System

Dimensional Quantity	Divisor	Non-Dimensional Quantity
X, Z	$\frac{1}{2}\rho U^2 A_r$	X', Z'
M	$\frac{1}{2}\rho U^2 A_r l$	M'
u, w, \dot{h}	U	u', w', \dot{h}'
$\dot{u}, \dot{w}, \ddot{h}$	U^2/l	$\dot{u}', \dot{w}', \ddot{h}'$
$D = \frac{d}{dt}$	U/l	D'
p, σ , ω , q	U/l	p', σ' , ω' , q'
d_f, d_a, x_f, x_a, k, h	l	$d_f', d_a', x_f', x_a', k', h'$
\dot{q}	U^2/l^2	\dot{q}'
m	$\frac{1}{2}\rho A_r l$	m'
I	$\frac{1}{2}\rho A_r l^3$	I'
$T_{\frac{1}{2}}$	l/U	$T_{\frac{1}{2}}'$

HYDRONAUTICS, INCORPORATED

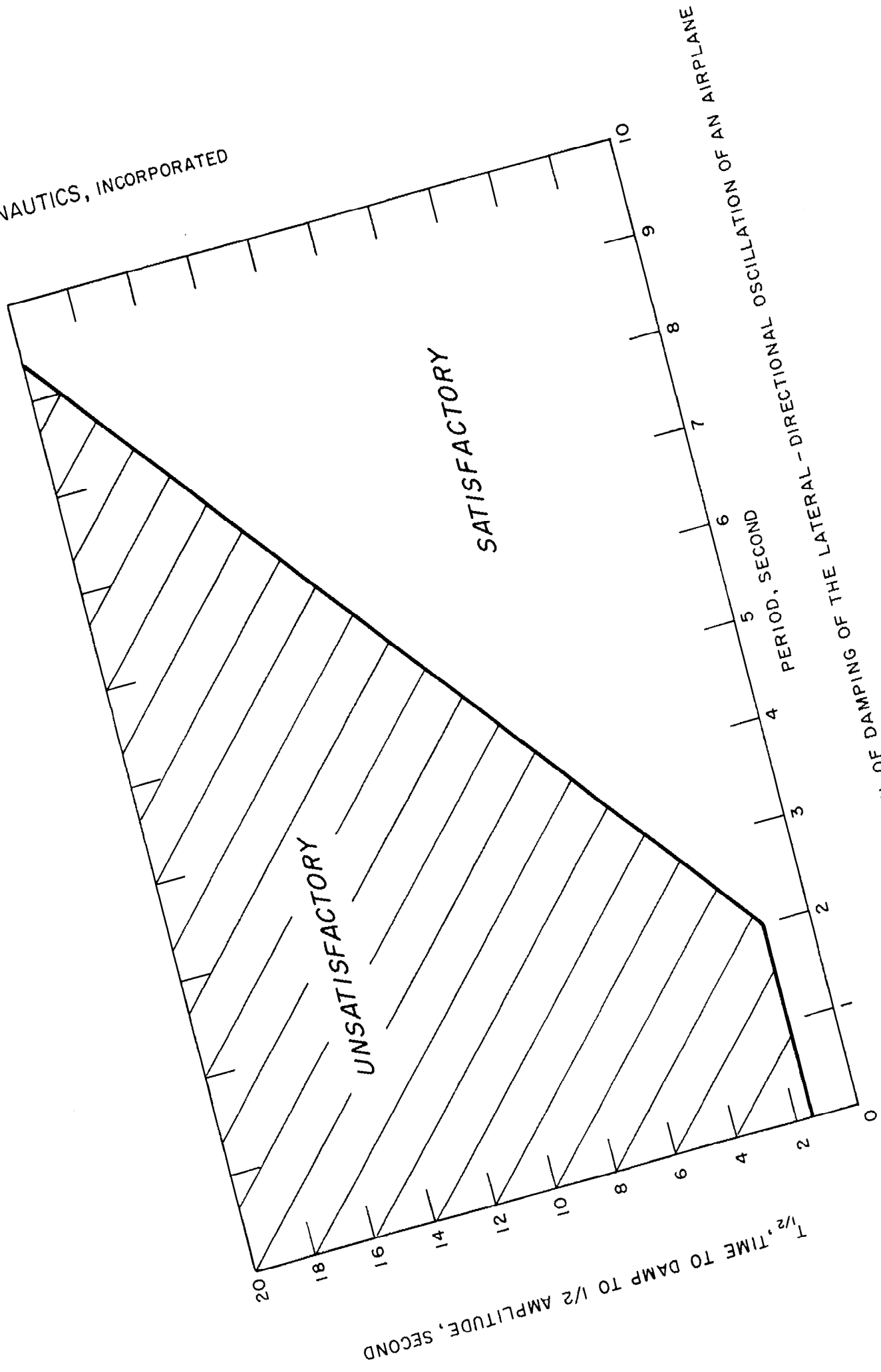


FIGURE 5.1- EXAMPLE OF SPECIFICATION OF DAMPING OF THE LATERAL-DIRECTIONAL OSCILLATION OF AN AIRPLANE

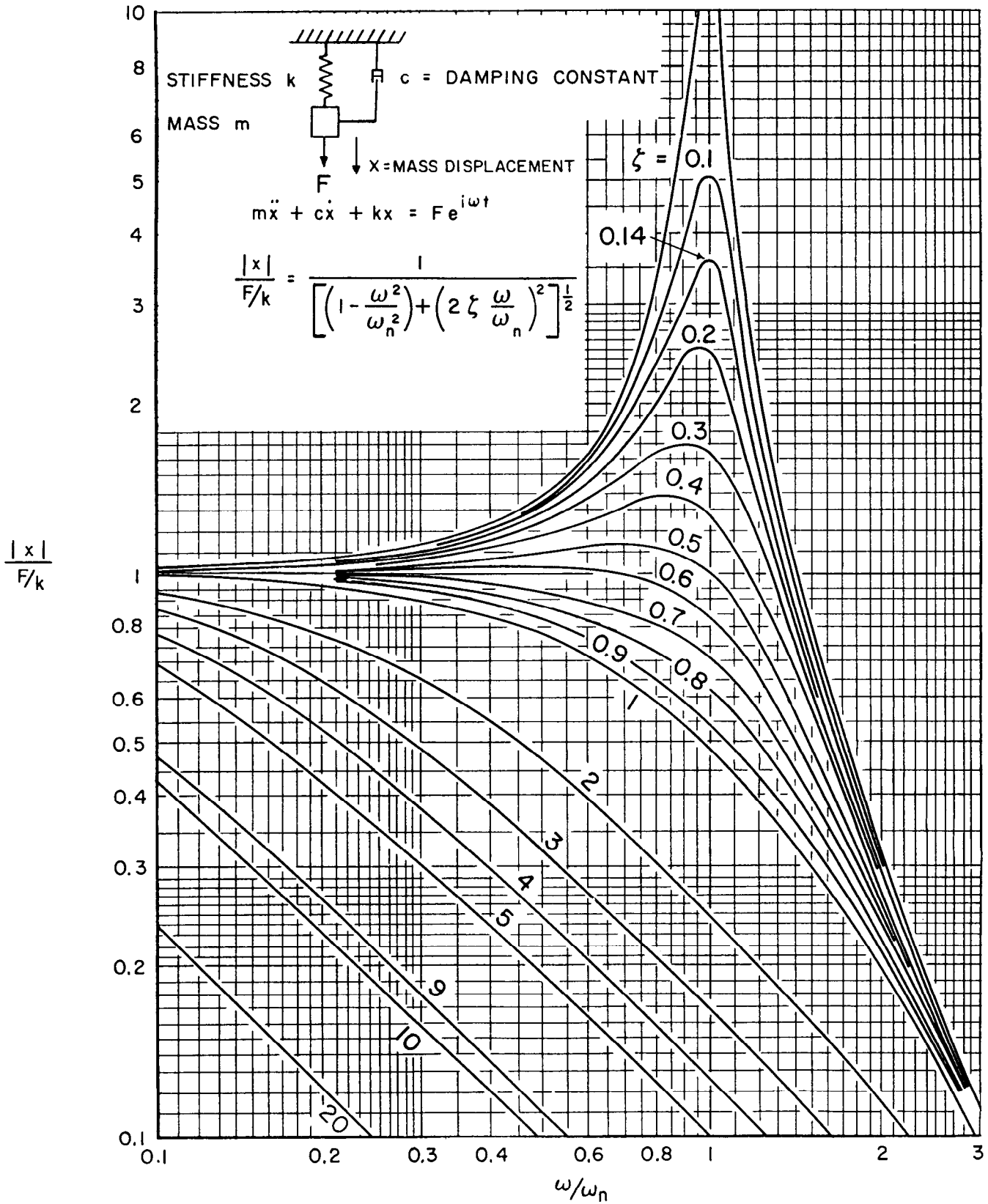


FIGURE 5.2— AMPLITUDE RESPONSE OF SECOND ORDER LINEAR SYSTEM

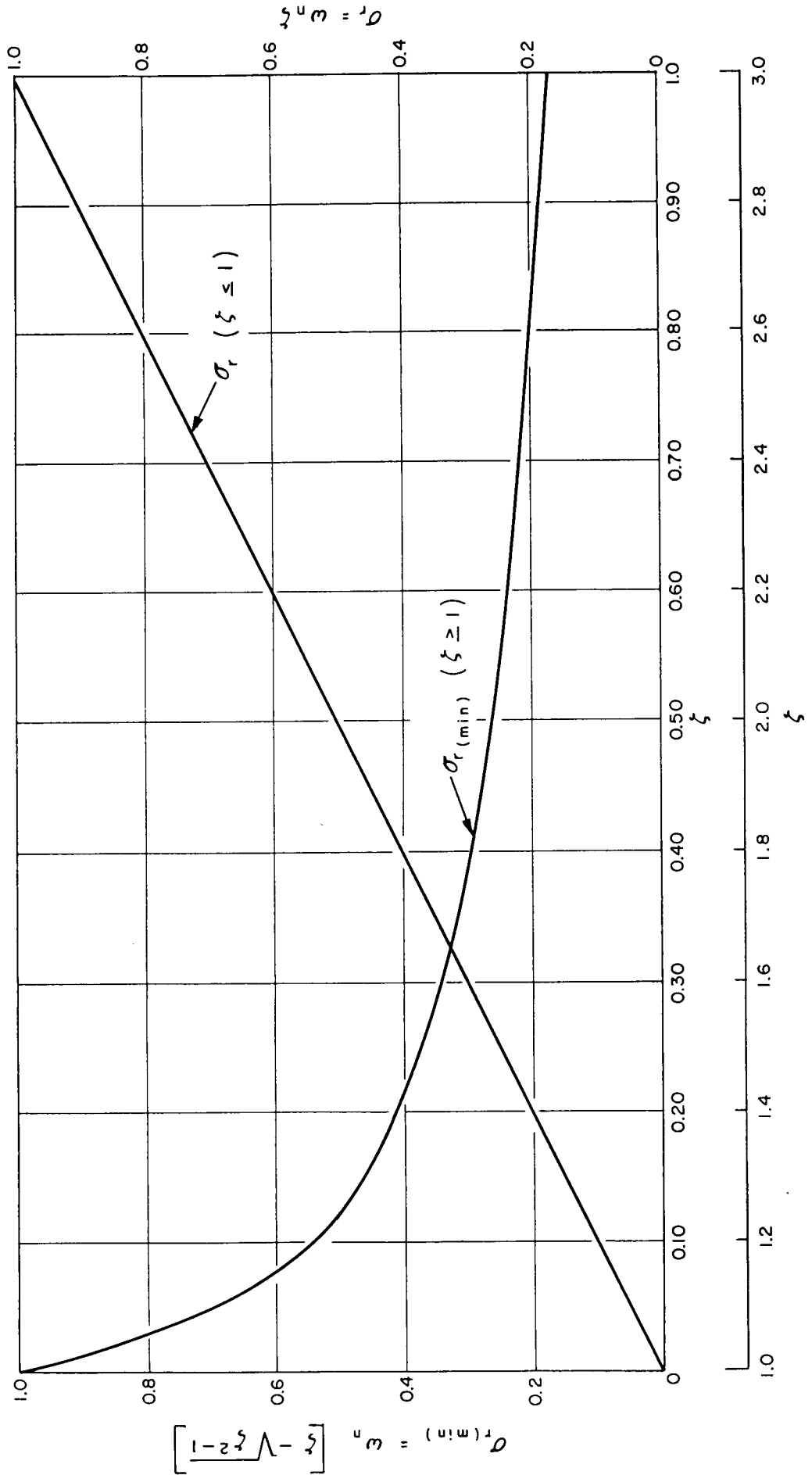


FIGURE 5.3-- VARIATION OF SMALLEST REAL ROOT WITH DAMPING RATIO FOR A SECOND ORDER LINEAR OSCILLATION ($\omega_n = 1$)

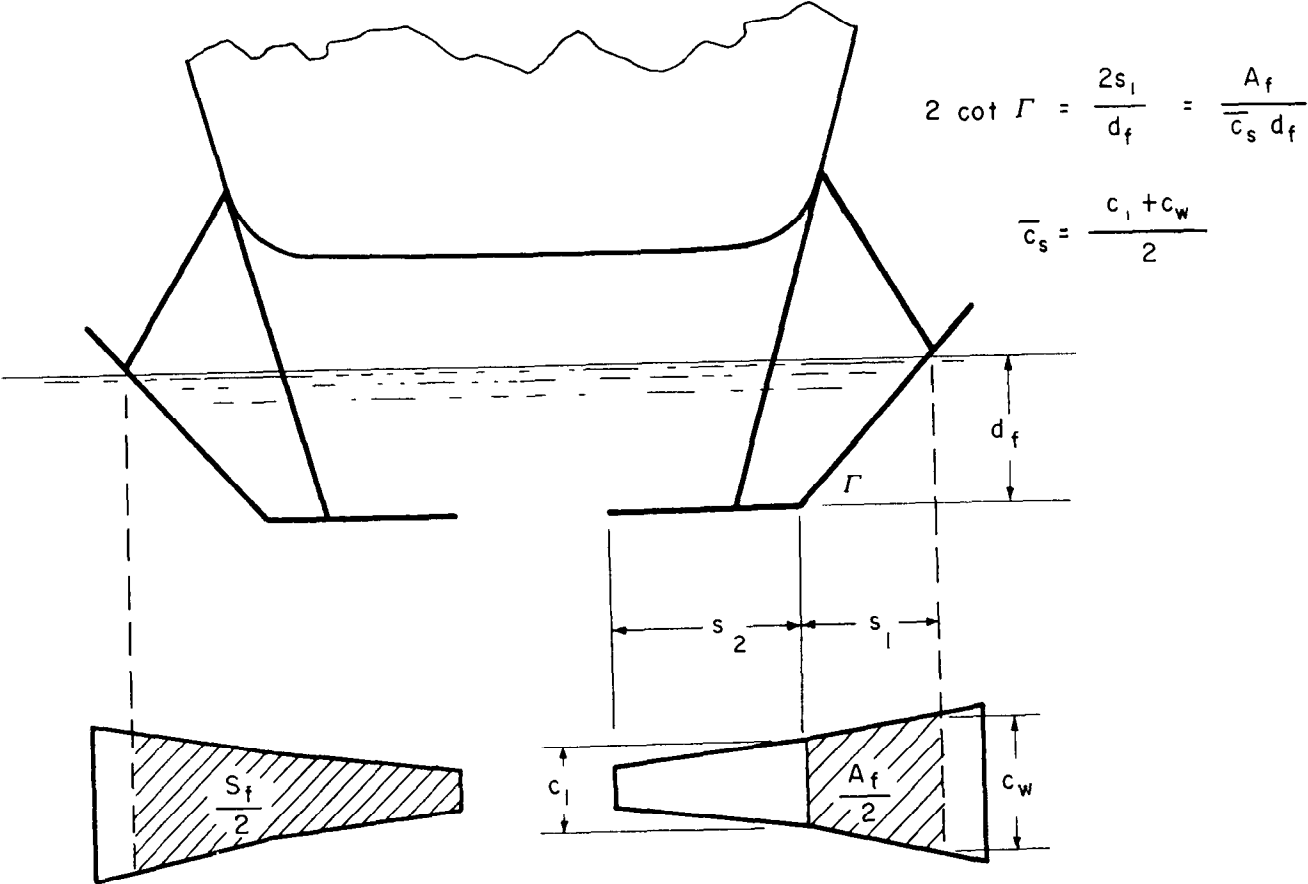


FIGURE 5.5— DEFINITION SKETCH

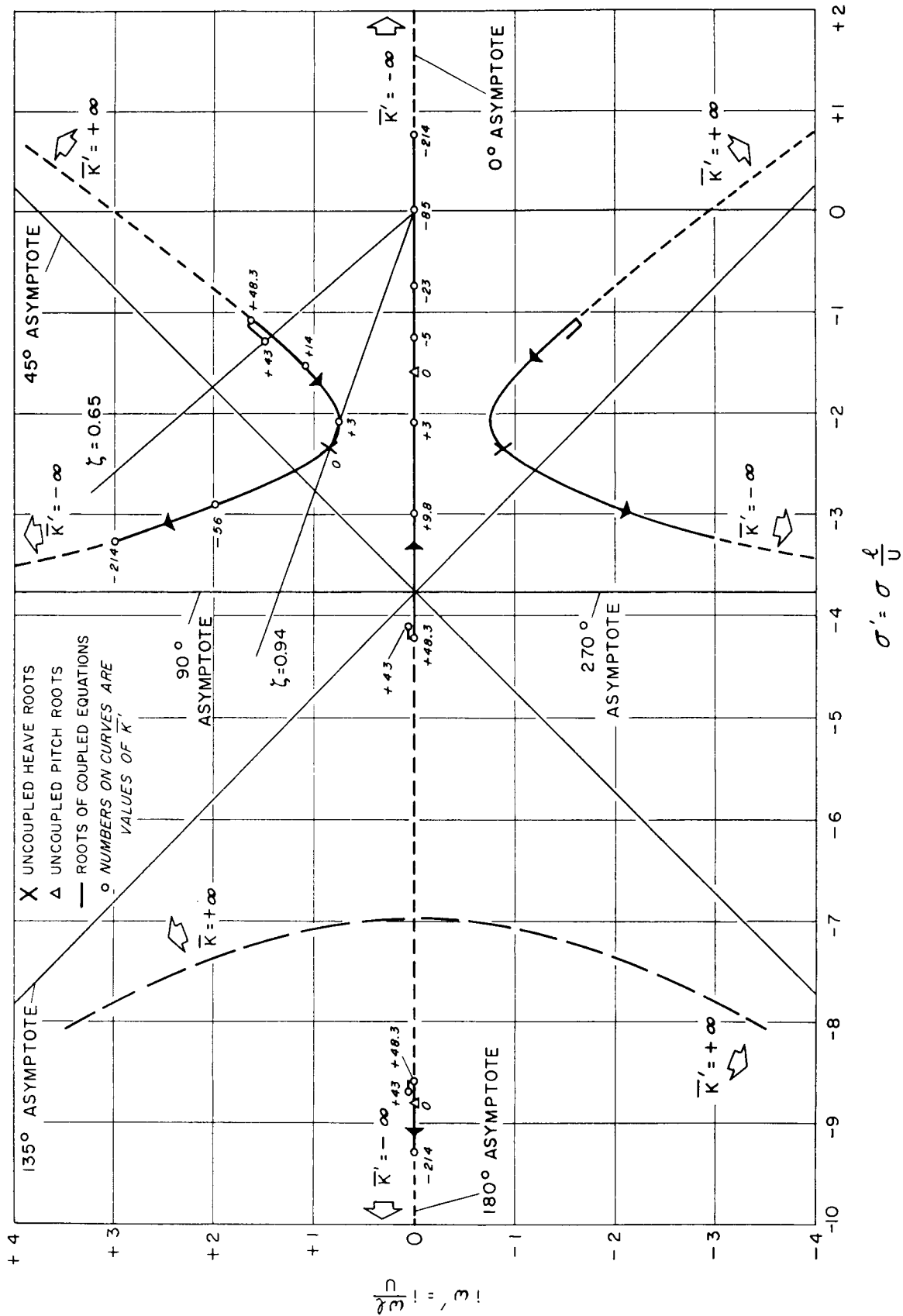


FIGURE 5.6— ROOT LOCUS PLOT FOR TANDEM FOIL SYSTEM EXAMPLE